ESA-QCA00109T-C

EUROPEAN SPACE AGENCY
CONTRACT REPORT

The work described in this report was done under ESA contract. Responsibility for the contents resides in the author or organisation that prepared it.

FINAL REPORT

Proton Radiation Testing of CCDs for the SILEX Programme

Author: G R Hopkinson

ESTEC ORDER No: 103607
SIRA REFERENCE No: A/9058/00

AUGUST 1991

SIRA RESEARCH & DEVELOPMENT

RESEARCH & DEVELOPMENT

SIRA LTD · SOUTH HILL · CHISLEHURST · KENT · BR7 5EH · ENGLAND
TELEPHONE: 081 467 2636 · INTERNATIONAL: + 44 81 467 2636
TELEX: 896649 · FACSIMILE: 081 467 6515

Sira Ltd is an independent organisation, incorporated in 1918, which operates internationally providing laboratory and engineering services for research, development, evaluation and applications of scientific and industrial instrumentation and control equipment.

The Research and Development Division undertakes research, development, design applications and consultancy with multi-disciplinary teams of engineers and scientists. The Division also supplies contracting services to national and international procurement agencies and engineered equipment on a commercial basis for specialist applications.

Quality Assurance registered to AQAP 1.

EUROPEAN SPACE AGENCY CONTRACT REPORT

The work described in this report was done under ESA contract. Responsibility for the contents resides with the author or the organisation that prepared it.

Final Report

Proton Radiation Testing of CCDs for the SILEX Programme

ESTEC Order No: 103607
Sira Reference No: A/9058/00

Author: G R Hopkinson

August 1991

Approved to AQAP 1
Registration No. 3873.01

Proton Radiation Testing of CCDs for the SILEX Programme

FINAL REPORT

ESTEC Order No: 103607
Sira Contract No: A/9058/00

Issue	Final
Authorisation	
Date	August 1991

CONTENTS

CONTENTS (continued)

1. EXECUTIVE SUMMARY

This report describes the results of 1.5 and 10 MeV proton radiation testing of two types of CCDs proposed for use in the SILEX programme for intersatellite communication links. The Thomson-CSF 14x14 pixel THX31160-1 device (for the tracking sensor) and the 288x384 pixel TH7863 device (for the acquisition sensor).

Four devices of each type were irradiated, two at 1.5 MeV and two at 10MeV. In each case one CCD was biased, and one not, during irradiation. The TH7863 devices received proton fluences calculated to give doses of 0, 3, 6 and 9 krad(Si) on separate parts of the CCD and the THX31160-1s received a single dose of 6 krad(Si). Low energy proton beams were used because time was conveniently available on the Tanden Van de Graaff accelerator at AEA Technology, Harwell, UK. This machine is the only one readily available in the UK with an energy as high as 10 MeV.

The results indicate that the damage caused by ionisation and charge trapping in the gate oxide layers of the CCDs is broadly similar to that found from a previous study of Co^{60} gamma ray effects [1]. However, although Co^{60} tests should be a good simulation of a predominantly high energy (~100 MeV) environment such as is found in space, the damage reduces as the proton energy is decreased so that at 10 MeV the effects are reduced by a factor 2-3 and by a greater factor at 1.5 MeV. It was found that the surface dark current originating from the CCD storage region (which is masked by an aluminium layer) quickly increased by a large factor and thereafter remained largely unchanged with long term storage after irradiation (as found for Co^{60} damage). Whereas the build up of dark charge in the image region was negligible until a high temperature annealing step was performed. In the Co^{60} tests the build up of damage in the image region was also slow but could be observed over periods of ~1 month for room temperature storage. Thus the activation energy for image area dark charge reverse annealing is increased somewhat in this case.

Increases in threshold voltages and power consumption, due to ionisation damage, were fully described in the previous report. Additional measurements were made here to confirm that no new effects are caused by proton rather than Co^{60} damage.

The opportunity of measuring full well capacity by spot-illumination was taken and it was found that for the TH7863 this parameter was reduced to ~6.4×10^5 electrons from its value of ~10^6 electrons as measured for uniform illumination in the Co^{60} study [1]. Further decreases occurred after irradiation. No changes in full well capacity were observed for the THX31160-1.

Lattice displacement damage is of low importance for gamma ray irradiation and a study of bulk effects was the main justification for the present proton campaign. Changes in dark current non-uniformity were studied in detail at a variety of CCD operating temperatures and storage times. It was found that dark current increases were independent of bias state during irradiation and, in the main, the radiation-induced dark current varied in the way expected for silicon. It was found that the amount of bulk damage decreased with storage at room temperature (and also after an anneal at high temperature). Some dark current spikes showed somewhat erratic behaviour and this is attributed to generation in regions of the CCD where there is a high electric field.

At room temperature the bulk-induced dark current for Thomson-CSF devices is of order a few nA/cm^2 and so is smaller than the changes in storage region dark current due to ionisation effects.

Modelling of the generation of dark charge nonuniformity was considered in detail in order to try and understand how performance might be predicted for other radiation environments. It was found that a dark current density of approximately 2.4 nA/cm^2 was

generated for the TH7863 device for every 1 MeV of non-ionising energy deposited in the lattice.

It was found that there was no appreciable degradation in CCD charge transfer efficiency (CTE) caused by the proton bombardment.

Dark current measurements were also made on two 288x385 pixel CCD-02 devices manufactured by EEV, UK. These showed smaller increases in dark current than the Thomson-CSF CCDs. Performance for these was compared for normal operation and operation in a mode (termed partial inversion) in which surface generated dark charge is partially suppressed. This latter mode of operation is not available for standard Thomson-CSF devices. However Thomson-CSF (and EEV) have recently developed special purpose CCDs which allow fully inverted operation with the surface dark current suppressed by a factor ~100. These devices are not being considered for SILEX however.

2. INTRODUCTION

This study is concerned with the proton radiation testing of Thomson-CSF CCDs for use in the SILEX programme for intersatellite communications links.

The report follows on from a previous study [1] on Co^{60} effects on these devices. The reason for performing this second set of irradiations is that cobalt 60 gamma rays, although useful for predicting ionization damage effects in the gate oxide and the SiO_2/Si interface, do not simulate the bulk displacement damage which accompanies the ionization damage in a space environment. Protons of low energy (1.5 and 10 MeV) were employed since these were conveniently available at the Tandem Van de Graaff accelerator at AEA Technology, Harwell, UK and the data can be used to predict the effects for the shielded proton spectrum encountered in space (which ranges from 0 to several hundred MeV).

Results are also presented on proton damage effects in EEV CCDs. This information has been gathered as a result of Sira internal Research & Development programmes but is included here for comparison purposes.

Now that both Co^{60} and proton data is available on Thomson-CSF devices it is possible to give a fairly complete description of the effects to be expected in space, although performance analysis of the SILEX instruments is not within the scope of the present report; nor is the prediction of the radiation environment behind the instrument shielding.

2.1 Background

The Semiconductor Laser Experiment (SILEX) is a communications system which uses semiconductor (GaAl/As) laser diodes as transmitters and silicon avalanche photodiodes (APDs) as receivers. Forward and return links are baselined at 819nm and 847nm wavelengths respectively. The primary aim is to set up communications terminals on the French SPOT4 earth observation satellite which is to be in low earth orbit (LEO) and on the ESA PSDE/SAT2 satellite (now called ARTEMIS) which is to be in geosynchronous orbit (GEO). These terminals will be used to establish a high data rate inter-orbit link (IOL) between the two satellites.

Because of limitations in the power available from laser diodes, high speed optical communication over large distances (up to 45000km in this case) is only possible because of the high antenna gain which is achievable at optical frequencies. However this entails highly directional beams with divergences in the sub arc second range. Accordingly beam pointing and tracking is an important issue.

In SILEX there are systems in each terminal for first acquiring either the communications beam or a beacon signal from a large field of view and then for accurate tracking. The acquisition sensors are baselined to use the TH7863 288x385 pixel CCD as a detector and it is proposed that the tracking sensors will use the 14x14 THX31160-1 CCD.

The performance of these CCDs is clearly directly related to that of the servo system which maintains the communications link. Since one terminal is in GEO and one in LEO the CCDs must be capable of withstanding the radiation environment in these orbits for a period of several years. This environment consists of electrons, protons and heavy ions which are a) trapped by the earth's magnetic field or b) in direct transit from the Sun or from other sources in the galaxy.

In LEO the majority of electrons have energy less than 5 MeV and are easily absorbed by the spacecraft and instrument structure before reaching the CCD. However the trapped proton spectrum extends up to several hundred MeV and is relatively hard (between 50 and 500 MeV the proton flux decreases only by a factor of 4).

In GEO there is a relatively larger number of electrons at high energies but, although the maximum energy is still ~5 MeV and the particles can be ranged out by aluminium thicknesses of 10mm, the bremsstrahlung created can still deposit an appreciable dose. The trapped proton spectrum is relatively soft (in contrast to LEO) and is essentially depleted of protons of energy greater than 1.75 MeV. However at solar maximum flare events can produce bursts of energetic particles - predominantly protons with 5-10% alpha particles and heavy ions and electrons. This solar proton flux will also give an appreciable dose.

There are three types of radiation effect on the CCD: transient, total dose and bulk damage. Transient effects are produced by the ionisation tracks of charged particles. In a semiconductor such as silicon the effects are short lived as the charge produced is collected and readout as spurious signal; though this in itself can be a problem during conditions of high event rate (such as passage through the trapped particle belts or the South Atlantic Anomaly).

In an insulator such as silicon dioxide or silicon nitride the ionisation charge can become trapped, thereby causing shifts in threshold voltages. This is the second (total dose) effect. Another by-product of this ionisation damage is an increase in the number of dark charge generating and charge trapping states at the silicon dioxide/silicon interface.

The third effect is the displacement of silicon atoms in the bulk of the device by collision with heavy particles. This again results in the creation of dark current generation and charge trapping states.

It is generally accepted that the effects of ionisation damage can be simulated by using any type of ionising radiation; of which Co^{60} gamma rays are one of the most convenient to use. This is not so with displacement damage, for which bombardment with representative particles (in this case protons and heavy ions) is needed. The present report concentrates on experiments using protons. As discussed above we expect the effects to be:

a) changes in threshold voltages, full well capacity and power consumption caused by ionisation damage.

b) increases in dark current due to i) increases in surface generation caused by increases in interface trap density; in turn caused by ionisation damage and ii) bulk displacement damage.

c) increases in the number of surface trapping states, again caused by ionisation damage (Note: the CCDs are buried channel devices and so this will not affect charge transfer efficiency except at saturation).

d) increases in bulk trapping states in the buried channel caused by displacement damage and hence reduction of charge transfer efficiency.

It should be emphasised that, although the effects of ionisation damage in creating oxide and interface traps are the same for all types of ionising radiation, quantitative comparisons of damage should take into account the recombination of the electron-hole pairs which are generated in the oxide. This recombination is particularly important for the dense tracks produced by low energy particles [2]. In this respect Co^{60} gives a high yield of e-h pairs, which gives a worst case result, but fairly representative of the effects of high energy protons which are the predominant species present in the environmental flux, after shielding by the spacecraft. The proton energies used in these experiments (1.5 and 10 MeV) give an under-estimate of the ionisation damage.

2.2 Overview

The devices tested were all frame transfer CCD imagers with front-illuminated polysilicon electrodes and n-type buried channels.

As discussed above, and in greater detail in section 3, the proton energies used in this study are expected to give relatively small amounts of ionisation damage as compared with Co^{60} gamma rays or indeed the space environment. Since the previous Co^{60} study [1] gave an almost complete study of ionisation effects to be expected for SILEX, parameters such as threshold voltages and power consumption were not systematically measured in this study and will not be discussed in detail here and the reader is referred to [1] which should be considered as the baseline data base for ionisation effects.

However some measurements of the threshold voltage and power consumption were made for Thomson-CSF devices and, although of low accuracy because of the small changes encountered, will be discussed where appropriate. The main part of this report is concerned with the changes in dark current and their behaviour with CCD temperature and annealing time. In addition some dark current data at room temperature were obtained for two EEV CCD-02 devices and the differences in radiation affects between the two types of CCD will be considered. The opportunity was also taken to perform linearity measurements on Thomson-CSF devices with both spot and uniform illumination.

A total of four TH7863 (288x384 pixel), four THX31160-1 (14x14 pixel) and two EEV CCD-02 (288x385 pixel) devices were subjected to proton bombardment at AEA Technology, Harwell, UK. For each CCD type, half of the devices were powered and clocking during the irradiations and half were not. Two TH7863 and two THX31160-1 CCDs received 10 MeV radiation and the same number were irradiated with 1.5 MeV protons. The EEV CCDs received 10 MeV protons.

For the larger TH7863 and CCD-02 chips the CCD area was divided into four zones each receiving a different proton fluence. This was achieved by selectively shielding each zone using an external aluminium mask. The proton fluences were arranged to give doses (ionisation damage) of 9, 6, 3 and 0 krad(Si) the last zone being used as a baseline reference for pre-irradiation behaviour. The masking allowed a study of dark current, charge transfer efficiency and full well capacity for different doses and for different annealing times after irradiation had ceased and also enabled the use of laboratory equipment (eg. spot illumination systems) not available at the radiation facility. The 14x14 pixel THX31160-1 devices were irradiated to 6 krad(Si) in one step.

The following section discusses damage mechanisms in some depth (particularly displacement damage). This treatment is felt to be necessary since an understanding of the processes involved is needed if the data is to be extrapolated to other CCD operating environments or conditions. Section 4 gives a description of the test objects and Section 5 considers the test facility, test histories and test methods used. These sections are kept brief with only details essential to the present study included. More information is given in [1]. There then follow results sections for each of the three CCD types. After these, Section 9 returns to the subject of device modelling and discusses how the previous bulk dark current results can be extrapolated for other environments. Section 10 briefly looks at the implications for SILEX and other missions and considers possibilities for future work. Finally Section 11 gives a list of published works referred to in this report. Note though that an exhaustive review of the literature has not been attempted - only those papers of particular importance are cited.

At the end of the Co^{60} experiments [1] and the start of this campaign we are faced with the following questions:

ionisation damage

i) How does the ionisation damage compare at different proton energies and with Co^{60} effects?

ii) Are the effects different for the present batches of CCDs compared with those used in the Co^{60} study?

iii) Is the annealing behaviour (particularly the reverse annealing of surface dark charge) the same in this case?

iv) How does linearity and full well capacity behave with spot rather than uniform illumination?

bulk displacement damage

v) Is charge transfer degradation caused by damage in the buried channel significant for SILEX conditions?

iv) What is the appearance of the dark charge nonuniformity (dark charge spikes) caused by bulk damage and how do dark charge histograms change with CCD temperature, bias state during irradiation and annealing time?

vii) Are there any large dark charge spikes caused by displacement damage in high field regions in the CCD (and subsequent field-enhanced emission), if so what is their behaviour with CCD temperature and annealing time?

viii) Can the damage observed be extrapolated to predict the effects in the general space environment?

and finally

iv) What are the implications for SILEX and other missions?

It is hoped that this report will furnish answers to some, if not all, of these.

3. BASIC MECHANISMS OF PROTON DAMAGE

3.1 Device Structure and the Effect of Ionising Radiation

Figure 3-1 shows the basic layout of a frame transfer CCD imager and shows the image, storage and readout registers and the overlapping electrodes (in the diagram these are 3-phase) which are used to transfer charge down each CCD column and then horizontally through the readout register to an output amplifier. These devices are fabricated using a planar MOS (metal-oxide-silicon) technology with overlapping polysilicon electrodes which are transparent to visible wavelengths. Separating these electrodes from the crystalline silicon is a dielectric layer (the gate isolation) which in the case of the present devices is a mixed layer of silicon nitride (Si_3N_4) on top of silicon dioxide (SiO_2) - with the SiO_2 nearest the silicon. These layers are of order 0.1μm thick (precise details of the structure are not available from the manufacturers). The overlapping polysilicon electrodes are ~0.5μm thick and the oxide isolation between each phase is again ~0.1μm. The whole structure is usually covered by a protective coating of SiO_2 ~0.5μm in depth. The silicon itself is epitaxially grown on a highly doped (Na ~$10^{18}cm^{-3}$) substrate. Standard devices were used with epi-layer resistivity ~10Ωcm (Na ~$10^{14}cm^{-3}$). Below the silicon front surface is the depletion region associated with the n-buried channel and this extends ~5μm into the device. The buried channel itself is formed by phosphorus ion implantation to a doping ~$10^{16}cm^{-3}$.

Figure 3-2 shows the effects which occur when the device is struck by an ionising particle such as a proton. Particles with energy greater than ~1.5 MeV will pass right through the electrode structure and epitaxial silicon layer and will not be stopped until they reach the substrate (particles with E> 10 MeV will pass through the CCD die and with E> 25 MeV through the whole package). Electron-hole pairs are generated all along the particle track by ionisation. In the insulating dielectric layers these can become trapped so as to impart a fixed charge to the layer (which produces a shift in flatband voltage). The generation of electron-hole pairs in the gate oxide also leads, by a complex process of transport, bond breaking and trapping to the generation of traps at the SiO_2/Si interface. These interface traps can communicate with the silicon and cause generation of thermal dark current and trapping of minority carriers if they happen to come into contact with the surface (eg. in a surface channel device or a buried channel CCD near saturation). In the bulk of the silicon the electron-hole pairs will be transported by drift or diffusion to the buried channel and be readout as transient (ie. spurious) signal charge. In the bulk there is also the possibility of silicon atoms being displaced from their lattice positions by collision with the bombarding particle. This gives rise to states with energy levels part way between the silicon valence and conduction bands which again can lead to dark charge generation or minority carrier trapping.

3.2 Ionisation Damage

Figure 3-3 shows the processes induced by radiation in MOS devices. As discussed in the previous section, radiation causes electron-hole pairs to be created in the gate dielectric. In the oxide the radiation-generated electrons are much more mobile than the holes and are soon swept out, in times ~1ps. However in this time some fraction of the electrons and holes will recombine (depending on the applied field and on the particle type and energy). Those holes which escape recombination are relatively immobile (especially at low temperatures) and remain for a while near their point of generation. However after times ~1s at room temperature (or longer at low temperatures) the holes undergo a hopping transport between localised sites in the oxide in response to any fields which are present. In the case most often considered by researchers in the field of radiation effects this field is positive and drives the holes toward the SiO_2/Si interface where they can become trapped at E centres which are trivalent silicon defects associated with an oxygen vacancy in the

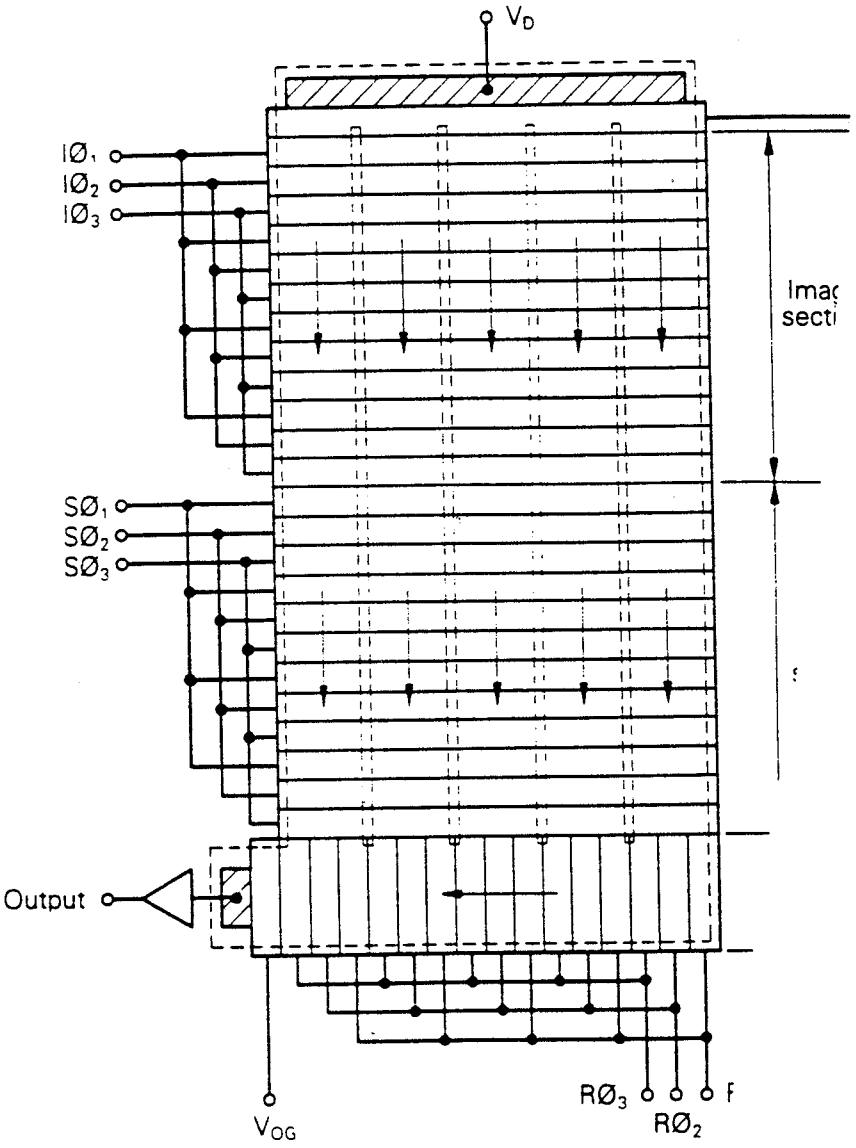

Figure 3-1 Schematic diagram of a frame transfer CCD imager

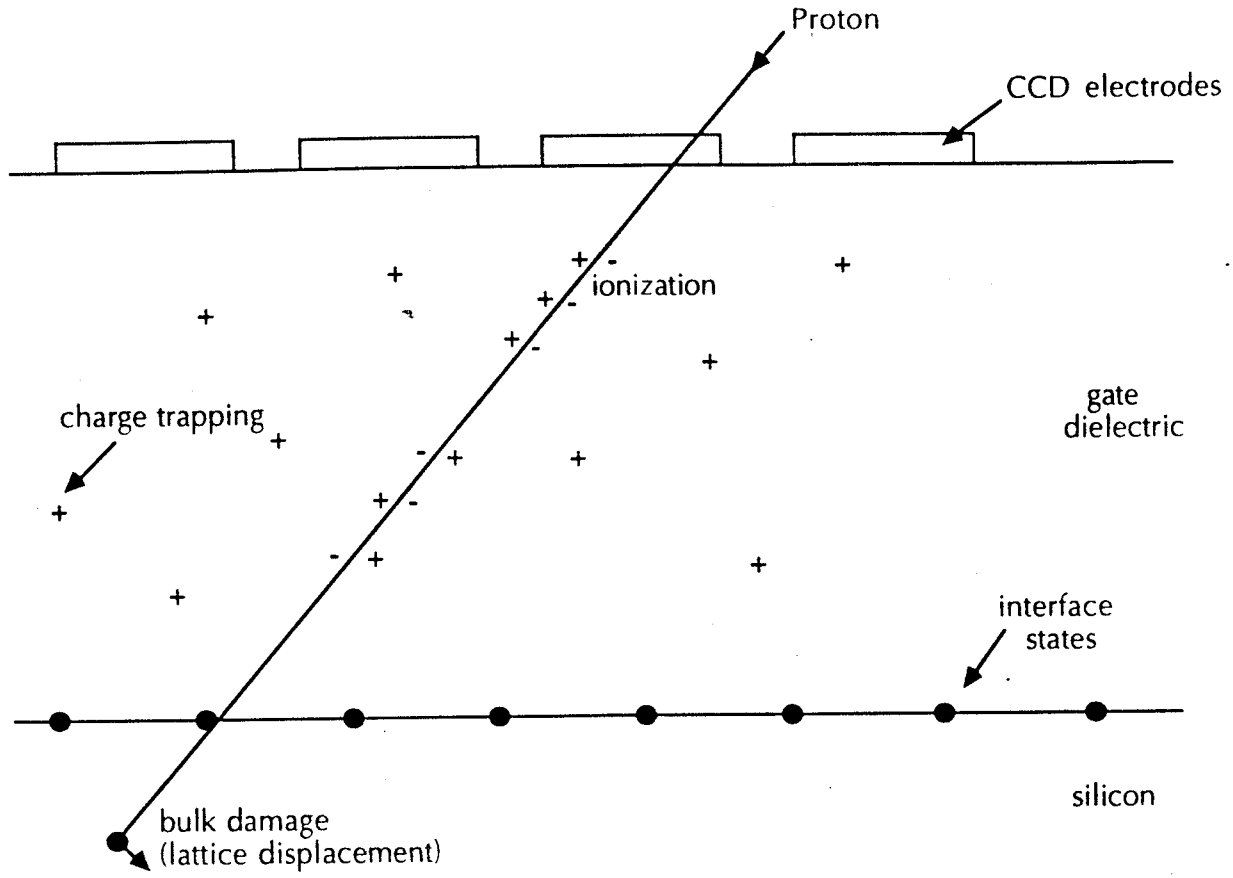

Figure 3-2 Effects occurring when a CCD is subjected to proton bombardment

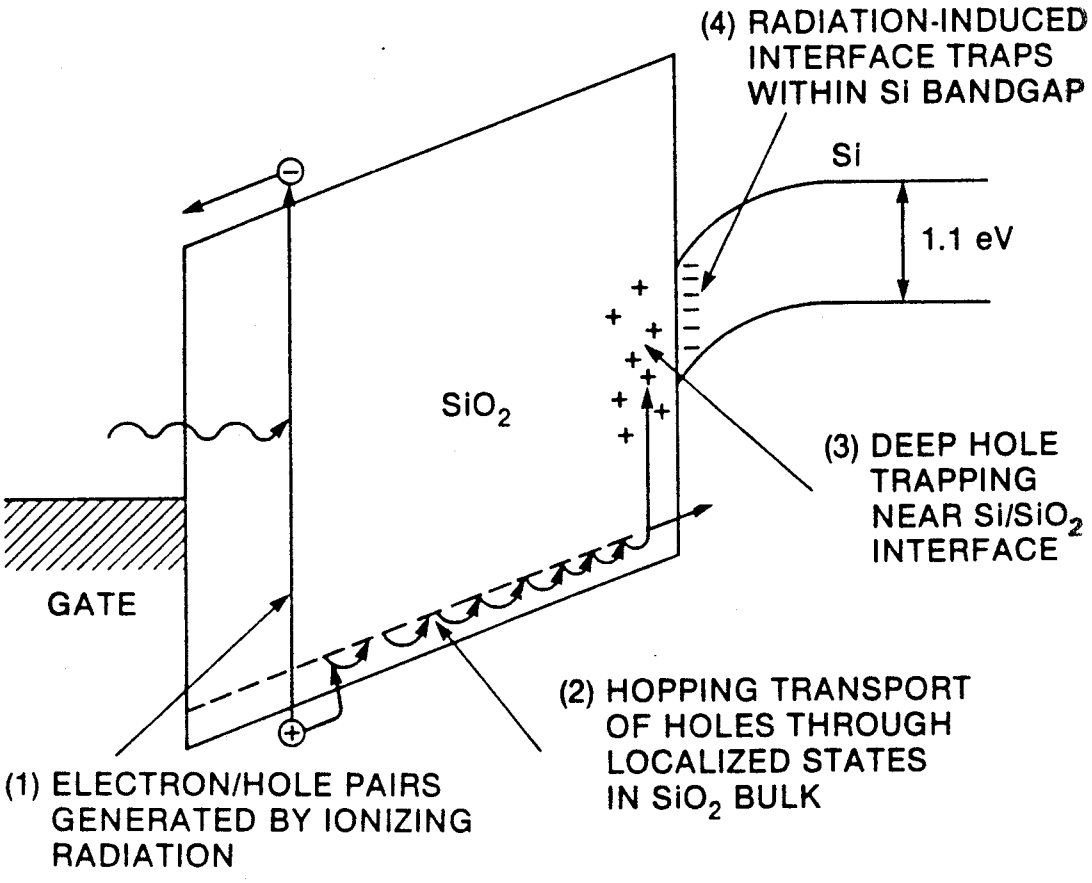

Figure 3-3 Schematic of ionising-radiation induced processes in MOS structures (positive oxide field) after McLean, Boesch & Oldham [3]

SiO_2 structure. These defects tend to occur in a Si-rich layer close to the interface: a position which maximises the effect on threshold voltage shift (since this depends on the first moment of the trapped charge distribution). However in the present case the field across the oxide is negative and tends to sweep the holes toward the gate electrodes. Significant effects can still occur however since it is possible that displacement damage induced during the n-channel ion implantation can create electron and hole traps in the oxide and enhanced oxide trap threshold voltage shift (ΔV_{ot}) can be caused for negative fields [3]. The role of the nitride layer should also not be forgotten. As well as giving an extra interface (Si_3N_4/SiO_2) where trapping can occur, SiN_4 acts as a source of electron traps (in contrast to SiO_2, in which hole traps dominate). Thus in the previous Co^{60} study [1] it was concluded that the increased radiation effects for biased devices (negative oxide field) compared with unbiased devices (zero field) was not implausible. It should also be noted that the biases in an unpowered device are not well defined (even with pins shorted) and it is possible that internal fields can occur.

The fourth process depicted in figure 3-3 is the creation of interface traps at the SiO_2/Si interface which lie within the bandgap of the silicon. These traps are generally thought to be P_b centres which are trivalent silicon atoms bonded to three silicon atoms at the SiO_2/Si interface. These centres can have charge states of zero, one or two electrons and can act as positive or negative charge traps depending on their energy relative to the fermi level, as well as generation centres (ie. producing dark charge). The charge trapping at the interface will act together with the trapped oxide charge to change threshold voltages and in fact, without detailed measurements on test structures it is not possible to separate the two contributions.

As discussed in [4], there are three basic sets of models to explain build-up of interface traps:

i) Hydrogen models, in which a water related species (H^0, H^+, H_2, OH^-) is created by bond breaking by the initial radiation generated holes.

   These species then migrate to the SiO_2/Si interface where traps are created (generally accepted to be P_b centres).

ii) Injection models, in which holes are trapped at the interface and are converted into interface traps by electron injection from the silicon.

iii) Stress models, in particular the bond-strain gradient (BSG) model, in which radiation generated holes rupture Si-O bonds near the interface and the oxygen defects migrate because of the BSG.

At this time it is not possible to decide on which mechanism (or combination of mechanisms) are responsible. We content ourselves with some observations. Firstly, since the oxide field is negative, only negative or neutral species will migrate to the interface and this tends to argue against the Injection models (though the electric field will enhance the possibility of electron injection). Secondly, commercial oxides often contain large amounts of hydrogen especially as, in the absence of radiation, the hydrogen tends to anneal process-induced states and reduce dark current. Also nitride processes often result in hydrogen incorporation. Thirdly, a certain amount of stress is to be expected at the interface because of the implantation process. Additional stress due to the deposition of the aluminium masking layer might explain the large dark current coming from the CCD storage regions. It has also been found [5, 6] that during high temperature annealing steps aluminium can react with traces of H_2O on the oxide and polysilicon surfaces to release active hydrogen species which can diffuse either through the SiO_2 or through grain boundaries in the polysilicon. Finally, we note that the majority of research has been

carried out into mechanisms occurring for the more common situation of positive oxide fields and so there is a scarcity of relevant experimental observations.

Regarding the time dependence of dark charge build up, it is plausible for interface trap generation to increase gradually with time depending on the speed of migration of chemical species to the interface. Also once defect states created at the interface their transformation to other states is possible. Note that the dark charge generation rate will depend greatly on the emission time constants of the states and on their charge state and energy in relation to the fermi level (the P_b centre itself is known to be amphoteric with ground state occupancies of zero, one or two electrons). It should not be too surprising that annealing at elevated temperatures (eg. as in the 100°C bake used in the Co^{60} study [1]) is effective in accelerating the changes which otherwise happen over several months since almost any change will be temperature dependent.

Since the numbers of both oxide and interface traps are expected to depend on the yield of unrecombined holes initially generated in the oxide it is interesting to consider this in more detail.

Two basic models have been developed to treat the problem of ionisation and recombination in insulators. The columnar model relates to the case where the electron-hole pairs are very close together compared with the diameter of the charge column produced by the particle. Numerical simulations have recently been performed by Oldham [2] and figure 3-4 shows the yield of holes surviving recombination as a function of the number of electron hole pairs/cm created in the SiO_2. The figure shows two cases (labelled T = 1eV and T = 0.006eV) depending on the initial carrier temperature. In the first case equilibrium with the lattice takes place at 10^{-13}s and in the second this is assumed to occur instantaneously. 3-4a) is more applicable to lower fields and high track densities and b) to high fields and low track densities so these plots can be assumed to bracket the possibilities.

The initial track densities for 1.5 and 10 MeV protons can be calculated from the energy loss (dE/dx) in SiO_2 and the energy needed to create an electron hole pair. The energy loss is conveniently modelled using the TRIM code [7] and Benedetto and Boesch [8] give the e-h pair creation energy as 17 $\pm$1eV and we have:

For SiO_2

Proton energy	dE/dx (MeV/mm)	e-h pairs/cm
10 MeV	8.82	5.19×10^6
1.5 MeV	35.3	2.08×10^7

Figure 3-5 is a plot of e-h yield versus electric field for 10 and 1.5 MeV protons for Oldham's two models. It is seen that this yield is much reduced at low fields (bias off) and at the lower energy (1.5 MeV) where the track density is higher and recombination correspondingly more likely.

The second basic model for ionisation and recombination in insulators is the geminate model and this applies to the case where the initial charges are created far apart. This occurs, for example, with electrons of any energy above a few hundred keV [3] and hence for the important case of Co^{60} irradiation (which generates Compton scattered electrons of energy ~1 MeV). The geminate model also applies to protons of energy greater than about 200 MeV. Also shown in figure 3-5 is the e-h yield for Co^{60} radiation (from [3]). It is seen that for biased devices the yield is near unity and this gives the worst case damage. Since this yield is representative for the majority of protons in the trapped radiation belts

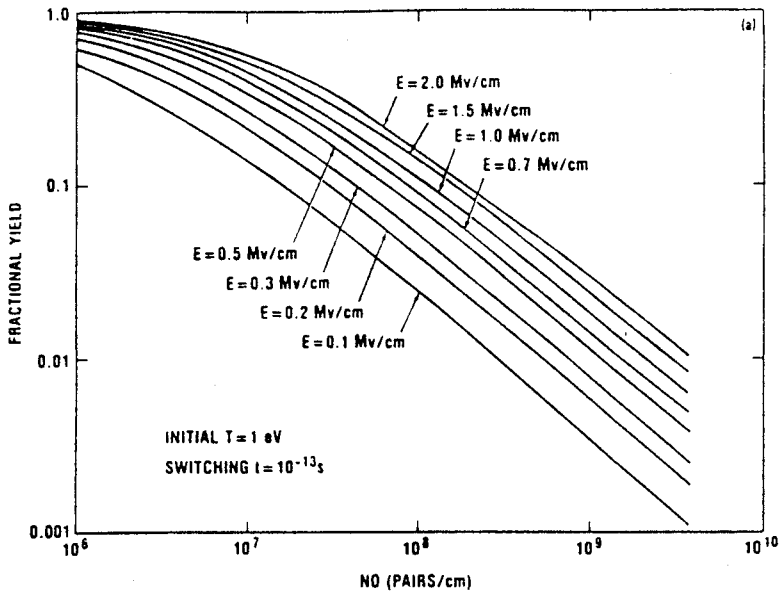

a)

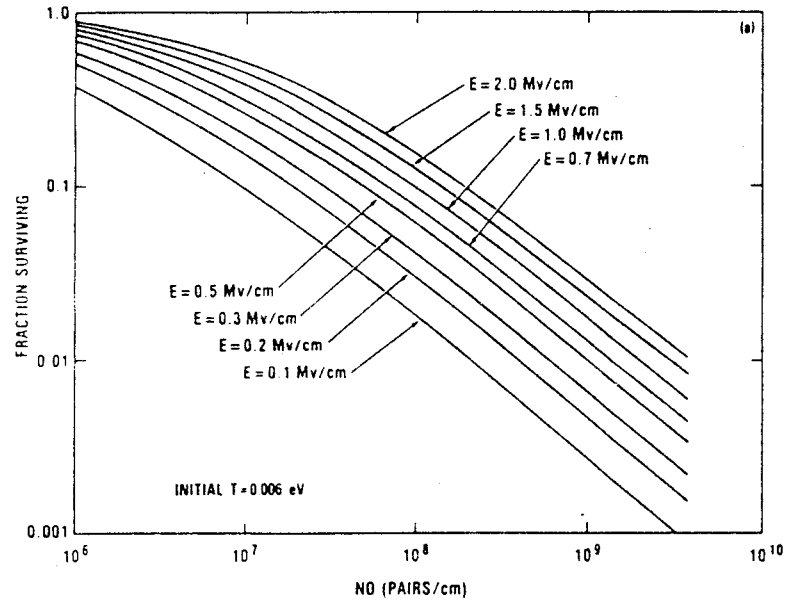

b)

Figure 3-4 Calculated yield of electron-hole pairs as a function of initial ionisation track density. After Oldham [2]

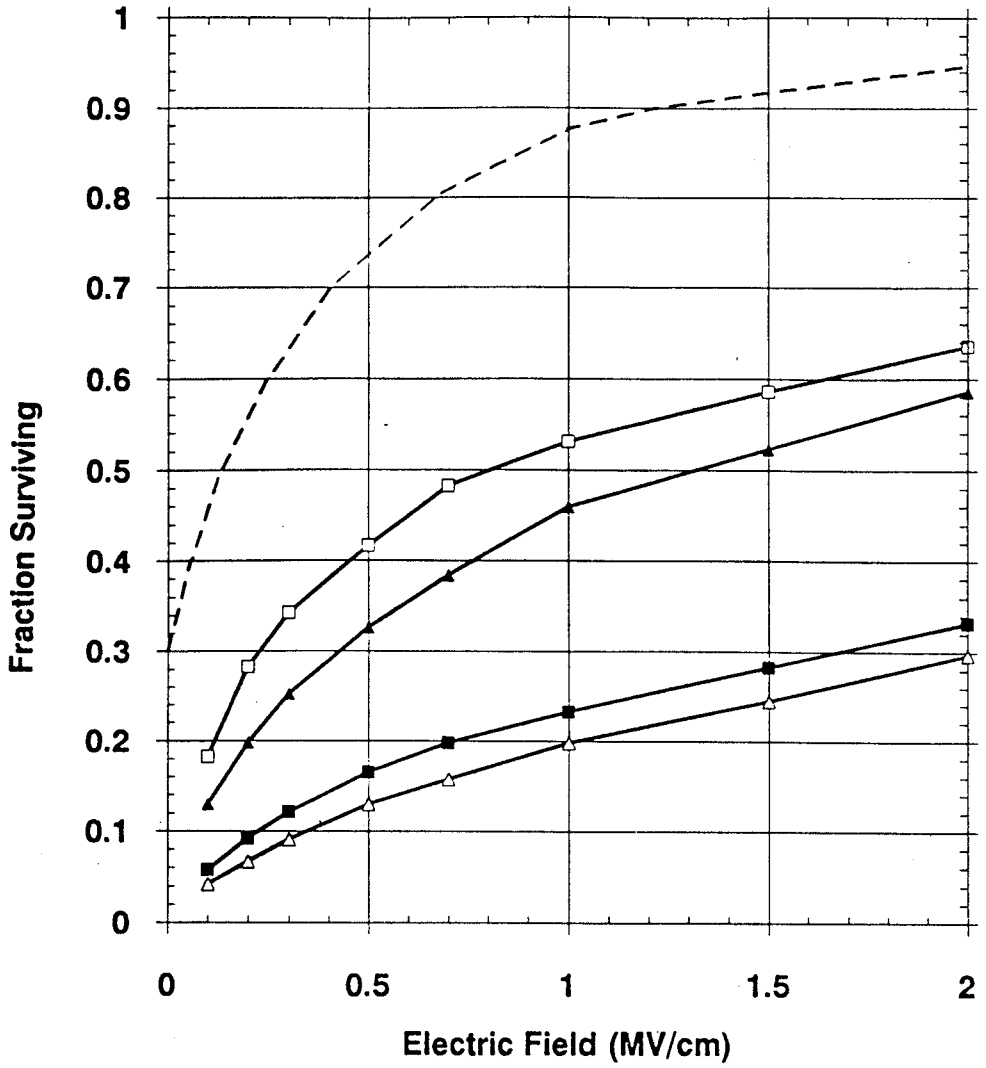

Figure 3-5 e-h yield in SiO_2 for 1.5 and 10 Mev protons and Cobalt 60 gamma rays

(and in solar flares); this, together with the relatively low cost and the ease of use, explains why Co^{60} facilities are widely used for testing ionisation damage in microelectronic devices. In contrast, low energy protons will under-estimate the ionisation damage in space by at least a factor 2.

For protons of energy between roughly 10 and 200 MeV the situation cannot be represented using either the columnar or geminate models and the e-h yield will be somewhere between the two cases (figure 3-6, from [3]).

Another good reason for preferring Co^{60} data is that the dose rate at the irradiation facility can be made low enough to represent quite well the rate occurring in flight. On the other hand ground based proton facilities inevitably give high beam fluences and exposures of the order of minutes. Thus dose rate effects are likely to be much more important for proton irradiations.

It is possible that damage levels closer to those measured with gamma rays might be experienced if the proton beam were incident at a glancing angle to the CCD surface (rather than normal). Tallon et al [8a] have found this to be the case with threshold shifts in MOSFETs.

3.3 Displacement Damage

When heavy particles (electrons, protons, neutrons etc) pass through silicon there is the possibility of collisions with silicon nuclei. These cause displacement of silicon atoms from their lattice sites and the creation of vacancy - interstitial pairs. These pairs are not stable above 80K and the vacancies migrate until a stable defect is formed (by association with other defects, impurities or dopants). These stable defects give rise to states with energy levels within the forbidden band gap and these can affect device properties such as dark current and charge transfer efficiency of CCDs or minority carrier lifetimes and gains of transistors.

It will be necessary to review the existing literature relating to displacement damage in order to

i) correlate the measurements made in this study with previous work

ii) model the effects and extrapolate to other radiation environments (other particle types, energies and fluences)

iii) understand the changes with device temperature and annealing time

and

iv) gain insight into the effect of device materials and manufacturing processes on the amount of damage. If these are unknown then it will be difficult, if not impossible, to predict the damage from device to device and to control batch quality.

The topics to be considered in this section are:

a) the types of collision and energy loss that occur in silicon
b) the types of defect that are created
and c) the effect of states in the bandgap on device properties

Device modelling will also be briefly considered but this topic, particularly dark charge modelling, will be studied in more detail in Section 9.

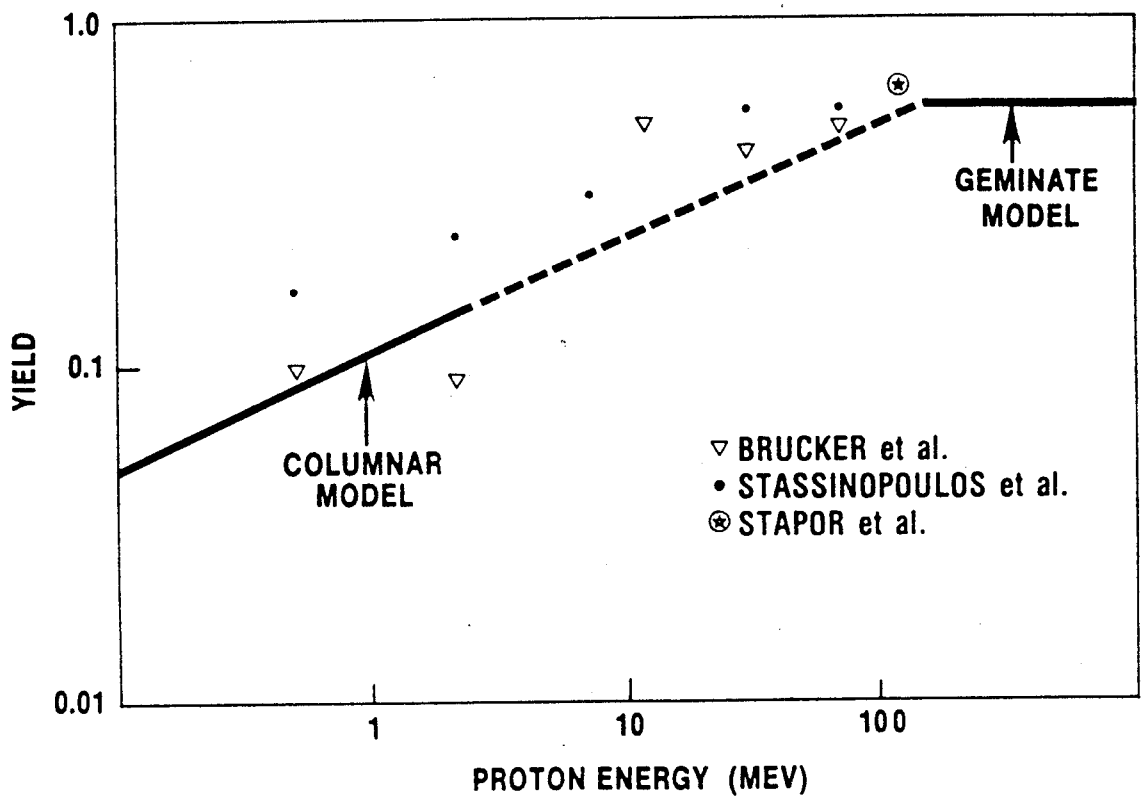

Figure 3-6 Recombination measurements and calculations for protons incident on SiO_2 (after [3])

3.3.1 Collisions and Energy Loss

During irradiation the incident particles can collide with silicon nuclei, transfering part of their energy, and producing primary knock-on atoms (PKAs). The recoil energy spectra, and the directions of the PKAs depend on the type, charge and energy of the incident particles. The PKAs in turn collide with other atoms in the lattice thereby producing additional knock-on atoms and lattice vacancies. The end result is that part of the particle energy goes into production of vacancies and phonons (lattice vibrations). This fraction is termed the non-ionising energy loss or NIEL. The rest of the energy (of the incident particle and of the knock-on atoms) goes into ionisation with no permanent effects. Typically only 0.1% of the total energy loss for an ion goes into non-ionising collisions.

The NIEL has been calculated for silicon by Burke [9] and figure 3-7 (taken from ref [10]) shows the NIEL for protons, neutrons and electrons as a function of particle energy. On a microscopic level there are a number of collision process which can take place depending on the energy. Below a particle energy of about 10 MeV almost all the displacement damage is caused by Rutherford scattering by the outer electrons of the silicon atoms and this gives elastic scattering via Coulombic interactions. A characteristic of these collisions is the $^1/E$ dependence (slope -1 on a log-log plot) of the NIEL - as shown in figure 3-7. At higher energies nuclear elastic collisions start to become important and the energy dependence of the NIEL changes to roughly the 0.4 power of the energy. At energies greater than ~10 MeV nuclear inelastic collisions start to occur and by 63 MeV these provide roughly half the damage energy that is imparted to the lattice (mean non-ionising damage = 0.1 MeV). These reactions dominate for proton energies greater than ~150 MeV. At the highest energies (above 100 MeV) the incident protons initiate intranuclear cascade processes followed by ejection of high energy nucleons which leave the nuclei in highly excited states (additional nucleons are subsequently lost by evaporation) and so the recoil energies can be very high. These reactions leave a wide range of product nuclei, each with its own cross-section for production and its own recoil energy spectrum. It is important to note that the average PKAs in this region have energies typically 1000 times higher than for Rutherford scattering [11].

At first glance it might be thought that the wide variety in PKA spectra from different incident particles would result in a corresponding variety of device damage and that models of cascade processes would be needed to correlate the effects. Fortunately, however, it turns out that the nature of the displacement damage does not depend on the energy spectrum of the PKAs. Thus the partioning of the incident particle energy into isolated defects, cascades and subcascades is independent of PKA energy (for PKA energies above 2 keV [10]). A higher energy PKA will produce more overall damage but the microscopic nature of the damage is not significantly different. Thus the non-ionising energy loss can be simply written as a sum of terms due to the elastic and inelastic interactions [12], ie.

$$\text{At any energy,} \qquad S_d = (N_A/A)\,[\sigma_e\, T_e + \sigma_i\, T_i]$$

where the subscripts refer to elastic and inelastic reactions, the σ's are cross-sections and the T's are the damage energies ie. the average PKA recoil energy partioned so that the energy going into ionisation is removed. S_d is the total energy which goes into damage (ie. displacements) in MeV cm^2/g, A is the gram atomic weight of the target (= 28 for silicon) and N_A is Avagadro's number). The number of displacements can then be calculated assuming that one vacancy/interstitial pair is created per 50eV of total damage energy (ie. one pair for every $2\,T_d$ of energy, where T_d is the threshold energy for a single displacement).

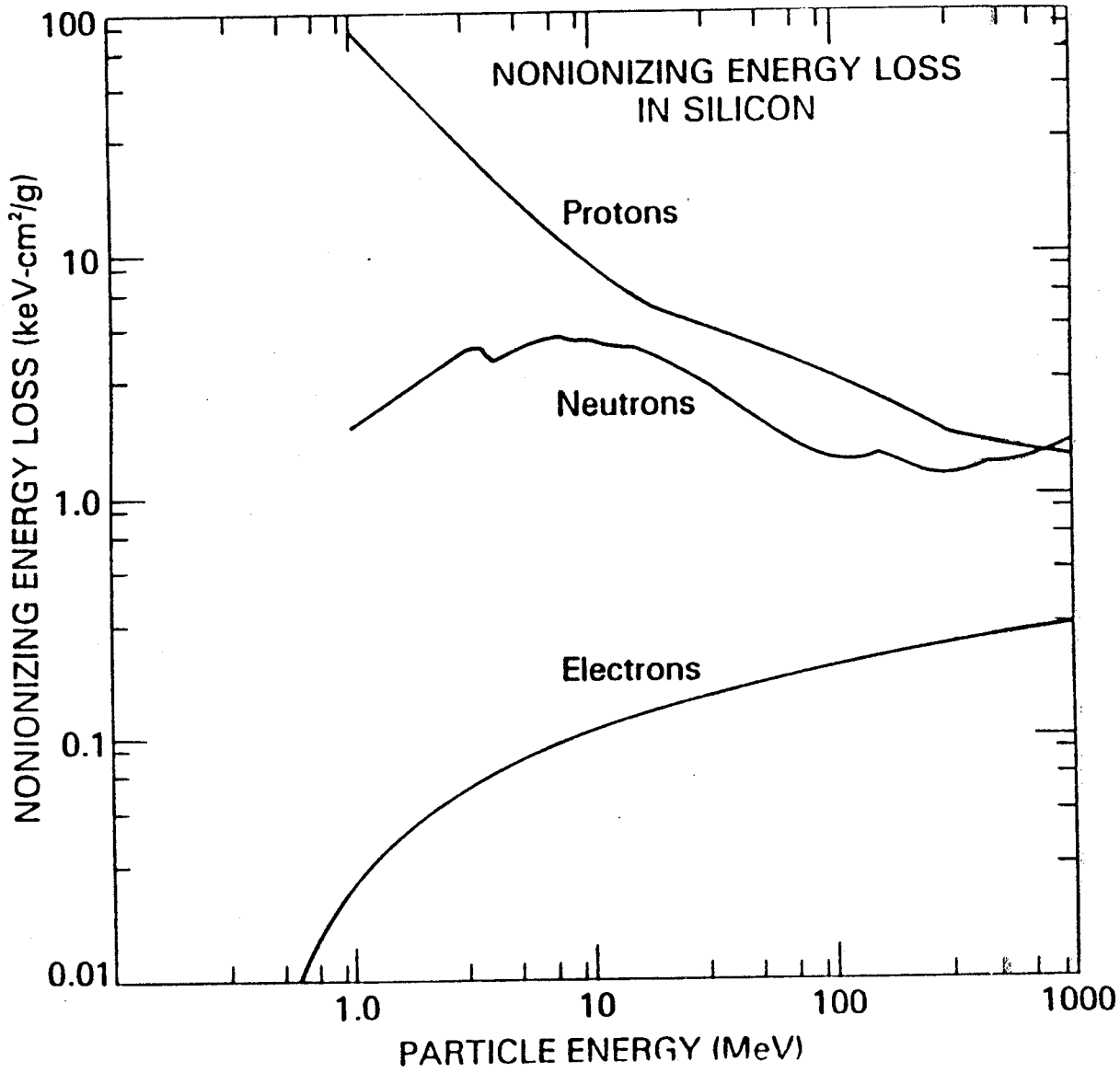

Figure 3-7 Non-ionising energy deposition in silicon (from [10])

3.3.2 Defects Produced

In the previous section we found that the number of vacancies produced in the lattice is proportional to the non-ionising energy loss (NIEL) of the incident particle - independent of particle type or energy. In n-type silicon, however, these vacancies are unstable at temperatures above 70K [13] (80K for p-type) and migrate through the lattice until they form a stable defect in combination with an existing defect or donor/impurity atom. In this process the majority of vacancies will recombine with interstitials; however it has been found that, in most cases, the number of stable defects also scales with NIEL [10]. An exception occurs for low energy electrons (for which the average PKA has energy <2 KeV) in that the initial defect density is low and the recombination rate is reduced so that the damage factor is high. Some departures from linearity due to lower recombination at low proton energies (below 10 MeV) have also been found.

The stable defects which are formed will have energy levels within the bandgap. Table 3-1 (from reference [14]) gives a reasonably up to date list. Note that defect levels are identified by the energy required to remove an electron (or hole in the case of p-type silicon) from the defect to the conduction band edge E_C and to the valence band edge, E_V, in the case of hole emission. In some literature levels such as, for example, E_C-0.17 eV and E_V+0.36 eV are labelled E(0.17) and H(0.36).

In n-type silicon the situation is at first glance fairly simple. The predominant defects are the oxygen-vacancy pair or A centre, located at E_C-0.17 eV (E0.17) and the phosphorus - vacancy pair (E centre) located at E_C-0.44 eV (E0.44). The P-V centre being of prime importance because phosphorus is present in large quantities in the n-buried channel. This centre anneals principally at 150°C (cf 350°C for the A centre). Another defect of importance is the divacancy which can be produced directly in the collision cascade or as a combination of two vacancies. The divacancy has three separate energy levels within the bandgap depending on its charge state [15] : E_V+0.31, E_C-0.41 and E_C-0.23 eV. Note that the level at 0.41 eV is close to that of the P-V centre (0.44 eV), but the two can be distinguished since the divacancy anneals out at a higher temperature (300°C). The position of the fermi level relative to the energy level, and the charge state of the defect (positive, neutral, singly or doubly negative) will affect the electrical properties. It has been reported [16] that divacancies are more common in collisions with heavier or more energetic particles.

In p-type silicon the situation is more complicated but divacancies and interstitial carbon are recognised as the dominant radiation-induced defects [13]. However interstitial carbon is not a stable defect (annealing in ~30 min at 330K) and other complexes can be formed. Interstitial boron complexes can occur also as described later and boron, of course, is the usual dopant in p-type silicon.

Note that in processed epitaxial silicon, as used in the present CCDs, the oxygen content will be relatively low (although some out diffusion from the Czochralski grown substrate will occur before precipitation of gettering centres occurs) and by far the largest "impurity" concentration is for substitutional phosphorus in the buried channel. Phosphorous is known to be an efficient trap for vacancies which are mobile and can be expected to diffuse through the lattice from their point of creation (either in the n-channel or the p-layer) until they are trapped at the buried channel. This has led previous workers to identify the P-V centre as the dominant defect responsible for displacement damage effects in CCDs (c.f., for example, ref [17]). Especially as the energy level of 0.44 eV is close to that found from electrical measurements. However the divacancy is another candidate (especially for higher proton energies). In addition, it has recently been established [18] that interstitial defect reactions are important in silicon. The original displacement event, of course, created both vacancies and interstitial silicon atoms. Whilst vacancy complexes have been well studied (as discussed above) reactions involving the latter Si_i have not been well

Table 3-1 Data on electron-induced defects in silicon (from [14])

Origin	Energy level (eV)	Capture cross section sigma (cm*2)	Annealing properties
V	Ec-0.09		out 90 deg K
	Ec+0.11	(p) 5 X 10*-17	out 150 deg K
	Ev+0.13		out 150 deg K
O-V	Ec-0.18	(n) 10*-14	out 350 deg C
	Ec-0.169	(n) 10*-14	out 350 deg C
V2-O ?	Ec-0.30		in 100 deg C, out 450 deg C
V3-O ?	Ec-0.20		in 300 deg C, out 450 deg C
(V-V)+	Ev+0.21	(p) 2 X 10*-16	out 300 deg C
	Ev+0.23	(p) 3 X 10*-16	out 300 deg C
(V-V)-	Ec-0.39	(n) 4 X 10*-15	out 300 deg C
	Ec-0.413	(n) 2 X 10*-15	out 300 deg C
(V-V)--	Ec-0.23	(n) 0.6 X 10*-16	out 300 deg C
	Ec-0.246	(n) 4 X 10*-16	out 300 deg C
P-V	Ec-0.44	(n) > 10*-16	out 150 deg C
	Ec-0.456	(n) 3.7 X 10*-15	out 150 deg C
C(I)	Ev+0.27	(p) 7 X 10*-18	out 315 deg K
	Ev+0.29		
C(I)-C(s)	Ev+0.33	(p) 8 X 10*-17	in 300 deg K, out 400 deg C
V-C-O	Ev+0.38	(p) 2 X 10*-18	in 30 deg C, out 400 deg C
C-related defect	Ev+0.36	(p) 4.4 X 1*-17	in 315 deg K, out > 470 deg K
Al(I)-V	Ev+0.48	(p) > 10*-16	out 200 deg C
Al(I)	Ev+0.25	(p) 7 X 10*-18	out 200 deg C
B(I)-B(s)	?Ec-0.26		out 150 deg C
B(s)-V	Ev+0.31	(p) 1.94 X 10*-19	in 200 deg K, out 300 deg K
	Ev+0.38	(p) 2 X 10*-17	
V-O-B	Ev+0.30	(p) 2 X 10*-16	in 170 deg C out 400 deg C
O(I)-B(I)	Ec-0.27	(n) 2 X 10*-13	out 170 deg C
dependent on oxygen	Ev+0.13	(p) 10*-18	out > 470 deg K
Vacancy-related defect	Ev+0.34		in 215 deg K, out 315 deg K

understood until recently, partly because Si_i is highly mobile and partly because the states generated overlap with previously identified peaks (eg. the P-V defect) on measurements obtained with techniques such as deep level transient spectroscopy (DLTS). Over the past few years these interstitial defect reactions have been the subject of intense interest.

According to Asom et al [19] the sequence in n-type silicon at 300K is i) the interstitial silicon is captured by a substitutional carbon atom C_s to produce interstitial carbon C_i by a replacement mechanism (Note: Carbon is a common impurity in silicon) and ii) mobile C_i reacts with impurities to form stable and metastable associates:

$$Si_i + C_s \rightarrow Si_s + C_i$$

$$C_i + X \rightarrow C_i - X$$

where X may be oxygen, carbon or, perhaps more likely in our case, phosphorus or boron. Note that the single interstitial carbon C_i gives rise to a single donor state at $E_v + 0.27$ eV and a single acceptor state at $E_c - 0.10$ eV [20]. These reactions considerably complicate the annealing behaviour. Instead of a simple P-V complex annealing at 150°C there are sets of metastable and stable states which can change into each other. This was first discussed by Song et al [21] (c.f. figure 3-8), who gave evidence for new states at 0.10, 0.26. 0.34 and 0.44 eV. The full range of energy levels and complexes are not yet identified; Asom et al [19] give the P_s-C_i complex energy levels of 0.21, 0.23, 0.29 and 0.30 eV.

Note that the introduction rate for the P_s-C_i pair increases with phosphorus content in a similar way to the P-V centre as shown in figure 3-9 which also shows the introduction rate for boron complexes [22]. Kimerling et al [18] comment that the 'two-stage' annealing of the E centre is actually dissociation of the P_sC_i pair at 100°C and of the P_sV at 150°C.

As well as a more complex defect annealing process it would seem that the boron, phosphorus and carbon content of the silicon are process parameters which may affect the yield of radiation-induced defects and which might result in batch-to-batch variations. Since C_i and B_i atoms are mobile (at least at room temperature) they can migrate from creation events anywhere in the epitaxial layer towards the buried channel to form the P_s-C_i pair (as for vacancies migrating to form the P-V pair) or to create defects in the P-layer (for boron). Hence the carbon or boron content does not necessarily have to be high for effects to be observed. The full range of reactions identified to date are given in figure 3-10 [18]. Note that the boron interstitial on its own has an energy level at 0.45 eV and is stable up to 240K.

Finally it should be considered that nearly all the research on basic defects to date has been carried out using electron irradiation. Recently Hallen et al [23] have suggested that defects at 0.319, 0.450 and ~0.5 eV are due to hydrogen from the proton irradiation itself.

To summarise we have:

i) The P-V centre, the divacancy, the P_s-C_i pair and possibly other complexes involving interstitial atoms (eg. boron) are likely candidates for stable (metastable in the case of P_s-C_i) radiation-induced defects.

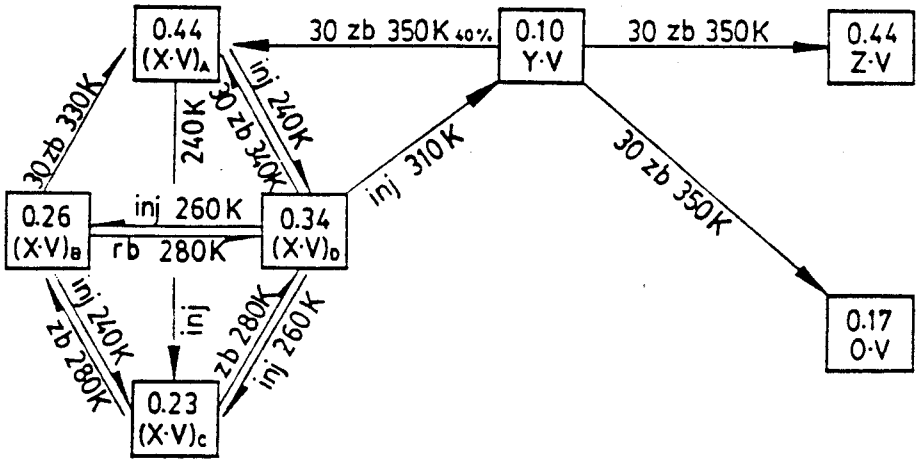

Figure 3-8
Conditions for interconversion between the vacancy-related centres (i) inj (T); forward bias injection (2.5 A/cm^2) for 5 min at T followed by cooling with zero bias to 80K. (ii) 30 zb (T); zero-bias annealing for 30 min at T followed by cooling with zero-bias to 80K. (iii) zb (T); zero-bias cooling from T to 80K. (iv) rb (T); reverse bias (5V) cooling from T to 80K (from ref [21])

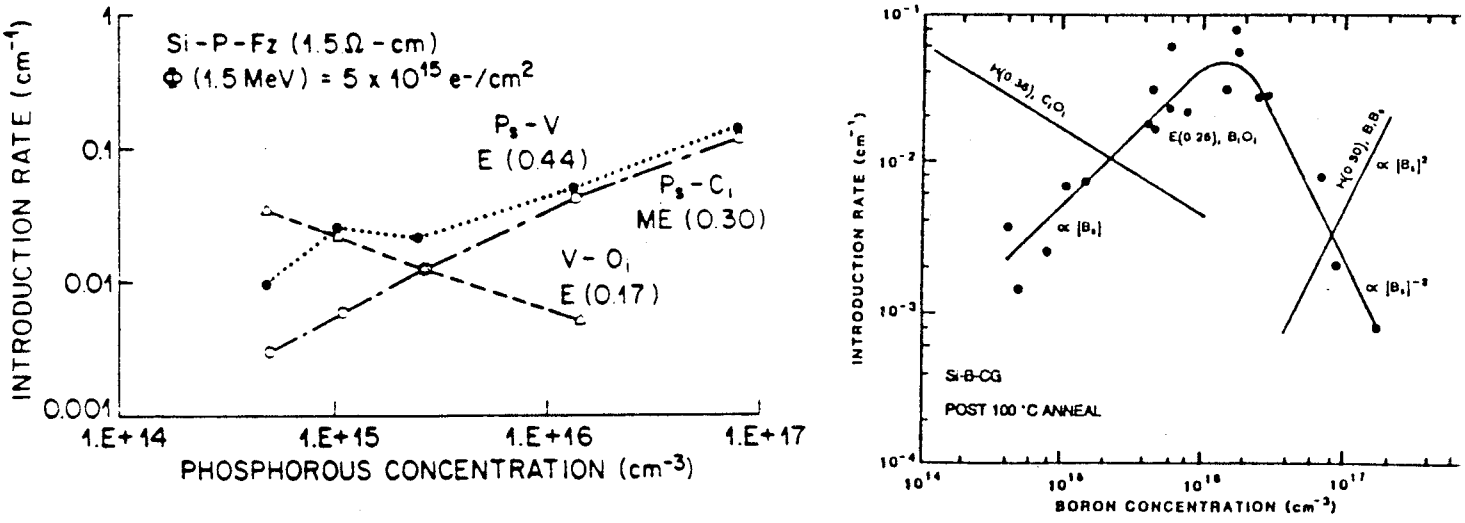

Figure 3-9 Introduction rates for P_S-C_i [22] and boron [18] complexes

Defect	E_T eV	Charge State	Stability
$(Si)_i O_i$	-	-	230 °K
B_i	E(0.13) E(0.45)	0/+ −/0	240 °K
$B_i B_s$	H(0.30)	-	>400 °C
$B_i O_i$	E(0.26)	-	150-200 °C
$B_i C_s$	H(0.29)	-	400 °C
C_i	E(012) H(0.27)	−/0 0/+	50 °C
$C_i C_s$	ME(0.17) ME(0.10) MH(0.09) MH(0.05)	−/0 -/0 0/+ 0/+	225 °C
$C_i P_s$	ME(0.30) ME(0.29) ME(0.23) ME(0.21)	- - -	125 °K
$C_i O_i$	H(0.36)	0/+	400 °C
Al_i	H(0.23)	+/++	200 °C

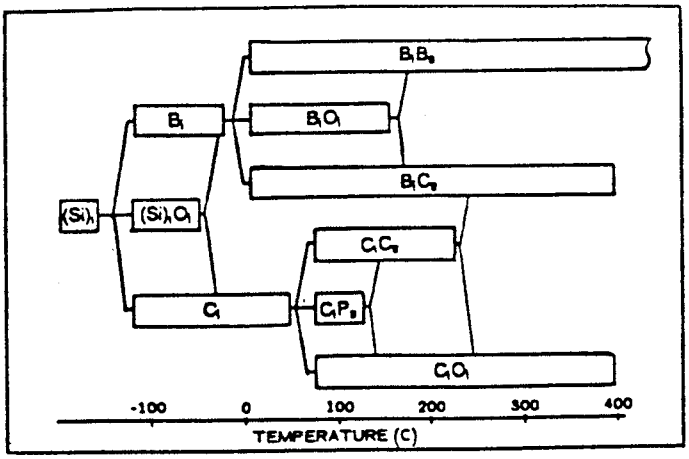

Figure 3-10 Interstitial defect states and hierarchy diagram indicating the temperature range for stability under quiescent conditions (after [18])

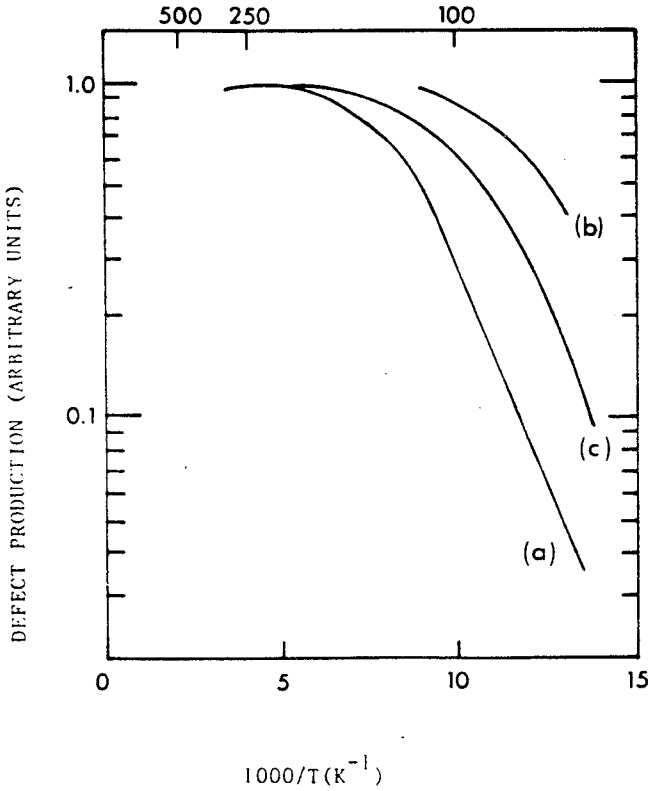

Figure 3-11 Variation of defect introduction rate with temperature for a) Czochralski (oxygen rich), b) GZ and c) float zone (oxygen deficient) silicon (after ref [24])

ii) annealing effects may be complex.

iii) both P and C concentrations may be important for the CCD manufacturing process as well as background oxygen content - and other elements such as boron (eg. in p^+ implants and in the p layer itself).

iv) if boron concentration is important then results would be expected to be different for high resistivity (low B concentrations) compared with standard resistivity silicon.

v) since the Si vacancy-interstitial pair is not stable for temperatures above about 100K and after formation will migrate through the lattice, we do not expect a significant dependence of the number of initial defects (before annealing) on the irradiation temperature - c.f. figure 3-11 from ref [24].

vi) different defects may be created depending on the type and energy of the incident particle and this may be reflected in the electrical performance. Thus although the number of initial vacancy - Si pairs scales approximately with non-ionising energy loss it does not necessarily follow that the device damage will do the same.

vii) additional defects may be present in proton, compared with electron, irradiated silicon.

3.3.3 Effect of Defects on Device Performance

In the previous sections it has been seen that vacancy/interstitial pairs are created in proportion to the non-ionising energy loss of the incident particles and that stable defects are formed approximately in proportion with the number of vacancy/interstitials (though some recombination effects may occur). These defects will have energy levels within the silicon bandgap and can give rise to five basic effects as shown in figure 3-12:

i) generation of e-h pairs
ii) recombination of e-h pairs
iii) trapping of carriers
iv) compensation of donors or acceptors
and v) tunneling of carriers.

A given level can manifest any of the above effects depending on the temperature, carrier concentration and the location in which it resides (eg. in a depletion region).

i) *Generation*

This is the thermal generation of electron-hole pairs through a level near midgap. This process can be viewed as the thermal excitation of a bound valence-band electron to the defect centre, and the subsequent excitation of that electron to the conduction band, thereby generating a free electron-hole pair. Alternatively, it can be seen as hole emission from the centre followed by electron emission. Only centres with an energy level near midgap make a significant contribution to carrier generation; an exponential decrease in generation rate occurs as the energy level position is moved from midgap [25]. Note that the emission processes only dominate over capture processes (recombination) when the free-carrier concentrations are significantly less than their thermal equilibrium values. Thus, thermal generation of electron-hole pairs through radiation-induced defect centres near midgap is important only in device depletion regions and at the surface. Introduction of such centres is the mechanism for leakage current increases in silicon devices and, in particular, for

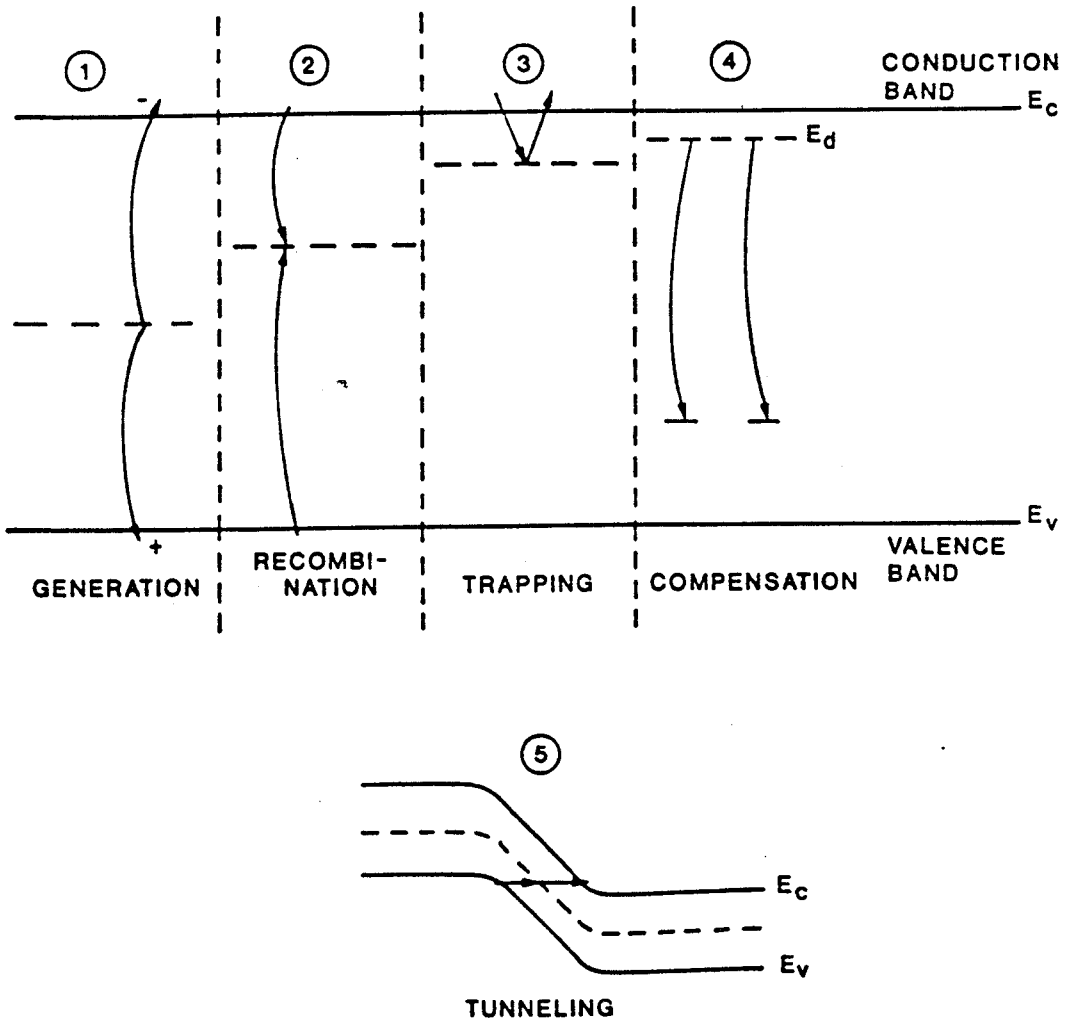

Figure 3-12 Illustration of effects due to defect centres in the silicon bandgap

dark current increases in CCDs. The temperature dependence of the dark current is discussed further in section 3.3.3.1.

ii) *Recombination*

In this process a free carrier of one sign is first captured at the defect centre. This is then followed by capture of a carrier of the opposite sign. Thus recombination removes electron-hole pairs, as opposed to the generation process which creates them. In general, the recombination rate depends on the defect centre density, the free carrier concentration, the electron and hole capture cross-sections, and the energy level position. The mean time a minority carrier spends in its band before recombining is referred to as the recombination lifetime, τ_r. Radiation-induced recombination centres cause τ_r, to decrease; this is the dominant mechanism for gain degradation in bipolar transistors.

iii) *Trapping*

Is the temporary trapping of carriers, typically at a shallow level. In this process, a carrier is captured at a defect centre and is later emitted to its band, with no recombination event taking place. In general, trapping of both majority and minority carriers can occur (at separate levels). The presence of radiation-induced traps, will reduce the CCD charge transfer efficiency. Note that in the buried channel the effect will depend on the capture and emission time constants of the minority carriers (electrons); τ_{nc} and τ_{ne} respectively (captive of holes can be neglected). We only need to consider traps in the upper half of the bandgap (traps in the lower half are always occupied by an electron since $\tau_{pe} << \tau_{ne}$) [26, 27, 28] and:

$$\tau_{nc} = 1/(\sigma V_{th} n_s)$$
$$\tau_{ne} = \tau_t (N_c/n_s) \exp(E_t/kT) \qquad (3\text{-}1)$$

where σ is the electron capture cross section for the trap, E_t is the trap energy level, (below the conduction band) n_s is the volume density of mobile electrons N_c is the effective density of states per unit volume in the conduction band and V_{th} is the average thermal velocity of mobile electrons. Thus the emission time is decreased for shallow levels and high temperatures. The effect on charge transfer efficiency depends on the magnitude of τ_e compared with the pixel transfer time [26, 27, 28] and for any given clocking scheme there is a temperature at which the two times are equal, giving a maximum charge deferred to the trailing pixel (and minimum CTE). Note that in equation (3-1) V_{th} is proportioned to $T^{1/2}$ and N_c to $T^{3/2}$ (σ_n and σ_p have only weak temperature dependence) and this should be taken into account when measuring activation energies (otherwise E_t is overestimated).

iv) *Compensation*

This process is the compensation of donors or acceptors by radiation-induced centres. In the example shown in Figure 3-12, some of the free electrons available from the donor level are compensated by deep-lying radiation-induced acceptors. The result is a reduction in the equilibrium majority-carrier concentration. This "carrier removal" process will cause an alteration in any device or circuit property that depends on carrier concentration. For example, the resistance of the collector in bipolar transistors will increase due to carrier removal.

v) *Tunneling*

This process is the tunneling of carriers through a potential barrier by means of defect levels. The defect-assisted (or trap-assisted) tunneling process can cause device currents to increase in certain situations. For example, there may be a defect-assisted tunneling component of the reverse current in a p-n junction diode.

In the case of CCDs effects i) and iii) ie. dark current generation and trapping (loss of CTE) are the only processes of importance and these are considered further below.

From the above descriptions it is implied that defect centres tend to act independently of each other so that damage effects are proportional to the number of stable defects of a given type that are created - and the experimental evidence, reviewed in the next two sections supports this. Note, though, that the total damage effect does not necessarily scale with NIEL since the type of defect may change with particle type or energy and so the damage (which depends on the trap level E_t) can change also. Nevertheless we shall see that, for the particular cases studied so far, an approximate scaling can be established.

3.3.3.1 Proton-induced dark current

In this section we are concerned with generation of dark current by defect centres located in the depletion region. We are interested in two parameters : the average increase in dark current and the increase in dark current non-uniformity (measured as the rms value or the histogram of pixel dark currents).

The results of Dale et al [29] have shown that, as expected, the average dark current is proportional to the particle fluence (defects act independently) and scales (at least approximately) with non-ionising energy loss (figure 3-13). These results were obtained using charge injection devices (CIDs). Janesick et el [17] have recently presented data for low energy protons (2, 5.6 and 9.7 MeV) incident on a Texas instrument 1024x1024 virtual phase CCD which are also reasonably in line with NIEL predictions, in this case obtained using TRIM Monte Carlo simulations [7]. Dale and Marshall [29a] have recently pointed out that using NIEL is the correct technique for predicting effects due to a shielded omnidirectional proton flux (as encountered in space) but the TRIM code should be used when low energy ($<$ 1MeV) protons are used in monoenergetic ground based experiments with protons at normal incidence. There is a difference in the number of displacements predicted in the two methods at low energies because in ground based experiments the particles slow down when passing through the silicon and the NIEL is not constant along the track and simulation needs to follow this by Monte Carlo methods (TRIM). However in a shielded space environment the proton spectrum does not appreciably change across the device active volume and the NIEL curve should be used. At energies $>$ 10 MeV there are other discrepancies between the two techniques and the reader is referred to reference [29a].

Note that differences in defect type (and hence energy level), in defect recombination rates (ie. in defect yield) and in defect annealing rates with changes in particle type or energy may all produce departures from linearity in the relationship with NIEL. These parameters will be technology and process dependent; hence it is prudent to check the dependence on non-ionising energy loss for a particular device type before considering it for flight use.

The dark current non-uniformity needs to be assessed separately from the average value since large fluctuations in pixel signals can occur because of i) inelastic nuclear collisions which produce events with large amounts of damage (and possibly large numbers of generation defects) and ii) defects (most probably from the large number of elastic collisions) which happen to be located in a part of the CCD depletion region which has a high electric field (eg. at or near the channel stops). This can lead to field-enhanced

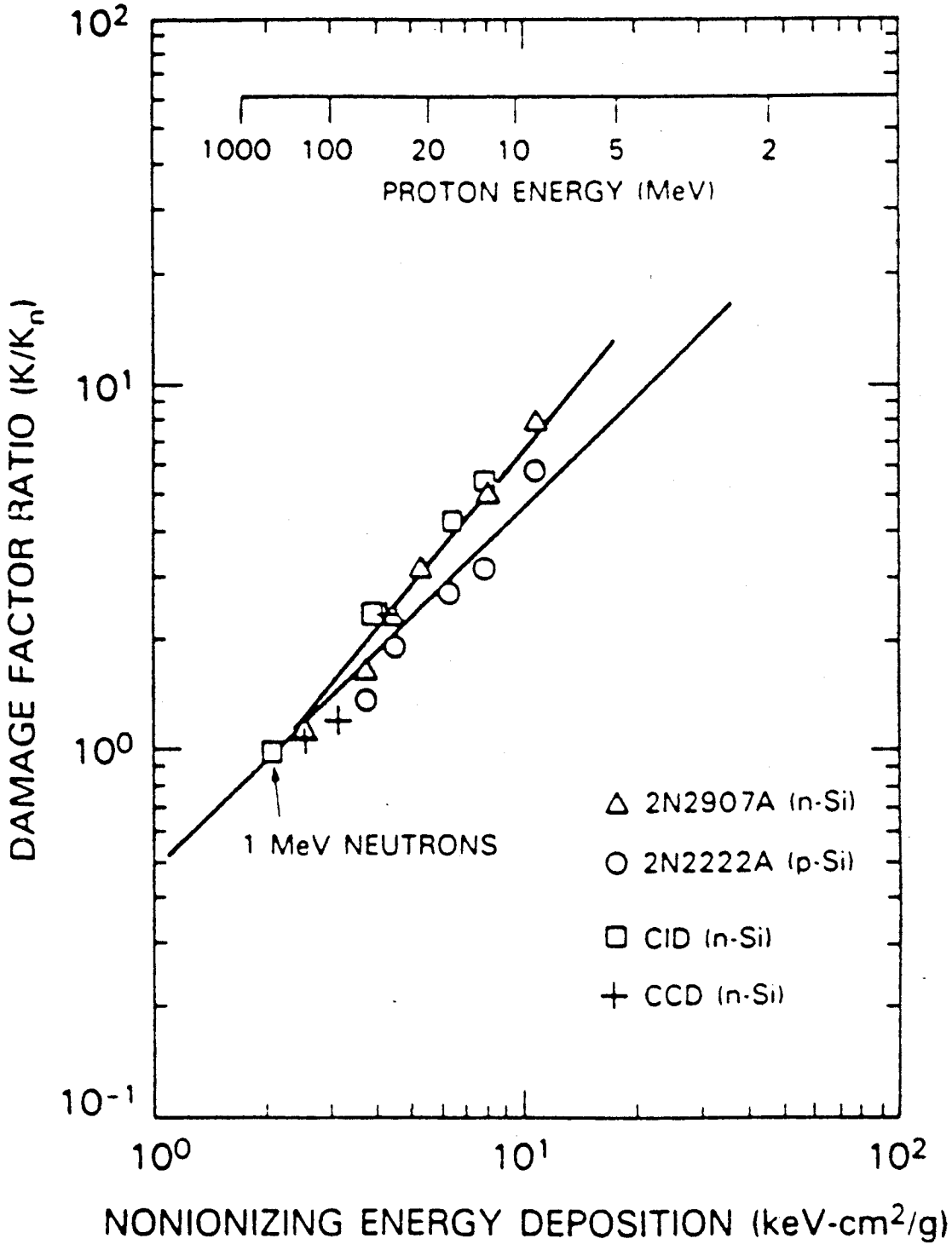

Figure 3-13 Measured damage factor ratios and calculated NIEL for various devices (from ref [29])

emission and increased dark current generation. The result is that dark current nonuniformity is not expected to scale with NIEL.

The equation for the dark charge generation rate (J_D) gives [25]:

$$J_D = \text{const.} \frac{WN_t T^{3/2} \exp(-Eg/2kT)}{\sigma_p^{-1} \exp[(E_t - E_i)/kT] + \sigma_n^{-1} \exp[(E_i - E_t)/kT]} \quad (3\text{-}2)$$

where W is the width of the depletion region, Eg is the bandgap energy, E_i is the intrinsic fermi level (midgap = 0.5x1.126 eV at 20°C) and σ_n and σ_p are the electron and hole capture cross-sections. Note that σ_n and σ_p are fairly temperature insensitive (activation energy = 0-0.1 eV). If we take the simple case $\sigma_p = \sigma_n$ (not T dependent) then J_D is proportional to $\cosh[(E_t - E_i)/kT]$ and at 20°C (kT = 0.025 eV) and we have the following relative values depending on E_t:

E_t(eV)	relative dark current at 20°C
0.56 (midgap)	1
0.44	0.015
0.4	0.003
0.35	0.0004

Thus levels with an energy less than ~0.35 eV are not likely to contribute significantly to the dark current and a level near midgap would have appreciably more effect than say the P-V centre (at 0.44 eV).

A departure from midgap effectively increases the overall activation energy for J_D - ie. causes the dark current to change more quickly with temperature [30].

For completeness we note that for σ_p not equal to σ_n, equation (3-2) gives a maximum dark current at $E_i - \frac{1}{2}kT \ln(\sigma_n/\sigma_p)$.

i) inelastic nuclear collisions

As discussed in para 3.3.1 the number of vacancy/interstitial pairs created by a proton undergoing a non-elastic collision with a lattice atom can be as much as 1000 times that from an elastic collision. Table 3-2 below gives the collision cross-sections, average damage energies and the variances of the damage energy for proton energies of 12, 22 and 63 MeV taken from reference [31]: The cross-section, σ, (in barns, 1 barn = 10^{-28} m^2) is defined such that the probability of a collision is:

$$\text{Probability} = \sigma V \rho N_A / A \quad (3\text{-}3)$$

where V is the interaction volume (in this case the depletion region volume), ρ the density, N_A Avagadro's number and A the gram atomic weight of the target (=28 for silicon). The local dark charge spikes created (largely in single pixels) due to these events will have a strong influence on the nonuniformity. Ways of modelling this are discussed in [31] and this is considered further in section 9.

PROTON ENERGY (MeV)	CROSS SECTION (BARNS)	MEAN RECOIL ENERGY (MeV)	MEAN DAMAGE ENERGY (MeV)	VARIANCE OF DAMAGE ENERGY $(MeV)^2$
ELASTIC REACTIONS				
12	1548	3.40×10^{-4}	1.76×10^{-4}	4.77×10^{-6}
22	857	4.68×10^{-4}	2.13×10^{-4}	7.71×10^{-6}
63	318	7.77×10^{-4}	2.87×10^{-4}	1.62×10^{-5}
INELASTIC REACTIONS				
12	0.670	0.267	0.0765	2.05×10^{-3}
22	0.723	0.569	0.111	2.71×10^{-3}
63	0.523	1.44	0.152	3.11×10^{-3}
COMBINED REACTIONS				
12	—	—	2.09×10^{-4}	8.17×10^{-6}
22	—	—	3.07×10^{-4}	2.03×10^{-5}
63	—	—	5.36×10^{-4}	5.90×10^{-5}

Table 3-2 Proton recoil spectrum parameters (from [31])

We note that, whatever happens on a microscopic level, the collision probabilities are governed by Poisson statistics and the variance of the resulting dark current distribution is proportional to the incident proton fluence [32].

ii) field enhancement

In the depletion region the generation from a trap level is increased in the presence of an electric field. There are three basic mechanisms (see [32] and references therein): 1) the Poole-Frenkel effect which results from a lowering of the Coulombic barrier surrounding the defect, 2) pure tunneling and 3) phonon - assisted tunneling, where an electron absorbs thermal energy from the lattice and then tunnels through the potential barrier at a higher energy. Pure tunneling takes place only at high electric fields (~10^7 V/cm) and can be neglected in practice. The enhancement predicted from one-dimensional Poole-Frenkel and phonon-assisted tunneling models is given, for example, in [32] and is shown in figure 3-14. It is seen that enhancement becomes important for fields greater than 10^5 V/cm, however this enhancement might be expected to be reduced if a 2-dimensional treatment were made. On the other hand Pavelka and Ferenczi [33] have recently shown that at the edge of the depletion region (in fact, within 1 Debye length of the edges) recapture of free carriers cannot be neglected. This gives an increase in the emission rate so that enhancement can be appreciable even at low fields.

A side-effect of field enhanced emission is a decrease in the activation energy (ie. the dark current changes slowly with temperature). This was noticed by Srour and Hartmann in the case of the avalanche fields within a virtual phase device [30] and has also been seen by the present author in the case of the smaller fields occurring in an EEV CCD [34]. Marshall et al [35] have given a way of identifying pixels with anomalously high dark current caused, for example, by field enhanced emission. This is based on the theory of extreme value statistics and is considered further in section 6.3.

Note that the average value of the dark current is not expected to be increased, since in most of the depletion region volume the fields are low (~10^4 V/cm). However if a collision (most likely an elastic collision) takes place in a high field region (eg. at the pixel edge) then a dark current spike can result.

3.3.3.2 Proton-induced changes in CTE

Defect states which are created in the CCD buried channel will act as trapping centres and result in reduced charge transfer efficiency. As discussed in para 3.3.3, the effects are temperature dependent, so that at low temperatures the trapping times are long. This has been seen for example by Janesick et al [17] who found that, for their CCD, operating at -80°C resulted in an almost complete recovery in performance (since the trap emission times were so long that traps were kept permanently filled). Figure 3-15 shows data at -50°C (also from ref [17]) showing the dependence on proton energy and the scaling with non-ionising energy loss as predicted. The departures from TRIM [7] calculations above 10 MeV are largely due to the neglect of nonelastic nuclear collisions in that code. The NIEL curve of figure 3-7 would give better agreement.

At low energies the Janesick data (for the CRAF/Cassini CCD) gives a radiation trap efficiency (RTI) factor of ~4.10^{-3} - this is the conversion factor from displacements/cm^2 to electrically active traps. Janesick also gives ~5.10^{-2} displacements/proton at 10 MeV (=D). Charge transfer inefficiency (CTI = 1 - CTE) is given by:

$$CTI = \frac{D.A.RTI \times fluence}{S} \qquad (3\text{-}3)$$

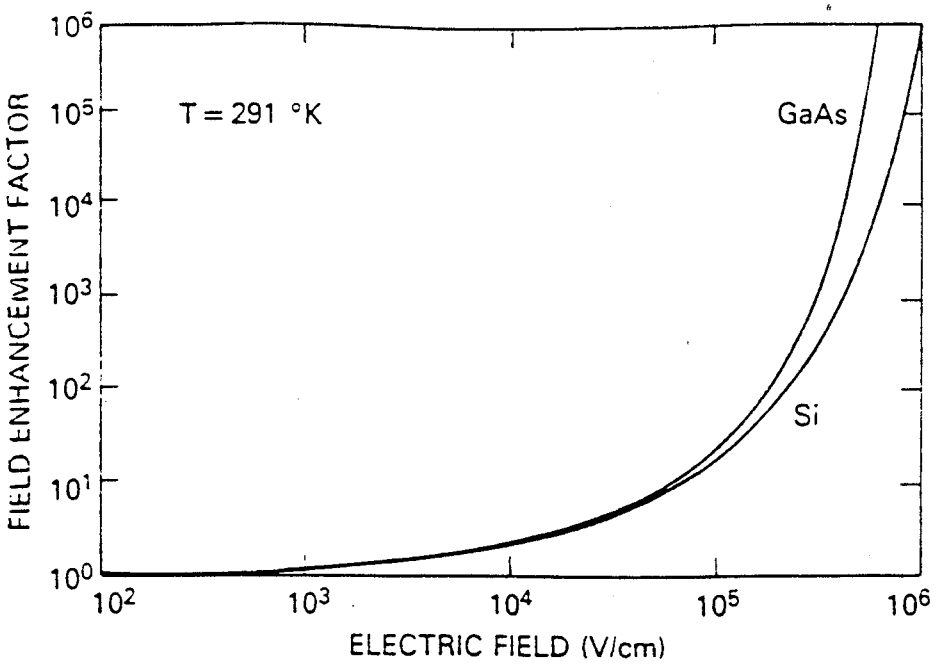

Figure 3-14 Field enhancement factors

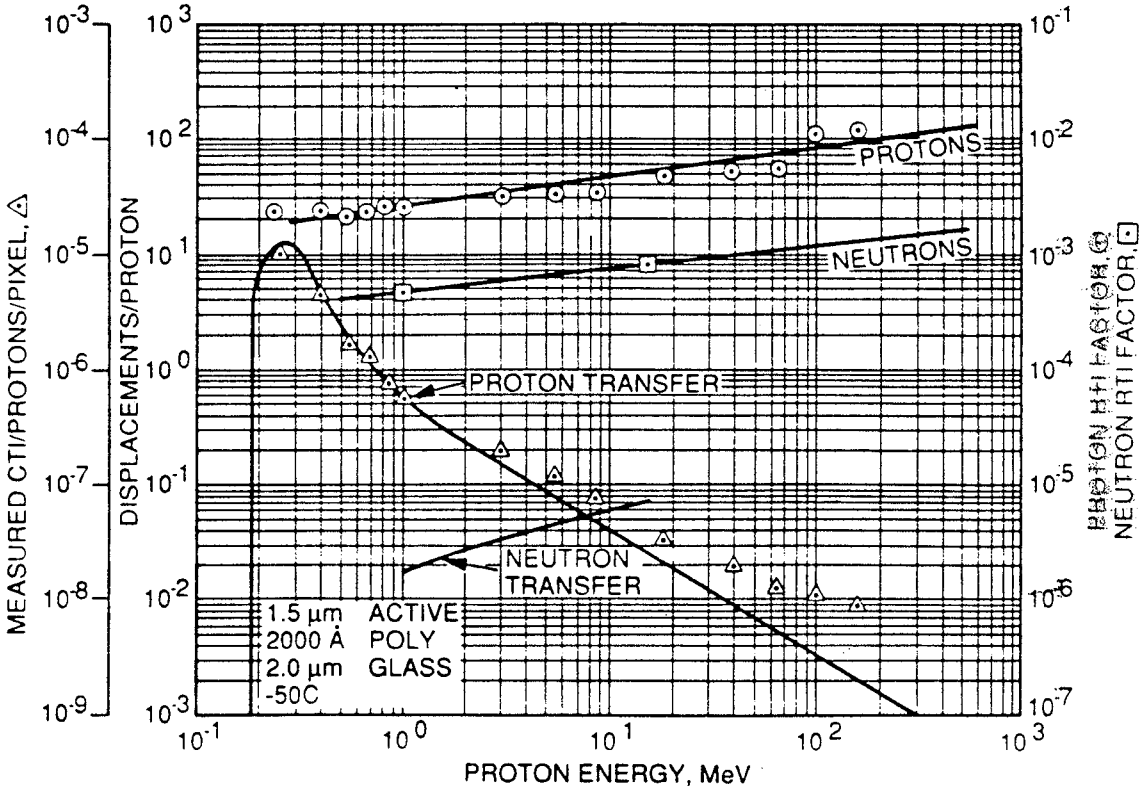

Figure 3-15 Charge transfer inefficiency and other parameters (from [17])

where A is the effective pixel area (=9.6 x 10^{-7} cm^{-2} for the Janesick CCD - with a notch channel, and 4.4 x 10^{-6} for a TH7863, assuming 4μm channel stops). Thus if the Janesick data were valid for a TH7863 we would expect for a fluence of $\underline{5x10^9}$ $\underline{10\ MeV}$ protons/cm^2

$$CTI = \frac{5.10^{-2} \times 4.4x10^{-6} \times 4.10^{-3} \times 5.10^{9} \text{ (electrons)}}{S \text{ (electrons)}}$$

$$\therefore \quad CTI = \frac{4.4}{S} \frac{\text{(electrons)}}{\text{(electrons}} \text{ per pixel at 10 MeV and -50°C}$$

The CTI is inversely proportional to the signal transferred since each defect is a single electron trap and the aggregate of all the traps encountered by the signal packet during readout gives a fixed charge loss - in this case an average of 4.4 electrons/pixel. Assuming a worst case value of 576 parallel and 385 serial transfers gives a global deferred charge loss of 3800 electrons. Comparable (though slightly lower) values for CTI have been presented by Abbey et al [36] for EEV devices (22x22μm^2 pixels). Note that in general, because of the differences in clocking speed, parallel and serial CTI will not be degraded to the same extent. Abbey et al found that parallel CTI increased more rapidly with radiation damage though pre-irradiation values were lower than for serial transfer. They also found that the damage was significantly (but not completely) annealed by baking at ~120°C.

4. TEST OBJECTS

The devices under test were samples of two types of CCD manufactured by Thomson-CSF, Military and Space Division, St Egreve, France: the TH7863 device which is a 288x384 pixel frame transfer CCD and the THX31160-1 device which is a 14x14 pixel, frame transfer CCD with on-chip drivers. Both types are front-illuminated, n-buried channel CCDs with a floating diffusion output and a source follower MOSFET amplifier (with an on-chip current source load). Both types of device were in ceramic DIL packages with permanent glass windows. Because the proton energies used would not penetrate these windows (the range of 10 MeV protons in glass is ~0.6mm) they were removed (by ESA personnel) by the simple expedient of heating the devices with a hot air gun and applying gentle force to the window with a scalpel blade.

Images were recorded before and after window removal and it was confirmed that there was no loss in functionality. It was an inevitable consequence however that some debris was caused to fall on the surface of the CCDs thus producing obscuration of some pixels and dark spot blemishes on bright field images. However since these bright field images were not a major consideration of this study, this was considered to be acceptable.

In addition to the Thomson-CSF devices, two CCD02-06 sample chips manufactured by EEV Ltd, Chelmsford, UK, were also tested. These had temporary windows attached with tape which were easily removed. The EEV devices were investigated as part of a Sira internal R&D programme; results are included in this report for comparison purposes. The EEV devices are also n-buried channel devices but with a 3-phase, three level, overlapping gate, polysilicon electrode structure. The three CCD types are briefly described; further details of the Thomson-CSF devices are given in reference [1].

4.1 The THX31160-1 CCD

The layout of the CCD is shown in figure 4-1. The CCD is manufactured using a two level polysilicon technology. There are 14x14 23μm square useful image area pixels plus a half shielded line at the top and bottom and two shielded columns at one edge making 16x16 pixels in all. The total storage zone is also 16x16 pixels and is covered by an aluminium mask which acts as a light shield.

The small size of the sensor allows a high frame rate (of the order of 10kHz) and leads to a low electrode capacitance which in turn allows the implementation of on-chip N-MOS clock drivers. The two phase image, storage and readout register clocks are generated from single phase 5.0V input clocks and the reset pulse is internally generated from the readout clock.

The pin-out of the device and applied voltages were as shown in table 4-1. The voltages correspond to the manufacturers' typical values. Since the devices were only irradiated to 9krad there was no need to increased V_{DR} to maintain performance (c.f. [1]). The devices were operated in frame transfer mode at a frame rate of 10kHz with 1MHz pixel rate parallel and 3MHz serial clocks. The line length was extended to give extra 'dummy' pixels thus giving a good baseline reference. The actual format of displayed images is given in section 4.4 of reference [1].

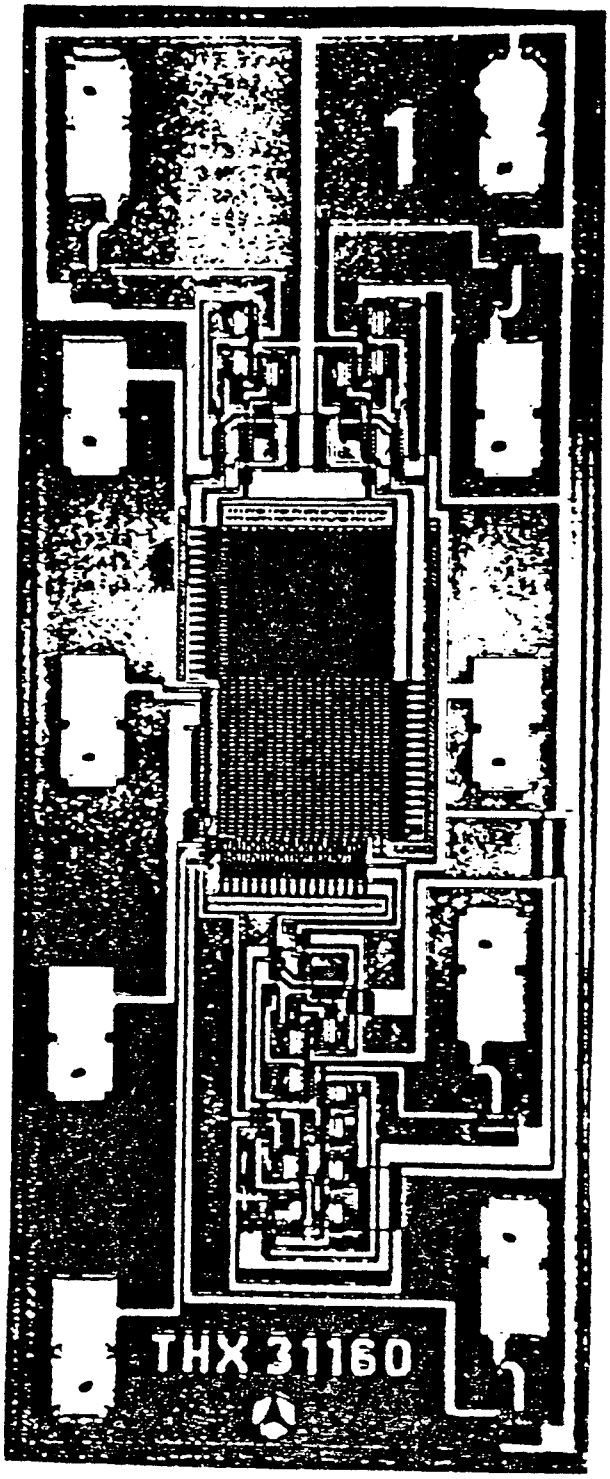

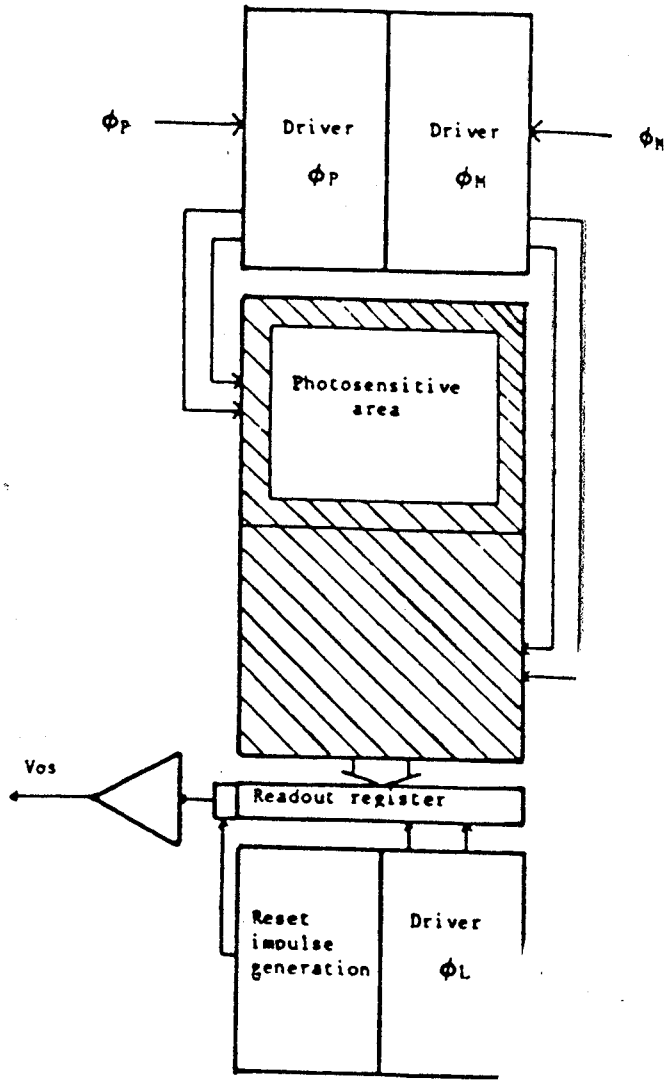

Figure 4-1 Layout of the THX31160-1 CCD

4.2 The TH7863 CCD

Figure 4-2 shows the layout of the device. There are 288x384 useful image area pixels, each 23μm square. The storage area is 290x384 pixels and is covered by an aluminium light shield. There is also a dark charge reference region (10 pixels wide) along one edge of the CCD and 7 inactive pre-scan elements as well as isolation elements for suppression of edge effects. The actual line format is: 7 inactive pre-scan elements, 1 isolation element, 384 image pixels, 4 isolation elements, 10 dark reference elements and 1 isolation element. As with the THX31160 the line length was extended by adding 'dummy' pixels to give an additional baseline (zero signal) region. This was done by overclocking the readout register. The format of displayed images is discussed in section 4.4 of reference [1].

The pin out of the device and applied voltages are given in table 4-2. The voltages correspond to manufacturers typical values. Since the devices were only irradiated to 9krad there was no need to increase V_{DR} to maintain performance (c.f. [1]).

In the main, the devices were operated at a frame period of 41ms with 1MHz pixel rate parallel 4-phase clocks and 3MHz serial 2-phase clocks. The clock overlap for both serial and parallel clocks was ~50ns. For some measurements of image area dark charge histograms at various temperatures after irradiation the integration time was increased by a factor 11.8 (to 484ms) with the readout time being kept the same (41ms).

4.3 The EEV CCD02-06

The devices tested were front illuminated frame transfer devices with 288x385 image area pixels each 22x22μm square. They were operated at manufacturers' typical voltages with the option of increasing the substrate voltage (V_{SS}) from its value of 7.5V to 9V or above so as to obtain inversion under two of the three image area electrodes and hence reduced surface-generated dark current [37].

The devices use 3-phase image, store and readout register clocks. In the clocking scheme used the integration and readout times were equal to 0.149s (0.250s for some of the later measurements).

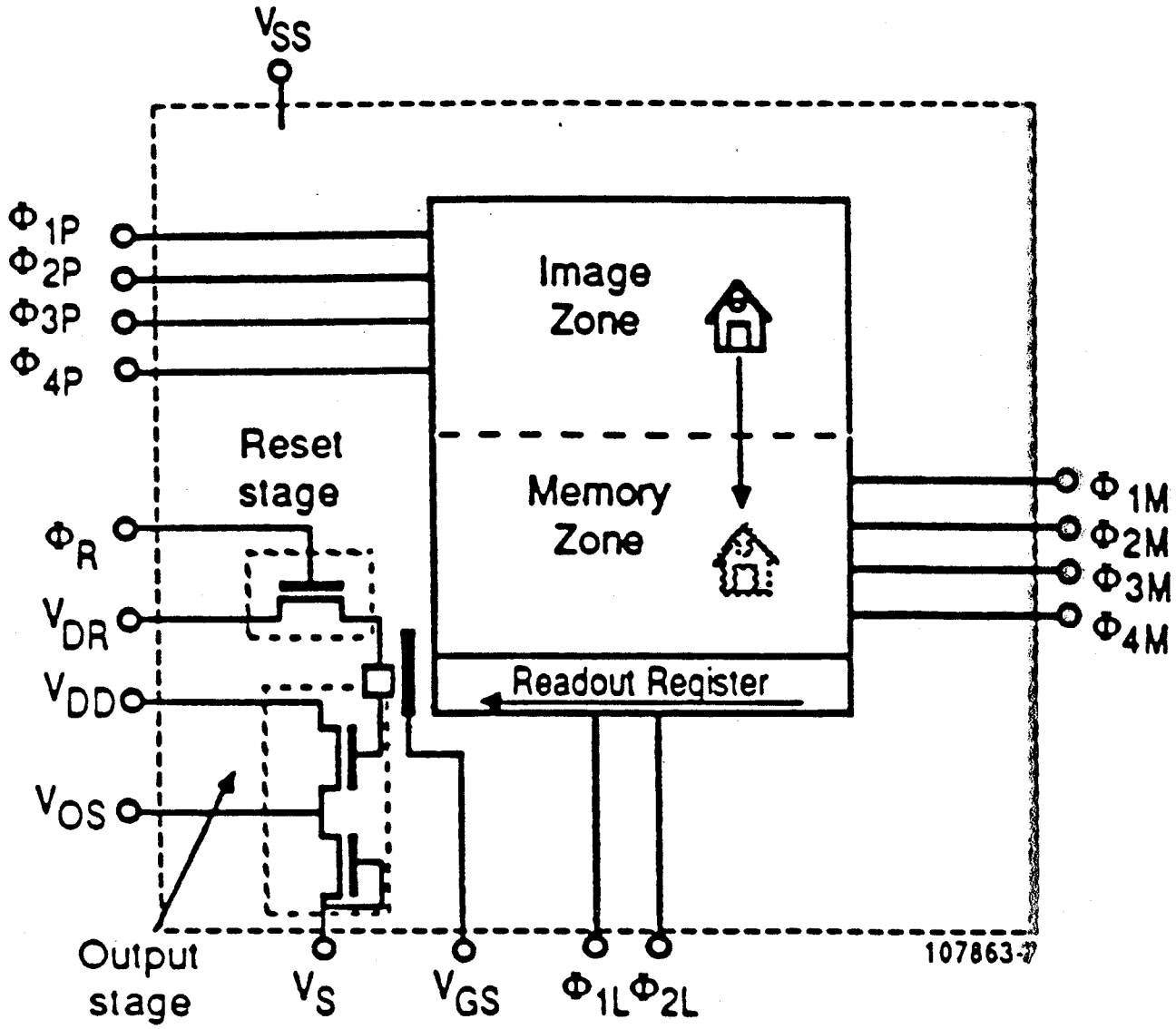

Figure 4-2 Layout of the TH7863 CCD

Table 4-1 Applied voltages for THX31160 devices (as measured at the CCD socket)

The following bias voltages were applied to the 2 powered devices during irradiation (two devices were unpowered) and to all 4 devices during electrical measurements; they correspond to the typical voltages as defined by the manufacturer. The tolerance in all cases is ±0.1V.

Pin Number	Designation	Symbol	Applied Voltage (Volts)
1	Image zone clock	ϕ_P	⎫ Low : 0.1V
7	Readout register clock	ϕ_L	⎬ High : 5.0V
9	Memory zone clock	ϕ_M	⎭
2	Output amplifier drain	V_{DDA}	15.0V
4	Output amplifier ground	V_{SSA}	0.0V
5	Reset bias	V_{DR}	12.0V
6	Output gate bias	V_{GS}	2.0V
8	Clock driver bias	V_{DDH}	15.0V
10	Substrate bias	V_{SS}	0.0V

Clock frequency: transfer frequency = 1MHz, readout frequency = 3MHz frame transfer mode

Temperature: room temperature for irradiation
a range of temperatures from 12 to 32°C for electrical measurements (but predominantly 22°C).

Table 4-2 Applied voltages for TH7863 devices (as measured at the CCD socket)

The following bias voltages were applied to the 2 powered devices during irradiation (two devices were unpowered) and to all 4 devices during electrical measurements; they correspond to the typical voltages as defined by the manufacturer. The tolerance in all cases is ±0.1V.

Pin Number	Designation	Symbol	Applied Voltage (Volts)
5 and 15	Output amplifier drain supply	V_{DD}	15.5
18	Reset bias	V_{RD}	13.3
1 and 10	Substrate bias	V_{SS}	-3.0
20	Register output gate bias	V_{GS}	2.5
17	Output amplifier source bias	V_S	-3.0
14	Image zone clock	ϕ_{1P}	See below
12	"	ϕ_{2P}	"
13	"	ϕ_{3P}	"
11	"	ϕ_{4P}	"
19	Reset clock	ϕ_R	"
4 and 9	Memory zone clock	ϕ_{1M}	"
7	"	ϕ_{2M}	"
8	"	ϕ_{3M}	"
6	"	ϕ_{4M}	"
3	Readout register clock	ϕ_{1L}	"
2	"	ϕ_{2L}	"

Table 4-2 Clock voltages (as measured at the CCD socket)

Designation	Symbol		Applied voltage (Volts)
Image zone clocks during integration period	ϕ_{1P}, ϕ_{2P} ϕ_{3P} ϕ_{4P}		10.0 0.3 1.8
Image zone clocks during frame transfer period	ϕ_P, ϕ_M, ϕ_L, ϕ_R	Low	0.3
Memory zone clocks, output register clocks and reset clock	ϕ_P, ϕ_M, ϕ_L, ϕ_R	High	10.0

Clock frequency: transfer frequency = 1MHz, readout frequency = 3MHz, overlap = 50ns frame transfer mode

Temperature: room temperature for irradiation
a range of temperatures from 6 to 37°C for electrical measurements (but predominantly 22°C)

5. EXPERIMENTAL DETAILS

5.1 The Radiation Facility and Dosimetry

The devices were irradiated with 1.5 and 10.0 MeV proton beams using the Tandem Van de Graaff generator at AEA Technology, Harwell, UK. The beam line arrangement is shown in figure 5-1. This was designed so that beam fluxes were sufficiently low ($\sim 10^7 p/cm^2/s$) that total fluences of $10^8 p/cm^2$ could be accurately delivered. At this rate a typical exposure of $5x10^9 p/cm^2$ took a few minutes. Beam uniformity was quoted as better than $\pm 5\%$ over the sample area. The beam line incorporated a pack of scatter foils 3.82m upstream from the sample position. These foils were selected such that the intensity profile of the beam at a distance of 3m from the foil (along the beam axis) would have a standard deviation (radius) of more than 20cm. Therefore, an area element of $1cm^2$ at the centre of this beam distribution would receive a very small fraction of the total beam produced by the machine and the variation of beam intensity across that element would, in fact, be very much less than 5%. The scatter foils were 100 microns of gold for the 10 MeV beam and 10 microns of molybdenum of for the 1.5 MeV beam. Since these energies were those required at the sample surface, the initial beam energies were 11.65 and 2.26 MeV respectively, in order to compensate for the energy lost in the scatter foil itself.

The alignment of the beam was first adjusted using a quartz scintillator marked with cross-lines and a pin-hole collimator. Once the alignment was satisfactory, this collimator and scintillator were removed and replaced by the scatter foil. The beam was monitored by means of a surface barrier detector positioned at an angle of 45 degrees to the beam axis, in a side arm adjacent to the scatter foil. At this position, the detector received only a very small proportion of the beam. At the entrance to the sample chamber, the beam was defined by a tantalum collimator with a diameter of 43mm.

Within the sample chamber, two CCD samples were positioned on a moveable holder. The CCDs were in zero insertion force sockets. In each case (ie. for each of the TH7863, THX31160-1 and CCD02-06 types) one device was unbiased during irradiations with its pins shorted and the other was kept biased and clocking by means of ribbon cables (with IDC sockets) connected to a programmable CCD timing generator (c.f. para 5.2). A second surface barrier detector with a 1.5mm diameter collimator in front of it was also mounted on the sample holder in order to calibrate the beam flux at the sample position with respect to the reference detector mentioned above.

A series of calibrations were performed by AEA personnel for each energy and scattering condition. These were made at low fluxes so that the count rate in each detector was not excessive ($< 1000Hz$), ie. to avoid pile-up. The calibration factor was calculated as follows:

$$CF = \frac{\text{Counts in Calibration Detector}}{\text{Counts in Reference Detector}} / A \ \left((p/cm^2)/count \right)$$

where A was the area of the collimator in front of the calibration detector ($1.77x10^{-2}$ cm^2).

The calibration data are shown in Tables 5-1 and 5-2, where it can be seen that a satisfactory statistical precision was obtained.

In addition to the measurements discussed above, beam current measurements were made using a Faraday Cup assembly situated between the two gate valves, upstream from the

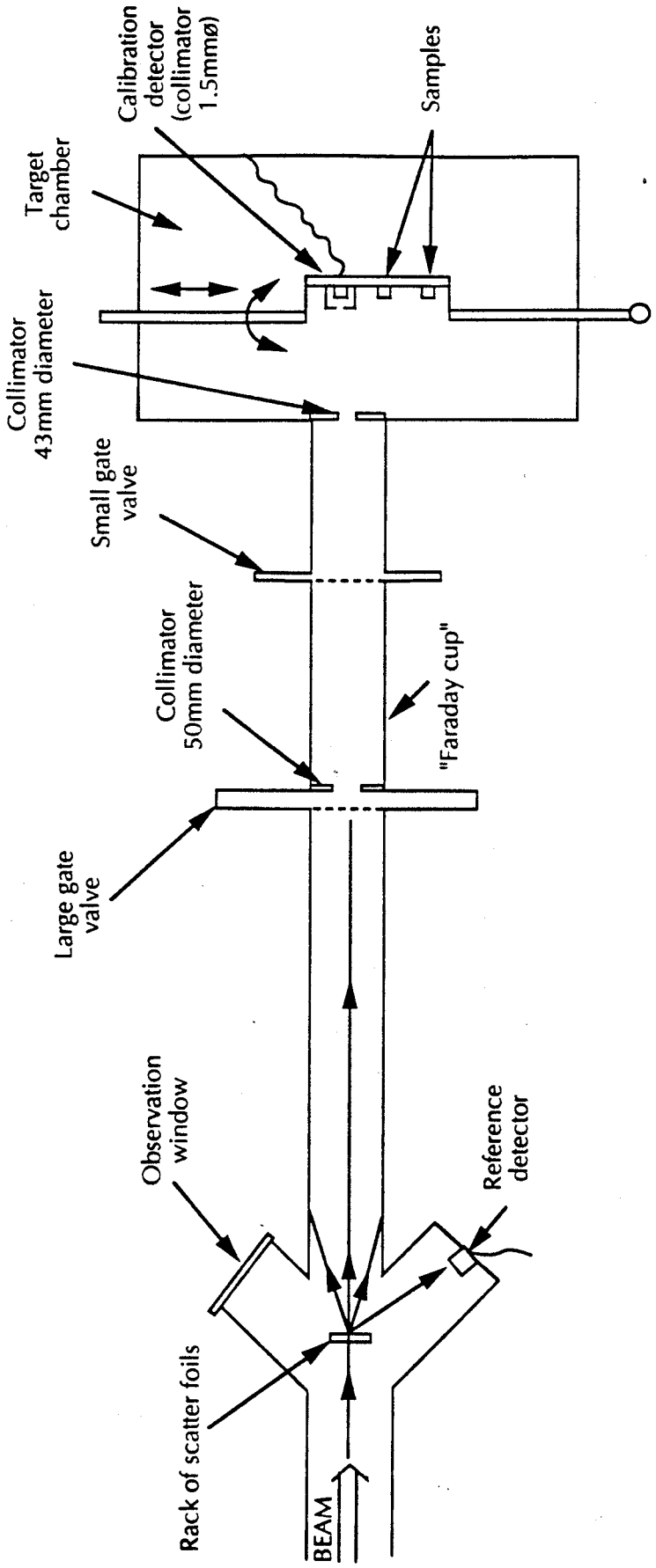

Figure 5-1 Schematic diagram of the proton beam line

sample chamber. These readings were for comparison with previous experiments as a check that the scattering characteristics had not changed.

Table 5-1 10 MeV Calibration Data

Reference Detector (counts)	Calibration Detector (counts)	Calibration Detector ((p/cm^2)/count)
269	189830	706
173	131297	759
94	70778	752
117	87679	749
89	66522	747
		Mean: 743 ±2.8%

Table 5-2 1.5 MeV Calibration Data

Reference Detector (counts)	Calibration Detector (counts)	Calibration Detector ((p/cm^2)/count)
109	22280	204
108	24692	229
128	29179	228
139	30411	219
104	21372	206
123	27574	224
100	24401	224
102	21698	213
		Mean: 218 ±4.2%

5.2 Equipment for Testing CCDs

5.2.1 Description of Test System

The CCD test equipment used at Sira consisted of the following units:

1. AT-computer with framegrabber card
2. Programmable CCD timing generator
3 Power distribution unit
4. CCD camera head and temperature controller (for single chip measurements)
5. Analogue interface and correlated double sampling (CDS) amplifier
6. Digital interface
7. Digital multimeters for voltage and current measurements
8. Optical test equipment
9. Equipment for driving EEV CCDs

Figure 5-2 shows how these units were connected together for detailed characterisation of single devices. For biasing during irradiation a ribbon cable was connected to the device socket in the camera head and this relayed power to a CCD socket in the scattering chamber.

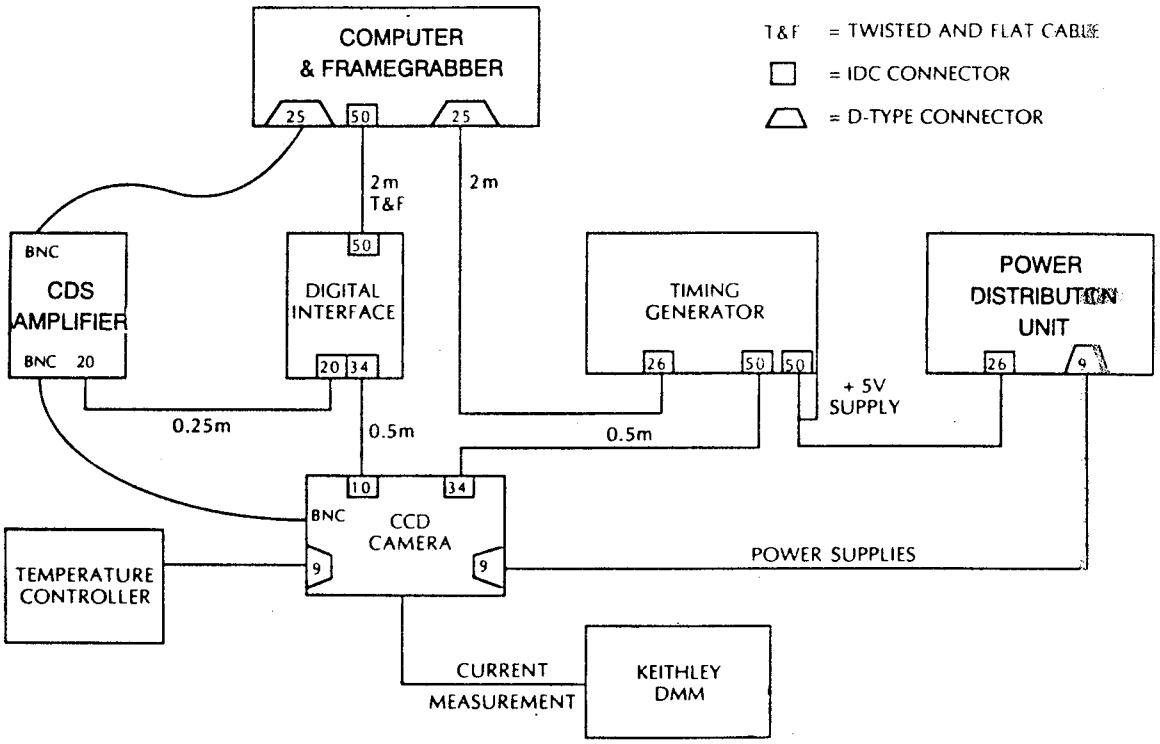

Figure 5-2 Block diagram of test equipment for detailed characterisation of single devices

5.2.1.1 Computer and Frame Grabber

Two AT-computers were used, one a Digitask 386 with maths coprocessor and 120 Mbyte hard disk (for data analysis) and a Dell 386X with 40 Mbyte hard disk (for data capture). Each computer operated under MS-DOS and was attached to two multisync colour monitors, one being used for entering commands the other for display of CCD images. Slotted into each AT-bus was a VS100 framegrabber/image memory card manufactured by Imaging Technology Inc. These are capable of capturing normal CCIR video signals or non-CCIR variable scan rate pictures up to a pixel rate of 10MHz. The image memory is 1024x1024x12 bits deep. A 512x512 window of this memory can be output to the display at any one time.

The variable scan rate pictures can be input either as digital data up to 12 bits deep or, as in this case, as an analogue signal to be digitised with an internal ADC. The internal ADC digitises to 8 bits. The synchronisation of the frame grabber with the variable scan rate outputs from CCDs is controlled from Digital Interface, (para 5.2.1.6).

5.2.1.2 Programmable Timing Generator

The Timing Generator produces TTL level clock waveforms for the CCD. It is non-specific and can generate waveforms for any current size of 3 or 2/4 phase device. It consists of a series of RAM-controlled sequencers. The number and frequency of pulses in a train and the grouping together of different trains to form the overall pulse sequence for the CCD are variable. Sequences are generated by typing user-friendly high level statements on the host computer to generate a file containing the sequence information. This file is then down-loaded to the RAM in the Timing Generator via the parallel printer port.

Because the pulse trains are variable, it is simple to generate the sequences necessary for functions such as on-chip binning, pocket pumping, variation of integration time etc.

The Timing Generator operates at clock rates of up to 32MHz, giving a maximum 16MHz pixel rate for devices with 2 phase output registers and 11MHz for 3 phase devices. There are 23 separate output lines, thus allowing for control of external circuitry such as clamps, sample and holds and ADCs, as well as clocking the CCD.

In general it is possible to store several different complete sequences in the timing generator at any one time, though the number depends on their complexity. Hence the operator can switch sequences without reloading from the host computer. This is particularly useful for example when changing integration times.

5.2.1.3 Power Distribution Unit

This was a set of bench power supplies for providing bias to the programmable timing generator and camera head(s).

5.2.1.4 CCD Camera Head and Temperature Controller

This unit enables operation of single CCDs during detailed characterisation of electro-optical properties. Two camera heads were used, one for the THX31160, the other for the TH7863. In each case the CCD was placed in a zero-insertion-force socket fitted with a copper heatsink bar coupled to two Melcor FC07-18-05 Peltier coolers (one at each end of the bar). The Peltier coolers were driven by a power amplifier contained in a separate temperature controller box. Servo control of the temperature, as monitored at the heatsink bar, was possible to $\pm 0.1\,^{\circ}C$ but note that the actual temperature at the CCD die will differ from the set temperature because of the contact resistance between the copper heatsink bar and the ceramic package and because of the heat dissipation in the CCD. Beneath the CCD

socket was a single board containing bias supply regulators, MOS level clock drivers and a preamplifier. The camera heads also contained voltage monitor points and adjustment potentiometers.

5.2.1.5 Analogue Interface

This contains a variable switched gain amplifier and correlated double sampling circuit of the clamp and sample type. The positions of the sample points were settable using tapped delay lines. The switched gains available were x1, x5.7 and x30.2 (a second switch on the camera units provided an additional gain of x1 or x2). A potentiometer allowed a continuous gain multiplier between 0 and x1. The sampled output was then passed to the 8-bit ADC on the VS100 board.

5.2.1.6 Digital Interface

This unit takes single ended TTL logic signals from the timing generator and camera heads and converts them to the differential TTL signals needed by the VS100 frame grabber; also some signals are inverted at this point.

5.2.1.7 Optical Test Head

A commercial quality 50mm lens was used to image light from a screen illuminated by a tungsten halogen lamp for bright field mapping of the CCD response and for linearity measurements with uniform illumination. A spot scanning system was also used for obtaining linearity measurements with spot illumination. This system consisted of a xenon arc lamp and fibre optic cable which relayed the light to a 20μm pin hole placed at the focus of an off-axis parabaloidal mirror. This system then gave a uniform beam of parallel light. The beam was used to illuminate the camera head (either TH7863 or THX31160-1) and commercial 50mm lens. The camera head was fixed to a two axis gimballed mount with Aerotech DC motor drives giving encoder positions to 0.003 arc sec. The DC motors were driven by a Unidex controller with an RS232 interface to the AT computer. Using the CCD test software the spot could be positioned to the centre of a pixel. No filters were used (ie. illumination was broadband). It was established that the spot size was much less than the pixel dimension but an accurate profile was not available (a purpose designed lens system for giving spots of diameter $<5\mu$m is under development).

5.2.1.8 Equipment for Driving EEV CCDs

For these devices a set of breadboard electronics was used with clocks provided by the programmable timing generator. The analogue CCD output was relayed (after preamplification) to the analogue interface and frame grabber as with the Thomson-CSF devices. No temperature control was available and the devices were operated at room temperature (19 ± 1°C).

5.2.2 Test Software

Sira has written system-level software which acts as an interpreter for the VS100 image memory board functions and allows these functions to be selected in a user-friendly manner and assembled together to form sequences for automated testing or data analysis. Examples of functions available with simple commands are:

* image acquisition (either continuously or as single frames)
* pan and zoom
* image scaling and off-setting

* display of a cursor on the image display and readout of a 5x5 matrix of pixel values on the computer console
* cursor movement from keyboard or mouse
* selection of points, lines, columns or areas of interest by keyed commands or by mouse
* calculation of mean and standard deviation of areas of interest and display of histograms. Also dumping of this data to a file
* recording of intensity profiles across slices through images
* detection of pixels above or below a set threshold (eg. for analysis of image non-uniformity)
* adding or averaging successive images to reduce random noise
* addition, subtraction, division or multiplication by previously stored images
* statistical analysis of values from one pixel (or a group of pixels) from successive frames for noise analysis
* saving of image data, either in VS100 or standard TIF (tagged image file) format
* operations on input and output look-up tables (LUTs)
* control of Unidex mirror drives
* control of Bentham Instruments monochromator.

Examples of sequences of operations are:

* definition of sequences of regions of interest and recording of mean, standard deviation etc.
* repeated searching for pixels above (or below) a threshold in successive images and recording data in a file - as used in analysing data from x-ray events from calibration sources.
* interaction with the programmable timing generator so as to form linearity plots by successive changes in integration time and recording of image values from a specified region of interest.

Data files (such as histograms) can be analysed and plotted using standard spreadsheet or graphics packages. This is made easy since it is possible to flip in and out of the command program without reloading any parameters or losing the screen display.

Built into the command program were safeguards to ensure that files could not be overwritten by giving two files the same name. The database was organised by giving each CCD a unique directory eg. (\TH7863\03, for TH7863 device 03). All files relating to a CCD were stored in its directory. To keep track of the current directory the directory name appears as the prompt from the command program. For each set of measurements in a given directory, the commands entered were appended to a session file. A fresh session

file being automatically created each day (on start up of the computer). The session file gives a record of tests performed, filenames given and CCD timing programs used. The display format for images is discussed in para 4.4 of reference [1].

5.3 Test Histories

5.3.1 TH7863 Devices

Four TH7863CRH devices from lot M63480R21 code 9013 were irradiated. Since the device windows were removed there was no individual marking on the CCDs and so a Sira numbering scheme was used (numbers being written on the side of the CCD packages):

Device number	Proton energy	Bias during irradiation
01	10 MeV	No
02	10 MeV	Yes
03	1.5 MeV	No
04	1.5 MeV	Yes

There are at present three spare devices.

The irradiations were carried out in two stages. In stage one half of the CCD area was masked by a 1mm thick aluminium plate as shown below:

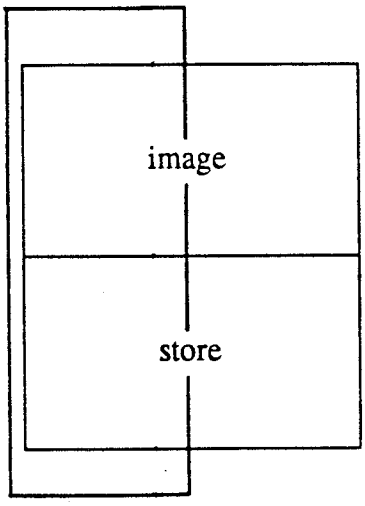

the device was then irradiated to a proton fluence calculated to give an ionising dose of 3 krad(Si), ie:

5.37×10^9 p/cm^2 at 10 MeV

1.40×10^9 p/cm^2 at 1.5 MeV

In step two the aluminium mask was moved to the centre of the CCD:

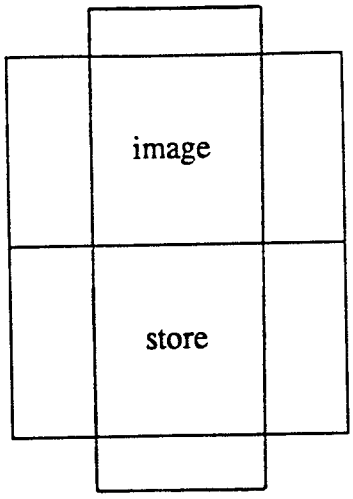

The CCDs were then irradiated so as to give an additional 6 krad(Si) of total ionising dose ie:

1.07×10^{10} p/cm^2 at 10 MeV

2.80×10^{9} p/cm^2 at 1.5 MeV

In this way four zones with different accumulated doses (0, 3, 6 and 9 krad) were produced on each CCD as illustrated in figure 5-3. Note that the output node received the maximum dose of 9 Krad(Si). Typical exposure times were ~2 minutes. The irradiations were carried out at room temperature. Electrical measurements were made before and immediately after each dose step and after unbiased storage at room temperature at Sira.

5.3.2 THX31160-1 Devices

These had date code CD-8944 but unknown lot number. They were selected as follows:

Device number	Proton energy	Bias during irradiation
01	10 MeV	No
02	10 MeV	Yes
05	1.5 MeV	No
04	1.5 MeV	Yes

and at present there are two spare devices (device 03 was accidentally destroyed during testing).

The CCDs were all irradiated to 6 krad(Si) ie. the fluences were 1.07×10^{10} p/cm^2 (10 MeV) and 2.80×10^{9} p/cm^2 (1.5 MeV). Electrical measurements were made before and immediately after irradiation and after unbiased room temperature storage at Sira.

5.3.3 EEV Devices

The CCD02-06 devices were tested with the same masking and dose steps as for the TH7863 CCDs. The device numbers were:

EEV number batch/wafer/CCD No.	Sira number	Biased during irradiation
8232/13/7	01	No
8232/13/9	02	Yes

The proton energy was 10 MeV. Again, electrical measurements were made before and after irradiation and after unbiased storage at room temperature.

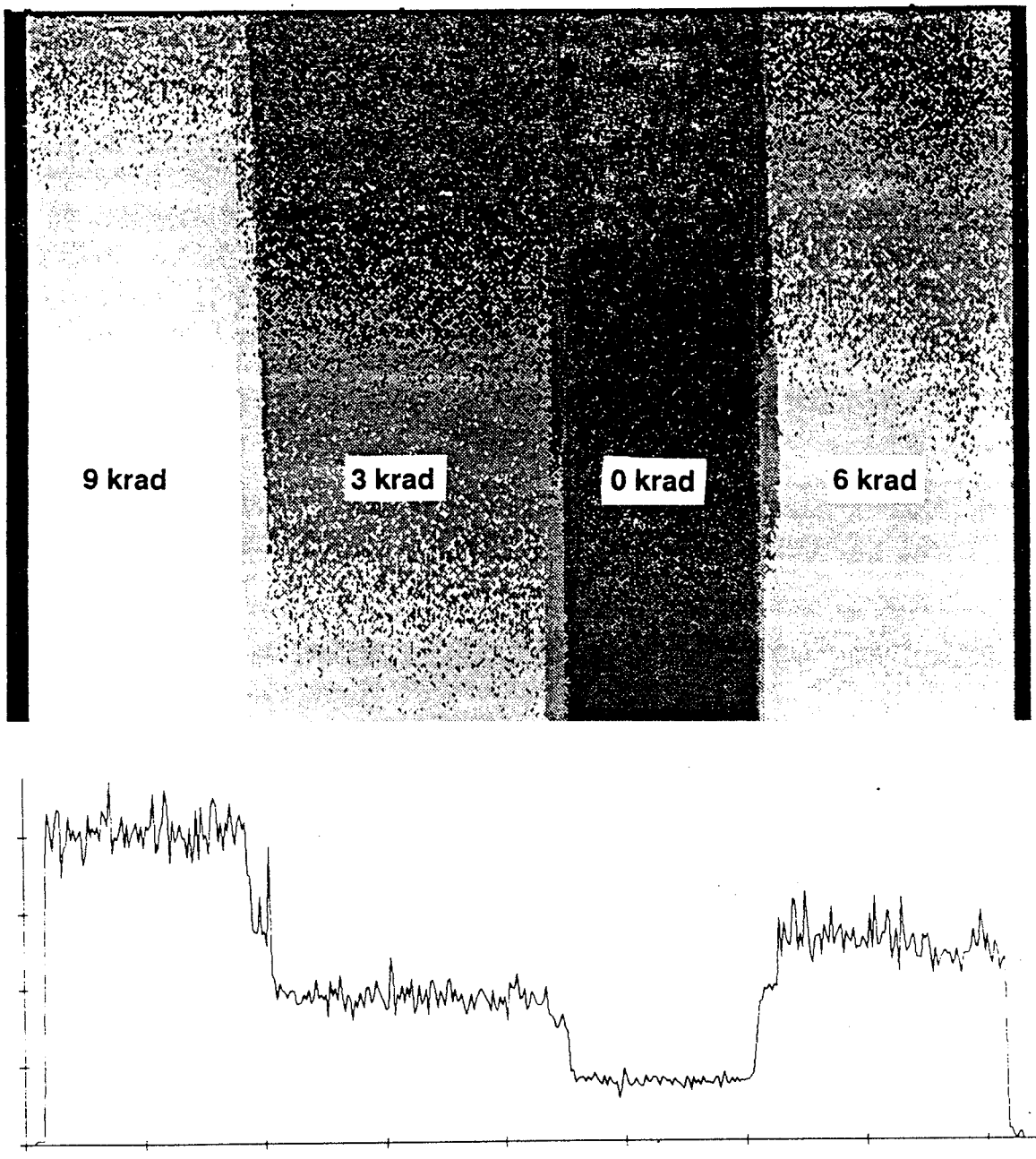

Figure 5-3 CCD image and line trace showing the four dose regions

6. RESULTS FOR TH7863 CCDS

6.1 Charge to Voltage Conversion Factor

This parameter is a measure of the voltage output from the on-chip amplifier for a given charge read out from the CCD. It is proportional to G/C_O where G is the gain of the amplifier and C_O the capacitance of the output node. It is this factor which is used to convert the ADC output (in digital numbers) to electrons/pixel or, knowing the readout rate and the pixel area (= 23x23μm), to nA/cm^2. CVF was measured in two ways. Firstly, by illuminating the device with uniform illumination at ~70% of the saturation level and measuring the output voltage (= video - reset level) and the current in the reset drain line (I_{RD}). The charge voltage to conversion factor is then given by:

$$CVF = 0.43 \quad \frac{V_{out} \ (V)}{I_{RD} \ (\mu A)} \quad \mu V/electron$$

In this study (in contrast to the Co^{60} programme [1]) a high precision current monitor was not available and so I_{RD} could only be measured to an accuracy of 0.01μA on a typical current of 0.22μA. At this accuracy all devices had the same CVF before and after irradiation

$$CVF_{I/V \text{ method}} = 1.95 \pm 0.1 \ \mu V/electron$$

The second method was to use x-rays from a Cd^{109} source. These have energies of 22.1 and 24 keV (giving signals of ~6000 electrons). The devices were run at the normal frame rate of 24Hz giving an integration time of 41ms. For measurements before irradiation each 288x384 pixel frame was searched of x-ray events above a set threshold and this was repeated for successive frames (after irradiation areas of interest were confined to a given dose region on the CCD: 0, 3, 6 or 9 krad). For each detected event, a block of 5x5 pixel values centred on the event were appended to a file. With appropriate choice of threshold the detected x-ray events were confined to one pixel. That is there was no significant charge in neighbouring pixels and no charge was split between two pixels or lost due to recombination (as would occur for spread events generated in the field-free region below the depletion layer). The sum of the pixel values in the 5x5 blocks gives the x-ray signal and the average value in pixels either side of the centre gives the deferred charge ie. the charge which is 'smeared' into the following pixels; a parameter which is related to the charge transfer efficiency (CTE). Values of deferred charge were typically ~2 ADC units in an x-ray signal of 100 ADU (ie. ~2%). This is comparable with the dynamic performance of the electronics system. There were no significant changes in deferred charge with radiation damage.

These x-ray measurements yielded a value of

$$CVF_{\text{x-ray method}} = 2.0 \pm 0.1 \ \mu V/electron$$

in agreement with the current/voltage result. This value was not noticeably changed by the radiation (in agreement with the previous study [1]). The value of 2.0μV/electron and the calibration of the framegrabber ADC (1 ADU = 2.46mV) gives 1230 electrons/ADU at unity amplifier gain and this value was used throughout to convert ADC values to electrons/pixel.

6.2 Linearity and Full Well Capacity

6.2.1 Uniform Illumination

Linearity was measured pre-irradiation and approximately 3 months afterwards by uniformly illuminating each CCD with broadband light from a tungsten lamp (ie. no colour filters were used). The light level was kept constant and the integration time was changed by switching the timing sequences. The shortest integration time was 41ms (corresponding to a 24Hz frame rate). The longest time used was 12 times this and there were 60 steps in all.

A block of pixels (roughly 70x40) was averaged for each dose region on the CCD. The integration time was then changed and several frame times allowed to elapse before the next image was captured (to allow all spurious charge to be cleared out and a steady state to be reached). During initial setting up before irradiations began the illumination level and amplifier gain and offset settings were selected so that at 10 times the minimum integration time blooming of the charge was just noticeable and the ADC value was ~200 counts (with a count of 15-20 in the zero signal 'porch' region). Thereafter the same amplifier conditions were used for all measurements. The light intensity was also kept approximately constant though it was allowed to change slowly throughout each day and from one switch on of the lamp to the next with only infrequent checks with a radiometer. The lamp was powered by a smooth DC supply so as to avoid high frequency fluctuations in its intensity.

The sequence of integration times used was (in percentages of the nominal integration time for saturation = 100%):

10%, 20%, 30% up to 110%
12%, 22%, 32% up to 112%
14%, 24%, 34% up to 114%
16%, 26%, 36% up to 116%
18%, 28%, 38% up to 118%

In this way there was an interleaving of results as a function of integration time. The saturation level (or full well capacity) was measured by least squares fitting a straight line to the linear portion of the plot between the 1st and 40th integration steps ie. between 10% and 80% of the nominal saturation level. The differences between the actual data and the straight line fit were then measured. Saturation was defined as the point at which the data differed from the line by more than 5%.

The results obtained were as follows:

Table 6.2-1 Full Well Capacity (uniform illumination)
unit = 10^5 electrons

	10 MeV		1.5 MeV	
Device	**01**	**02 (powered)**	**03**	**04 (powered)**
Dose				
0	10.1	9.3	-	9.58
3*	10.3	9.24	-	9.71
6*	10.3	9.2	-	9.91
9*	10.3	9.03	-	9.57

* After 3 months storage

Thus the full well capacity was ~10^6 electrons, unaffected by the proton irradiation. The preirradiation values are consistent with the findings of the Co^{60} study [1]. From that work we expect some degradation due to surface states produced by the proton ionisation damage but taking into account the factor 2 decrease in electron-hole yield in the oxide for low energy protons (figure 3-5) the results are not too surprising (there will also be dose rate effects to take into account: for the proton testing the irradiation time was ~2 minutes compared with several days for the Co^{60}).

Strictly speaking, we should distinguish between the 'real' saturation level and the level which is useful for signal detection (= real level - average dark charge). In this case the dark charge levels were relatively low, presumably again because of electron-hole yield and dose rate effects (discussed further in para 6.3) and so the distinction is small. The slight change in V_{SAT} noticeable in table 6.2-1 can, in fact, be attributed to the changes in dark current level (the values quoted have the dark charge subtracted).

6.2.2 Spot Illumination

The optical set-up used is described in para 5.2.1.7. Results obtained after 3 months storage unbiased at room temperature are given below. As for the uniform illumination, 'useful' values of V_{SAT} are listed (ie. with the average dark charge level subtracted) but, again, the dark charge was not significant compared with full well capacity and the distinction between 'useful' and 'real' saturation value can be neglected.

Table 6.2-2 Full Well Capacity (spot illumination)
unit = 10^5 electrons

	10 MeV		1.5 MeV	
Device	**01**	**02 (powered)**	**03**	**04 (powered)**
Dose				
0	6.41	6.48	6.53	6.35
3*	5.68	5.08	5.60	5.66
6*	5.41	4.39	5.26	5.16
9*	5.30	4.34	5.16	4.91

* After 3 months storage

These results, together with the uniform illumination data of table 6.2-1, are plotted in figure 6.2-1. It is seen that for spot illumination V_{sat} drops from 10^6 to ~$6.5x10^5$ electrons, presumably because surface traps are no longer kept full of charge. With radiation V_{sat} drops further especially for biased devices. As would be expected from electron-hole yield considerations (figure 3-5) the damage is worse at 10 MeV. It might be expected that for high energy protons, as present in the flight environment (and Co^{60} gamma rays) - and considering possible dose rate effects, it might be prudent to expect a V_{sat} value of $2\text{-}3x10^5$ electrons after 6krad (Si).

Figures 6.2-2 and 6.2-3 show the linearity curves themselves - note that each set of plots was obtained from a single device and identical operating conditions.

There is a suggestion of saturation effects since the 9krad results are not much worse than the 6krad - but note that annealing and dose rate effects may be important and similar effects were noticed for image region dark current (para 6.3) but after an elevated temperature annealing step the dark current anomalies disappeared.

Another important characteristic not investigated during the Co^{60} study [1] was the behaviour under oversaturated illumination conditions: when signal from the spot 'overflows' (or blooms) to surrounding pixels. The effect is shown in figure 6.2-4 for device 02 (10MeV radiation, powered) for the four dose levels (0, 3, 6 and 9 krad(Si)). The key to the figures shows the nomenclature used in identifying the pixels (ie. pixels are identified as ij where i is the row number and j the column number).

The spot was initially centred on the pixel shown shaded. All plots came from the same CCD with the same temperature, gain and amplifier offset conditions. As well as the drop in saturation level with dose it can be seen that the linearity curve for the illuminated pixel sharpens after irradiation and the rise in the signal from the pixel immediately below is more pronounced. This is to be expected since charge transfer efficiency is greatly reduced at saturation (because of the effect of interface traps) and it is a well known characteristic of CCDs that signals bloom in the column direction towards trailing pixels. With ionising radiation the number of interface traps is increased and these effects will be exaggerated. Again we see somewhat anomalous behaviour at 9krad, probably accounted for by annealing/dose rate effects. It is interesting to note that at ~4x the saturation light level the signal in the pixel below exceeds that in the illuminated one. The signal in the preceeding pixel (column direction) also increases markedly. These effects will be important when considering thresholding strategies for SILEX. Note that the effects might be somewhat dependent on the spot profile and wavelength of illumination used, but the results for SILEX conditions should be qualitatively similar.

6.3 Dark Field Measurements

The radiation-induced dark current from the TH7863 CCDs can be divided into two components. The first is due to surface generation which is influenced by the creation of interface traps by ionisation damage (c.f. para 3.3.3.1). The second is bulk (depletion layer) generation due to midgap centres created by displacement damage. The latter effect will lead to both an increase in the average image and storage area components and to dark charge nonuniformity. Since in the TH7863 CCD surface damage cannot be suppressed (by operating under inversion [37]), the two bulk and surface contributions to the mean level cannot be distinguished. However since the ionisation damage in these devices is particularly pronounced this will dominate any effect on the mean level and shifts due to displacement damage can be ignored. All the data in this section was obtained from 16 frame averages of dark images obtained at a variety of CCD temperatures in the range 6 to 37°C.

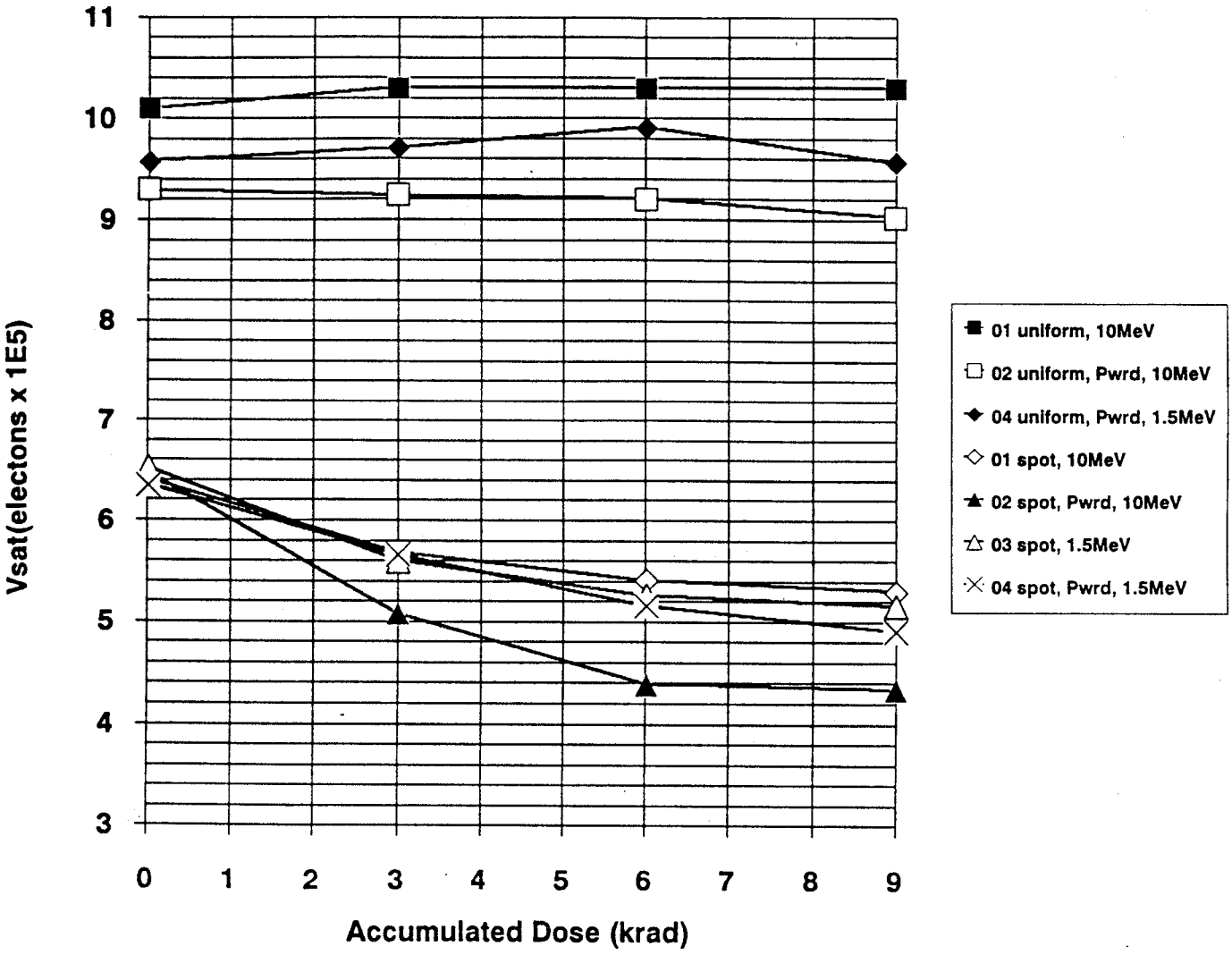

Figure 6.2-1 V_{sat} values for uniform and spot illumination versus accumulated dose

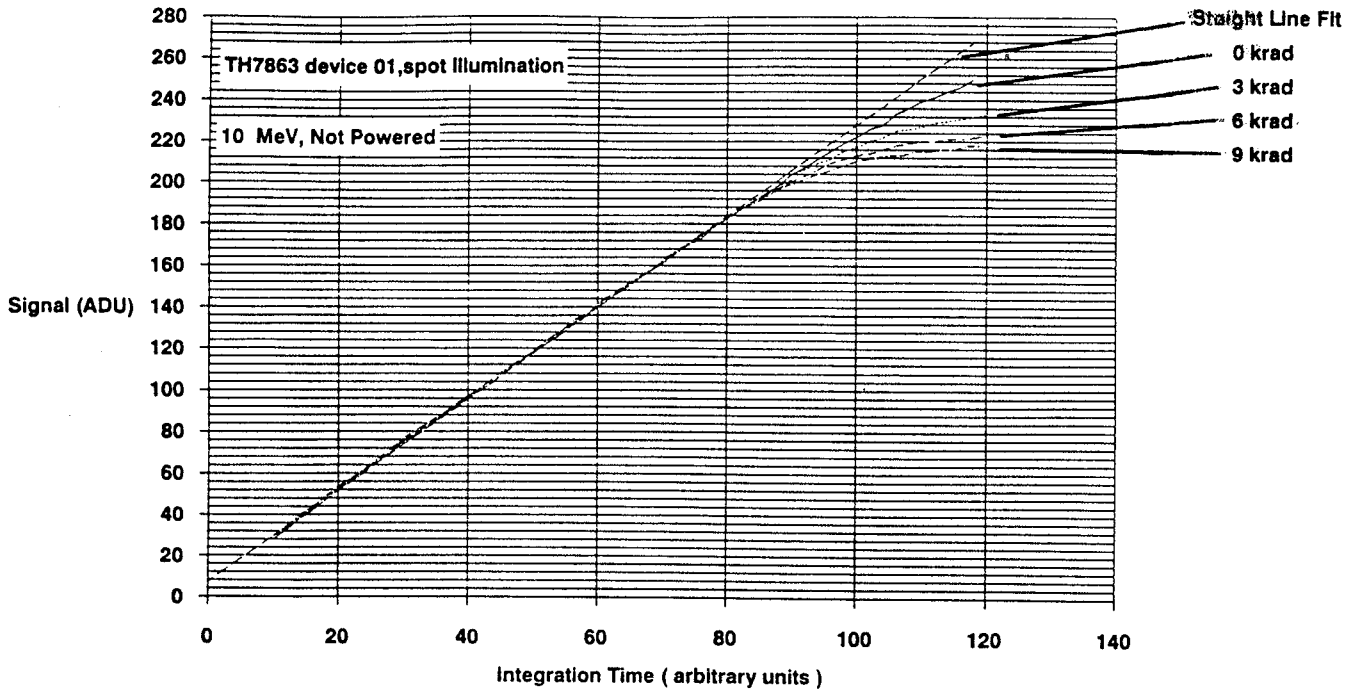

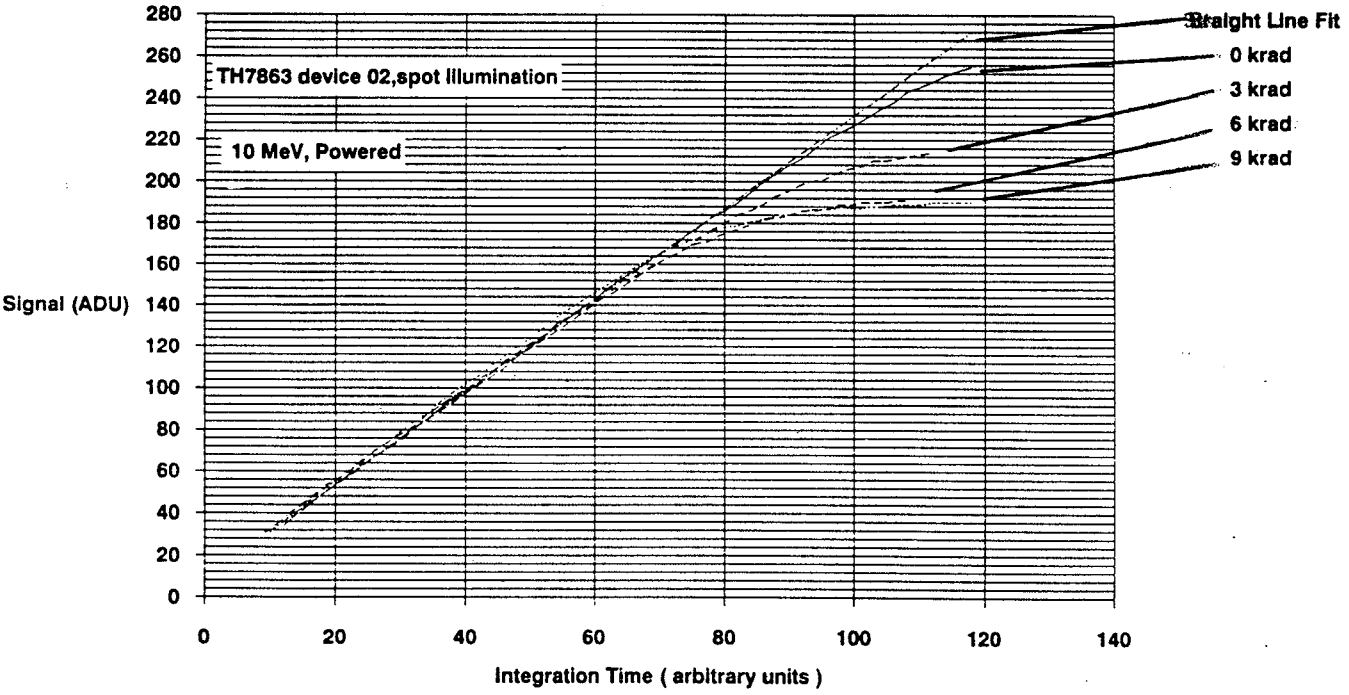

Figure 6.2-2 Linearity plots for TH7863 devices after 10 MeV proton irradiation

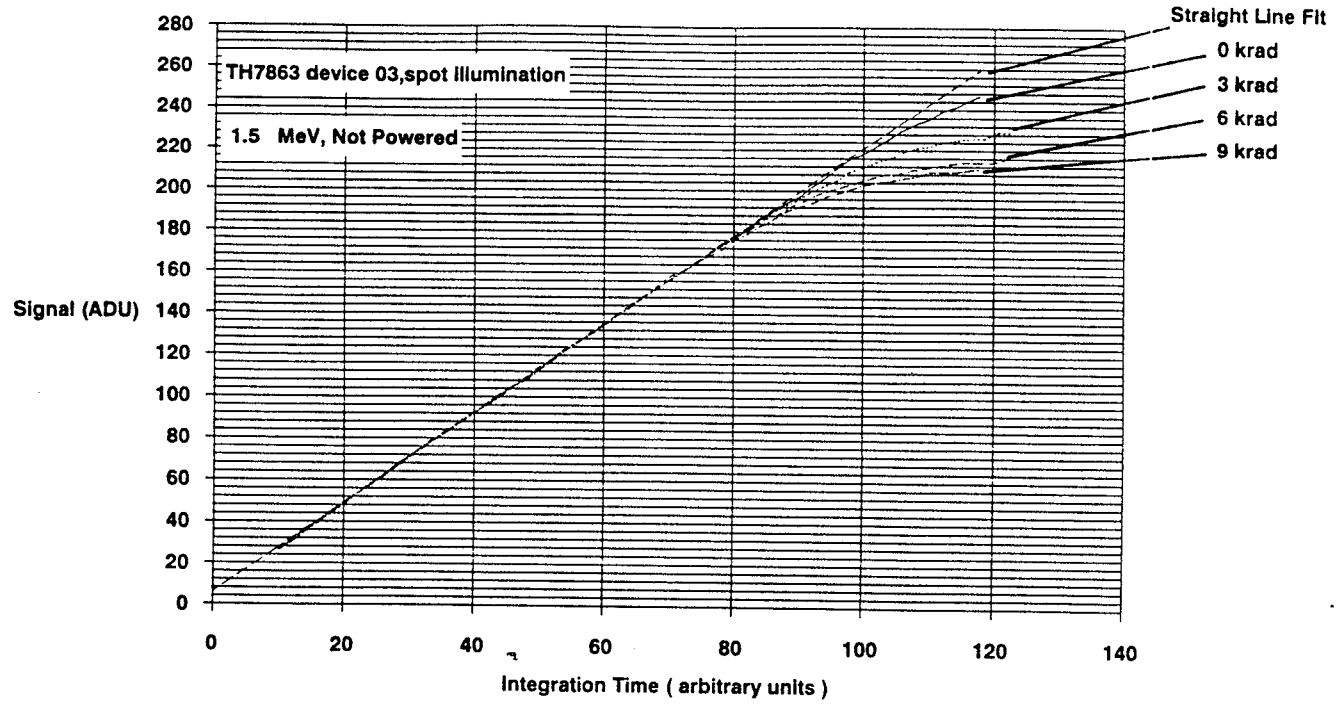

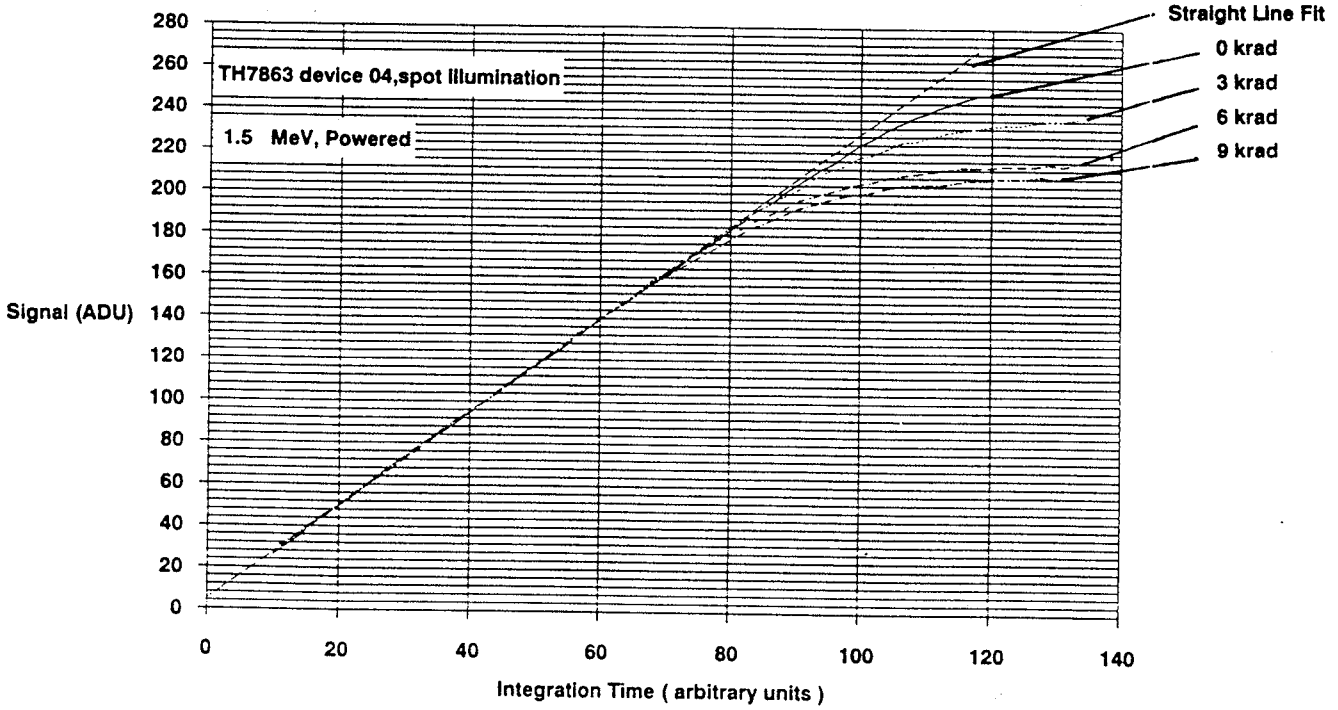

Figure 6.2-3 Linearity plots for TH7863 devices after 1.5 MeV proton irradiation

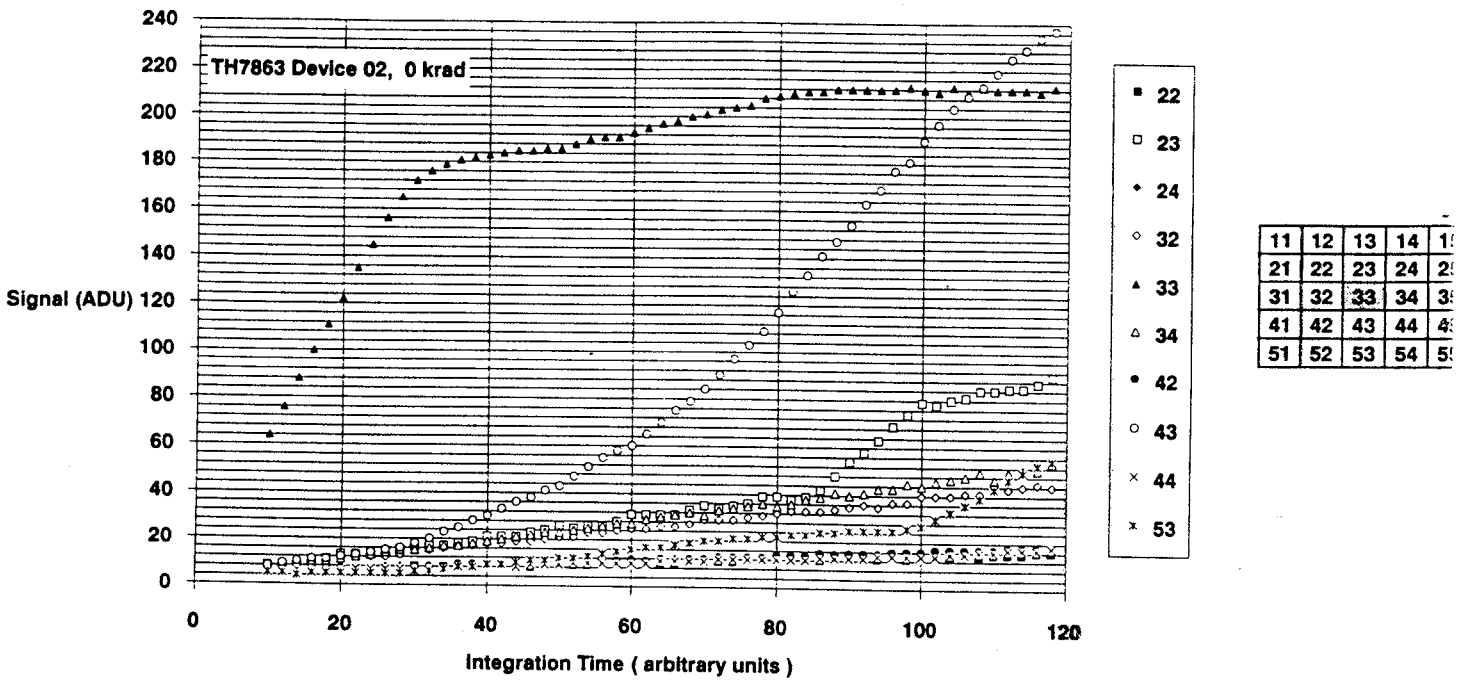

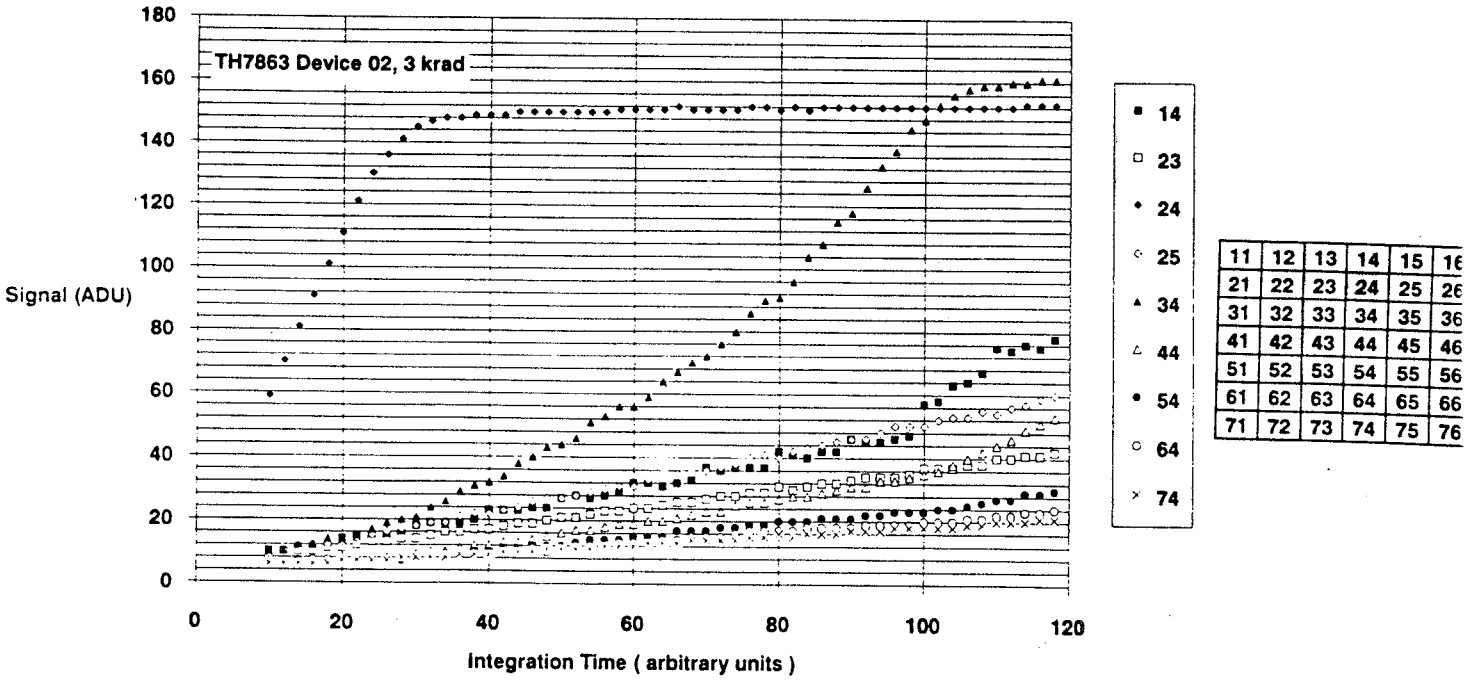

Figure 6.2-4 a) linearity plots for device 02 showing behaviour in oversaturated conditions

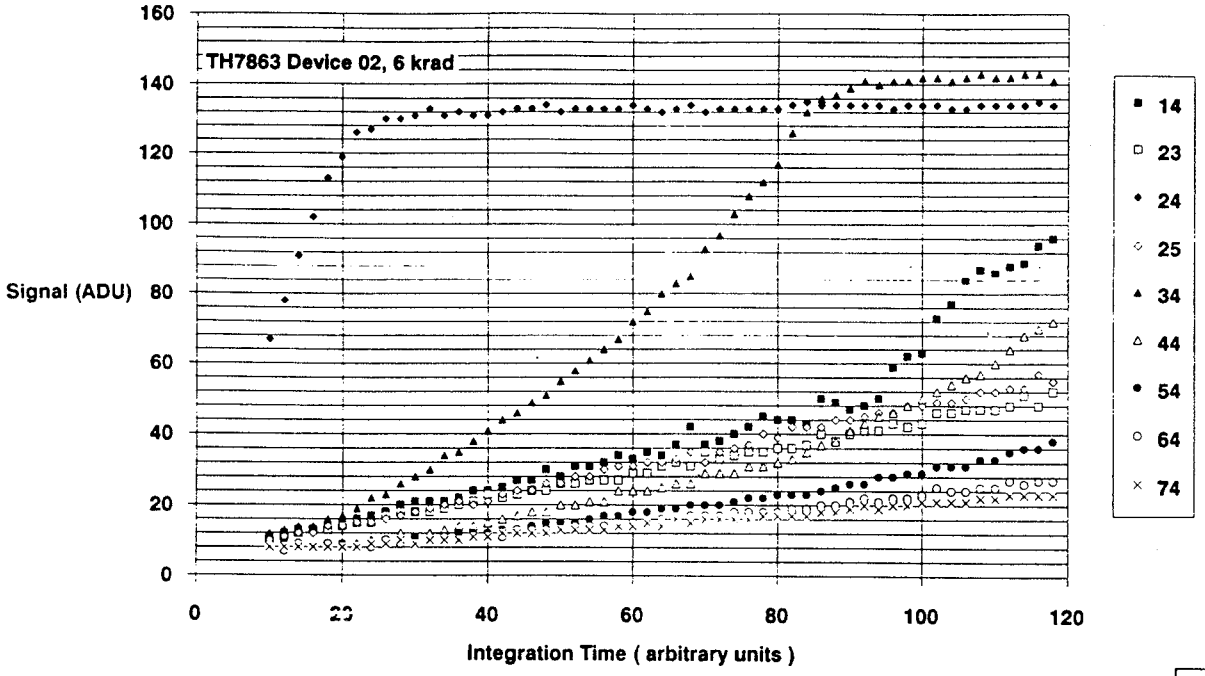

11	12	13	14	15	16	17
21	22	23	24	25	26	27
31	32	33	34	35	36	37
41	42	43	44	45	46	47
51	52	53	54	55	56	57
61	62	63	64	65	66	67
71	72	73	74	75	76	77

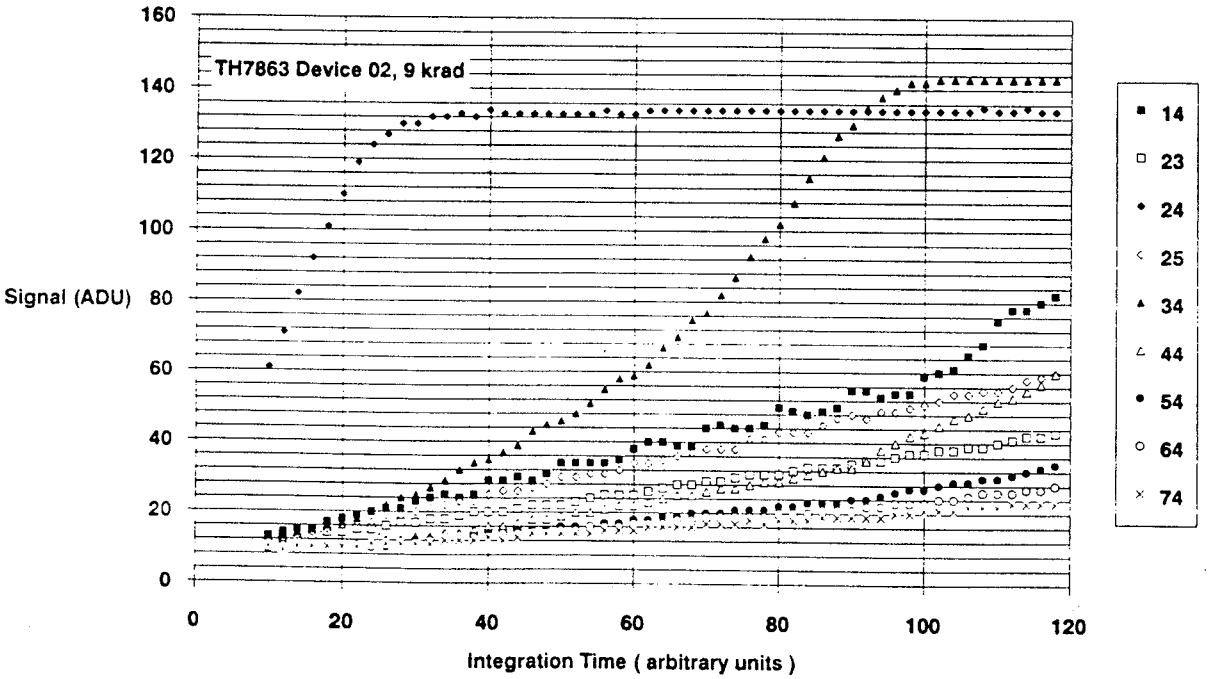

Figure 6.2-4 b) Linearity plots for device 02 showing behaviour in oversaturated conditions

6.3.1 Ionisation Damage

Figure 6.3-1a) shows a slice down column 200 of a dark image from a TH7863 CCD. It is seen that the dark signal steadily increases because of the progressively longer time that charge spends in the storage region. The first line readout has only the dark charge generated in the image region during the 41ms integration time, whereas the last line readout has, in addition, the dark charge generated during the 41ms it takes for charge packets to be progressively clocked through the storage region during readout. The image and storage region components can be separately measured as shown in the figure. Alternatively, figure 6.3-1b) shows a column slice for a clocking sequence which operates the CCD in a full frame mode : charge is continuously clocked through the image and storage regions. Thus the first line has no signal (zero integration line) and dark charge progressively builds up as succeeding lines are clocked through the CCD. The difference in image and storage region generation rates is indicated by the change in slope of the column trace (in the case shown the image region component is small).

Table 6.3-1 shows average dark current values for the four irradiated devices for a variety of storage times (storage unbiased, at room temperature). Since the dark charge slope, illustrated in figure 6.3-1, is linear:

$$\text{the average value} = \text{image component} + \text{storage component}/2$$

The values in nA/cm^2 were calculated knowing the charge to voltage conversion factor of $2.0\mu V$/electron (para 6.1) and the framegrabber ADC calibration of 1 ADU (1 ADC unit) = 2.46mV give 1230 electrons/ADU with unity gain on the TH7863 camera head and that the conversion factor between dark current in nA/cm^2 and the value in electrons/integration time (=41ms) is given by

$$\frac{1.6\times10^{-19}\times10^{9}\times1000}{(23\times10^{-4})^2 \times 41} = 0.000738$$

given that the pixels are $23\mu m$ square ie. the conversion between ADU and nA/cm^2 is $1230\times0.000738 = \underline{0.908}$.

As expected from the Co^{60} work [1] there are large increases in dark current. This builds up slowly with storage time after irradiation - although there is a noticeable decrease in the 3 month values compared with 35 days (particularly for device 03). This return to the level just after irradiation was also seen in ref [1] as were the larger increases for devices powered during irradiation. Note that devices irradiated with 10MeV protons show more damage than those irradiated at 1.5MeV.

Figure 6.3-2 Shows the average dark charge as a function of accummulated dose after 10 days and 3 months storage (ie. for the four dose regions on each chip at those times). It is seen that damage increases fairly linearly with dose, although the plots after 3 months are somewhat distorted, presumably because of uneven annealing. From table 6.3-1 we can calculate the damage ratios for powered/unpowered devices and 10/1.5 MeV irradiation and these are given in table 6.3-2.

Note that the ratios measured after 3 months will be influenced by the deviations from linearity with dose noted from figure 6.3-2 and also that there is a tendency for the damage ratios to increase with dose. Nevertheless it appears that there is roughly a factor 2 more damage for powered devices at 10MeV and a factor 2 difference between 10MeV and 1.5MeV devices which are powered. There is also a factor 1.4 more damage for powered devices at 1.5MeV and between 10MeV and 1.5MeV which were not powered during irradiation. Factors of this order are to be expected from considerations of electron-hole yield in the oxide as discussed in para 3.2. The Co^{60} study [1] gave an average dark

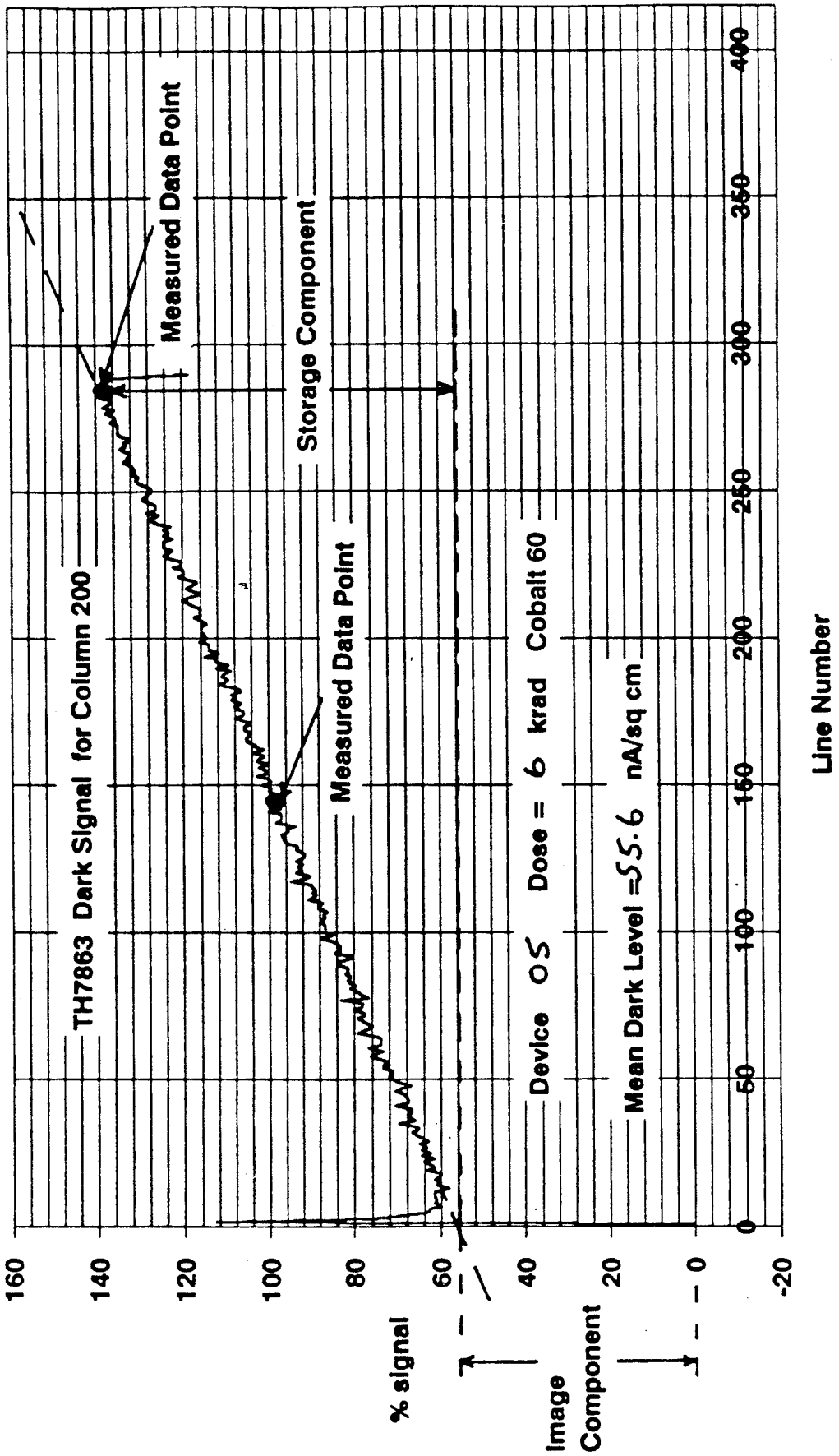

Figure 6.3-1a) Vertical slice down column 200 of a TH7863 CCD operated in frame transfer mode

A/9058/00

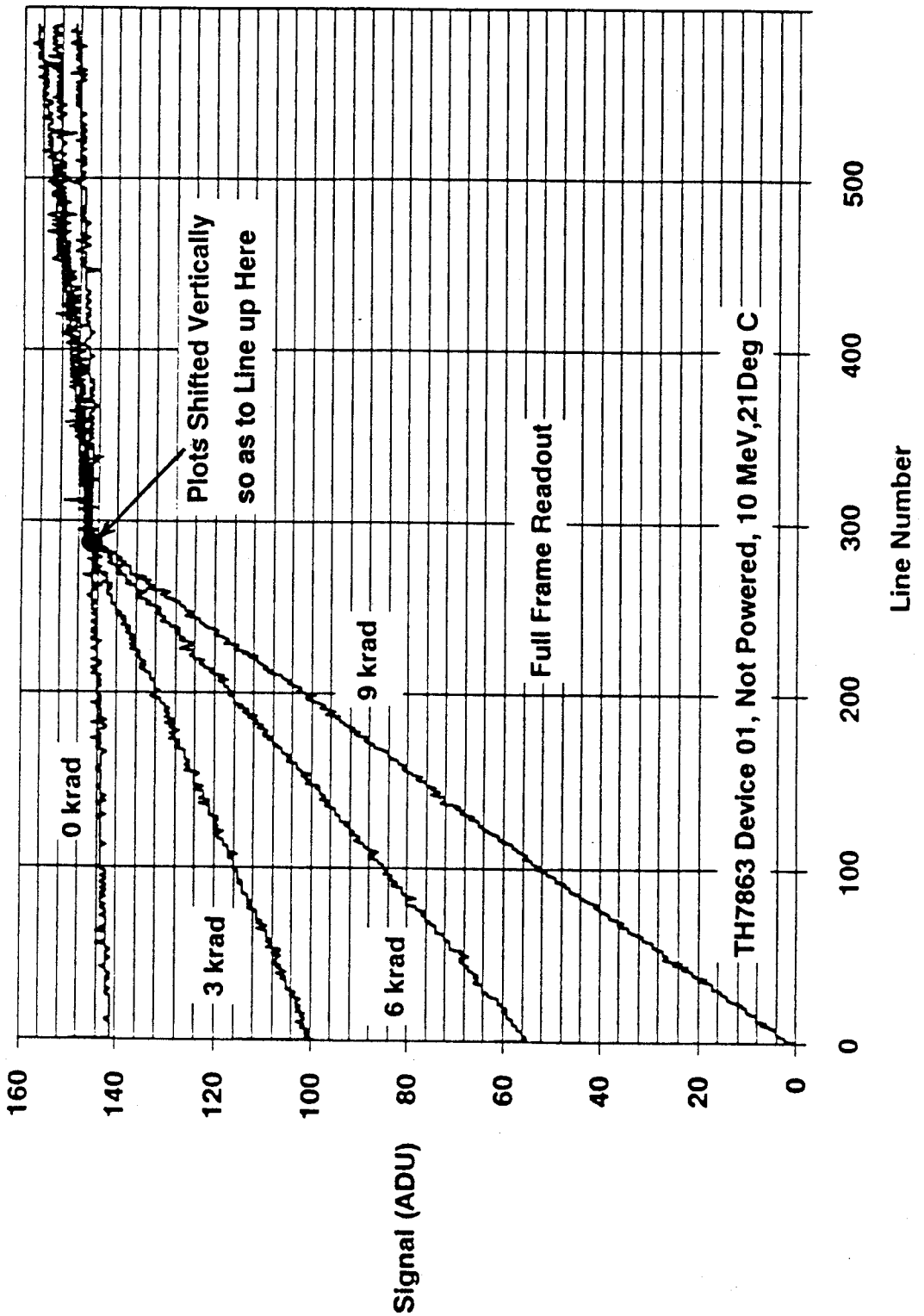

Figure 6.3-1b) Vertical slice down column 200 of a TH7863 CCD operated in continuously clocked full frame mode

Table 6.3-1 Values of average dark current for TH7863 devices (in nA/cm^2)

		Dose, krad(Si)			
		0	3	6	9
CCD01					
10MeV protons, not powered	immediate	-	-	-	-
	10 days	0.98	5.6	9.1	15.6
	35 days	1.19	8.2	11.5	19.5
	3 months	1.14	8.1	9.2	14.5
CCD02					
10MeV protons, powered	immediate	-	-	-	-
	10 days	0.83	12.6	25.0	46.2
	35 days	1.36	12.2	25.0	44.5
	3 months	1.17	13.7	20.1	34.4
CCD03					
1.5MeV protons, not powered	immediate	0.93	2.4	3.3	5.2
	10 days	0.96	4.2	6.8	10.5
	35 days	1.14	5.8	8.9	13.6
	3 months	0.97	3.0	3.25	7.1
CCD04					
1.5MeV protons, powered	immediate	0.86	3.3	5.3	9.1
	10 days	0.93	6.3	11.4	18.9
	35 days	0.80	7.6	12.3	20.1
	3 months	1.12	4.4	8.8	15.1

Table 6.3-2 Average dark current damage ratios

	Powered/unpowered		10MeV/1.5MeV	
	10MeV	1.5MeV	Powered	Unpowered
After 10 days				
dose (krad)				
3	2.25	1.50	2.00	1.33
6	2.75	1.68	2.19	1.34
9	2.96	1.8	2.44	1.49
average	2.65	1.66	2.21	1.39
After 35 days				
dose (krad)				
3	1.49	1.31	1.60	1.4
6	2.17	1.38	2.00	1.3
9	2.28	1.48	2.20	1.4
average	2.00	1.39	1.93	1.37
After 3 months				
dose (krad)				
3	1.70	1.46	3.11	2.67
6	2.19	2.72	2.26	2.82
9	2.37	2.13	2.27	2.04
average	2.09	2.10	2.55	2.51

current of ~200nA/cm^2 for powered TH7863 devices after 15 krad(Si). Thus at 9krad we would expect roughly 120nA/cm^2. For 10MeV protons we get a value ~40nA/cm^2, ie. a factor 3 down, and we expect a further factor 2-3 reduction for unpowered devices. From figure 6.3-3 we see that a factor ~2 is expected from Oldham's theory [2]. A factor 3 difference in threshold voltage shift has recently been noticed between Co^{60} and 10MeV proton irradiated PMOS RADFETS (A Holmes-Seidle, Private Communication, July 1991). Figure 6.3-4 shows the ratio between the electron-hole yields for 10 and 1.5MeV proton irradiation as a function of oxide field. From this we would expect a factor 2-3 decrease in 1.5MeV damage compared with 10MeV and for the ratio to be higher at low fields (ie. unpowered devices). However we should avoid too detailed a comparison with theory since we would expect the pure columnar model to start to breakdown at 10MeV. In addition there are mechanisms other than the initial e-h yield which influence the production of dark charge generating surface states. For example the chemical species responsible for interface trap generation (H^0, H^+, H_2 or OH^-) must first be produced by the trapping of the holes and then must diffuse to the interface. These processes may be dependent on electric field, space charge effects and on dose rate. Nevertheless the qualitative features of the recombination models seem to be consistent with the experimental data ie. that damage is less for

i) low energy protons compared with Co^{60} gamma rays
ii) unpowered compared with powered devices
and iii) for 1.5 compared with 10MeV protons.

The reduced damage observed for low energy proton irradiations suggests that Co^{60} testing is a better method for assessing ionisation damage in MOS devices especially as dose rates more closely related to the space environment can be used.

We have not yet considered the large scale uniformity of the dark charge (small scale pixel-pixel uniformity is discussed in the next section) or the split between image and storage region components. Regarding the former question, figures 6.3-5 to 6.3-8 show line traces for each CCD for various annealing times. The 'immediate' and '10 day' traces show the maximum, average and minimum pixels values for each CCD column. The middle trace (ie. the average) is the average dark charge as discussed above. The 'maximum' trace will show any large dark current spikes (due to displacement damage) but otherwise will relate to pixels at the bottom of the image (ie. the last lines readout) which contain the maximum amount of dark current (integrated in both the image and storage regions for the full 41ms); the 'minimum' trace relates to pixels at the top of the image which contain only image region dark charge and it can be seen that this component is small. The traces at 35 days and 3 months are slices along either line 200 or 144 showing individual values for each pixel in the line.

Devices 01 and 03 show nonuniformity in the horizontal (line) direction which does not significantly change over periods of tens of days (at least). Similar behaviour was noted in the previous Co^{60} results [1]. Nonuniformity in the vertical (column) direction is small and only the linear slope (relating to the gradual increase in storage time for each line readout) is observed. It could be that further annealing (eg. at high temperatures) might reduce the horizontal uniformity - the annealing experiment to be described below was performed on device 02 which showed little large scale uniformity to start with.

The traces also show the behaviour relative to the dark charge reference region of the CCD which is masked in both the image and storage regions and thus shows large dark current increases for both components.

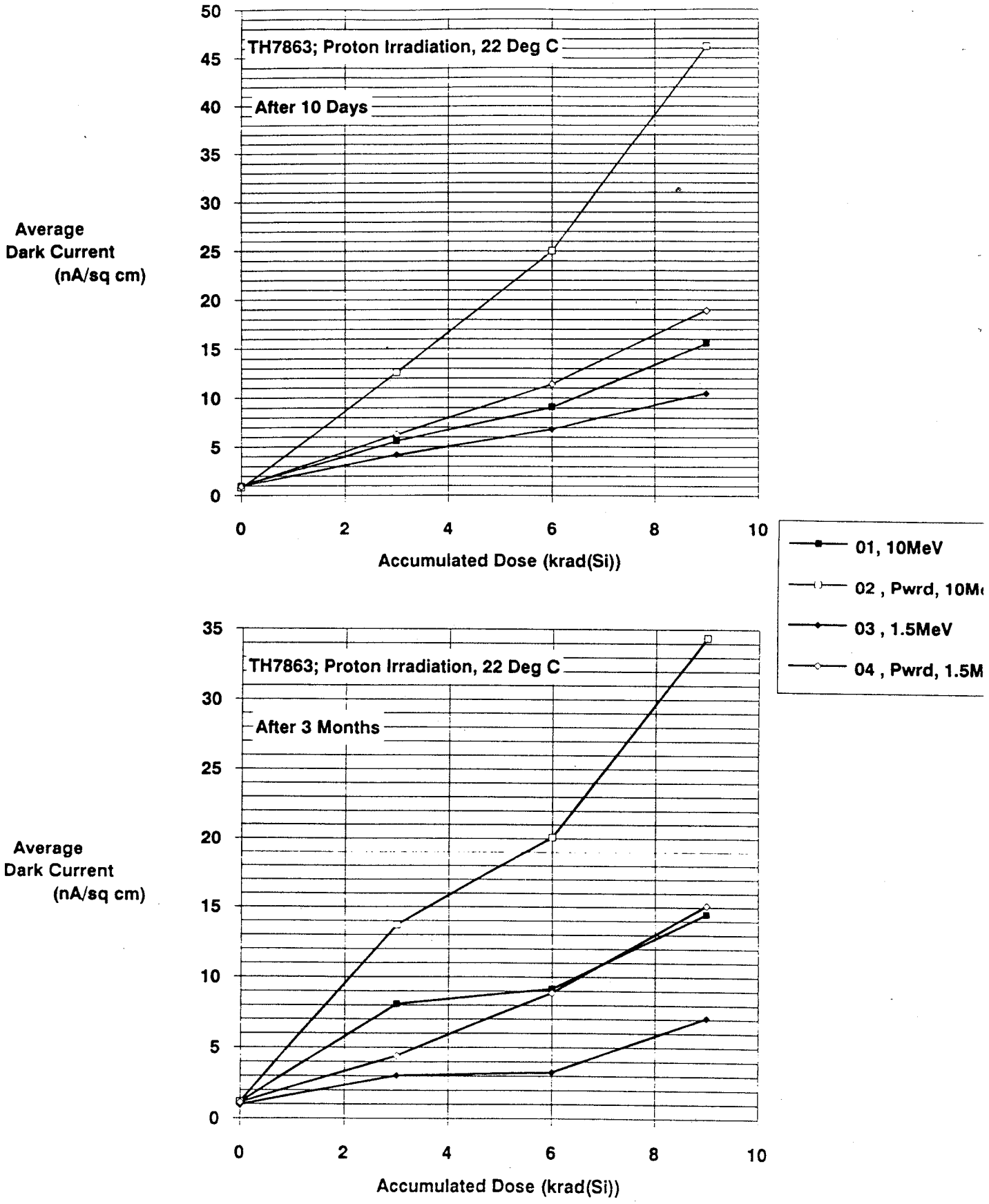

Figure 6.3-2 Average dark charge versus dose for TH7863 devices 10 days and 3 months after irradiation

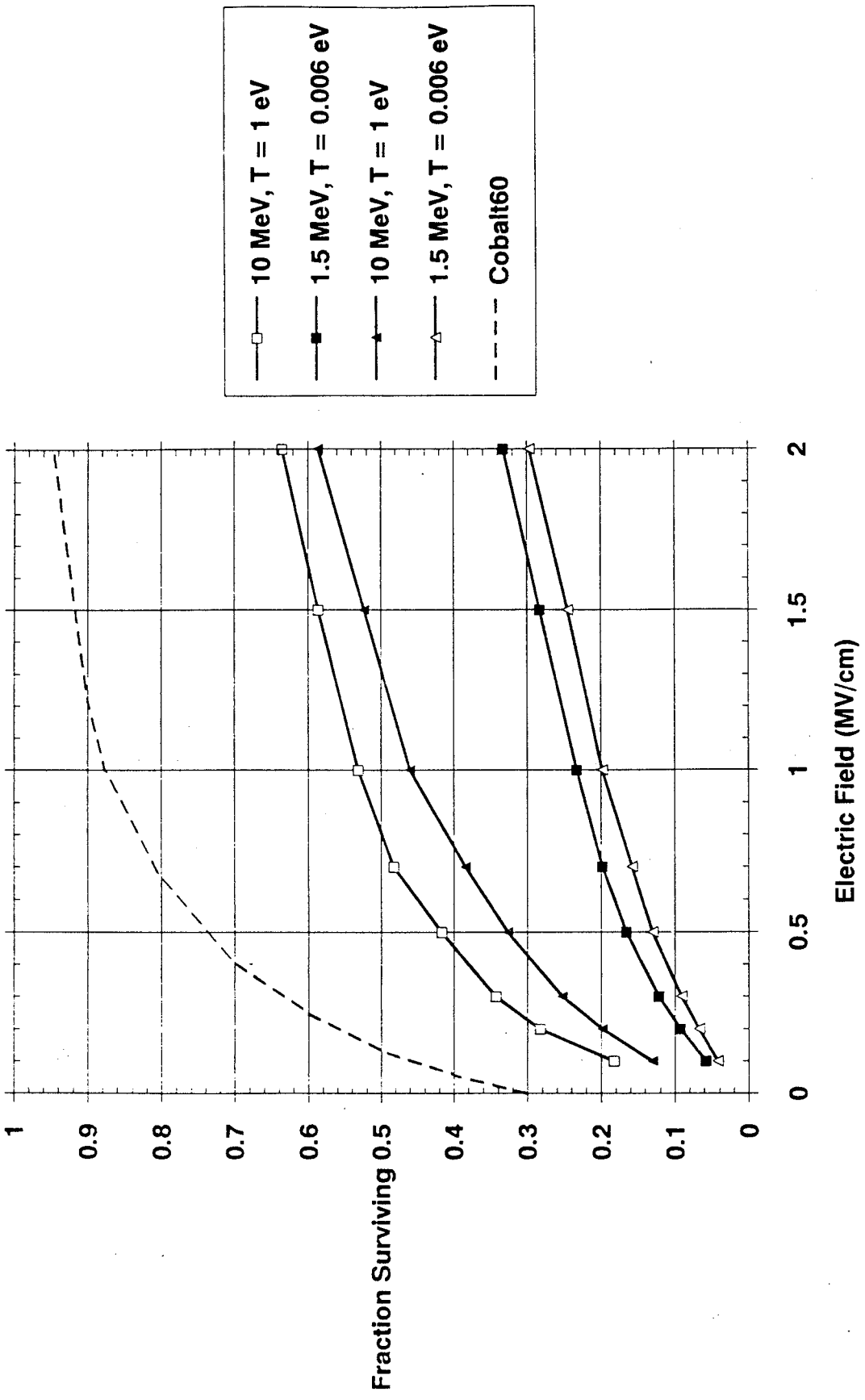

Figure 6.3-3 Fraction of electron-hole pairs surviving recombination in the oxide (from Oldham [2])

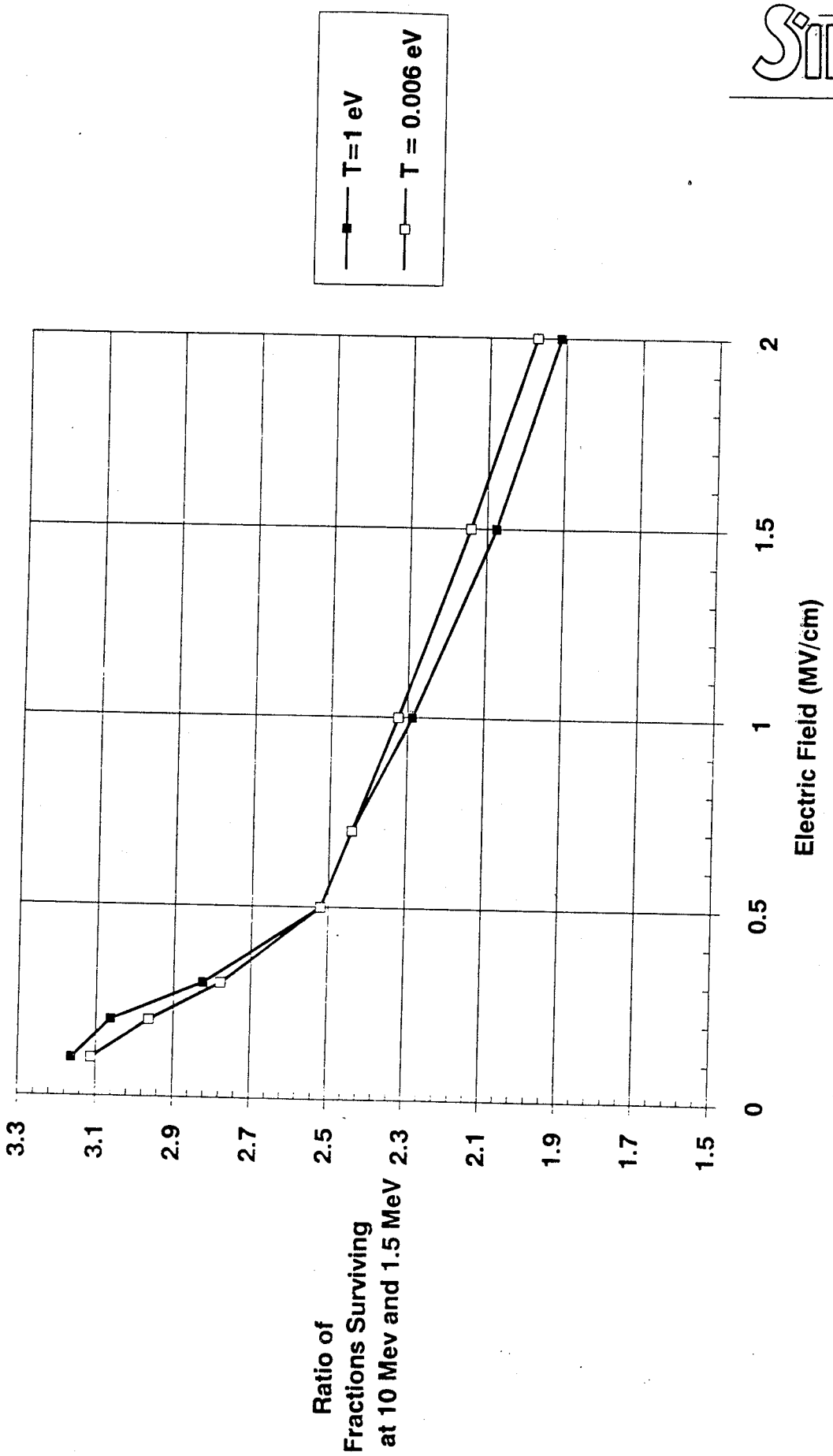

Figure 6.3-4 Ratios of electron-hole pairs surviving recombination for 10 MeV and 1.5 MeV protons for the two models given in ref [2]

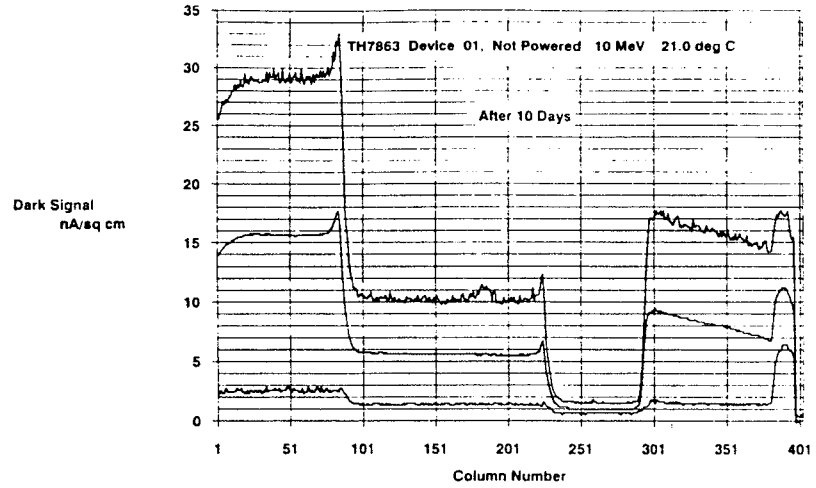

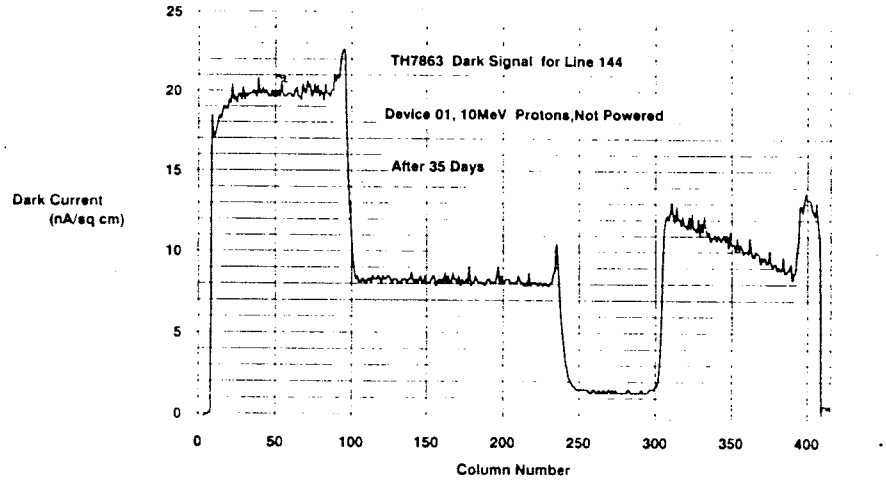

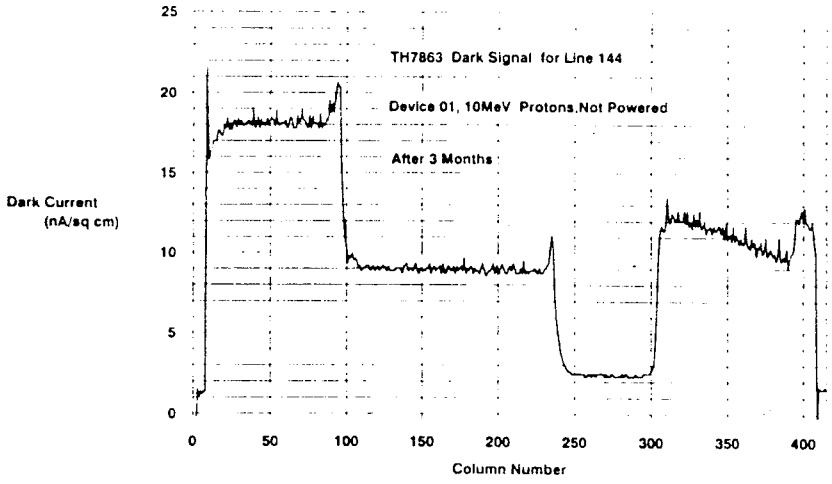

Figure 6.3-5 Line traces for TH7863 device 01 : 10 day plot shows maximum, minimum and average dark charge and 35 day and 3 month traces show pixel values for a single line

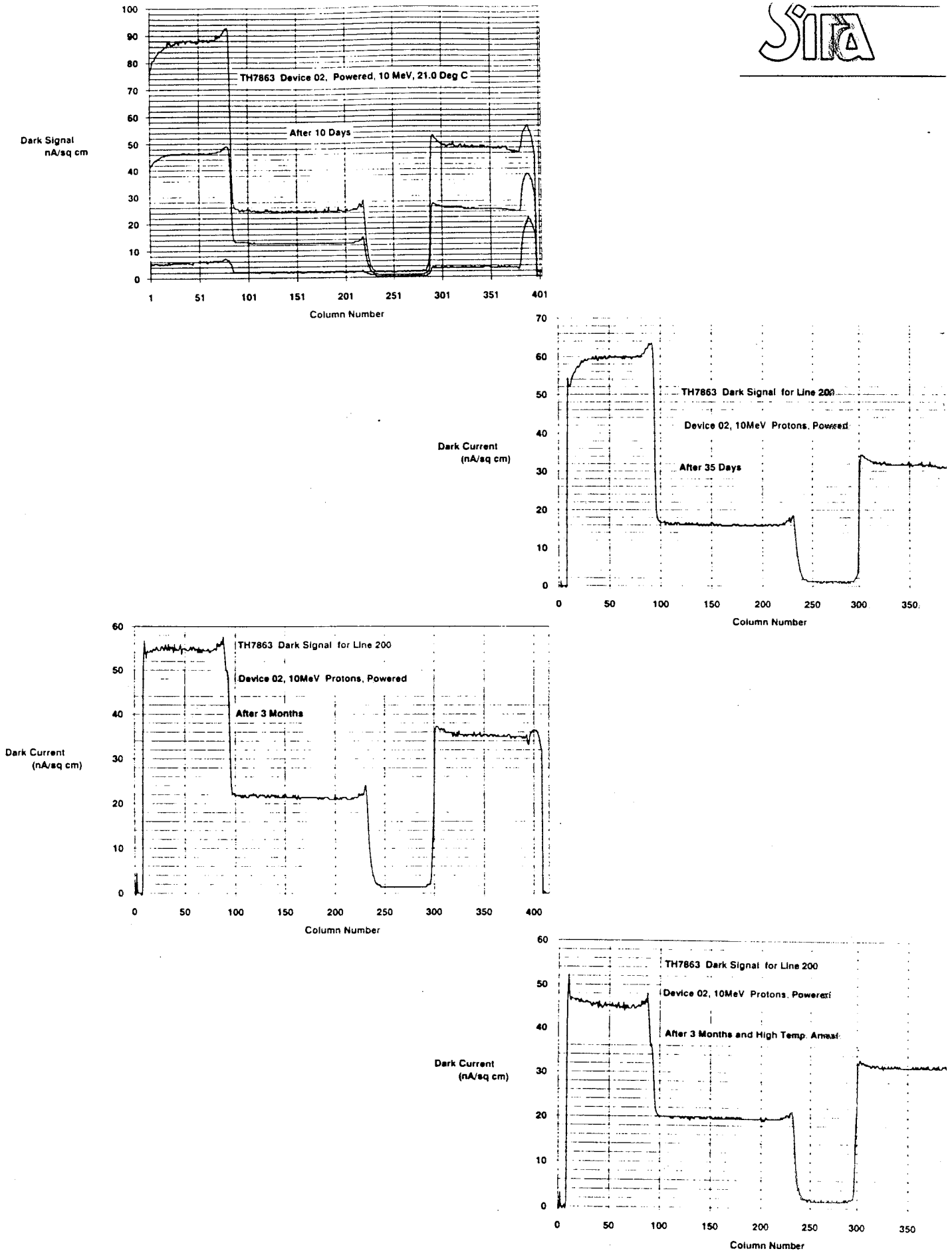

Figure 6.3-6 Line traces for TH7863 device 02 : 10 day plot shows maximum, minimum and average dark charge and 35 day and 3 month traces show pixel values for a single line

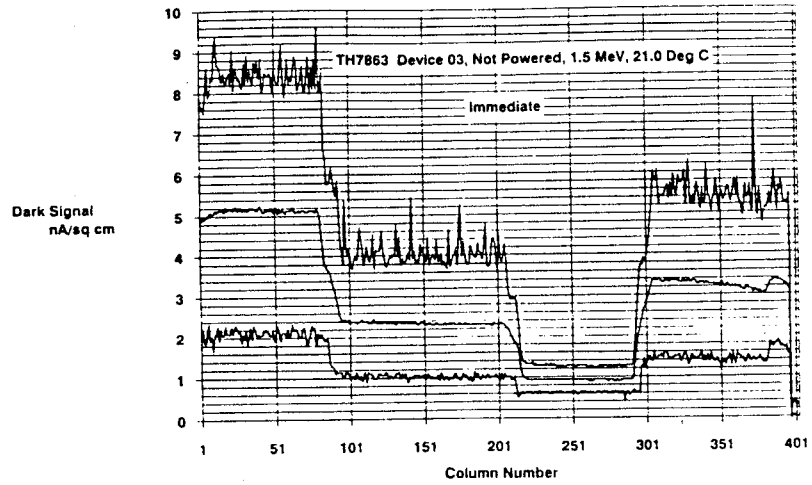

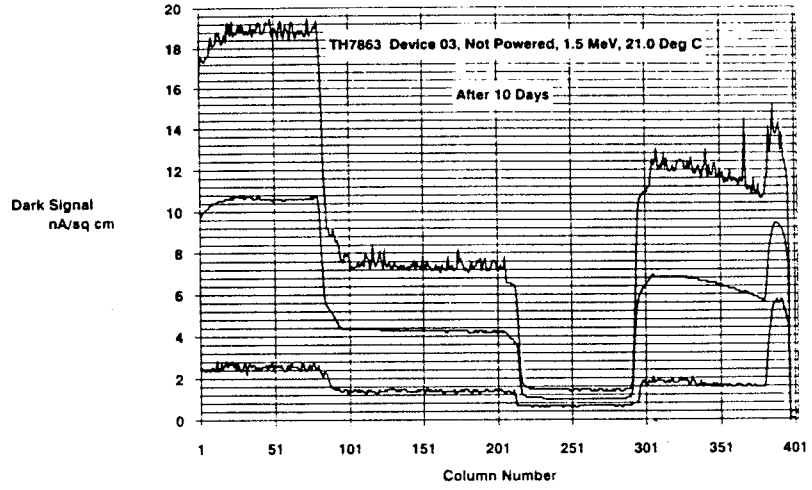

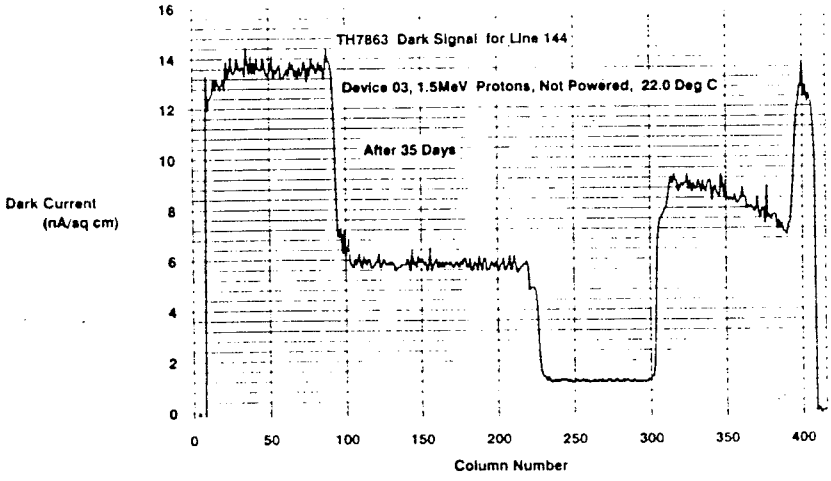

Figure 6.3-7 Line traces for TH7863 device 03 : Immediate and 10 day plots show maximum, minimum and average dark charge and 35 day traces show pixel values for a single line

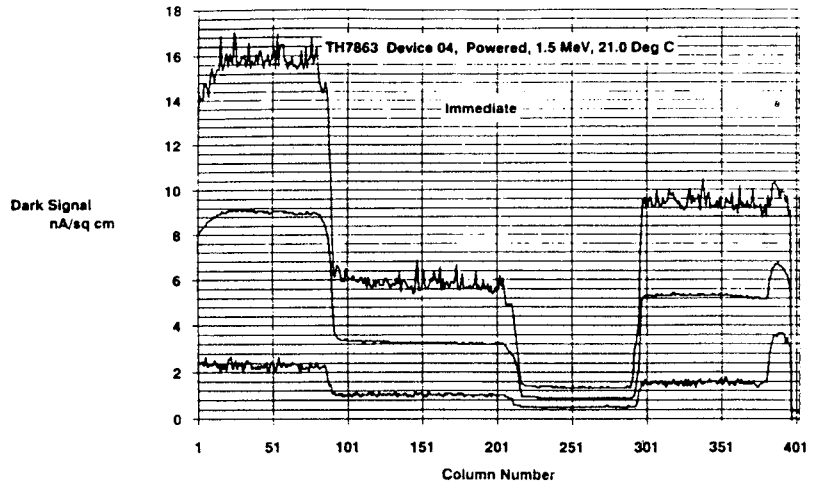

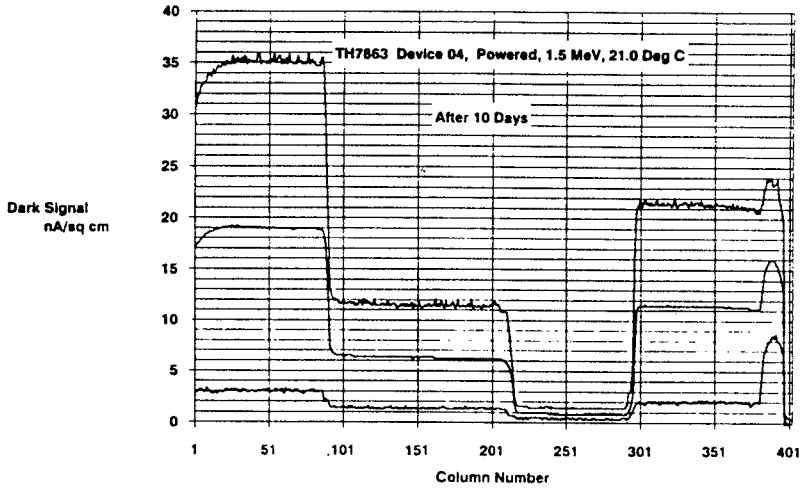

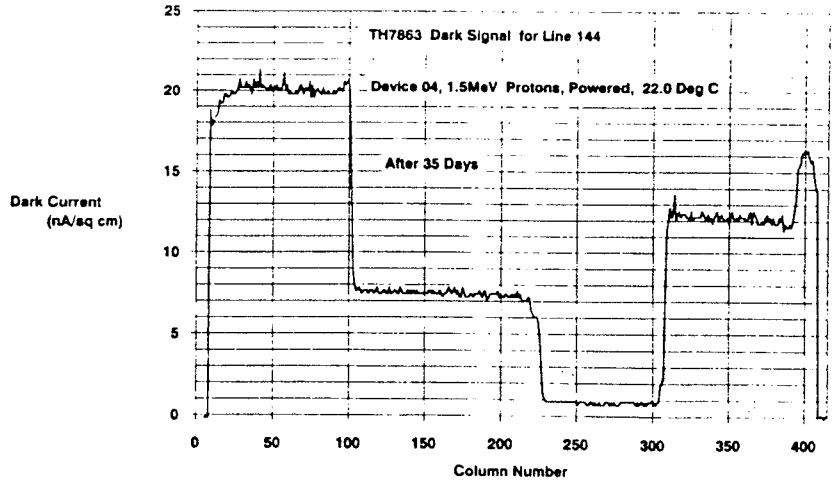

Figure 6.3-8 Line traces for TH7863 device 04 : Immediate and 10 day plots show maximum, minimum and average dark charge and 35 day traces show pixel values for a single line

It is seen from the maximum and minimum traces of figures 6.3-5 to 6.3-8 that the dark charge generated in the CCD image regions is relatively small. When the dark signal was separated into its image and storage region components by the method indicated in figure 6.3-1 it was confirmed that the image component for these proton damaged devices was much less than that generated in the storage region. From the Co^{60} results [1] it was expected that the image region dark current would reverse anneal more slowly than the storage region dark current (which we recall arises from a part of the CCD covered by an aluminium mask). However even after three months there was no significant increase. Figures 6.3-9 and 6.3-10 show the image and storage dark currents after three months and it is also seen that the image components for each of the four dose regions on the CCDs (ie. 0, 3, 6 and 9krad) do not have a linear relationship. There are lesser departures from linearity for the storage region - as noted previously in connection with the average dark current shown in figure 6.3-2.

In fact the anomalous image region behaviour can be seen quite strikingly in the line trace of figure 6.3-11 which came from an image obtained with the usual readout sequence but with the integration time (and hence the image region dark signal) increased by a factor 11.8 (though the absissa normalises this factor out to get back to a dark current density in nA/cm^2). It can be seen from the figure that, for example, the 9krad signal is less than that for the 3krad region.

The explanation for this behaviour is not known but it is possible that space charge effects arising from the high density of trapped holes in the 9krad region inhibit the diffusion of interface trap precursors (perhaps H^0, H_2, H^+ or OH^-) to the interface - and possibly this effect is exacerbated by the high dose rate (~krads/min) used in the proton beam irradiation.

To gain further insight into this phenomenon one of the devices (02), which was subjected to 10MeV proton bombardment when biased, was given a sequence of isochronal high temperature anneals with 2 hours at temperatures of 100, 120, 140, 160 and 180°C and finally a further 18 hours at 180°C to reach a point where one would confidently expect all annealing processes to have come to an end. The final line trace (ie. after the last anneal) is shown in figure 6.3-12 where we note that the 9krad and 6krad dark signals have significantly increased and are now in their proper relationship. Figures 6.3-13 and 6.3-14 show plots of the image and storage components versus anneal temperature and figure 6.3-15 shows the ratio of the storage to image region generation rates - which falls to a value ~2 after annealing so that these components eventually end up being of comparable magnitude as was found from the Co^{60} data [1]. Thus it would seem that the production of latent radiation-induced damage centres (presumably linked to trapped holes in the gate oxide) is the same for these devices and the lot given Co^{60} irradiation but that the activation energy for build up of the image region interface traps is higher - but note that because of the exponential dependence of the Arrhenius relationship the change in activation energy need only be small. For example a value of 0.5eV would give an acceleration factor of 70 between temperatures of 20 and 100°C and thus give the same result for 24 hours at 100°C as 70 days at 20°C. But if the activation energy is increased to 0.7eV the acceleration factor is increased by a factor 10 and little change would be noted for 70 days at room temperature - we would have to wait 700 days (2 years!).

The annealing has little effect on the average dark charge since the increase in the image component is matched by a decrease in the storage component (figure 6.3-16): so the previous remarks an average dark current and the comparison of Co^{60} with 10 and 1.5MeV proton data remain valid.

We can summarise this section by noting that the results are broadly in agreement with predictions from the previous Co^{60} study if the reduced electron-hole yield in the oxide is taken into account. The rather anomalous behaviour of the image region component and its slow build up with time could be explained if the activation energy for interface trap

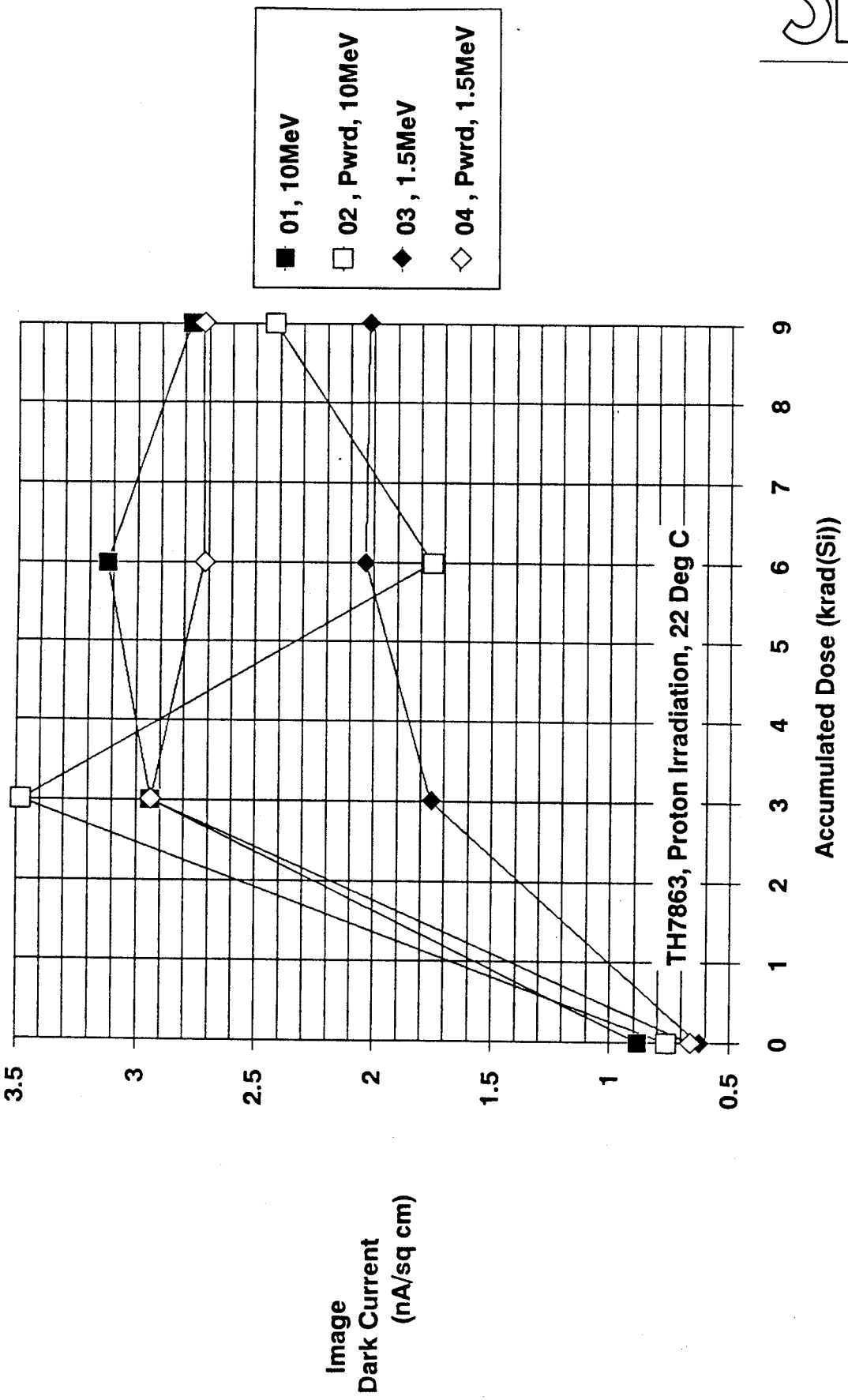

Figure 6.3-9 Image region dark current versus dose after 3 months storage unbiased at room temperature

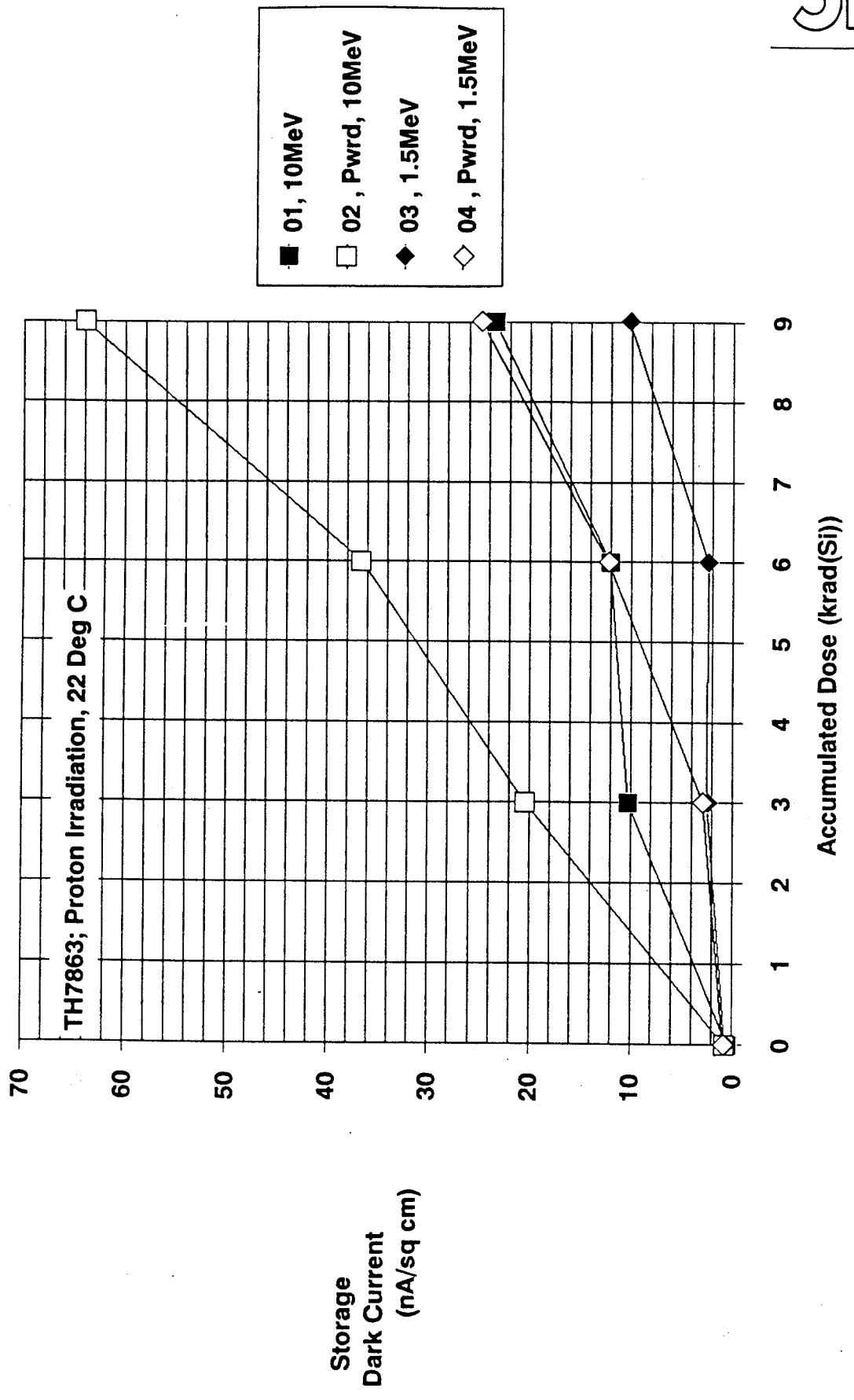

Figure 6.3-10 Storage region dark current versus dose after 3 months storage unbiased at room temperature

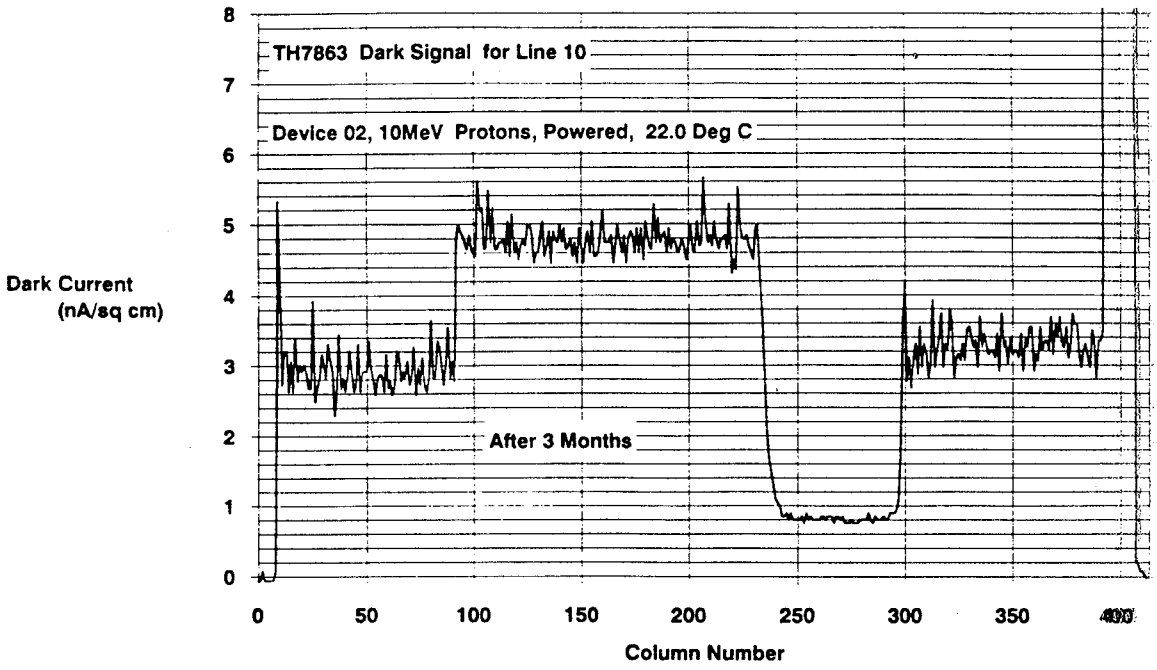

Figure 6.3-11 Line trace for device 02 showing image region dark current after 3 months but before high temperature anneal

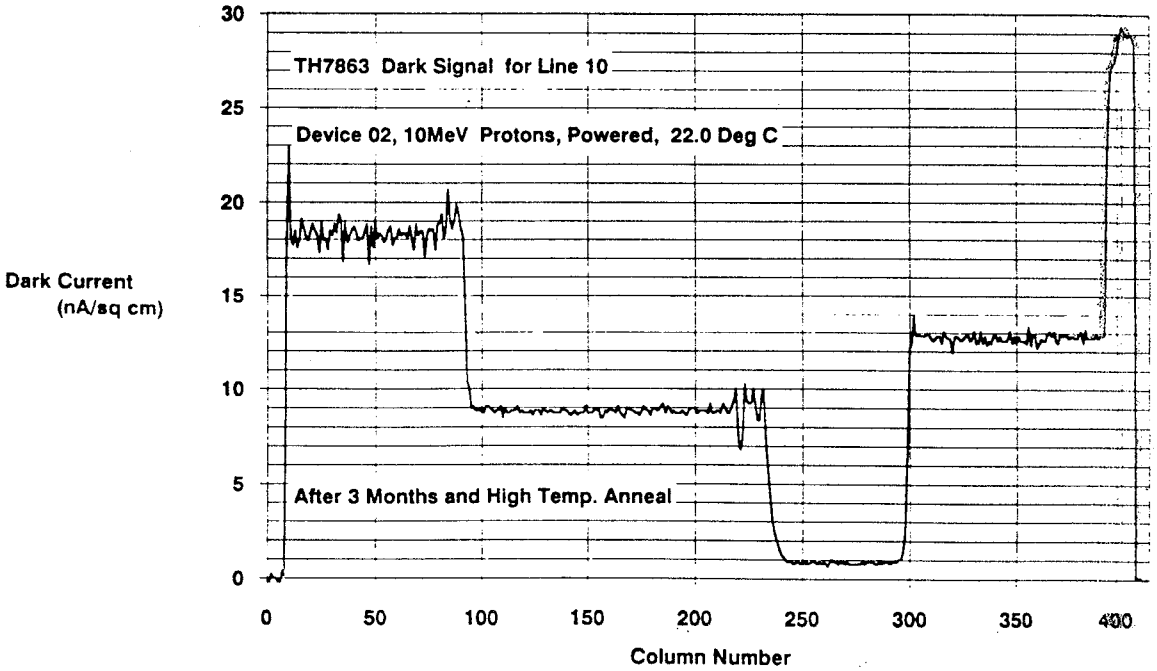

Figure 6.3-12 Line trace for device 02 showing image region dark current after 3 months and after a high temperature anneal (2h at each of 100, 120, 140, 160 and 180°C plus 18h at 180°C)

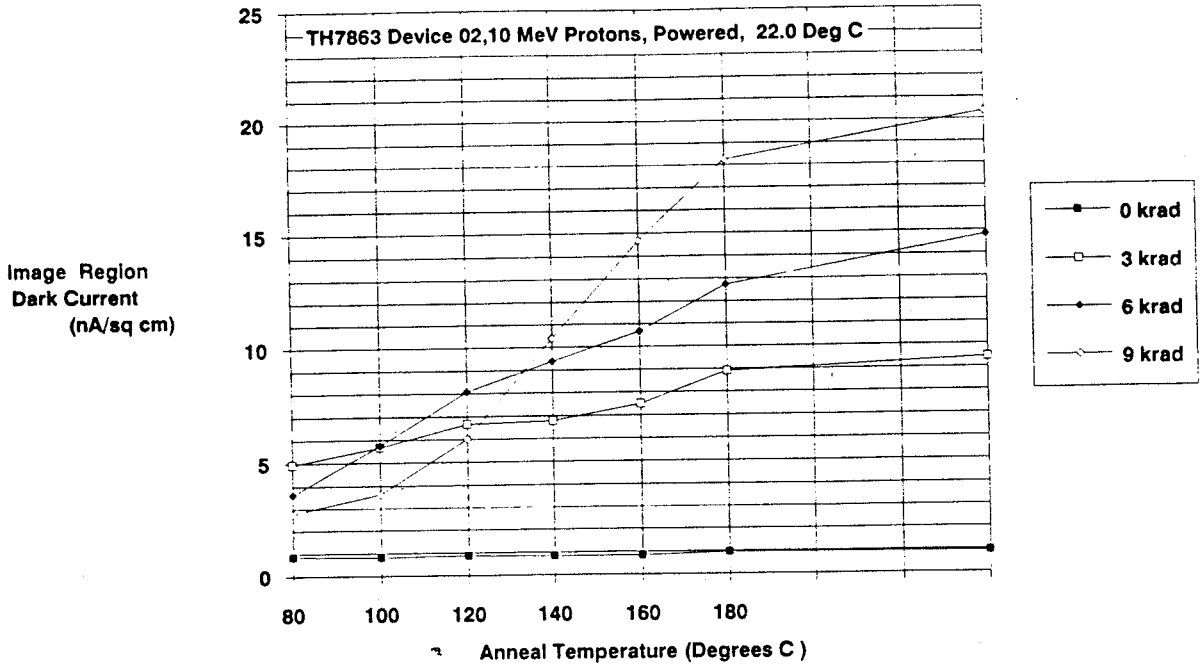

Figure 6.3-13 Image region dark current versus anneal temperature

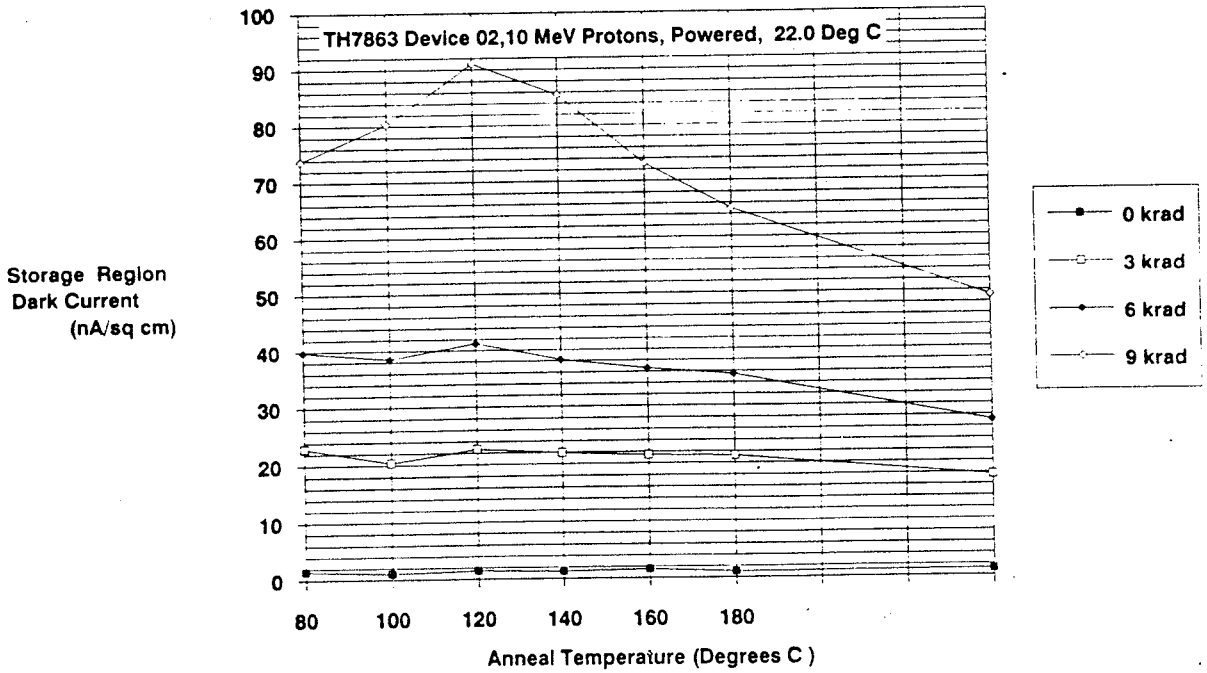

Figure 6.3-14 Storage region dark current versus anneal temperature

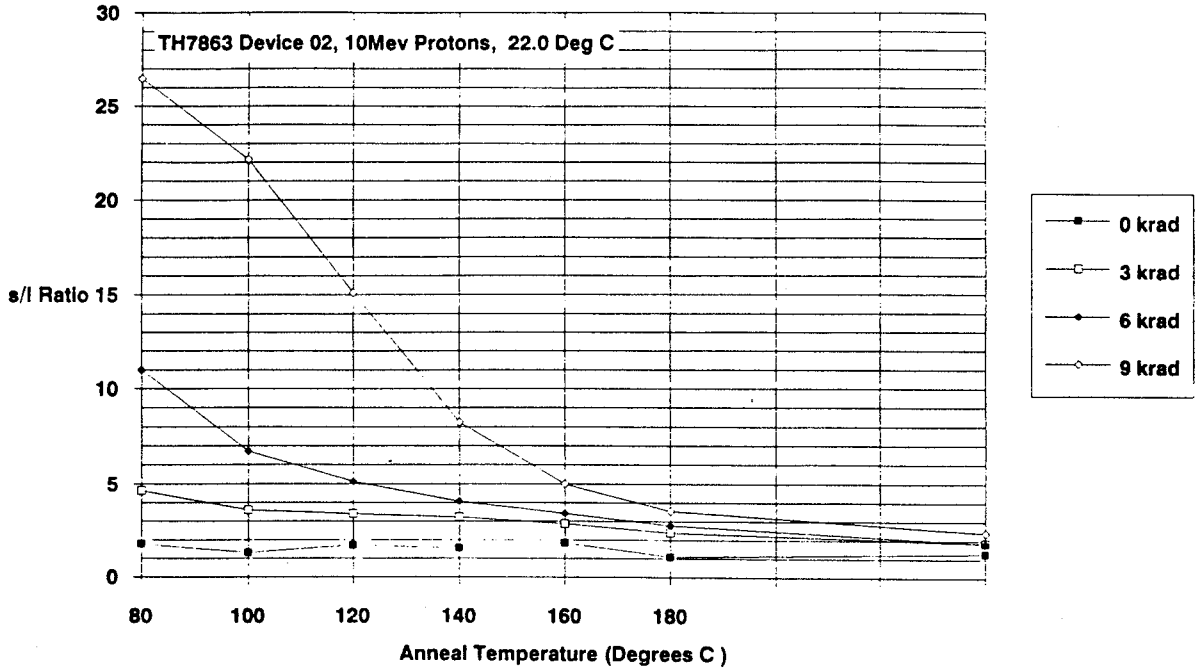

Figure 6.3-15 Ratio of storage to image region components versus anneal temperature

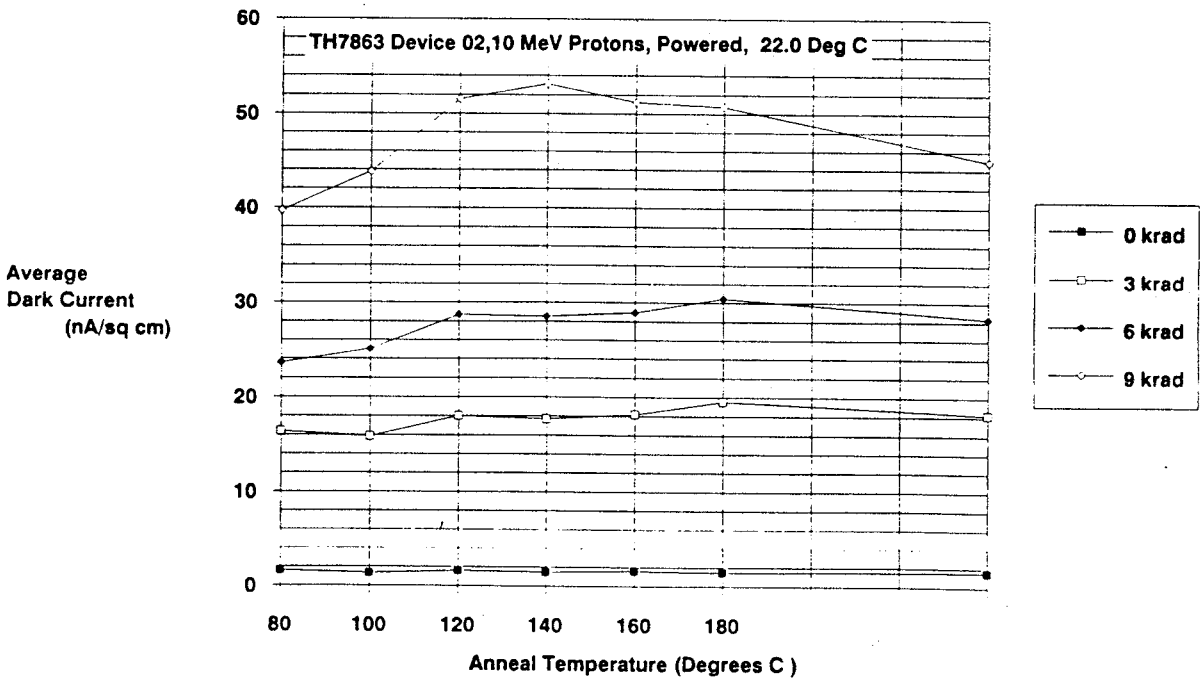

Figure 6.3-16 Average dark current versus anneal temperature

generation were 0.7 instead of 0.5eV - this change might be due to space charge or dose rate effects or to a batch dependence in the CCD behaviour (these devices are not from the same diffusion lot as those studied previously).

Hence we can conclude that these results are not in disagreement with the previous Co^{60} work and since the latter is more representative in terms of dose rate and simulation of electron-hole yield for the high energy protons in the earth's environment the previous report should be taken as the baseline data base for TH7863 ionisation damage. Note that because of the possibility of dose rate (and related) effects in this study, little can be said about batch dependence of CCD behaviour.

6.3.1.1 Temperature dependence of the ionisation-induced dark current

It is expected that the ionisation damage creates interface traps with a distribution of energy levels within the silicon bandgap. However from the discussion of para 3.3.3.1 we note that only those generation states which are created with energies close to midgap are effective in producing dark current. Hence it is expected that the radiation-induced surface dark charge will obey the usual relation for surface dark charge:

$$\text{dark current} = \text{constant} \times T^{3/2} \exp(Eg/2kT)$$

where T is the absolute temperature and Eg is the silicon bandgap, given by [38]:

$$Eg = 1.170 - \frac{4.73 \times 10^{-4} T^2}{T + 636} \text{ eV} \qquad (6.3\text{-}1)$$

Any contribution from states away from midgap has the effect of slightly increasing the activation energy.

Although the previous Co^{60} investigation [1] did not consider temperature dependence in great detail, measurements at 16, 22 and 37°C were broadly in line with the predictions of equation 6.3-1.

In this section we consider further measurements of temperature dependence which confirm the expected behaviour for surface dark charge and can be used as a comparison with bulk damage induced generation - which, if field enhanced, might show a different temperature behaviour.

Figures 6.3-17 and 6.3-18 show the image and storage region dark currents for all four proton-irradiated devices obtained after 3 months storage, unbiased at room temperature. The clocking waveforms had the usual CCD readout sequence (readout in 41ms) but had an integration time increased by a factor 11.8 (to 484ms). This sequence was used so as to enhance the image region signal relative to the large radiation-induced surface dark charge of the storage region so that the distribution of bulk dark charge spikes could be studied (c.f. para 6.3.2). The data were obtained for CCD heatsink temperatures of 6.0, 12.0, 17.0, 22.0, 27.0, 32.0 and 37.0°C. In the plots the two higher temperatures were amended to 32.5 and 38.0°C to allow for additional on-chip heatsink dissipation. It is seen that the logarithmic plots are essentially linear with 1000/T as expected. In fact the lowest temperature data points (6.0°C) should probably be adjusted to a lower temperature since

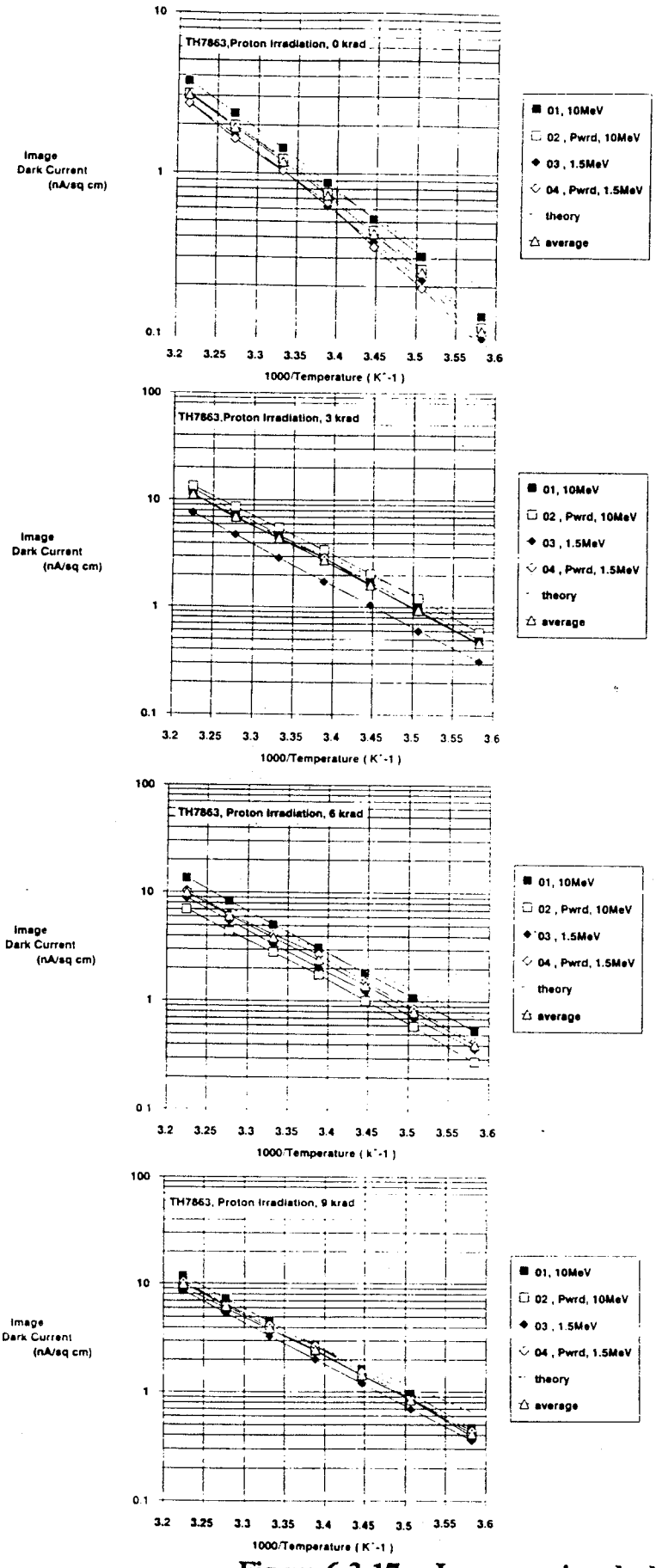

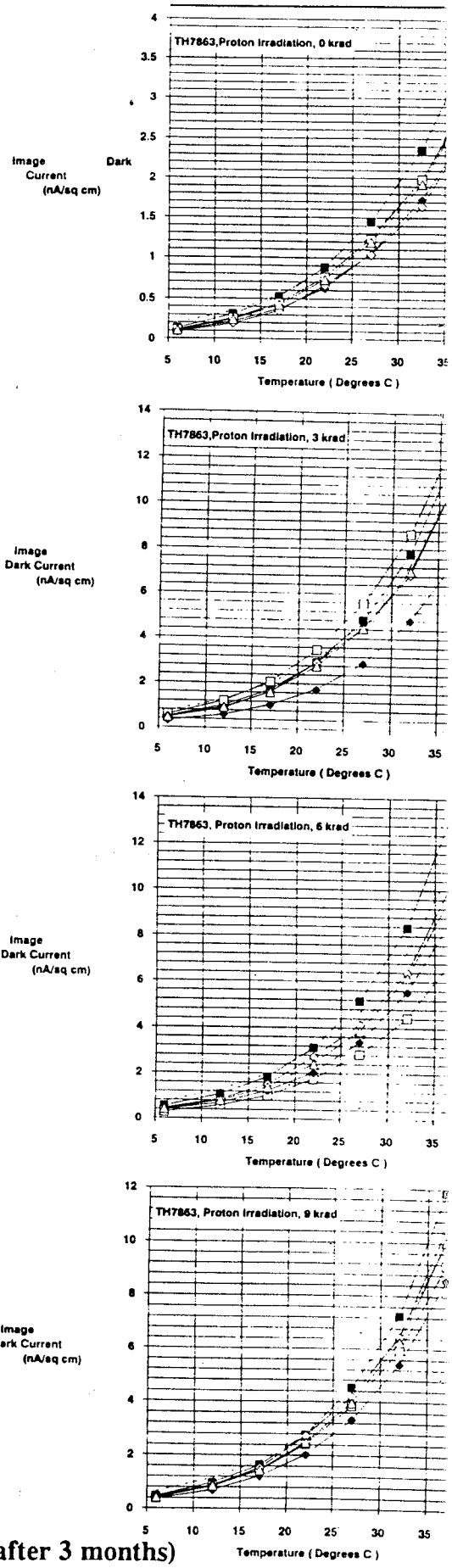

Figure 6.3-17 Image region dark current (after 3 months) as a function of temperature

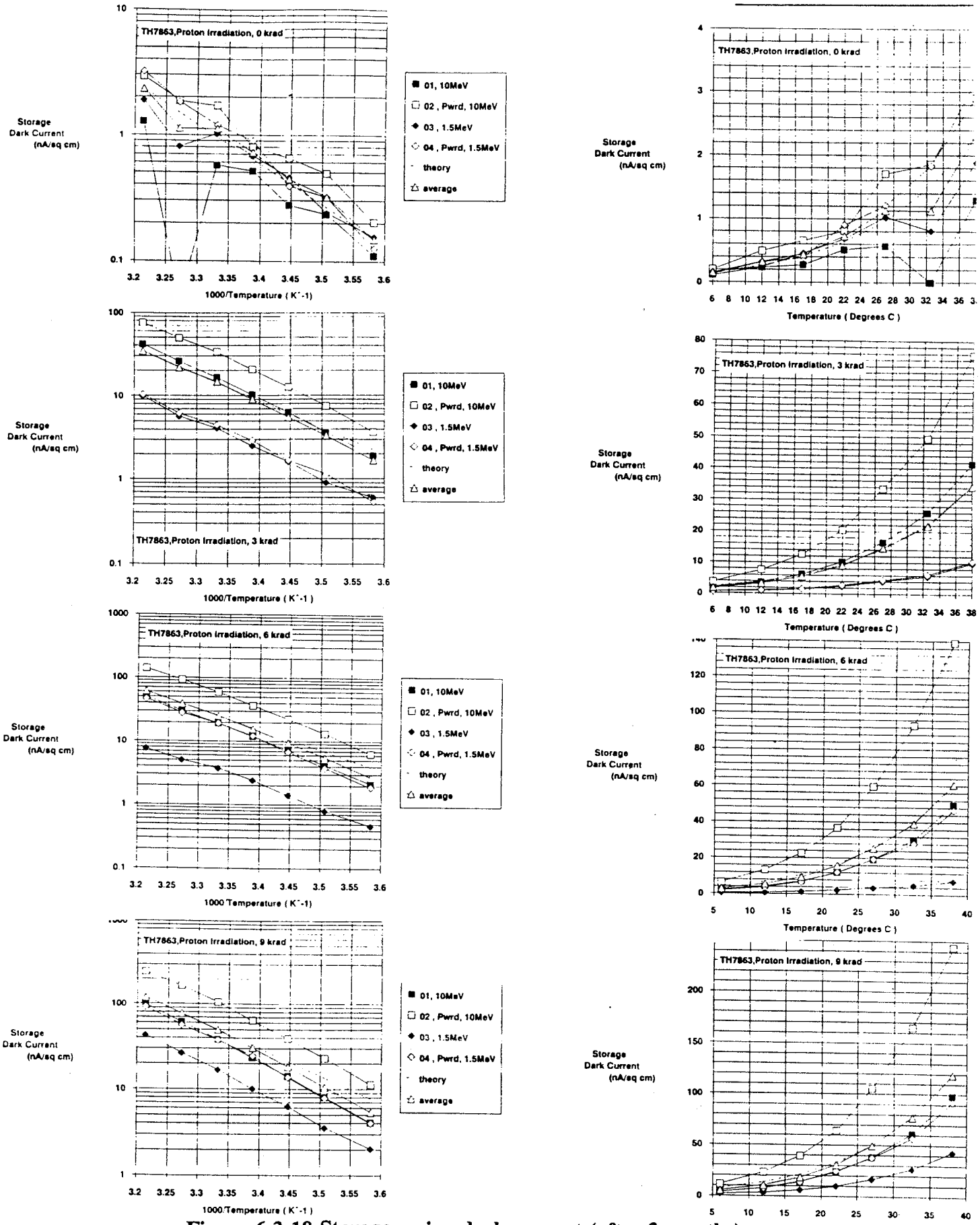

Figure 6.3-18 Storage region dark current (after 3 months) as a function of temperature

these were consistently made immediately after CCD power-up, before the CCD temperature had risen (because of on-chip dissipation). This would improve the agreement with a straight line fit. Also shown in the plots is the theoretical line derived from equation 6.3-1.

Figure 6.3-19 shows the normalized dark current (average of image and storage components divided by the average at 37°C) averaged over all the devices and dose regions. A linear fit gives an activation energy of 0.68eV in agreement with previous measurements by this author [34] and others (c.f. refs [39] and [40]). Note that this energy will differ from Eg/2 (=0.56 eV) because of the $T^{3/2}$ dependence and the temperature behaviour of Eg (as well as any effect of states away from midgap and any temperature dependence of emission and capture constants). Note that equation 6.3-1 applied on its own gives an activation energy of ~0.63eV. Since the same set of measurements were used for measuring ionisation and bulk damage components the CCD temperatures were the same in both cases and figure 6.3-19 can be used to compare with the displacement damage histograms of the next section. The average ionisation dark charge temperature dependence taken from figure 6.3-19 is:

Table 6.3-3

Nominal CCD temperature (at heatsink) °C	Ionisation dark charge (normalised to value at 37°C)
6	0.044
12	0.089
17	0.153
22	0.256
27	0.413
32	0.643
37	1

6.3.2 Displacement Damage

In this section we consider the dark charge nonuniformity caused by the production of bulk defect states in the silicon depletion regions of the CCDs by proton displacement damage. The mechanisms for this were discussed in para 3.3.3.1. The bulk damage will also produce an increase in the average dark current but this is expected to be much smaller than the increases due to ionisation damage in TH7863 devices. As previously noted, it is not possible to separate the two contributions to the average dark current and these results can say nothing about the increase in mean level due to bulk damage. For a detailed study on bulk damage on its own it is best to use devices operated in inverted mode [37], where surface generation is suppressed, as have been used by the groups at NRL and JPL (see refs [29], [31], [32], [35] and [17]). Fortunately at the time of making the CCD measurements described here the image region dark current had not shown significant reverse annealing (the increase was only from ~1nA/cm^2 to ~3nA/cm^2 at 22°C: c.f. figure 6.3-9) and so the contribution to the nonuniformity arising from surface damage can be assumed to be small. It only becomes significant after a high temperature annealing step which causes a large reverse annealing in the image region ionisation dark current; though, as for the mean level, the ionisation damage-induced nonuniformity cannot be separated out and there is no way of checking this assumption other than by comparison with previous Co^{60} data (from [1]).

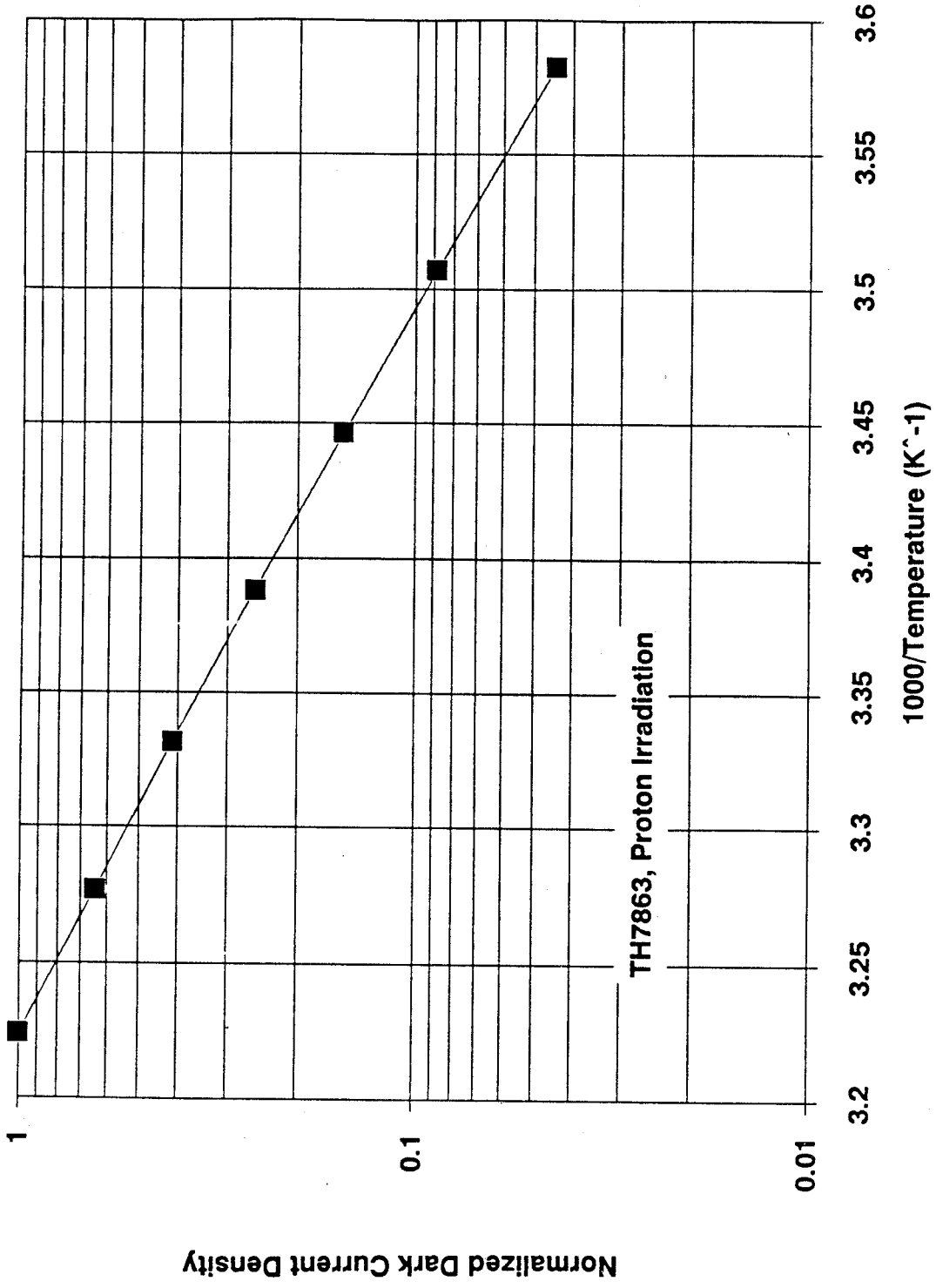

Figure 6.3-19 Average temperature dependence of the ionisation-induced dark charge for all measurements on TH7863 devices

Note that the large ionisation-induced dark current from the storage region does not produce significant dark charge nonuniformity since it is averaged out along each column as the CCD is readout. The subsequent vertical slope in the CCD image is easily subtracted, along with any other large scale nonuniformities (such as the horizontal slope seen in figures 6.35 and 6.3-7 and discussed in para 6.3.1). All the data to be discussed in this section relates to images with storage region dark charge and other large scale nonuniformities subtracted. This subtraction process precludes an exact knowledge of the mean level which, as we have said, is in any case contaminated by the presence of ionisation damage. The subtraction was performed separately in the row and column directions by forming an array for each CCD line (or column in the case of subtracting variations in the column direction) where each pixel value is calculated from a running average of the 16 pixels on each side (or above and below for a column subtraction). The running average is calculated in two passes so as to remove distortions due to large fluctuations (dark current spikes) in the original data. The process has been found to give excellent removal of large scale nonuniformities without distorting the profile of dark charge spikes (ie. the function subtracted is smoothly varying). Because of edge effects, pixels close to the boundaries of the dose regions were not included in the histograms.

In the following sections results will be presented in terms of histograms of pixel dark currents and as rms values. For each CCD there were a small number of dark current spikes which were anomalously large and these are best considered separately (para 6.3.2.3). Further interpretation and the prediction of damage effects for other proton environments are discussed in section 9.

6.3.2.1 Dark current histograms

Dark current measurements were made immediately after irradiation and at intervals afterwards to determine any annealing behaviour. Figure 6.3-20 shows a histogram of 'immediate' dark current density values (with the mean value subtracted). We note the following points:

i) the histograms are asymmetric, with a 'tail' extending toward high dark current values. This tail is due to the effects of inelastic collisions (c.f. para 3.3.1)

ii) The shape of the distributions are different for 10 and 1.5MeV protons, with the 10MeV data extending to higher dark currents and having a different slope to the tail (which is approximately a straight line on a logarithmic plot or exponential on a linear one). The differences are due to the higher cross sections (ie. greater probability) for inelastic collisions at 10MeV. As discussed in para 3.3.3.1, an inelastic collision (though rare) can deposit large amounts of energy and hence create large numbers of bulk states - thus producing a dark current spike. It should be emphasised that when comparing displacement damage it is the particle fluence which is important not the dose (in krad). Thus it should be noted that the fluence of 10MeV particles was a factor 3.8 higher than that of the 1.5MeV protons. Unfortunately, as will be discussed in section 9, simple scaling of the histograms is not possible.
Note that

3krad(Si) is equivalent to 1.40×10^9 p/cm^2 at 1.5MeV
or 5.37×10^9 p/cm^2 at 10MeV

iii) Damage is the same whether the device is powered or unpowered during irradiation. This is as expected for bulk damage : the author is not aware of any published data which shows a bias dependence for CCD displacement damage. However this need not necessarily be the case since many of the initial defects created by displacement damage are charged and the kinetics of migration through the lattice (until stabilised by association with existing defects or impurities) might be expected to be influenced by the presence of an electric field.

iv) There are a small number of spikes which are anomalously large and lie outside the main distribution at dark current densities of several nA/cm^2 (at 22°C). These are expected to be due to field enhanced emission as discussed in para 3.3.3.1

The histograms for zero dose were obtained from the same CCD images but from the regions totally masked during irradiation by an external aluminium plate. This gives an approximation to the histogram without bulk damage but it is not exact because:

i) there will be a contribution to the nonuniformity from the ionisation damage

ii) the amplifier gain values were set so as to be able to digitise the full dynamic range of the CCD images to 8 bits. In the cases where there was a substantial ionisation-induced increase in average dark charge (subsequently subtracted in computer memory) the gain had to be reduced - thus making the low signals from the 'zero dose' portion of the image affected by digitisation noise.

To gain an idea of the histogram due to causes other than bulk damage (ie. due to the pre-irradiation nonuniformity and to ionisation damage) the Co^{60} database [1] was examined for images which showed similar image region ionisation-induced dark currents. From figure 6.3-9 we see that prior to a high temperature anneal the post-proton irradiation image region dark current was ~$3nA/cm^2$ for all dose regions. Figure 6.3-21 shows histograms on linear and logarithmic scales for a device receiving 3krad(Si) of Co^{60} gamma rays whilst unpowered. The resultant image region dark current was $2.4nA/cm^2$ ie. comparable with the proton cases. Hence the dark current histogram should be fairly representative. The rms value is $0.077nA/cm^2$ and the histogram is gaussian. In comparison with figure 6.3-20 and later histograms it can be seen that the nonuniformity will be dominated by effects due to displacement damage and to a fair approximation (accuracy ~10% or better) other contributions can be ignored.

After storage unbiased at room temperature it was found that the nonuniformity decreased. This can be seen in figure 6.3-22, which gives data immediately after irradiation and after 3 months storage. This is an important result since the implication is that the damage for the low dose rate environment in flight is less than would be predicted from immediate post-irradiation measurements. The cause of this annealing is not fully understood. The P-V centre (c.f. para 3.3.2) does not fully anneal until 150°C, but presumably annealing can occur at lower temperatures at a slower rate. The implication is that all proton damage assessments should take into account the possibility of long term annealing (ie. over periods of months to years). Note that annealing after 3 months storage has been previously observed by this author for a proton damaged EEV device [34]. The majority of results presented hereafter were obtained after three months storage and so should be comparable with those expected for the flight environment.

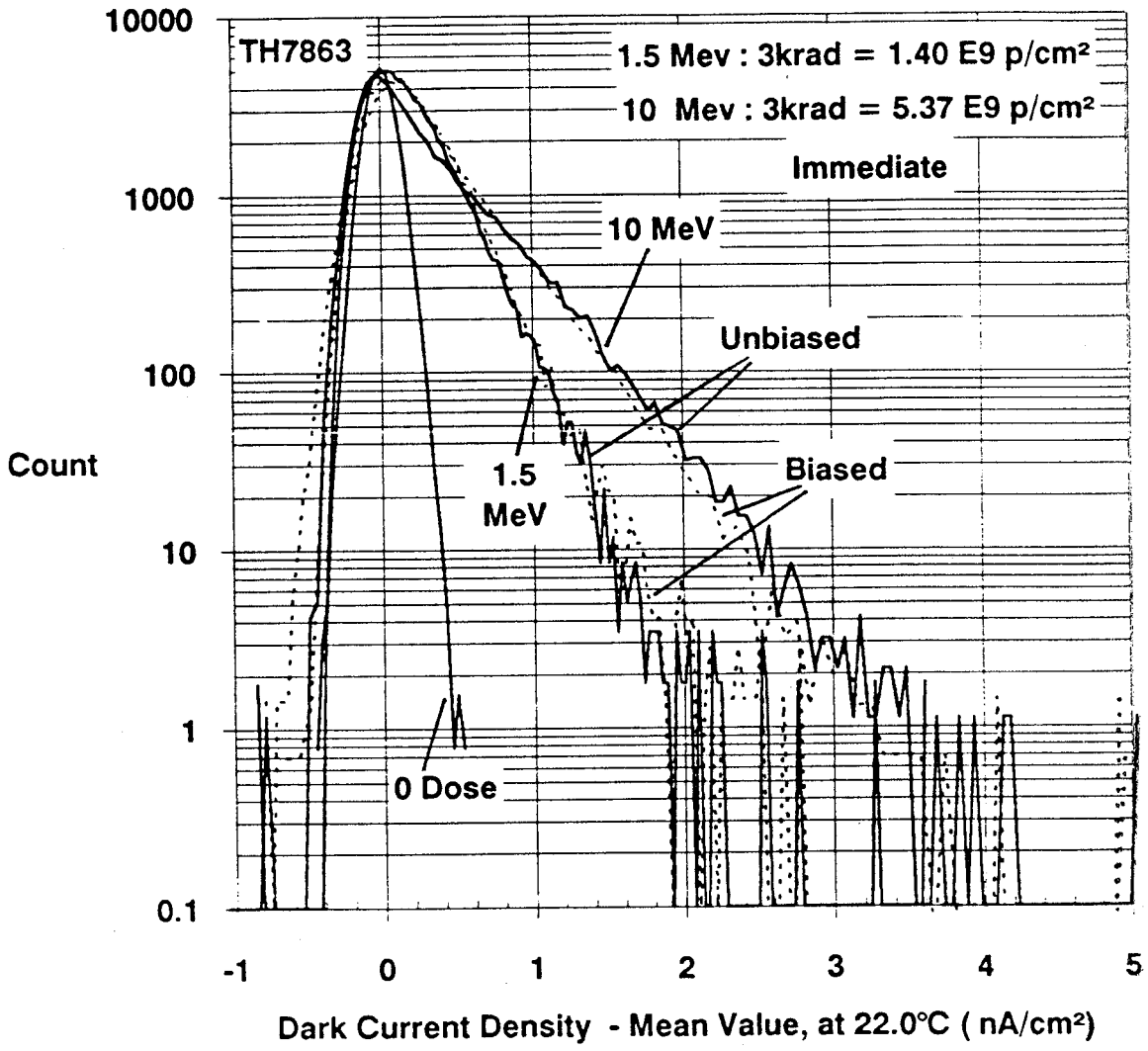

Figure 6.3-20 Dark current density histograms (mean value subtracted) at 22°C, immediately after irradiation for TH7863 devices powered and unpowered during irradiation

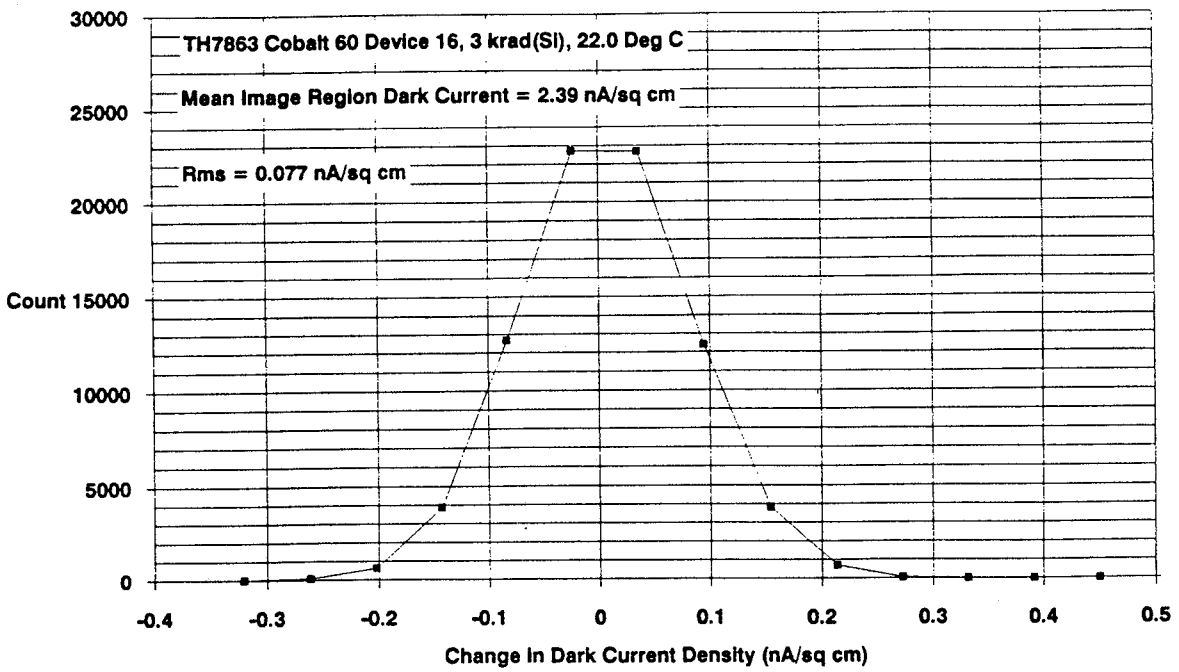

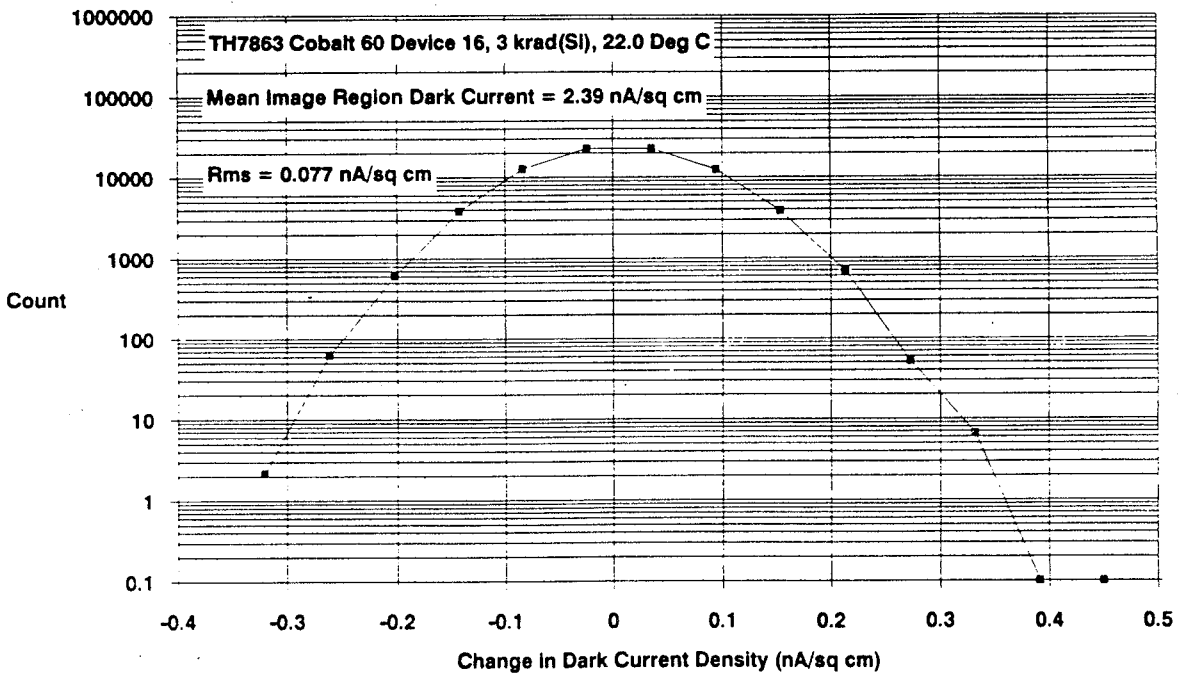

Figure 6.3-21 Histograms (22°C) for a device receiving 3krad Co^{60} radiation (unbiased) the resultant image region dark charge was 2.39nA/cm^2 (pre-irradiation value = 0.69nA/cm^2)

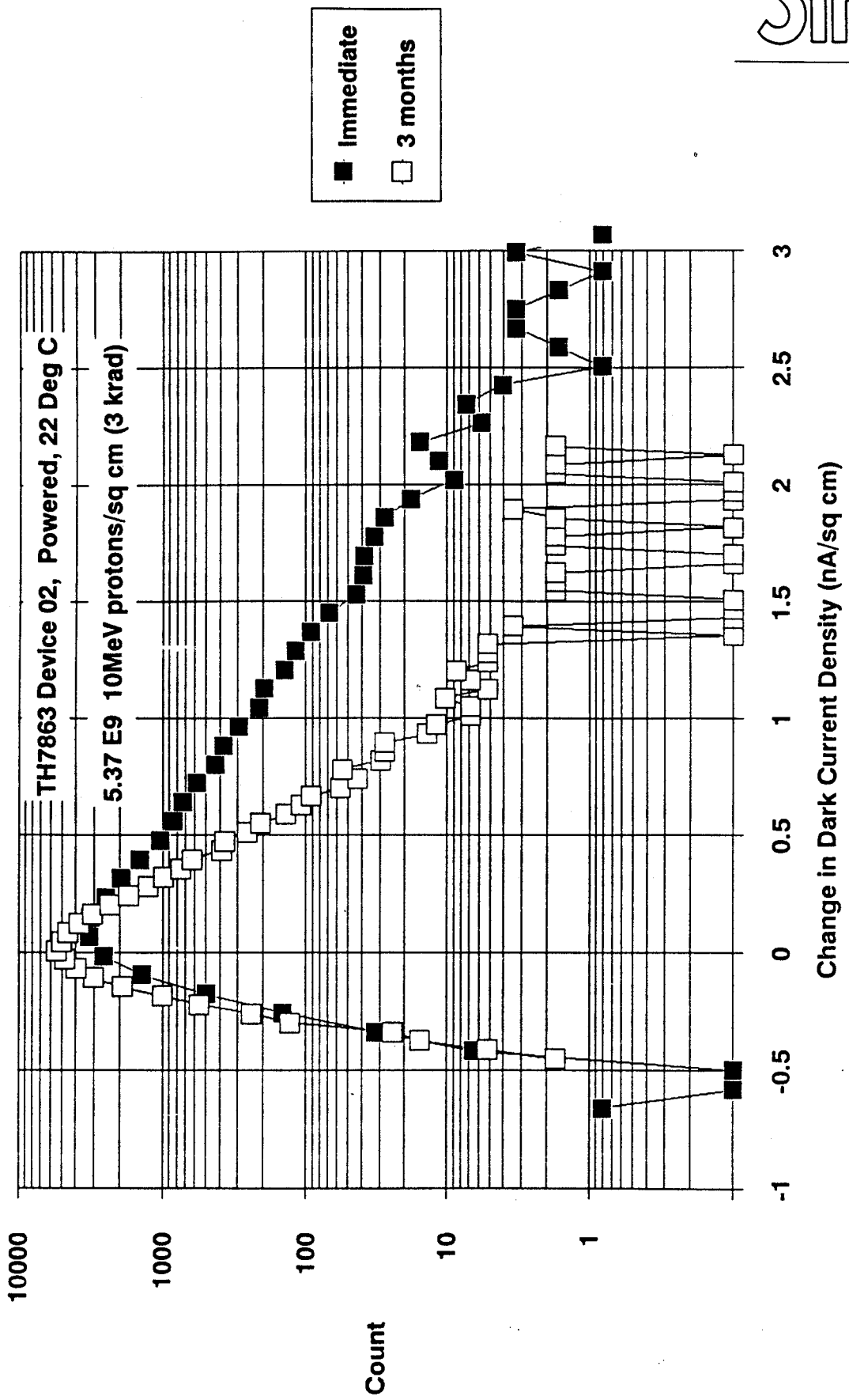

Figure 6.3-22 Dark current histograms for device 02 : immediate and after 3 months storage unbiased at room temperature

Figure 6.3-23 shows histograms similar to figure 6.3-20 but after 3 months. There is a plot for each of the CCD dose regions (3, 6 and 9krad) and, again, the damage is independent of CCD bias. Figure 6.3-24 shows results for the three dose regions for CCD02 (10MeV, powered) showing the increase in damage with proton fluence.

We turn now to the temperature dependence of the dark current nonuniformity. The temperature dependence of the average ionisation-induced dark charge was derived in para 6.3.1. Histograms of pixel values were obtained for the same images as used in that study but with large scale uniformities, such as the slope due to storage region generation, removed as discussed above. Figures 6.3-25 and 6.3-26 show these histograms for the 3krad dose regions. The dark current density values have been scaled by the values derived in para 6.3.1 (normalised so that the 22°C data is scaled by x1), ie.

temperature (°C)	dark charge scaling factor
6	5.77
12	2.89
17	1.67
22	1
27	0.620
32	0.398
37	0.256

It is seen that the curves for the different temperatures are coincident, implying that the shapes of the distributions do not change with temperature and that the scaling factors are the same as those derived for ionisation damage. That is, the temperature behaviour for the majority of pixels is the usual one for silicon. This scaling also holds for the other dose regions. For example figure 6.3-27 shows results for 9krad of 10MeV radiation incident on device 02. Note that the previous comments on the accuracy of the 'zero dose' histogram apply to figures 6.3-25 to 6.3-27 also.

6.3.2.2 Effect of high temperature annealing

After three months storage at room temperature a single device (number 02), which had received 10MeV irradiation whilst biased, was given a high temperature isochronal anneal, again whilst unbiased. The CCD was placed in an oven for 2 hours at 100, 120, 140, 160 and 180°C and finally given a further 18 hours at 180°C.

The effect on the dark current histograms is shown in figure 6.3-28. As the annealing progressed the histograms became more gaussian in shape as the 'inelastic' tail diminished; though for the 9krad region it is hard to tell whether the tail has annealed out or become lost in the main peak - which is considerably widened. This broadening may be due to ionisation-induced nonuniformity since the 9krad region, in particular, shows a large increase in image region dark current as the bake progresses (c.f. figure 6.3-13). However a reduction in the tail can be seen at the lower doses and particularly in the 3krad data. This tends to argue against divacancies being a major contributor to the generation of dark spikes at 10MeV, since these would be expected to anneal only at temperatures in the range 300-400°C. We note that from the 3krad data after the anneal there is still left an appreciable gaussian distribution (much broader then the pre-irradiation histogram). Unfortunately it is not possible to say whether this is due to a different defect being responsible for the 'elastic' main peak or whether the gaussian distribution is caused by increased nonuniformity due to the ionisation damage (which certainly increases the mean level as shown in figure 6.3-13).

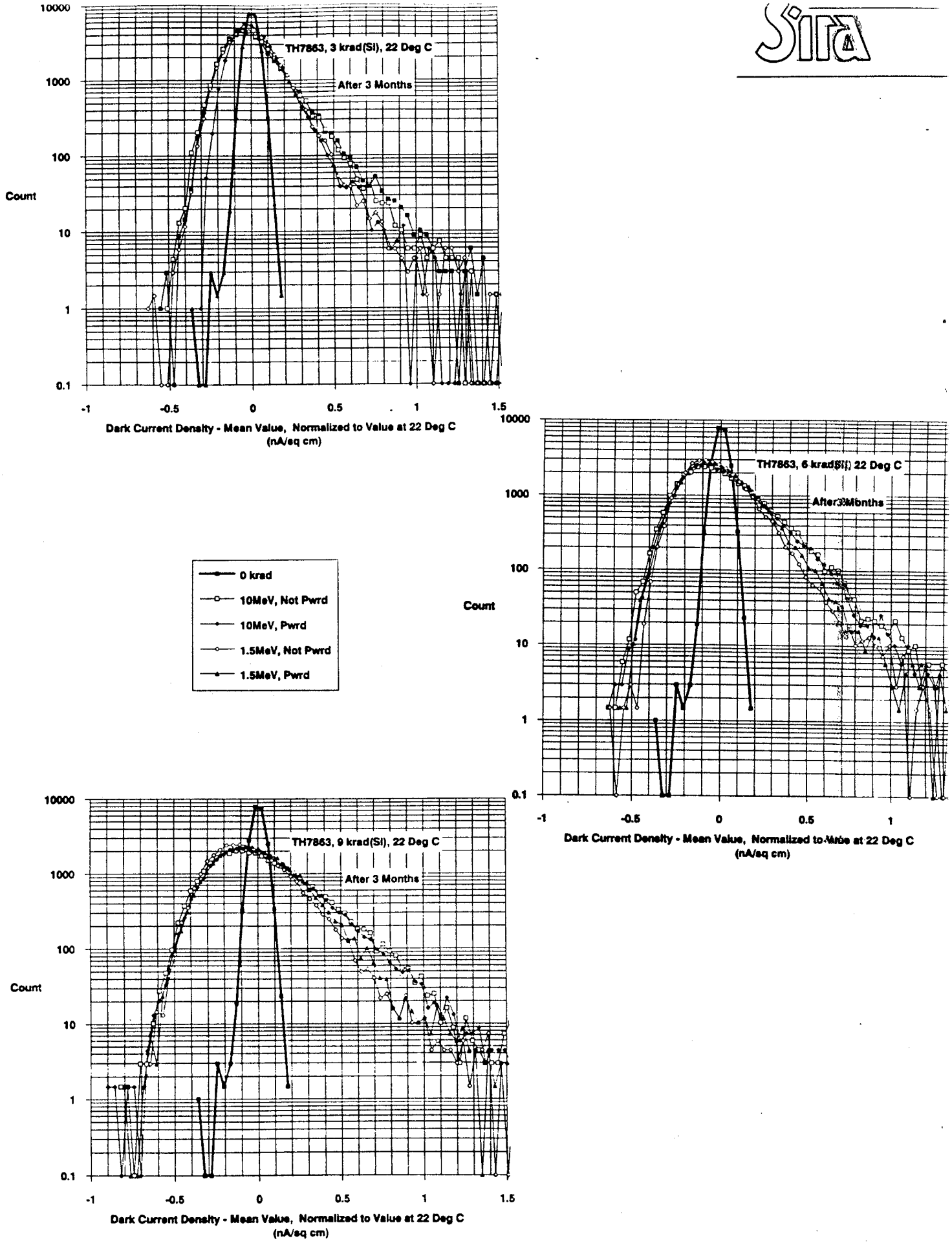

Figure 6.3-23 Histograms of dark current density after 3 months

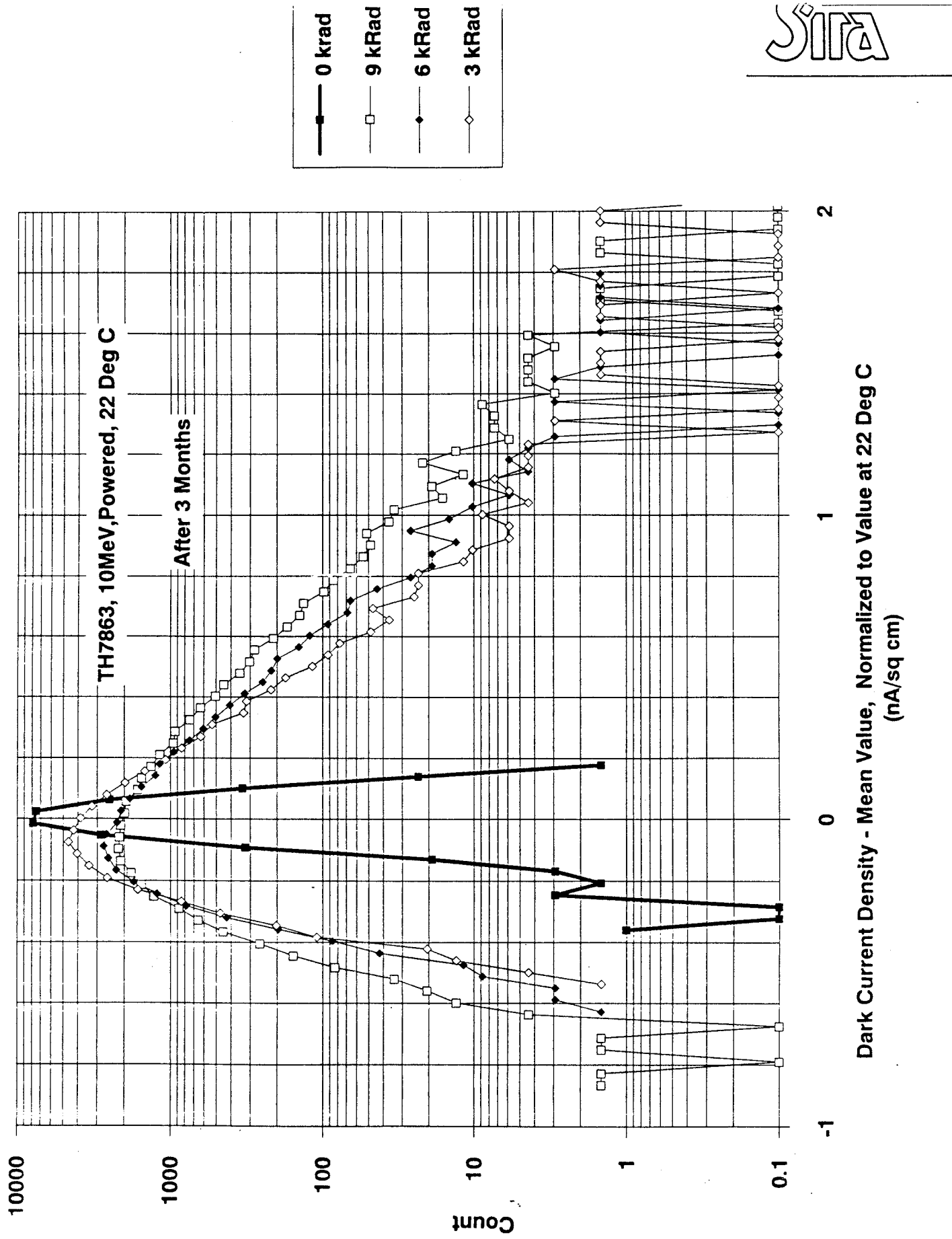

Figure 6.3-24 Histograms of dark current density for device 02 with doses of 3, 6 and 9 krad(Si), biased, after 3 months storage (unbiased)

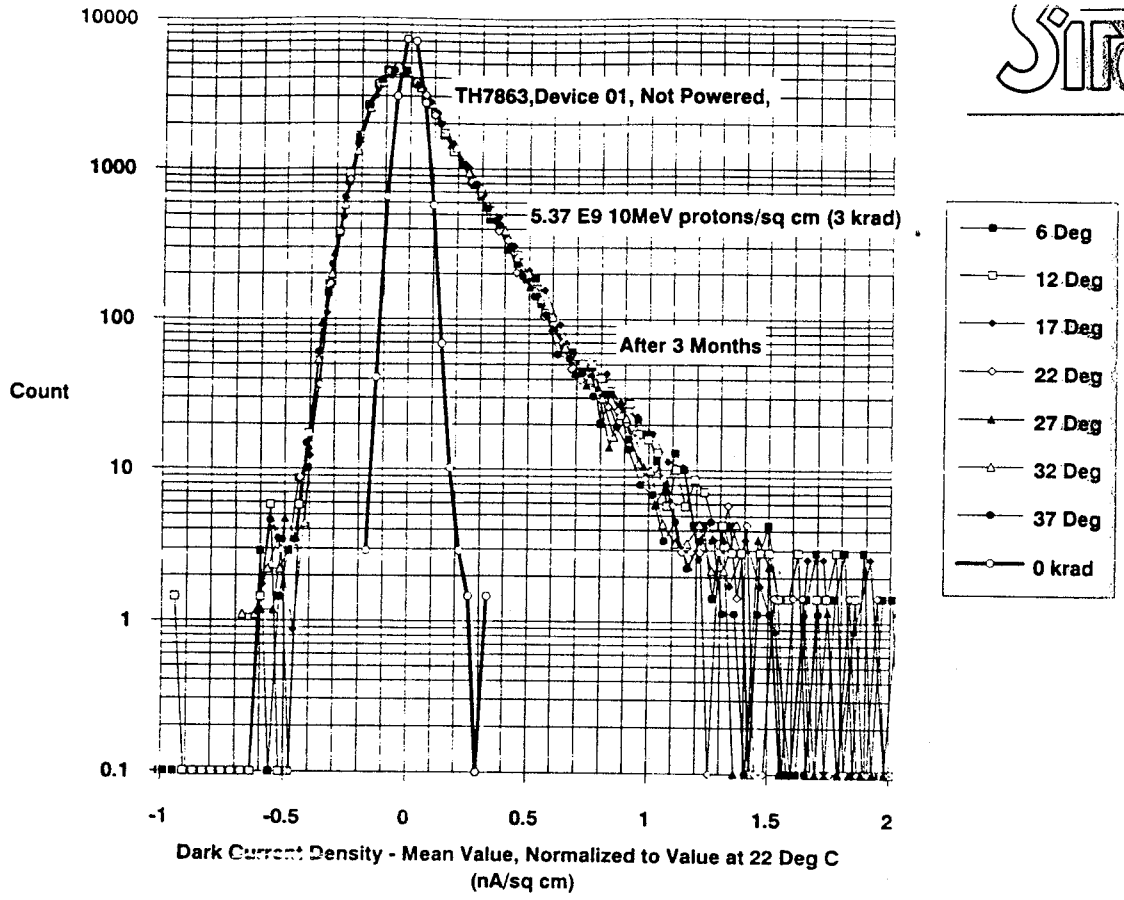

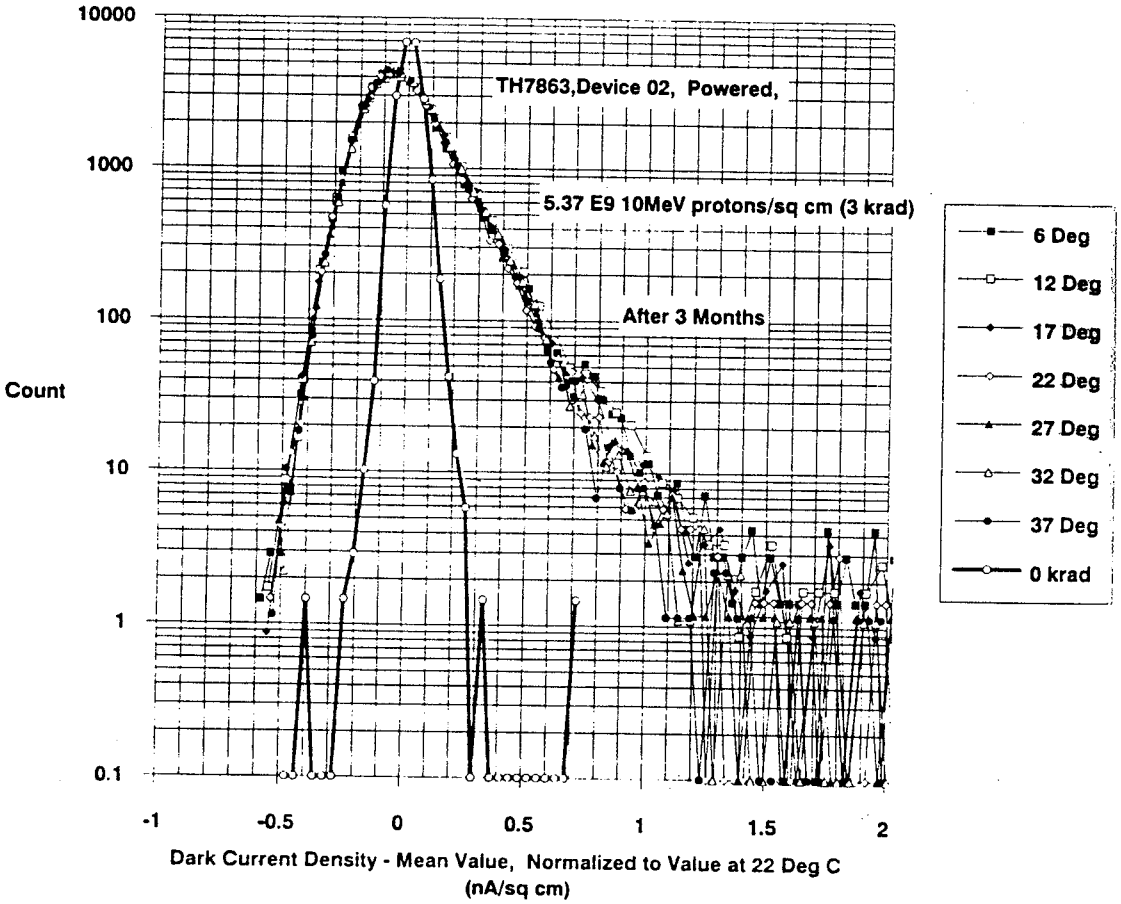

Figure 6.3-25 Histograms of dark current density for 3 krad(Si) of 10MeV proton irradiation. Measurements carried out at a variety of CCD temperatures (after 3 months)

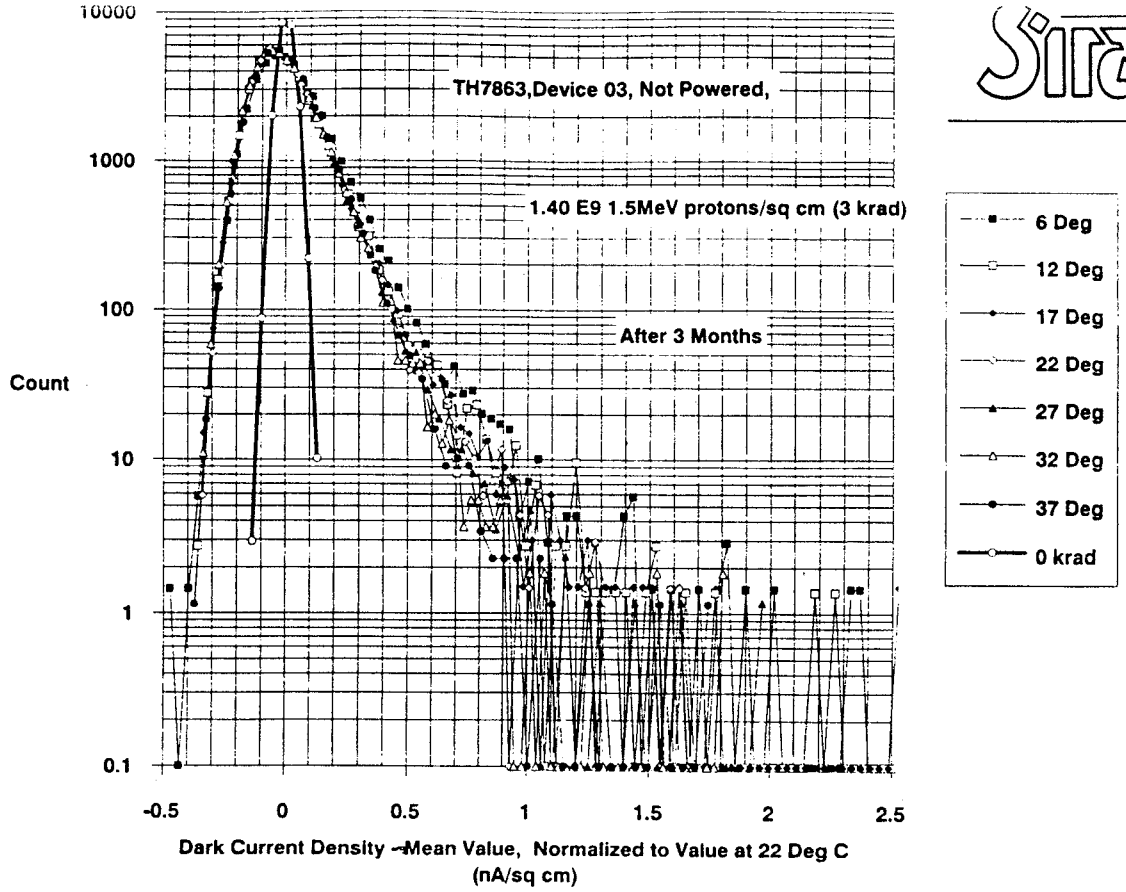

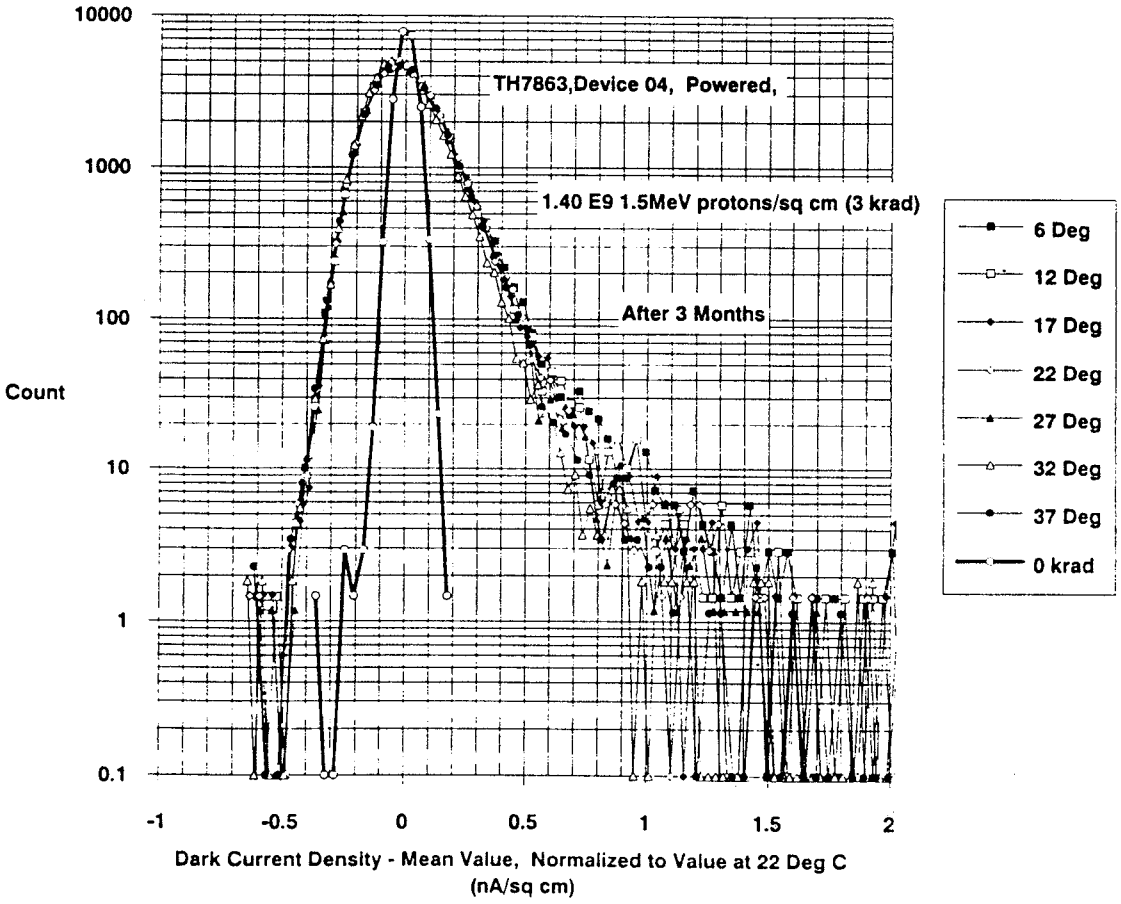

Figure 6.3-26 Histograms of dark current density for 3 krad(Si) 1.5MeV proton irradiation. Measurements carried out at a variety of CCD temperatures (after 3 months)

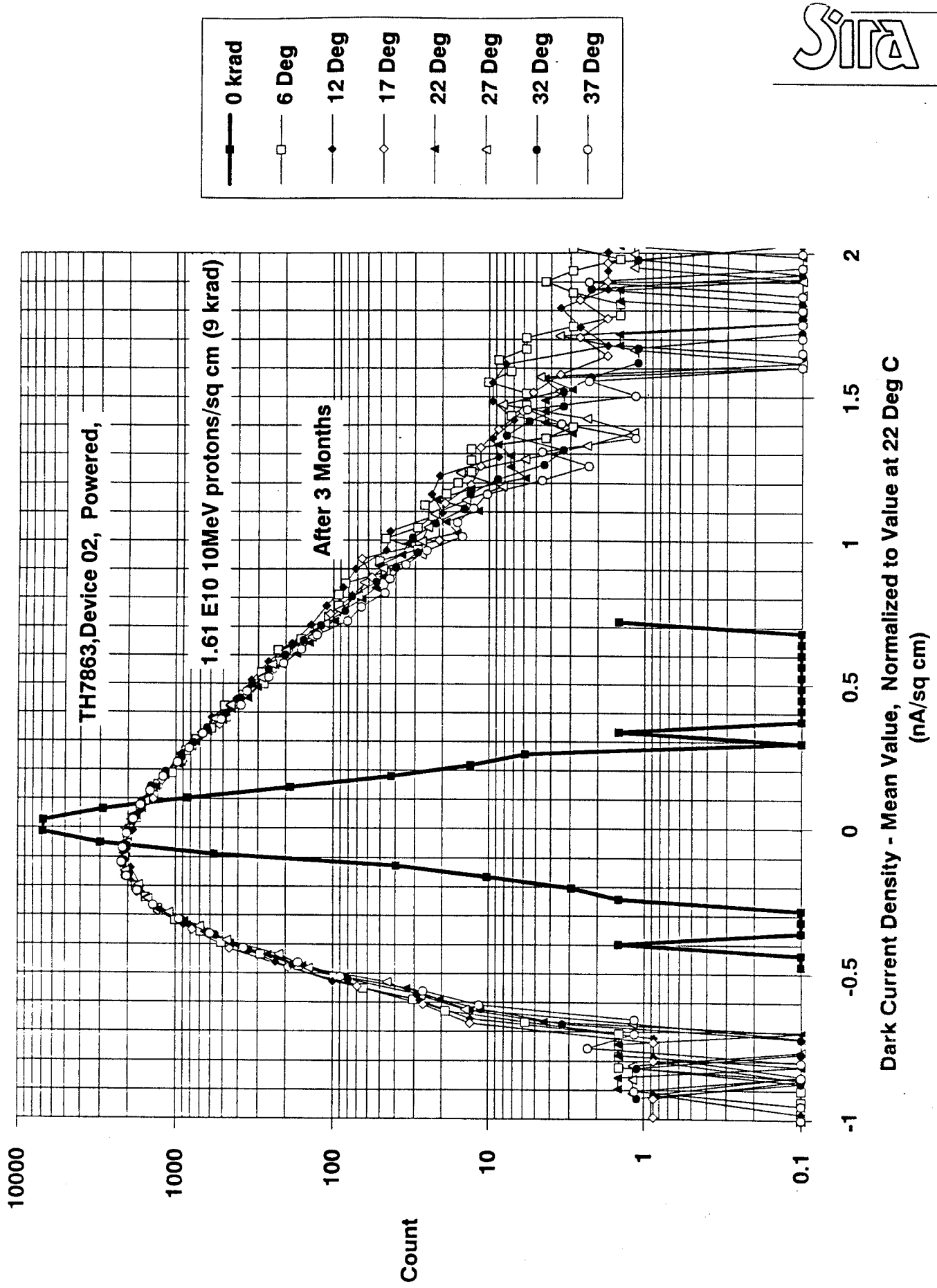

Figure 6.3-27 Histograms of dark current density for 9krad(Si) 10MeV proton irradiation on device 02 for a variety of CCD temperatures (after 3 months)

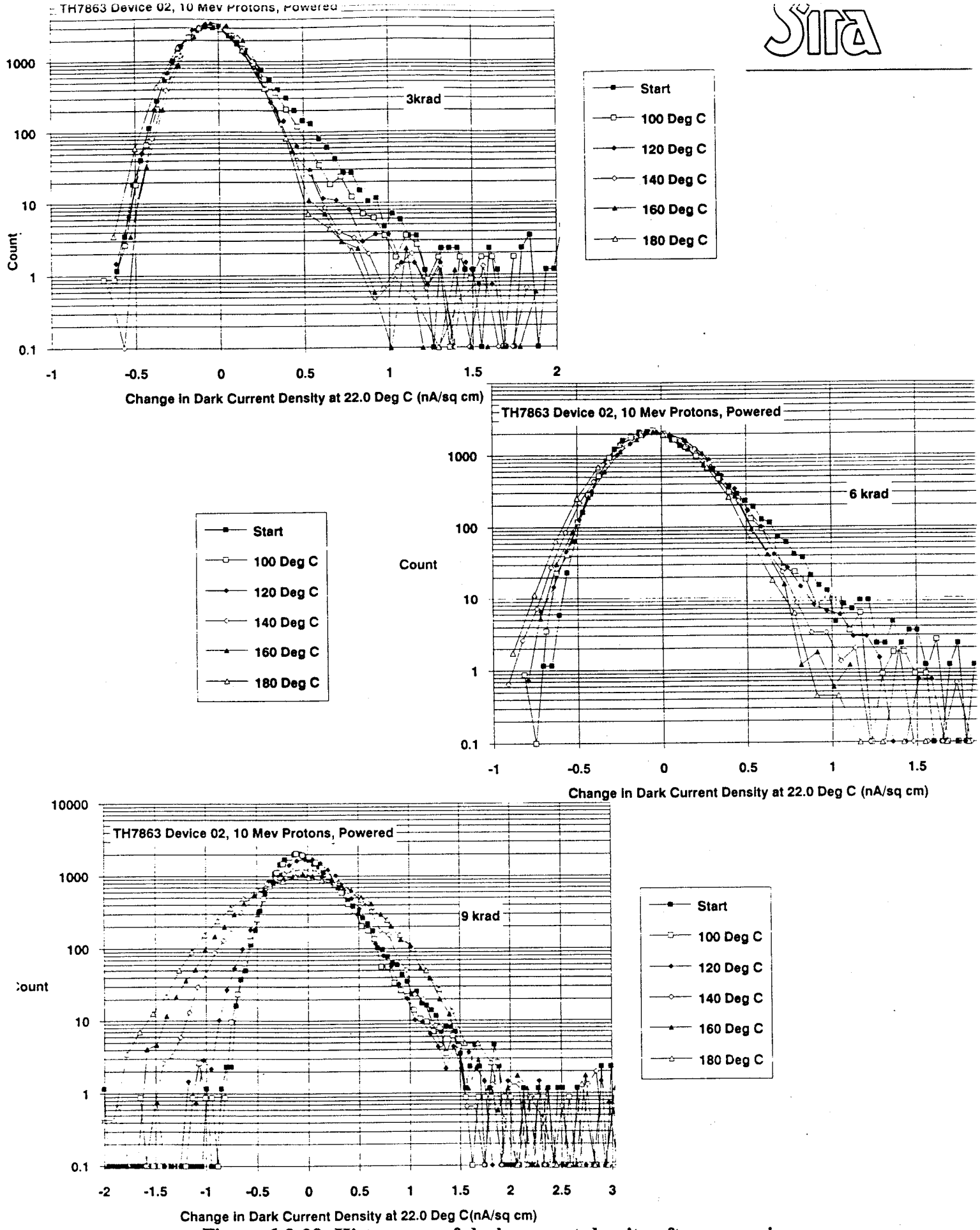

Figure 6.3-28 Histograms of dark current density after successive 2 hour annealing steps at 100, 120, 140, 160 and 180°C

A/9058/00

6.3.2.3 RMS Values

The standard deviations of the 3 month histograms discussed in para 6.3.2.1 were measured. As would be expected from the temperature behaviour discussed above, the rms values show an exponential dependence on 1/T giving an activation energy of 0.68eV. Figure 6.3-29 shows both linear and logarithmic plots as well as the theoretical line derived from equation 6.3-1 of para 6.3.1.1 (slope equivalent to an activation energy of 0.63eV). All the plots show the same trend as can be seen in the combined plot of figure 6.3-30. RMS vales for each dose region (3, 6 and 9krad) averaged over all four devices are shown in figure 6.3-31 from which figure 6.3-32 was derived. This gives average variance values for all devices and temperatures as a function of dose. The conclusion, as predicted in para 3.3, is that the variance of the dark current is proportional to dose (or to proton fluence).

Note that, although the tails of the displacement-damage histograms discussed in the previous section are easily visible on a logarithmic plot, the number of pixels showing large dark current spikes is relatively small and not easily discernable on a linear graph. Thus their contribution to the increase in rms value is small and at 22°C typical rms values at 3krad are only of the order of 0.16nA/cm^2. On the other hand, with such an asymmetric dark current distribution, it can be argued that the rms value is not a useful parameter since there are significant numbers (ie. hundreds) of pixels showing dark currents of at least 1nA/cm^2 at 22°C.

For completeness we give the ratios of the rms values for powered and unpowered devices and for 10MeV compared with 1.5MeV irradiation:

Dose region (krad)	rms value for biased devices / rms value for unbiased devices, averaged over all temperatures: 10MeV	1.5MeV
3	1.01	0.89
6	1.11	0.92
9	1.05	0.99
average	1.06	0.94

Dose region (krad)	rms value at 10MeV / rms value at 1.5MeV, averaged over all temperatures: Unpowered	Powered
3	1.34	1.17
6	1.34	1.11
9	1.26	1.18
average	1.31	1.15

There is an indication here that the bias state of the device during irradiation has a small effect.

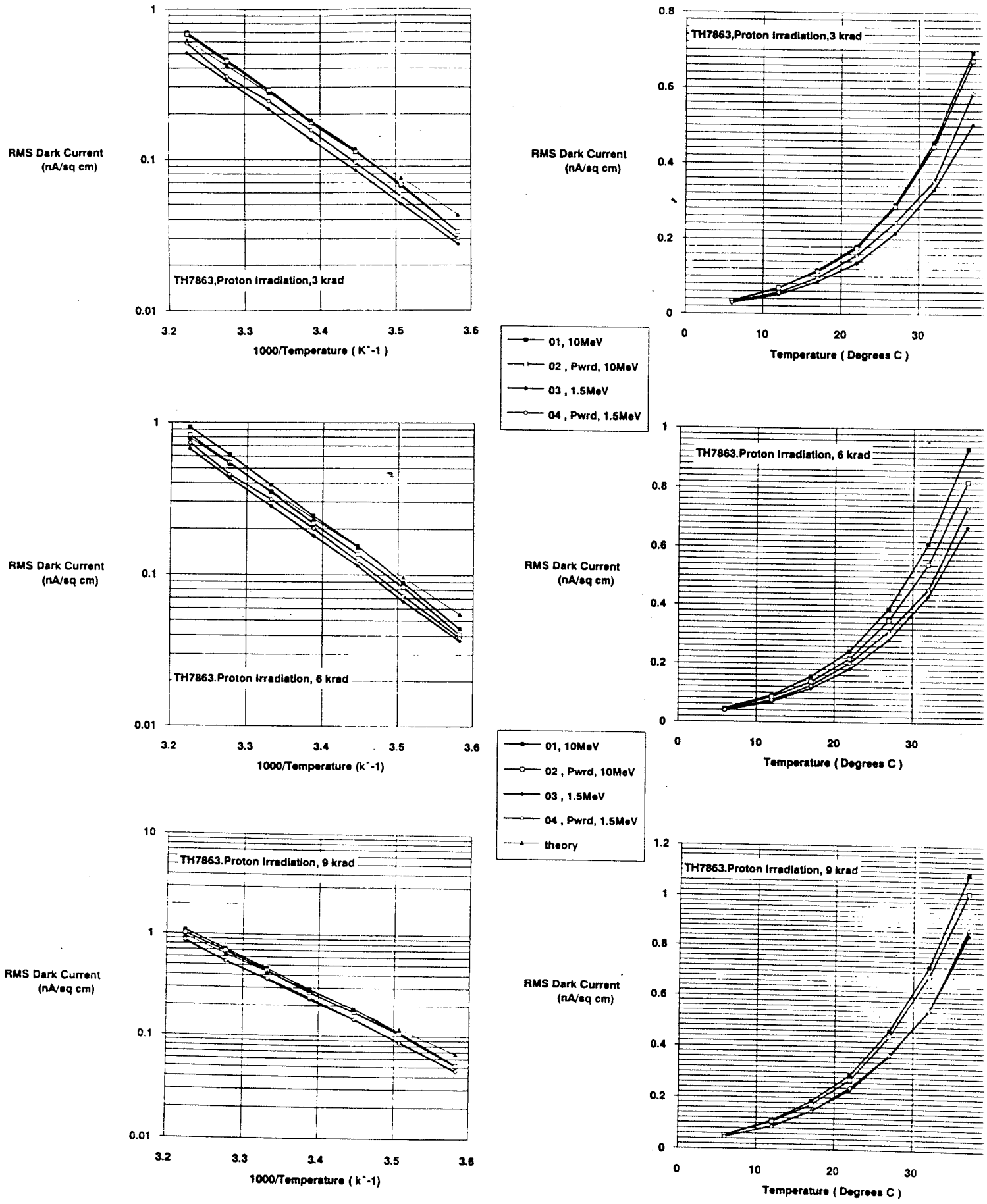

Figure 6.3-29 Plots of rms dark current for various temperatures

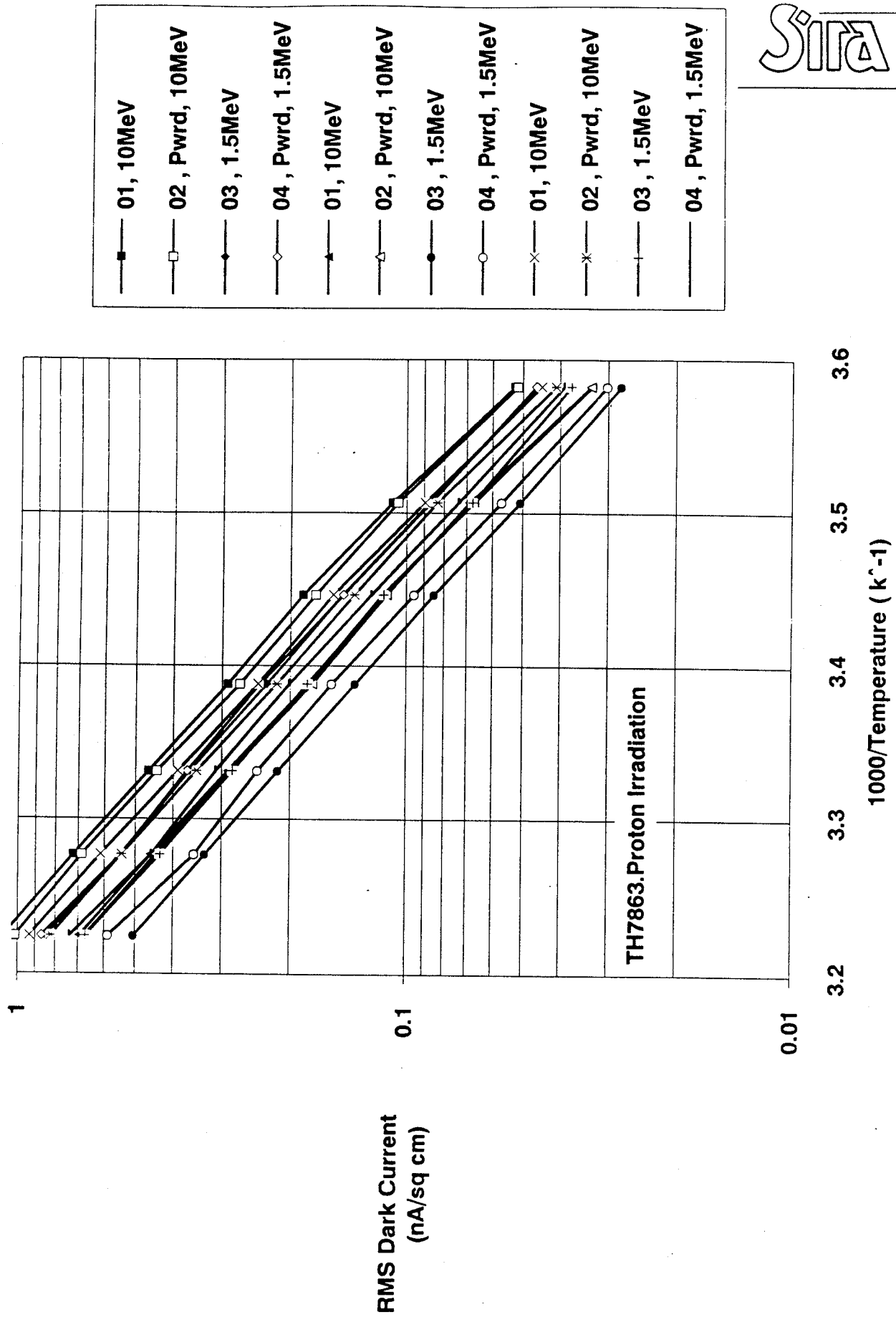

Figure 6.3-30 Combined plot of rms values

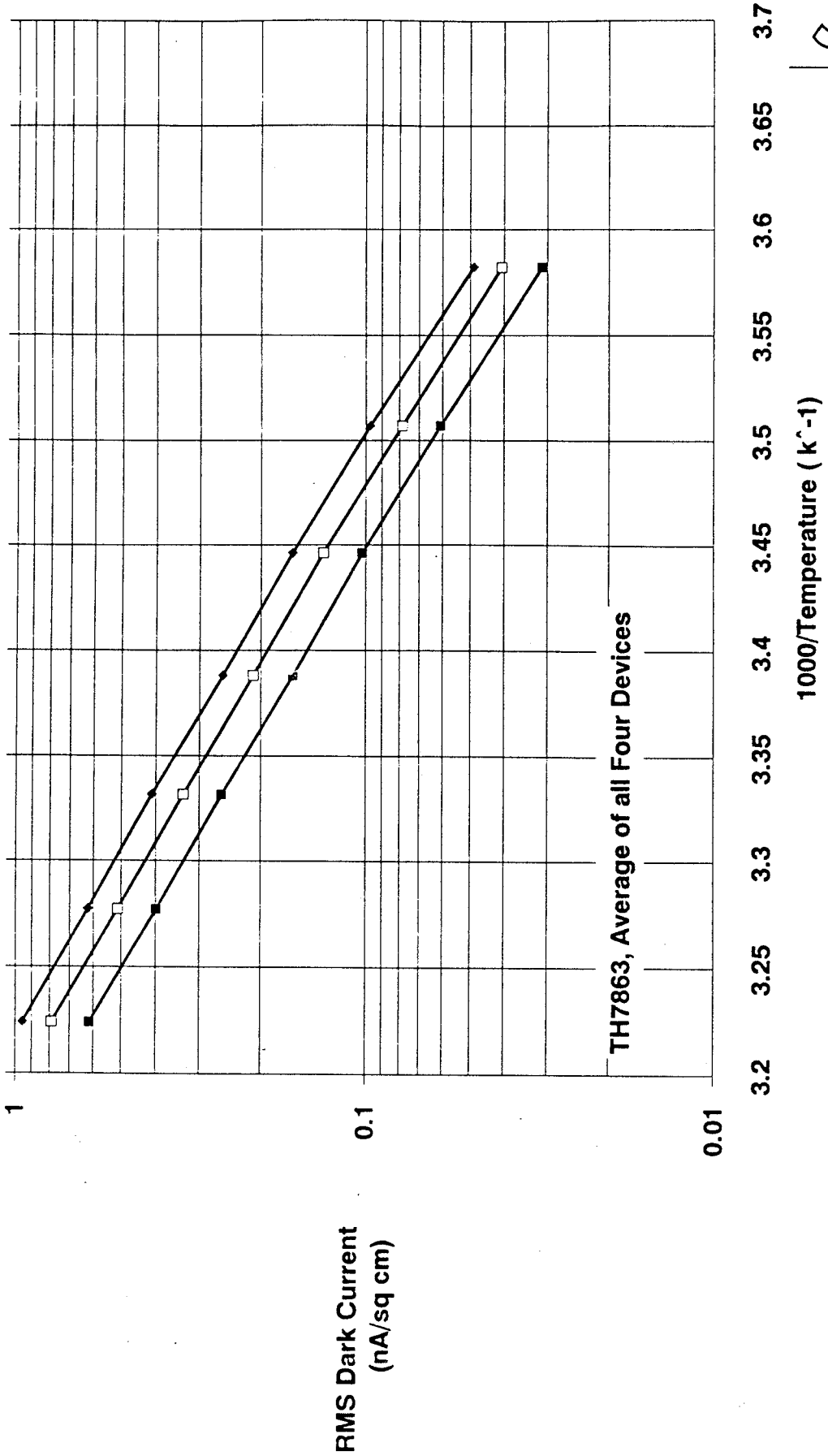

Figure 6.3-31 rms values averaged over all four devices

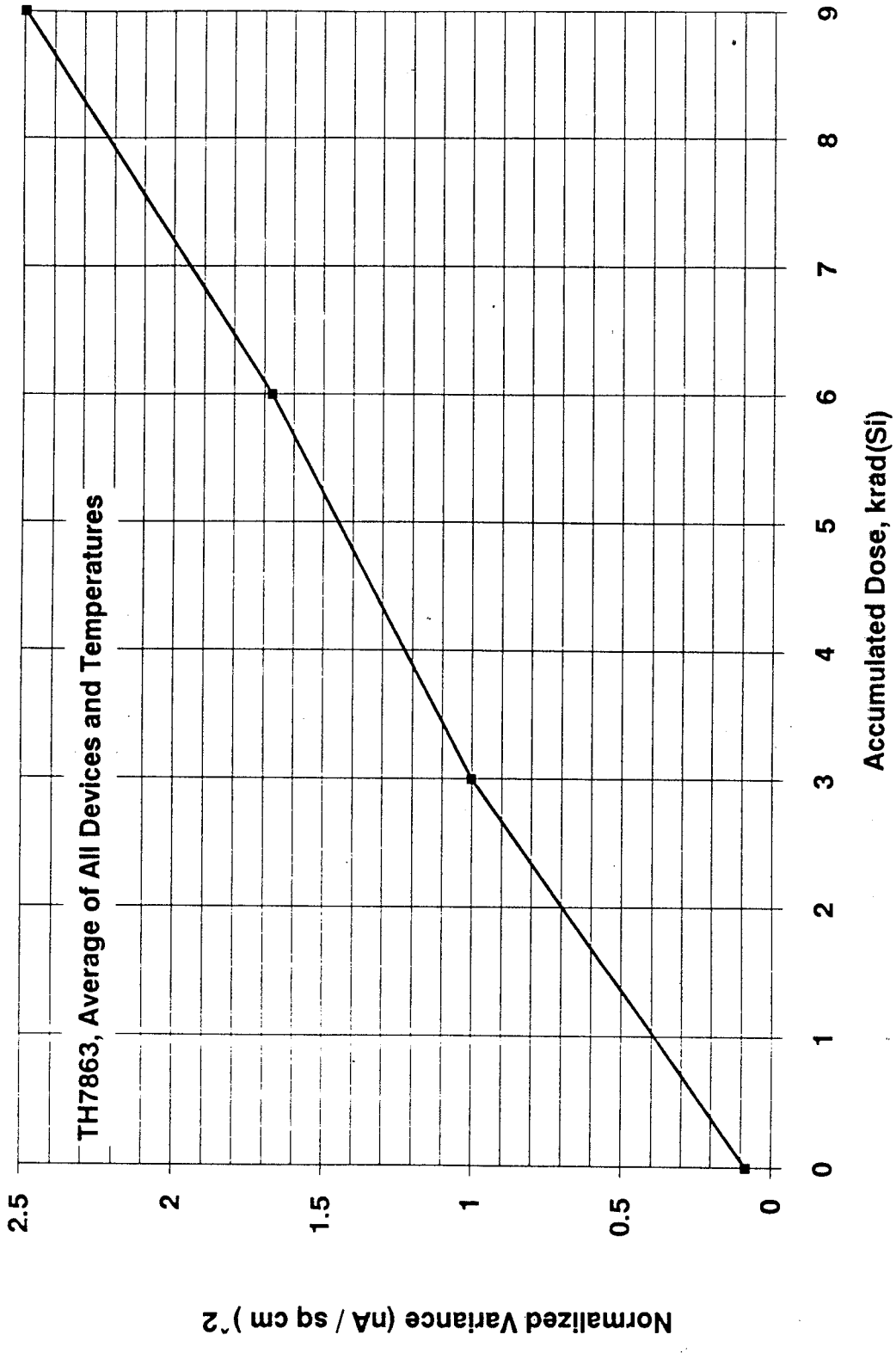

Figure 6.3-32 Variance (normalised to the value at 3krad) versus dose : average over all measurements

6.3.2.4 Anomalous dark charge spikes

In para 3.3 it was stated that several workers have found radiation-induced dark charge spikes which are anomalously large and whose existence is attributed to field enhanced emission (c.f references [30], [34] and [35]). Large dark current spikes can also be seen in the histograms of para 6.3.2.1. Following the work of Marshall et al [35] these have been examined further using the methods of extreme value statistics. According to those authors, it is possible to tell whether all the dark current values arise from a single mechanism or whether the extreme values are larger than can be explained by statistical fluctuations and arise instead from another mechanism (with a different size distribution). They suggest the following 'recipe':

i) divide the dark image into bins of ~10x10 pixels, there being n bins in all
ii) for each bin find the largest pixel value
iii) rank these values in order of magnitude (rank 1 is the smallest and n the largest)
iv) assign a probability P=rank/(n+1) to each extreme value
v) plot extreme value against a parameter termed the reduced variate, given by

reduced variate = -ln[-(lnP)]

The plot should be a straight line if all the extreme values follow a type I Gumbel distribution. This will be so for any probability distribution which has an exponential tail (ie. linear on a logarithmic plot) as is the case for the histograms of para 6.3.2.1 and for theoretical functions such as the Lorentzian, normal, lognormal and gamma distributions.

The usefulness of extreme value statistics is in the capability to predict the largest values that are likely to occur in a given situation and in clearly identifying those values which arise from different mechanisms.

Figures 6.3-33 and 6.3-34 show extreme value plots for the four irradiated CCDs at 6°C and 22°C. It can be seen that for most dose regions there are several anomalously large values with signals up to ~4nA/cm^2 at 22°C. These we expect to be due to mechanisms such as field-enhanced emission and to show departures from the usual behaviour with temperature. We note that whereas, in general, the dark current tail tends to disappear after a high temperature anneal (figure 6.3-28) the anomalous pixels tended to show first an increase and then a decrease as seen in figure 6.3-35 which shows plots during annealing for device 02 (the only one given a high temperature isochronal bake). The reason for this is unknown. Figure 6.3-36 shows plots before and after annealing (including the final 18 hours at 180°C). The anomalous pixels are not diminished significantly by the anneal. As noted in para 3.3 we expect that these large spikes are not due to inelastic collisions (which are rare) but to elastic collisions (which are common) that happen to occur in a high field region of the CCD. Thus their behaviour with annealing temperature might be expected to be closer to that of the main (gaussian) peak - though as stated above the annealing behaviour of that is confused by the presence of ionisation-induced nonuniformity.

Many of the anomalous pixels are associated into groups of adjacent pixels. This is clearly seen in figure 6.3-37 for device 02. In this particular image the largest spikes are enhanced because of the high temperature anneal. The grouping of defect pixels is consistent with the field enhancement hypothesis since high-field regions are most likely to occur at pixel boundaries where spreading of charge to adjacent pixels by diffusion is also likely. There is also a preference for 'hot' pixels to be grouped in the horizontal direction - ie. each side of a channel stop.

We now consider the variation in the size of the larger dark current spikes in more detail. The brightest pixels for devices 01 and 02 (10MeV protons) were studied for temporal variations. Figure 6.3-38 shows plots of spike magnitudes immediately after irradiation compared with three months later for the region receiving 3krad (5.37 E9 p/cm^2). It is seen that many of the spikes have decreased in size but the behaviour is erratic with some showing a significant increase.

The effect of CCD temperature variation was studied for device 01 (for the 3krad region) and devices 02 and 03 (for the 3, 6 and 9krad regions). These measurements were made after 3 months storage and from the same images that were used to determine the average levels and histograms discussed in previous sections. The brightest spike positions are as shown in figure 6.3-39 and they are random over the CCD. The changes in spike size with 1000/T are shown in figures 6.3-40 to 6.3-42. It is seen that in some cases the variation is erratic but overall there is a straight line trend. For each defect a least squares line was fitted to the data to determine activation energies which are shown in figure 6.3-43. There is a considerable scatter to these plots but most spikes have an activation energy ~0.7eV as expected (c.f. para 6.3.1.1). Some defects have activation energies as low as 0.4eV suggesting field-enhanced emission, but there is no evidence for a systematic trend for activation energy to decrease with increasing spike size as was found by Srour and Hartmann [30] for a virtual phase CCD. In that case field enhancement effects were large because of the particular construction of the CCD.

In summary, we note that the largest dark current spikes show erratic behaviour with annealing time and with CCD operating temperature. With fluences of the order of 10^{10} particles/cm^2 it can be expected that there will be roughly 10 to 30 spikes of size 2nA/cm^2 or more at 22°C for a TH7863 device.

It was also noticed that devices 01 and 02 showed dark field image blemishes extending over large numbers of pixels. Figures 6.3-44 and 6.3-45 show, respectively, a large bright patch on device 01 and a dark 'streak' on device 02. The latter was much more pronounced after high temperature annealing and only shows up on dark images (ie. has no effect on sensitivity to light).

Both image blemishes are thought to be due to nonuniformities in ionisation damage-induced dark current. In neither case was there any visibly apparent defect on the CCD surface.

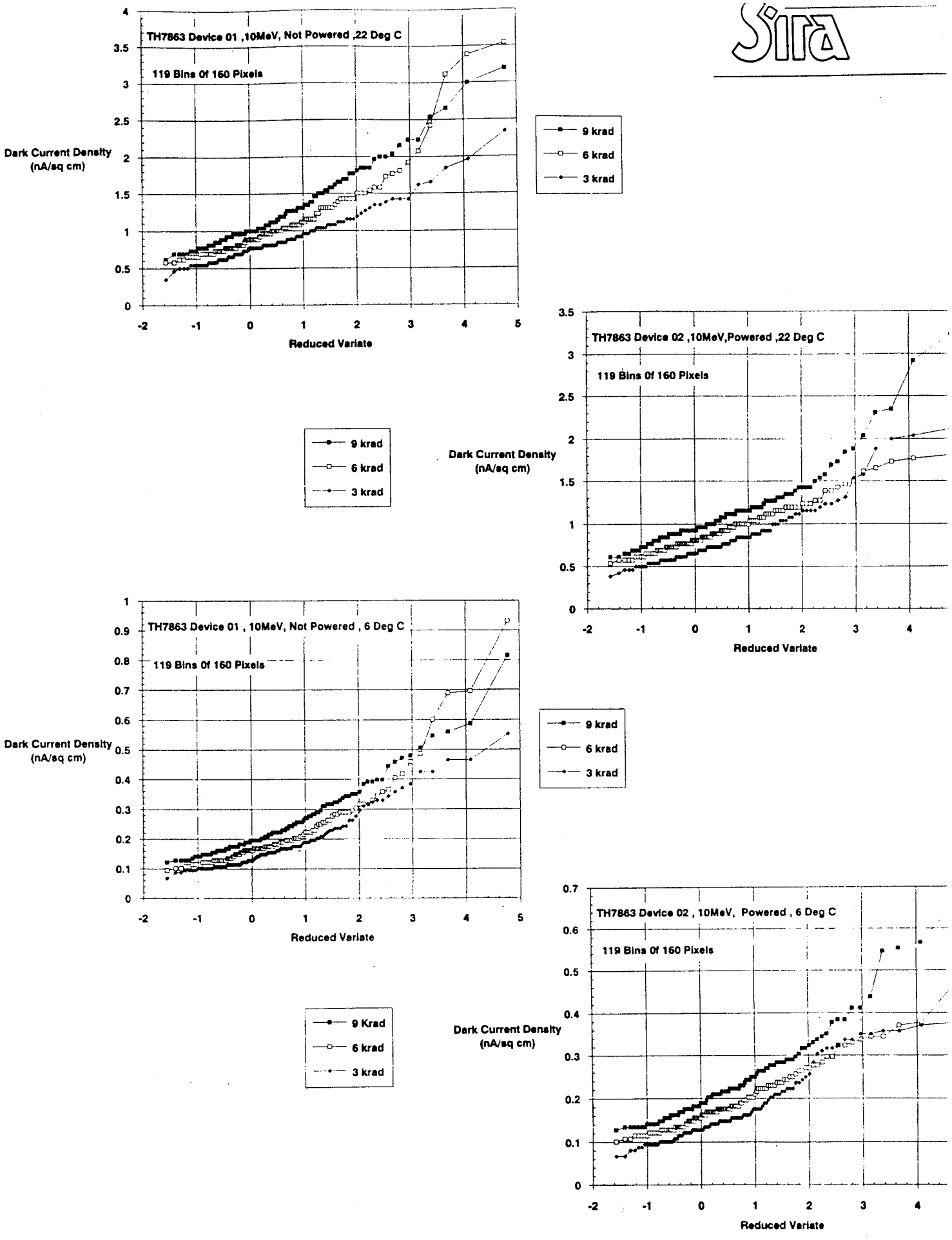

Figure 6.3-33 Extreme value statistics plots for devices 01 and 02 (10MeV) after 3 months

A/9058/00

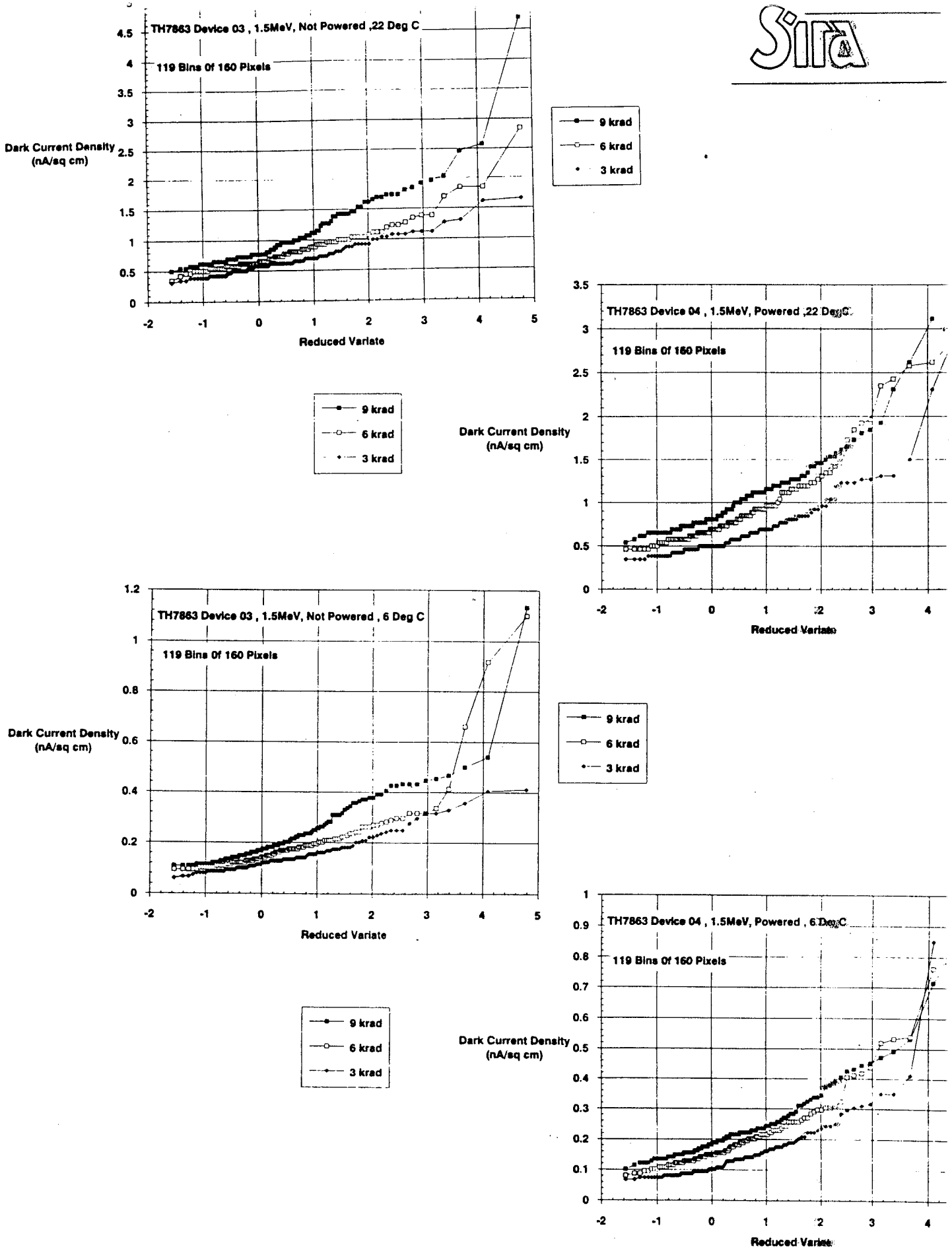

Figure 6.3-34 Extreme value statistics plots for devices 03 and 04 (1.5MeV) after 3 months

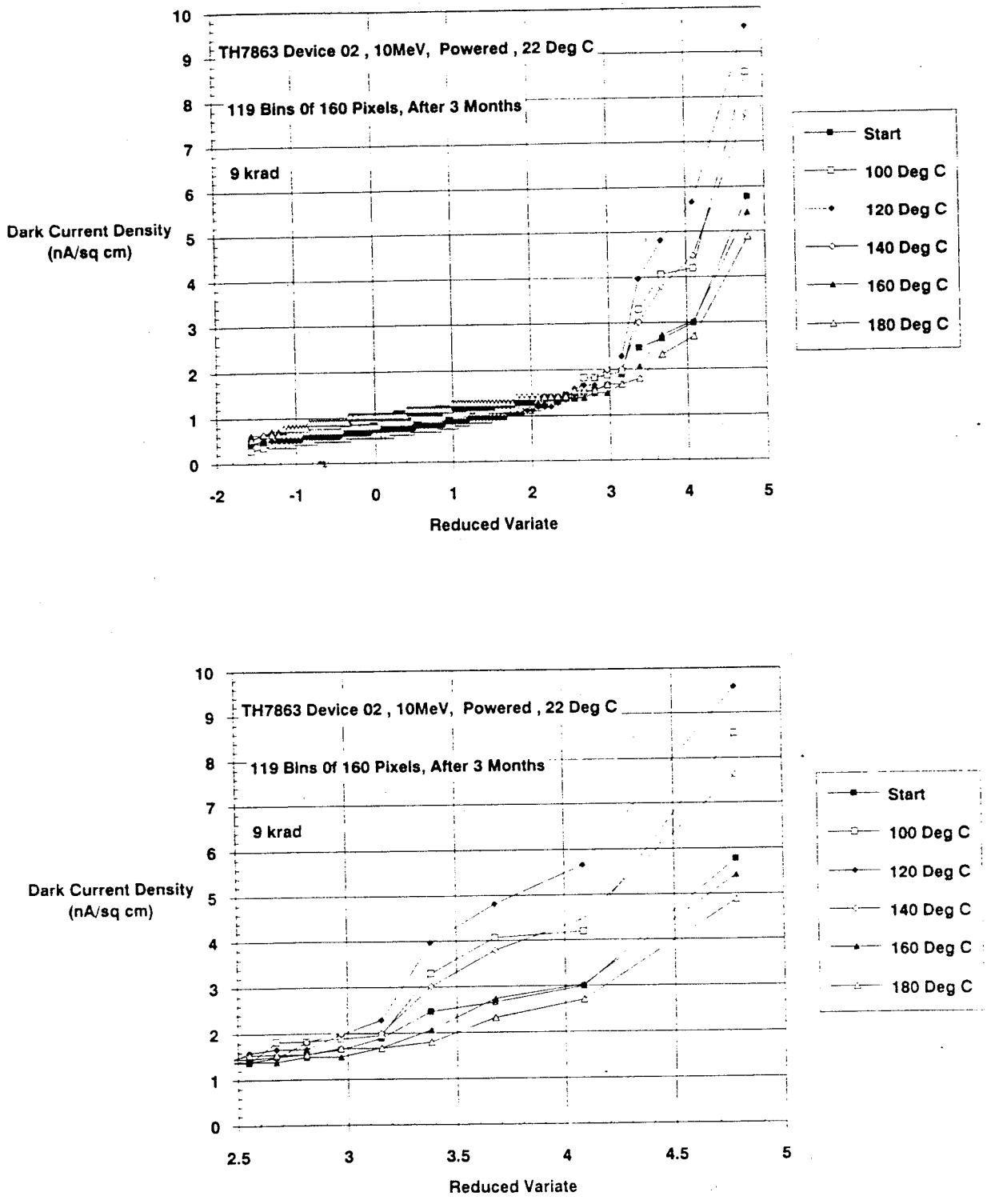

Figure 6.3-35 Extreme value statistics plot for device 02 before and during high temperature annealing (9krad region)

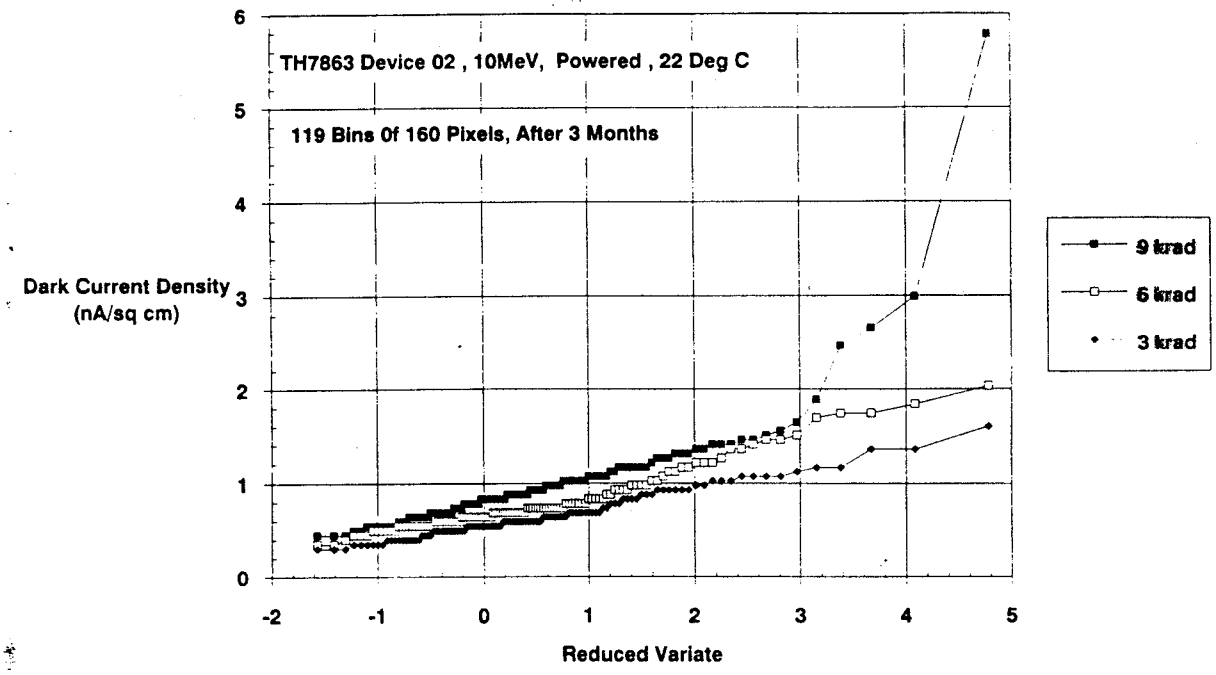

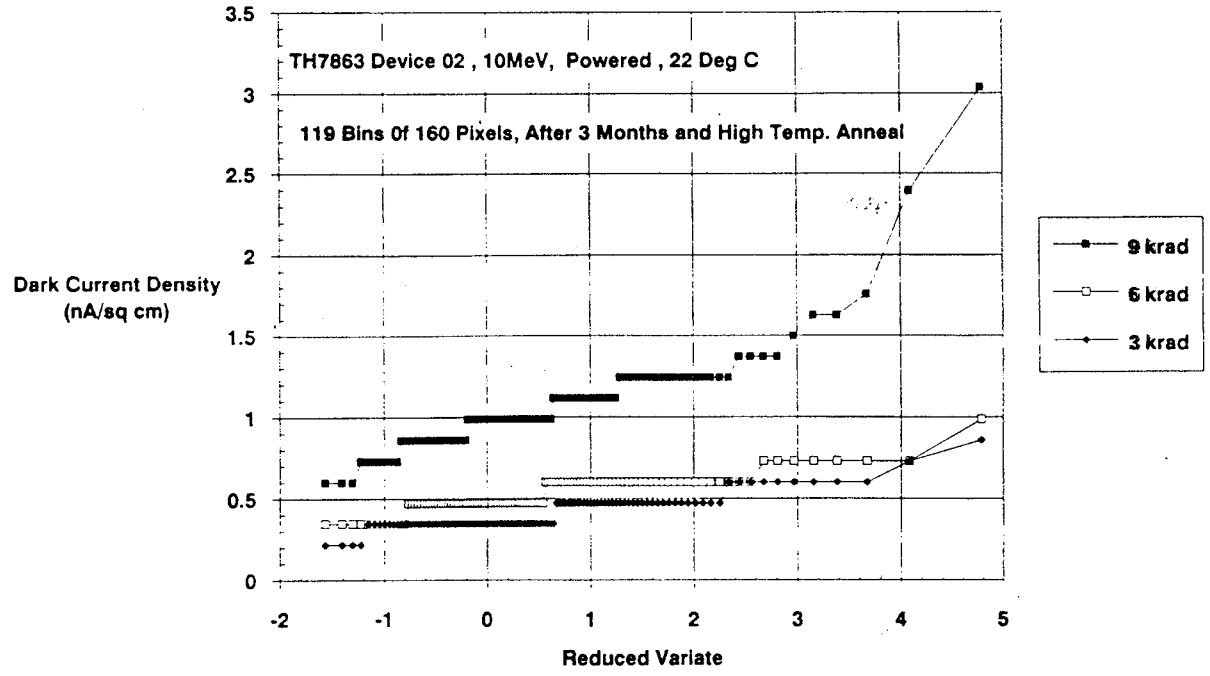

Figure 6.3-36 Extreme value statistics plot for device 02 before and after high temperature annealing (including final 18 hours at 180°C)

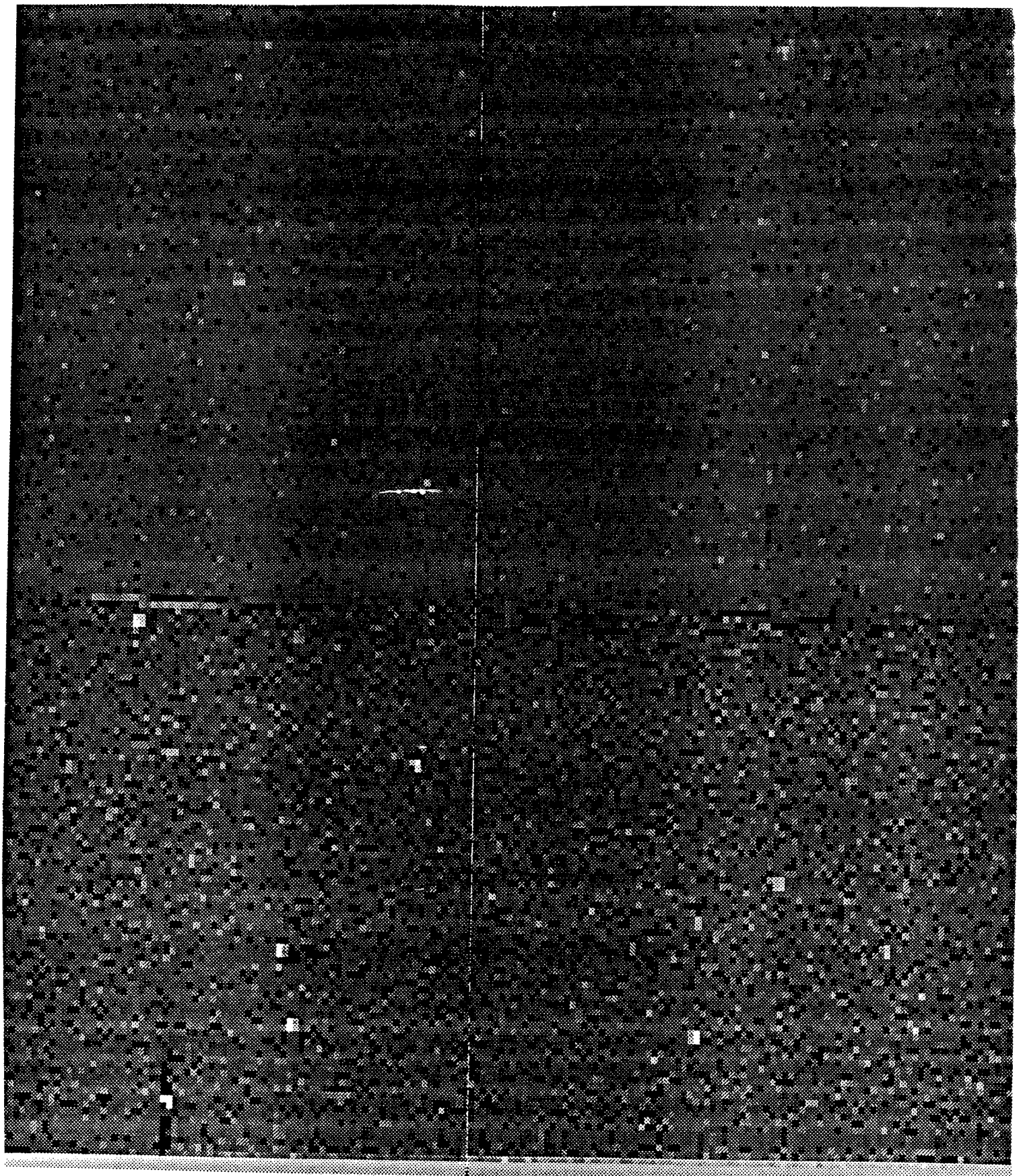

Figure 6.3-37 Part of a dark image for device 02 during high temperature annealing (after the bake at 120°C) showing clustering of defects

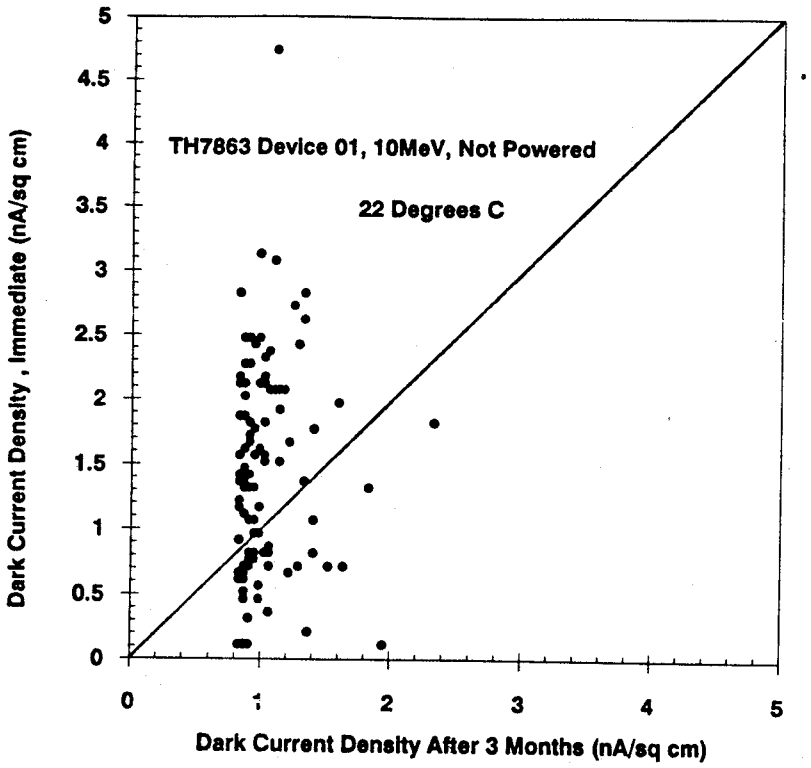

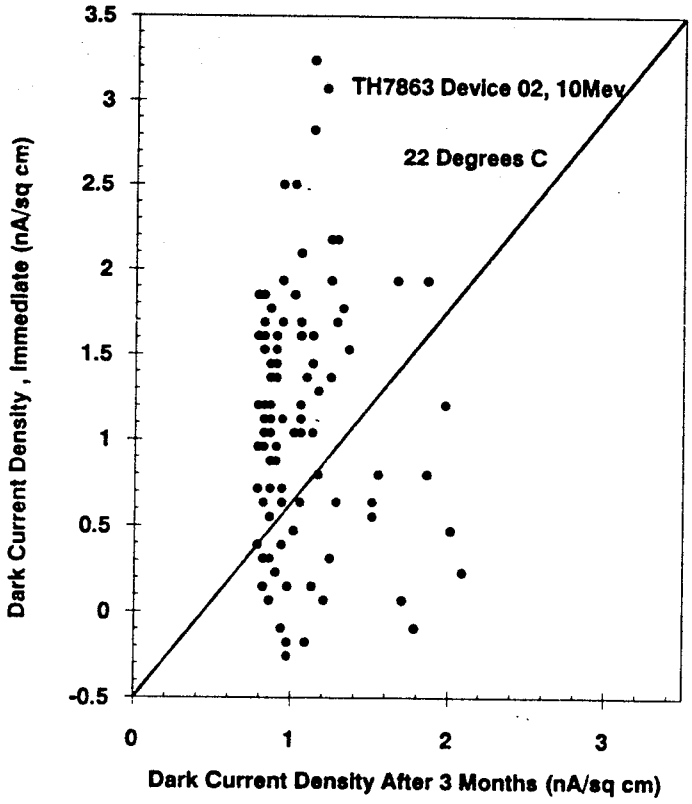

Figure 6.3-38 Sizes of dark current spikes for devices 01 and 02 (10MeV protons) immediately and 3 months after irradiation (3krad region)

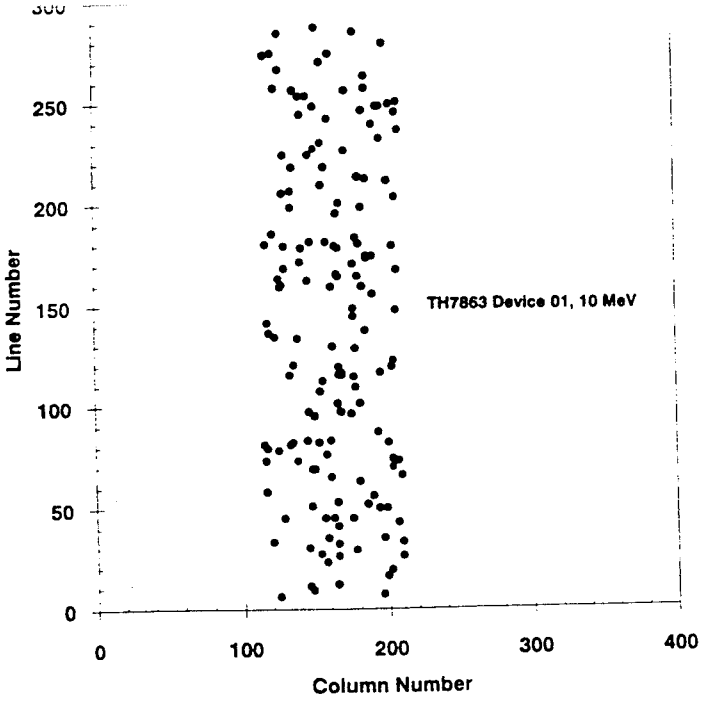

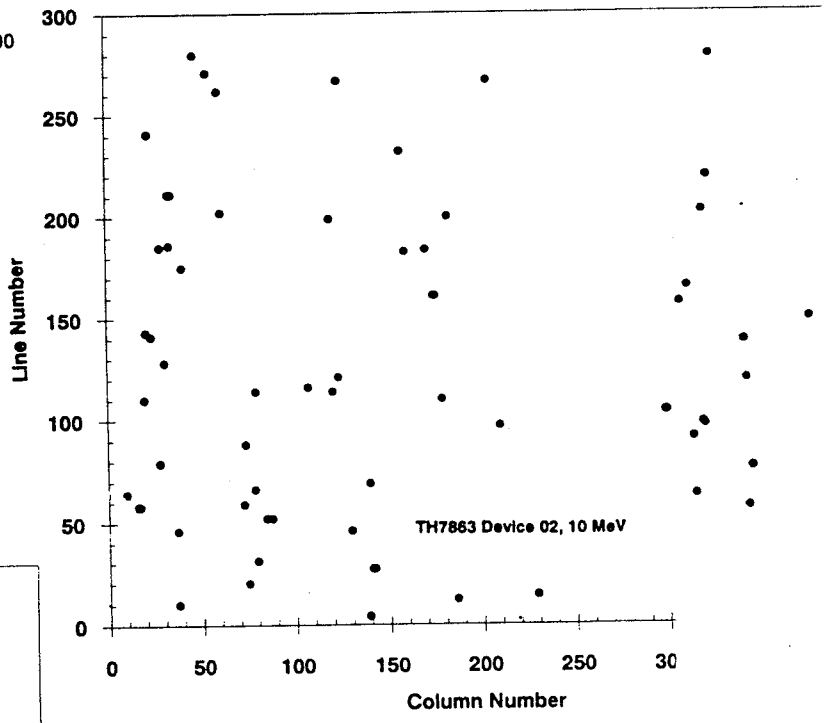

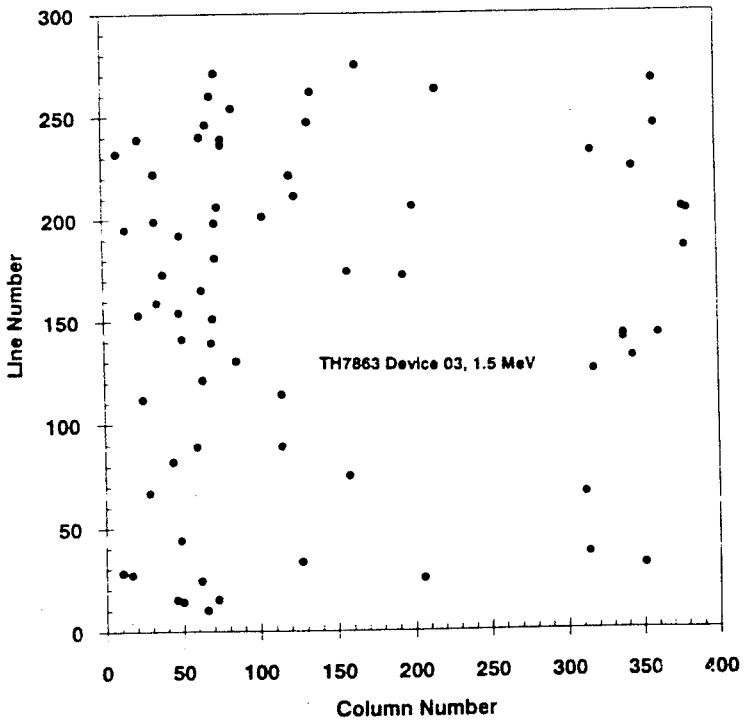

Figure 6.3-39 Maps of spike positions for CCD01 (3krad region), 02, 03 (3, 6 and 9krad regions)

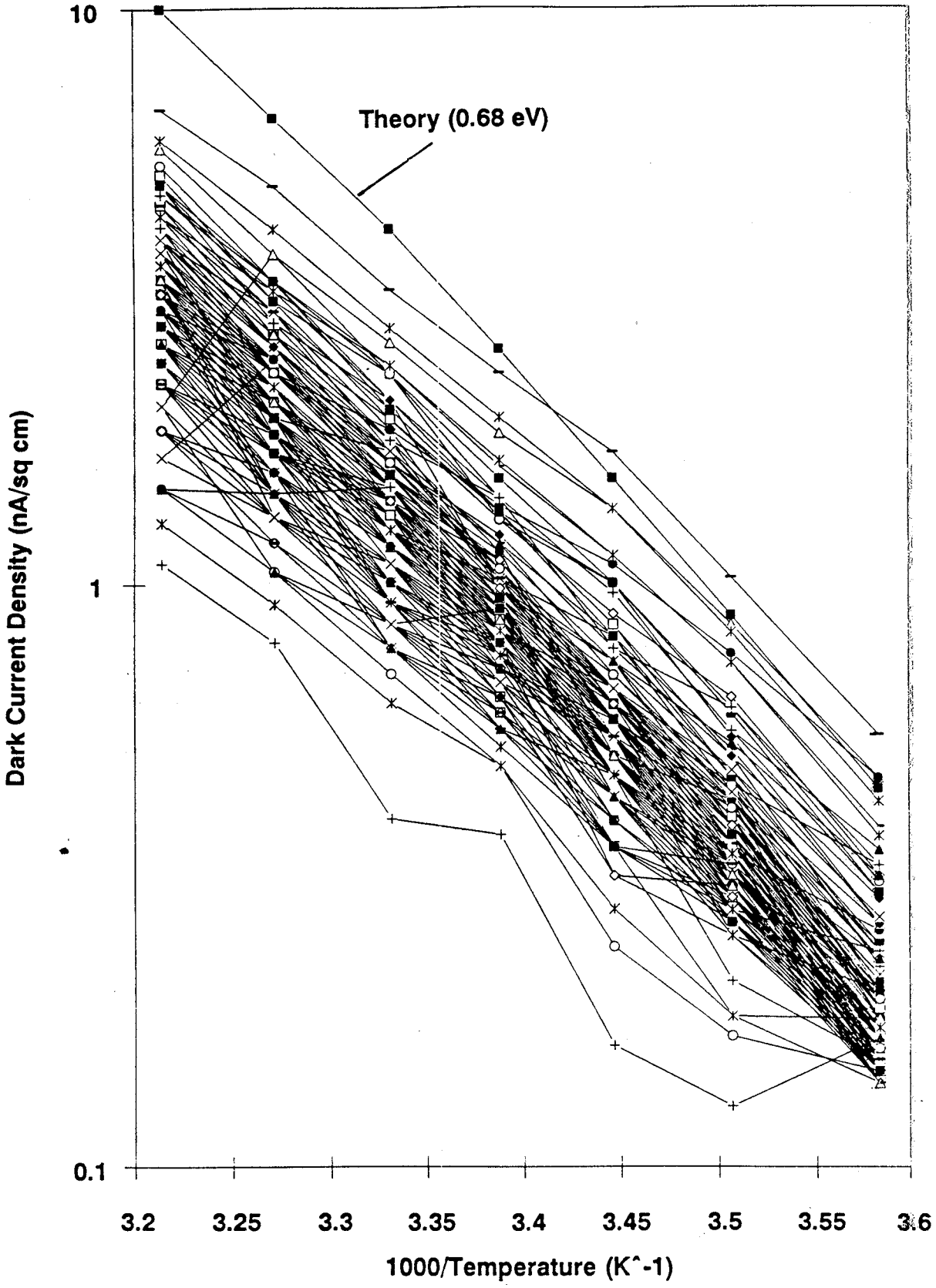

Figure 6.3-40 Variation in dark current spike size with temperature (device 01, 3krad region)

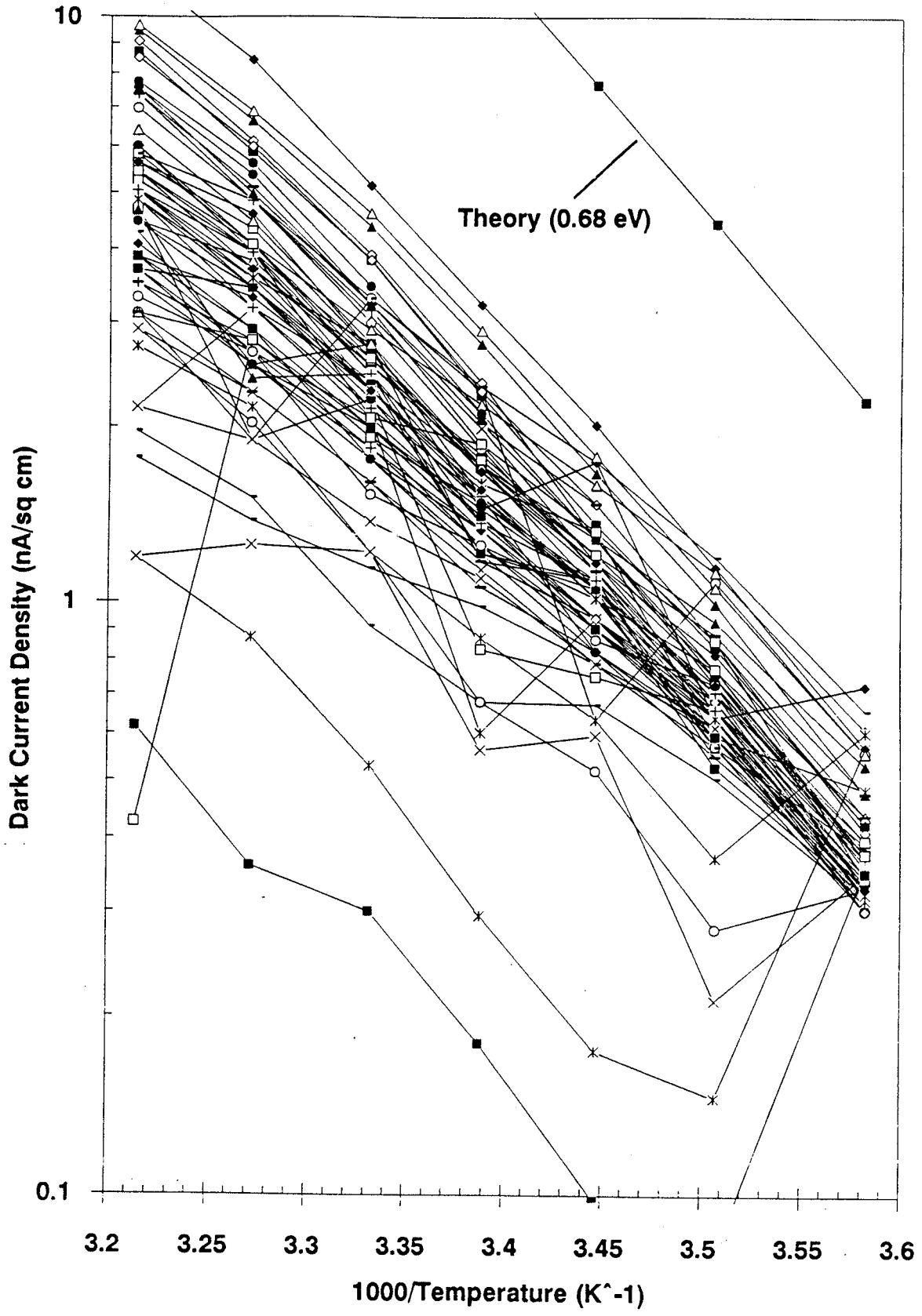

Figure 6.3-41 Variation in dark current spike size with temperature (device 02, 3, 6 and 9krad regions)

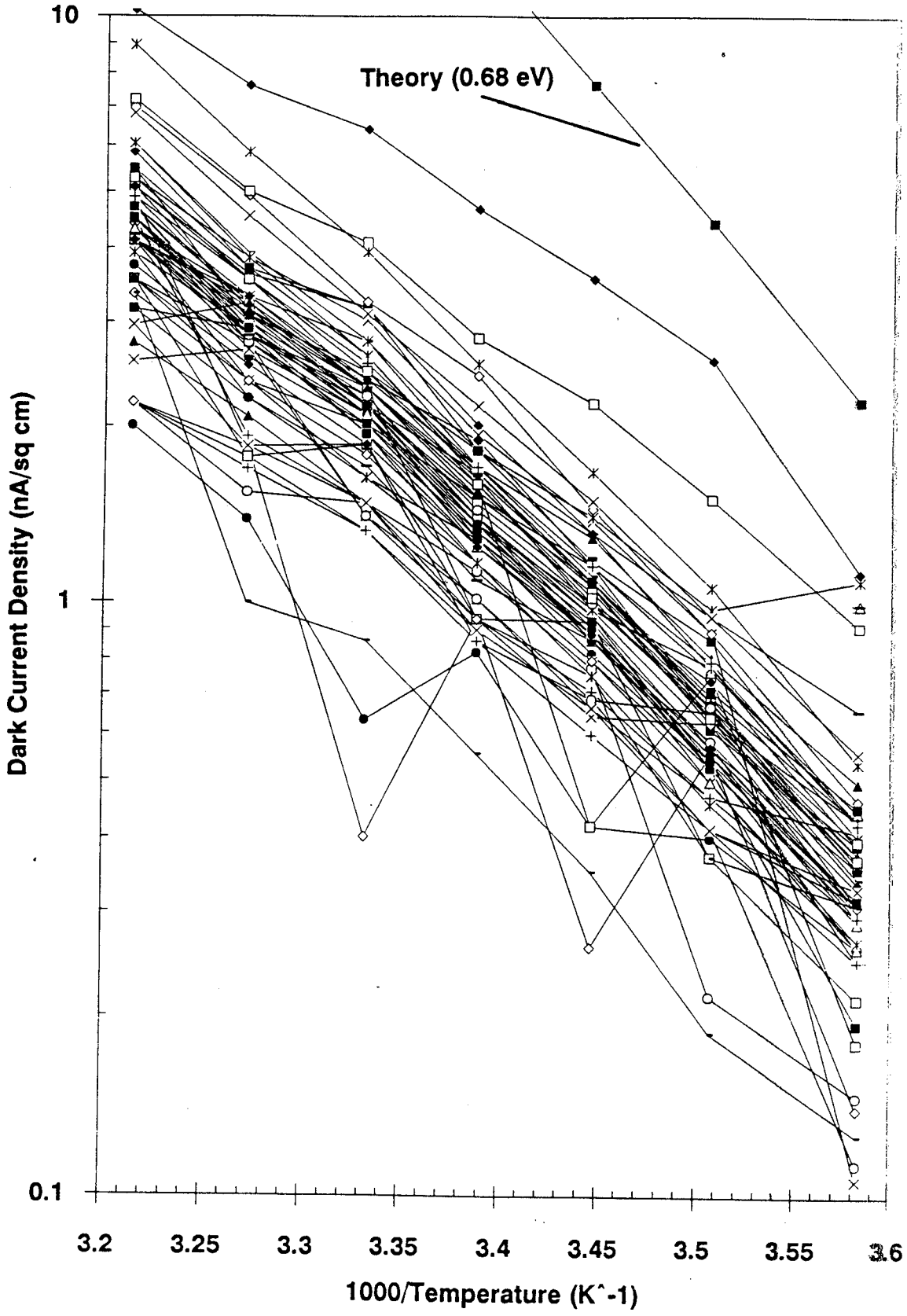

Figure 6.3-42 Variation in dark current spike size with temperature (device 03, 3, 6 and 9krad regions)

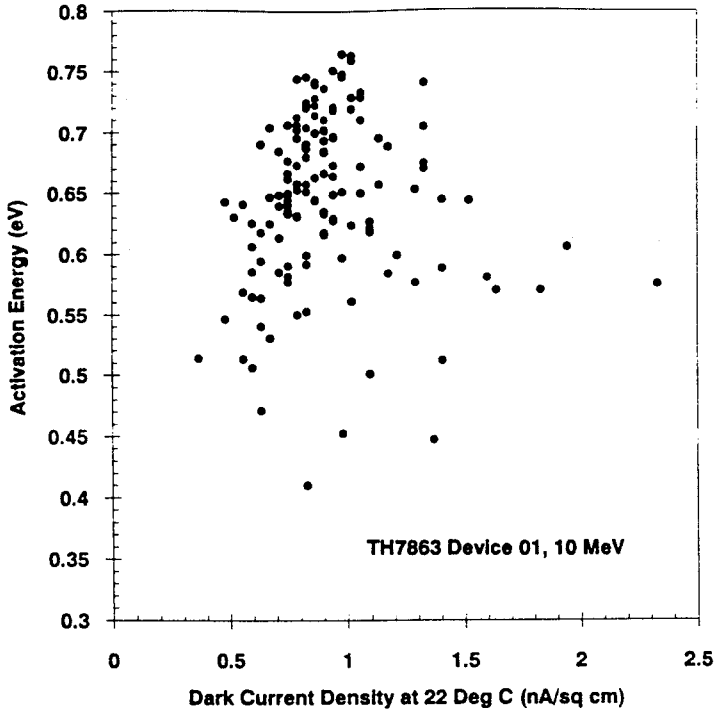

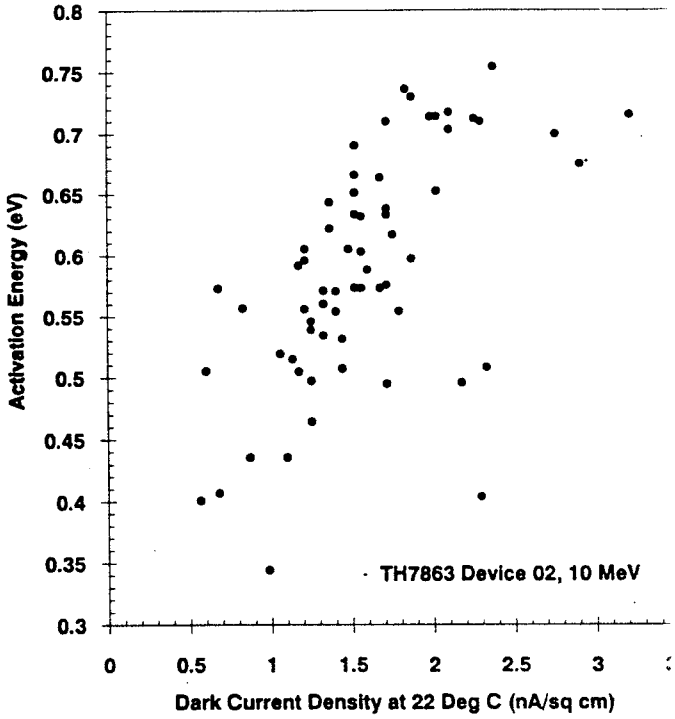

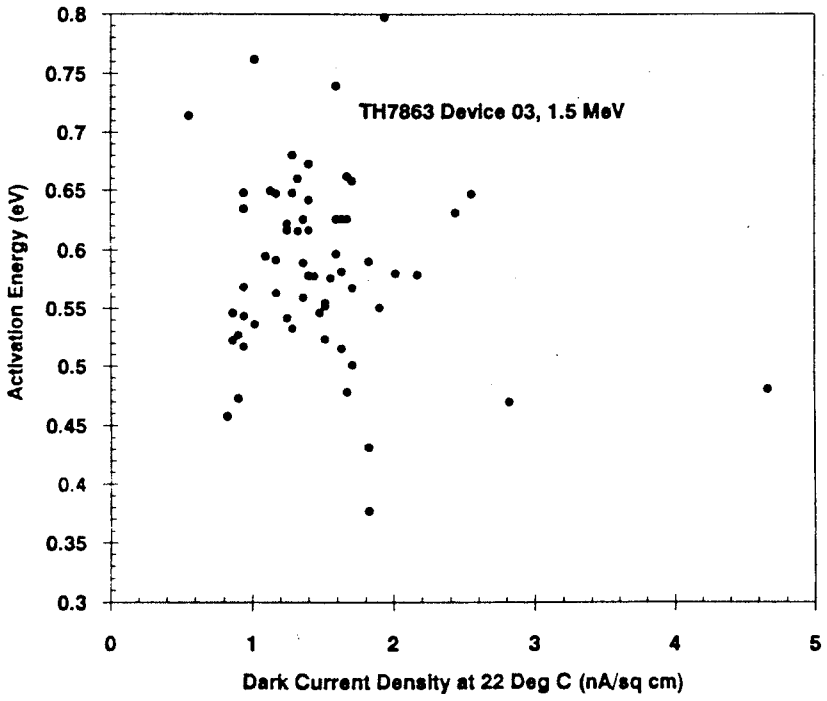

Figure 6.3-43 Dark charge spike activation energies (determined after 3 months for devices 01, 02 and 03)

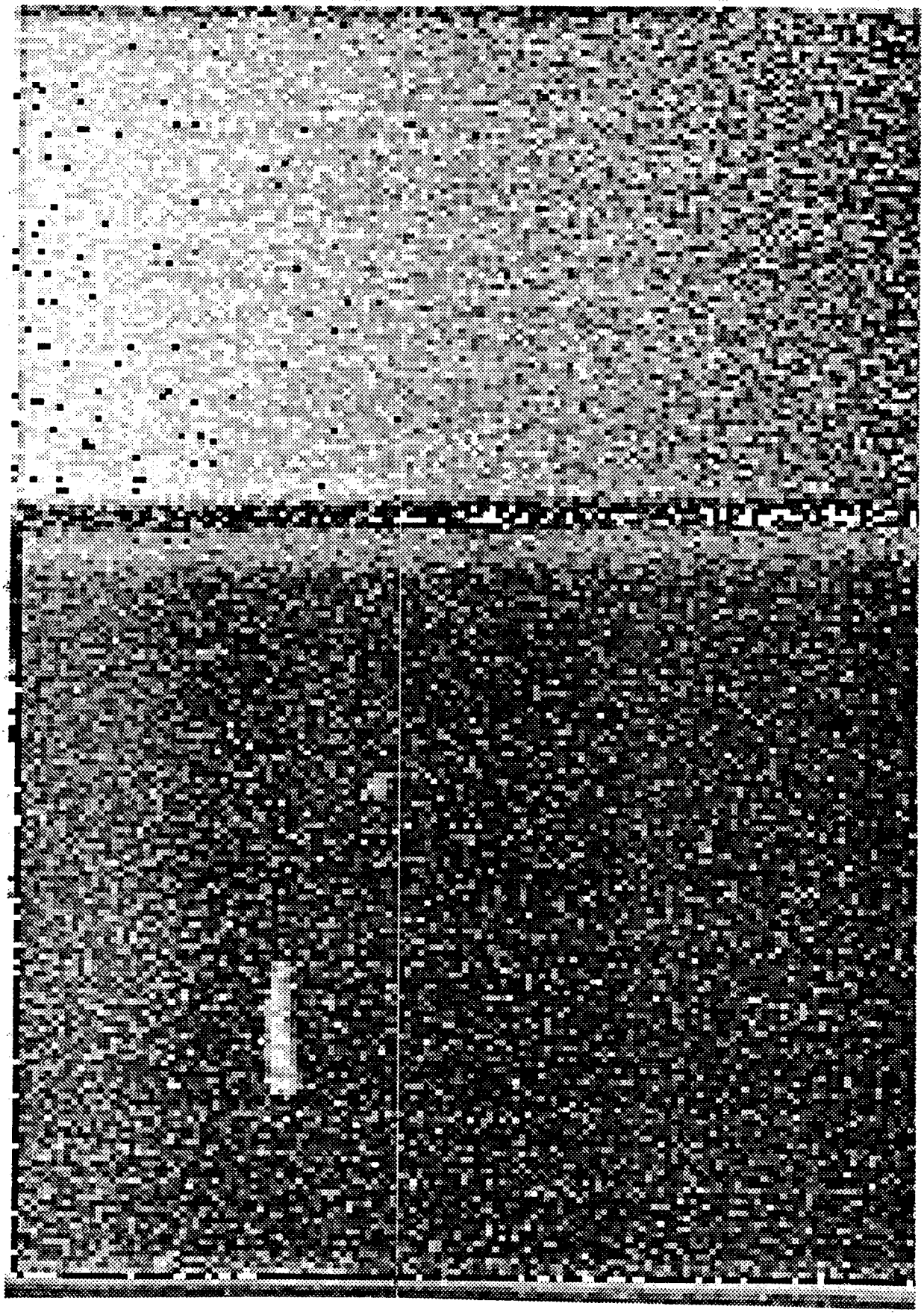

Figure 6.3-44 Large bright patch on a dark field image for device 01

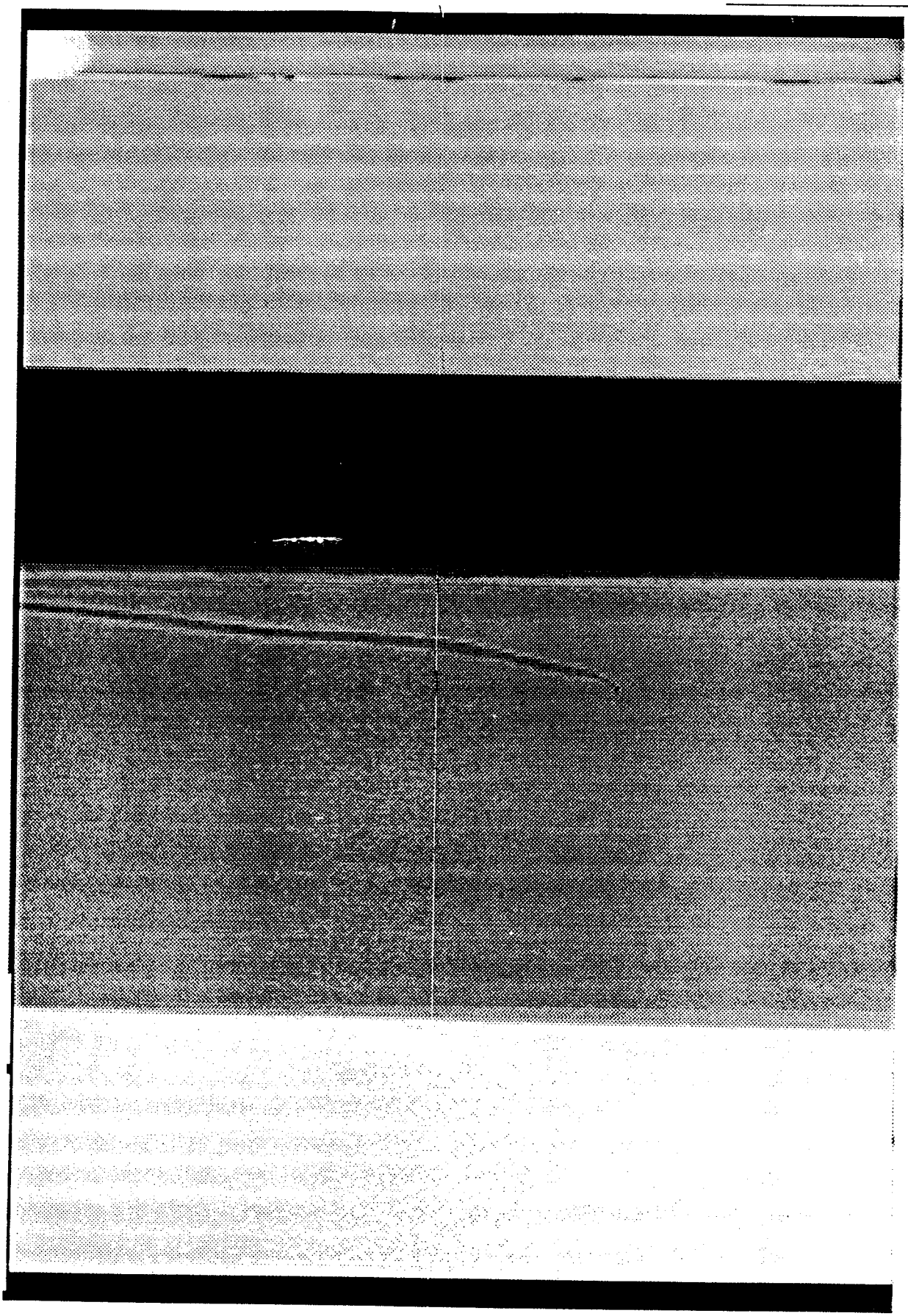

Figure 6.3-45 Dark 'streak' on a dark field image for device 02

6.4 Bright Field Measurements

The operation without windows on the chip packages inevitably meant that there was particulate contamination of the surface of the CCDs. Accordingly no serious attempt was made to measure dark-spot image blemishes (since in most cases these would have been due to the contamination). In any case, as discussed in the Co^{60} report [1], no change in bright field response with radiation was expected.

6.5 Readout Noise

This was measured for zero signal pixels in the over clocked porch region of the CCD waveform (c.f. para 4.4 of [1]). These values therefore represent the noise from the on-chip amplifier and the external electronics system. The noise for valid CCD pixels will be the root sum square of this noise and the shot noise on both the signal and the dark charge.

A correlated double sample (CDS) amplifier was used. This was of the clamp and sample type. Previous versions of this amplifier used by Sira have achieved noise levels of ~40 electrons rms with the TH7863 device at the present readout rates (pixel rate = 3MHz). However in this case the camera head was of general purpose design which gave a readout noise of roughly 100 electrons rms, unchanged by radiation. This is considerably below the required noise level for SILEX.

6.6 Threshold Voltages

6.6.1 V_{DR} Threshold Voltage

As in the previous Co^{60} investigation [1], the V_{DR} voltage supply to the reset transistor was decreased until there was a noticeable change in the appearance of bright field images. This method was found to give a consistent measure of the V_{DR} threshold voltage to an accuracy of ~0.1V. An investigation of more quantitative methods is to be carried out in future but is outside the scope of the present report.

The results were as follows:

Table 6.6-1 V_{DR} Threshold Voltages (V)

Device	Pre-irradiation	Post-irradiation		
		Immediate		5 months
		3krad	9krad	9krad
01	12.0	11.9	-	11.8
02	12.1	12.0	-	12.3
03	11.35	-	11.8	11.9
04	11.75	-	12.2	12.2

Thus the increases are comparable with the experimental accuracy. There is a suggestion however that, on average, there is an increase of ~0.3V after 9krad. A small increase is expected because of the decreased yield of electron-hole pairs in the oxide occasioned by low energy proton rather than high energy or Co^{60} radiation (c.f. para 3.2). The results of reference [1] remain the baseline database for changes in V_{DR} voltage.

6.6.2 Reset Clock Threshold Voltage

The height of the reset clock pulse was reduced from its nominal value of 10.0V until the image quality was affected. In all measurements taken before and after irradiation the voltage could be reduced to the limit provided by the test equipment (-5V) without any change. However the above comments on the use of low energy protons apply.

6.6.3 V_{OS} DC Output Voltage

In the Co^{60} study [1] it was found that throughout all irradiations the smoothed value of the DC output voltage from the CCDs remained in the range 9.3 $\pm$0.2V for all the devices studied, indicating that this parameter is not sensitive to radiation damage and varies little from device to device. Accordingly V_{OS} DC was not measured during these tests.

6.7 Power Consumption

Measurements of the I_{DD} drain current to the output amplifier were made using a DMM. The CCDs were in the dark and operating at room temperature with the standard clocking sequence (frame time = 41ms). The results were as follows:

Device	Pre-irradiation	I_{DD} (mA) Post-irradiation		
		Immediate		5 months
		3krad	9krad	9krad
01	-	-	-	8.3
02	-	8.4	-	8.9
03	8.2	-	8.5	8.6
04	-	-	9.0	9.1

Due to the limited time available (especially before and during the irradiations) a complete set of measurements was not made. However it can be seen that the results are broadly consistent with the more detailed measurements of ref [1], given that the yield of electron-hole pairs in the oxide (and hence the damage) is reduced for low energy protons.

6.8 Charge Transfer Efficiency

The discussion of para 3.3.3.2 indicated that from JPL measurements at -50°C [17] we might expect that for a fluence of 5×10^9 10 MeV p/cm^2 the charge transfer inefficiency would be given by

$$\text{CTI} \sim \frac{4.4}{S} \frac{\text{(electrons)}}{\text{(electrons)}} \quad \text{per pixel at -50°C}$$

where S is the signal size. Therefore for Cd^{109} x-ray radiation (S = 6000 electrons) we would expect a CTI of ~7.3 10^{-4} per pixel, giving an overall value of ~0.36 for ~500 transfers ie. substantial deferred charge and degradation in the appearance of nominally 'single pixel' events. In fact, as discussed in para 6.1, there was no measurable deferred charge with Cd^{109} x-ray illumination - measurement to an accuracy of ~2%. Hence the conversion factor from proton fluence to electrically active traps must, in our case, be

substantially less than Janesick quoted for his test conditions (slow-scan CCD, -50°C). The x-ray results are substantiated by the spot-illumination linearity measurements of para 6.2. In these it was noticed that the appearance of the spot was not measurably degraded even where the 9krad region of the CCDs was illuminated. In addition the dark images themselves show that many of the dark current spikes have signal confined to a single pixel (again measurement accuracy ~2%). The reasons for the improvement in radiation tolerance at fast clocking speeds and room temperature are not fully understood but the change in speed and temperature will imply that a different population of traps (with different trap time constants) will be involved. Also the high dark current for these conditions will help to keep any trapping states full of charge, provided that the CCD wells are 'flat-bottomed' ie. that the fresh traps are not brought into play as the wells fill with charge (note that in our case the horizontal and vertical clock overlap times are ~50ns - very much shorter than used for full frame imaging at low readout rates).

We conclude that for 24Hz operation of TH7863 CCDs at room temperature there was no measurable degradation in CTE (accuracy of spot signal measurement ~2% ie. CTI measured to be less than 0.02 anywhere on the device). Hence no degradation in SILEX performance is expected.

This is not to say that other applications using the TH7863 in a similar way will not be affected. For example a high accuracy star tracker, even if operated with the CCD close to room temperature, is much more sensitive to radiation-induced changes in CTE. This is not because these instruments inherently need good CTE (indeed the tolerances for an as-built instrument, pre-launch, might be similar to those for SILEX). Rather it is because a relaxed pre-launch specification can be tolerated only because spot image profiles can be accurately measured and calibrations performed during ground testing; but since the calibrations cannot usually be changed post-launch, any in-orbit changes in CTE will degrade performance and give bias errors in star positions (especially for faint magnitudes). We note that more detailed measurements of CTE than discussed here would require purpose-built test equipment (for example with signal measurement to better than 12 bits).

6.9 Pocket Pumping and EPER Measurement

These techniques were discussed in para 6.9 of the previous study [1]. The pocket pumping technique allows the location of individual trapping states. In the present case however it was found that, due to the high fluences used (presumably giving high trap densities) and the high dark charge nonuniformity (because of the high temperature), the pocket pumping images were confused and hard to interpret and accordingly were not analysed in detail (especially as there does not appear to be a problem with CTE in this application).

Extended pixel edge response (EPER) measurements (which allow a determination of global CTE) were also hard to interpret: because of the good CTE performance and the high rate of dark charge generation; hence these were not analysed in detail either.

It should be noted that one of the main reasons for using a high particle fluence in these experiments was that, although pocket pumping measurements might be confusing to interpret, x-ray and spot measurement techniques might reveal a degradation in CTE. In fact this was not seen, as discussed above, and this is a good result for SILEX since there can be some confidence that CTE degradation is not a problem in the present application.

7. RESULTS FOR THX31160-1 CCDS

7.1 Charge to Voltage Conversion Factor

This parameter is a measure of the voltage output from the on-chip amplifier for a given charge read out from the CCD. it is proportional to G/C_o where G is the gain of the amplifier and C_o the capacitance of the output node. It is this factor which is used to convert the ADC output (in digital numbers) to electrons/pixel or, knowing the readout rate and the pixel area (= 23x23 μm), to nA/cm^2. CVF was measured in two ways. Firstly, by illuminating the device with uniform illumination at ~70% of the saturation level and measuring the output voltage (= video - reset level) and the current in the reset drain line (I_{RD}). The charge voltage to conversion factor is then given by:

$$CVF = 0.31 \frac{V_{out}\ (V)}{I_{RD}\ (\mu A)} \quad \mu V/electron$$

In this study (in contrast to the Co^{60} programme [1]) a high precision current monitor was not available and so I_{RD} could only be measured to an accuracy of 0.01 μA on a typical current of 0.1 μA. At this accuracy all devices had the same CVF before and after irradiation.

$$\underline{CVF_{\ I/V\ method}} = 1.6 \pm 0.1\ \mu V\ electron$$

The second method was to use x-rays from a Cd^{109} source. These have energies of 22.1 and 24 KeV (giving signals of ~6000 electrons). The devices were run at a frame rate of 1 kHz giving an integration time of 1 ms. As described in section 4 of [1], each 14x14 frame is readout as one line on the image memory display. 512 successive display lines then gave a 'super image' on the display which could be searched for x-ray events and this could be repeated for successive super-frames. These images were reformatted into 16x14 pixel blocks (cf. figure 4-4 of [1]) and then searched for events above a set threshold. For each detected event a block of 5x5 pixel values centred on the event were appended to a file.

With appropriate choice of threshold the detected x-ray events were confined to one pixel. That is, there was no significant charge in neighbouring pixels and no charge was split between two pixels or lost due to recombination (as would occur for spread events generated in the field-free region below the depletion layer). The fact that most x-ray events were either confined to one pixel or significantly split between two pixels indicates that the field free region thickness is small in comparison with the depletion depth. The average pixel value of the 5x5 blocks gives the x-ray signal and the average value in pixels either side of the centre gives the deferred charge, ie. the charge which is smeared into the following pixels; a parameter which is related to the charge transfer efficiency (CTE). Values of deferred charge were typically ~2 ADC units in an x-ray signal of 100 ADU (ie. ~2%). This is comparable with the dynamic performance of the electronics system. There were no significant changes in deferred charge with radiation damage.

These x-ray measurements yielded a value of

$$\underline{CVF_{\ x\text{-}ray\ method}} = 1.72 \pm 0.1\ \mu V/electron$$

in agreement with the current/voltage result. This value was not noticeably changed by the radiation (in agreement with the previous study [1]). The value of 1.72 μV/electron and the calibration of the frame grabber ADC (1 ADU = 2.46 μV) gives 1426 electrons/ADU at unity amplifier gain and this value was used throughout to convert ADC values to electrons/pixel.

7.2 Linearity and Full Well Capacity

As with the TH7863 device (para 6.2) measurements were made both with uniform and spot illumination using a light source with a constant irradiance and by changing the CCD integration time. For each integration time the signal was averaged over 10 frames (8 frames for spot illumination) and a typical plot is shown in figure 7.2-1. Further details are given in para 5.5 of reference [1] (uniform illumination) and para 5.2.1.7 (spot illumination). Saturation was taken as the point at which the straight line fit departed from the data value by 5%.

Values of the full well capacity immediately after 6 krad(Si) and after 3 months unbiased storage at room temperature were:

Table 7.2-1 Vsat after 6 krad
(unit = 10^5 electrons)

Device	Proton energy P = powered	Immediate (uniform)	3 months uniform	3 months spot
01	10 MeV	3.10	3.15	3.26
02	10 MeV,P	3.20	3.38	3.27
05	1.5 MeV,	3.13	3.25	3.13
04	1.5 MeV,P	3.10	3.23	3.17

It is seen that, in contrast to the TH7863 devices, the full well capacity is the same for both uniform and spot illumination. The results are consistent with there being negligible change in full well capacity with radiation up to 6 krad (low energy protons).

7.3 Dark Field Measurements

As with the TH7863 devices (para 6.3), radiation-induced changes in dark current can be divided into two components. The first is due to surface generation which is influenced by the creation of interface traps by ionisation damage. The second is bulk (depletion layer) generation due to mid gap centres created by displacement damage. The latter effect will lead to both an increase in the average image and storage area components and to dark charge non-uniformity. Since in the THX31160-1 CCD surface damage cannot be suppressed (by operating under inversion [37]), the two bulk and surface contributions to the mean level cannot be distinguished; but, since the ionisation damage in these devices is particularly pronounced this will tend to dominate any effect on the mean level. However with the small number of pixels in the present device (14x14) it can be expected that an average dark current level will be hard to define in the presence of significant numbers of proton-induced dark current spikes. All the data in this section was obtained from 1000 frame averages of dark images obtained at a variety of CCD temperatures in the range 12 to 32 °C. The integration time was 10 ms ie. 100 times the readout time, hence in all the

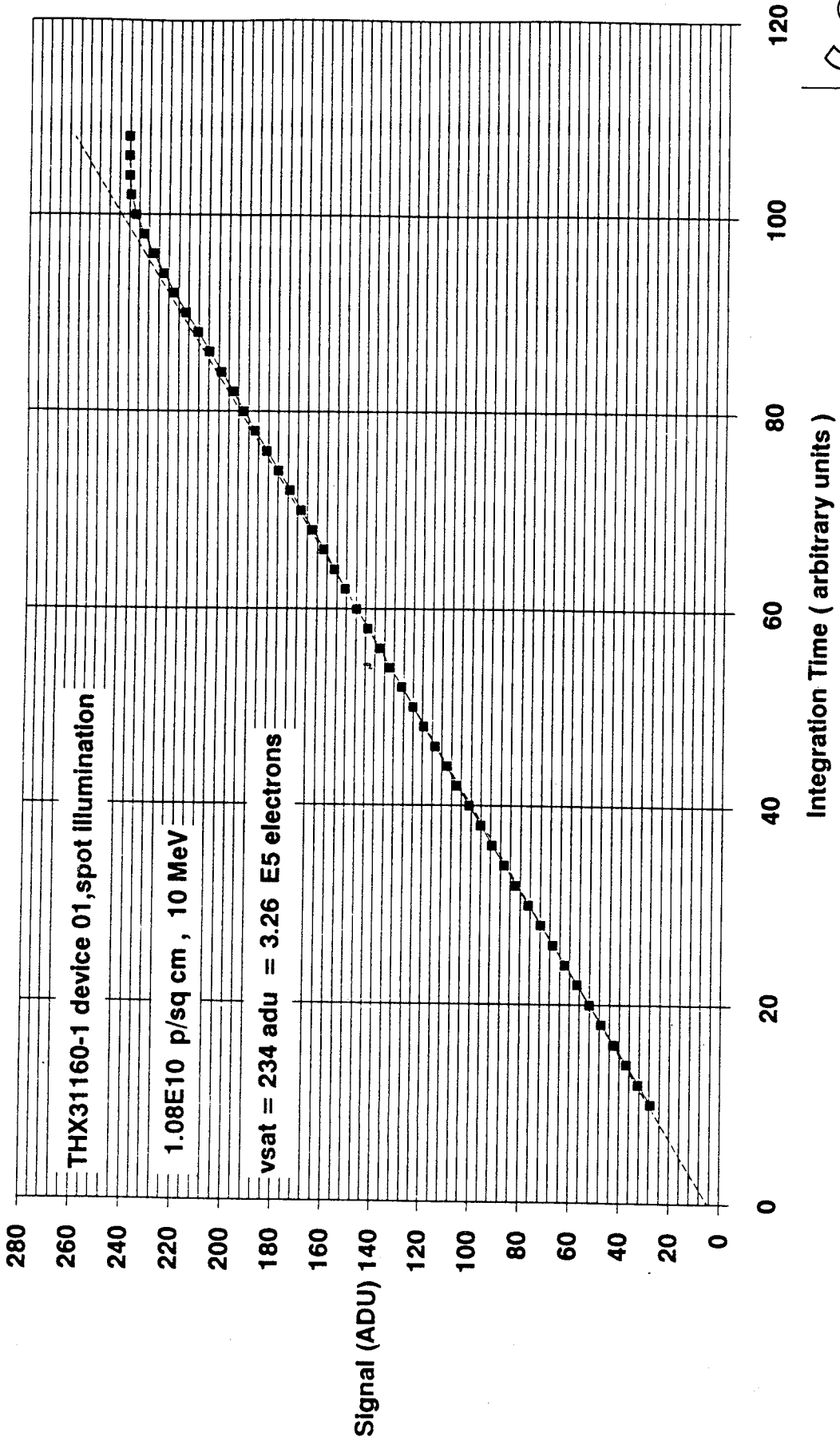

Figure 7.2-1 Linearity plot for a THX31160-1 device
(spot illumination, after 6 krad)

A/9058/00

measurements the storage region dark current can be ignored. For the TH7863 device this component quickly showed a large increase due to ionisation damage and this might be expected for the THX31160-1 also. Hence, fast changed these measurements (and the Co^{60} results [1]) will underestimate the effects for operation at shorter integration times (where the integration and storage times are comparable).

Values of dark current in ADU were converted to electrons using a factor 1426 electrons/ADU at unity amplifier gain. These were converted to nA/cm^2 using the convertion factor

$$\frac{1.6 \times 10^{-10}}{(23 \times 10^{-4})} \times \frac{1000}{10} = 0.00303$$

(since the pixel size is 23 μm^2 and the integration time was 10 ms).

7.3.1 Ionisation damage

In this section we consider the changes to the mean level of the image area dark current and the behaviour with annealing time and CCD operating temperature.

Figure 7.3-1 shows the changes in average dark current at 22.0 °C; the corresponding data values (in nA/cm^2) are given below:

Table 7.3-1 Average dark current for THX31160-1 devices 22 °C (nA/cm^2), storage : unbiased at room temperature dose = 6 krad(Si); P = powered during irradiation

device	01,10 MeV	02,10 MeV,P	05,1.5 MeV	04,1.5 MeV,P
Pre-irradiation	1.11	1.30	1.36	1.20
Immediate	3.83	6.34	5.03	7.20
After 21 days	6.54	8.25	5.08	4.40
After 90 days	6.25	4.79	3.67	2.88

It might be expected from the TH7863 data that, for a given bias state, the 10 MeV devices would show the most damage and that powered devices would show larger increases than those unpowered. In this case, we have different relative values and the suggestion of a general decrease after irradiation had ceased. This may be due to changes in the sizes of the dark charge spikes which distort the estimation of the mean level; but, as for the THX31160-1 devices measured previously [1] and for the TH7863 image region component in this study, it would seem that reverse annealing is not apparent after short to medium term storage at room temperature. A high temperature annealing step (or storage over several hundred days) may be needed before significant increases are observed. It is fortunate that the relatively small increases in dark charge do allow a more accurate determination of the bulk damage induced dark spikes.

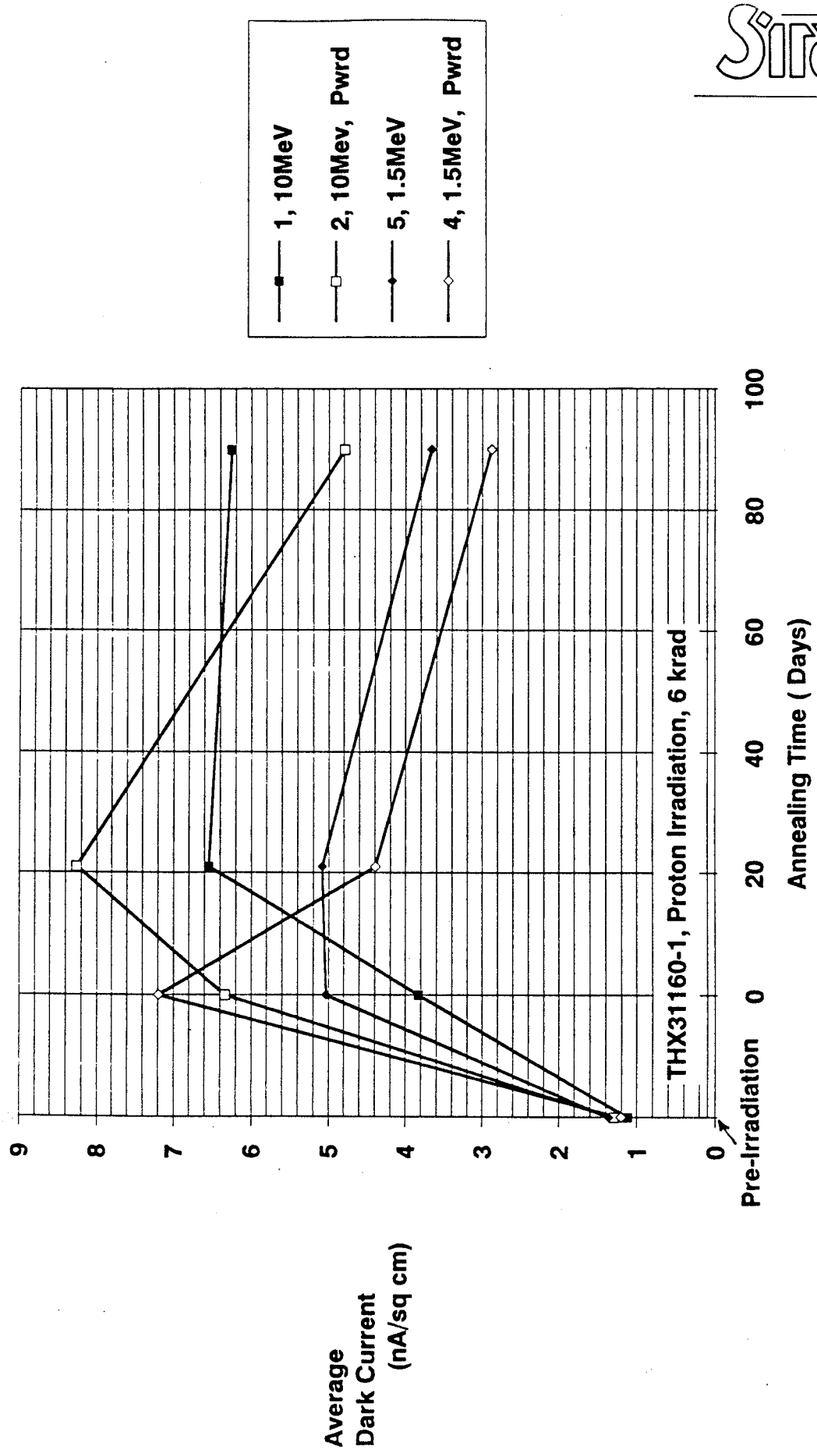

Figure 7.3-1 Average dark current for THX31160 devices at 22 °C

A/9058/00

The temperature behaviour of the average dark current is shown in figure 7.3-2. It is seen that, as expected, the logarithmic plot varies linearly with 1000/T. Also shown are the average behaviour and expectations from equation 6.3-1 ('theory'). A best fit to an Arrhenius relation gives an activation energy of 0.68 eV which is again in line with expectations (c.f. the discussion in paragraph 6.3.1).

7.3.2 Displacement Damage

In this section we look predominantly at the nonuniformity of the dark current. Figure 7.3-3 shows dark current maps before irradiation. These are flat with an rms value ~0.19 nA.cm^2 at 22 °C. The largest spikes were only ~0.1 nA/cm^2.

As discussed in para 4.4 of [1], 14x14 pixel images can be displayed by the framegrabber computer as single lines of 196 pixels (ie. each CCD line follows directly on from the last). Figure 7.3-4 shows a trace of such a line for a typical CCD showing, in addition, the dummy first and last CCD lines and the overclocked 'porch' or baseline reference region. Figures 7.3-5 to 7.3-8 show non-uniformity results for all four devices after irradiation. It is seen that immediately after irradiation the non-uniformity is appreciable with spikes as large as ~4 nA/cm^2 at 22 °C. After storage at room temperature the non-uniformity decreases somewhat but the largest spikes are still ~2 to 3 nA/cm^2 at 22 °C.

Note that the fluences received were:

$$1.07 \times 10^{10} \text{ p/cm}^2 \text{ at 10 MeV}$$
$$2.80 \times 10^{9} \text{ p/cm}^2 \text{ at 1.5 MeV}$$

From the TH7863 data (para 6.3.2) it might be expected that for a small array the chances of getting a large spike would also be small (it was argued that these spikes arise from high field regions in the CCD). Hence we might expect spikes of ~1nA/cm^2 (22 °C) but not larger. The present results might indicate that field enhanced emission is more probable with the THX31160-1, though with a small number of pixels it could be that the non-uniformity is simply the result of statistical fluctuations.

Figure 7.3-9 shows a typical histogram of pixel values and figure 7.3-10 shows the increase in non-uniformity for a typical device in pictorial form.

Figure 7.3-11 shows that the standard deviation decreases after irradiation, presumably because of dark spike annealing. But note that with the very skewed non-gaussian distributions obtained for bulk damage, the rms value is of limited use as a performance parameter. Values of rms non-uniformity are given below:-

Table 7.3-2 Values of rms dark signal non-uniformity at 22 °C, in nA/cm^2

device	01,10 MeV	02,10 MeV,P	05,1.5 MeV	04,1.5 MeV,P
Pre-irradiation	0.19	0.21	0.16	0.18
Immediate	1.03	1.00	0.84	1.04
After 21 days	1.06	0.81	0.54	0.52
After 90 days	0.60	0.41	0.33	0.32

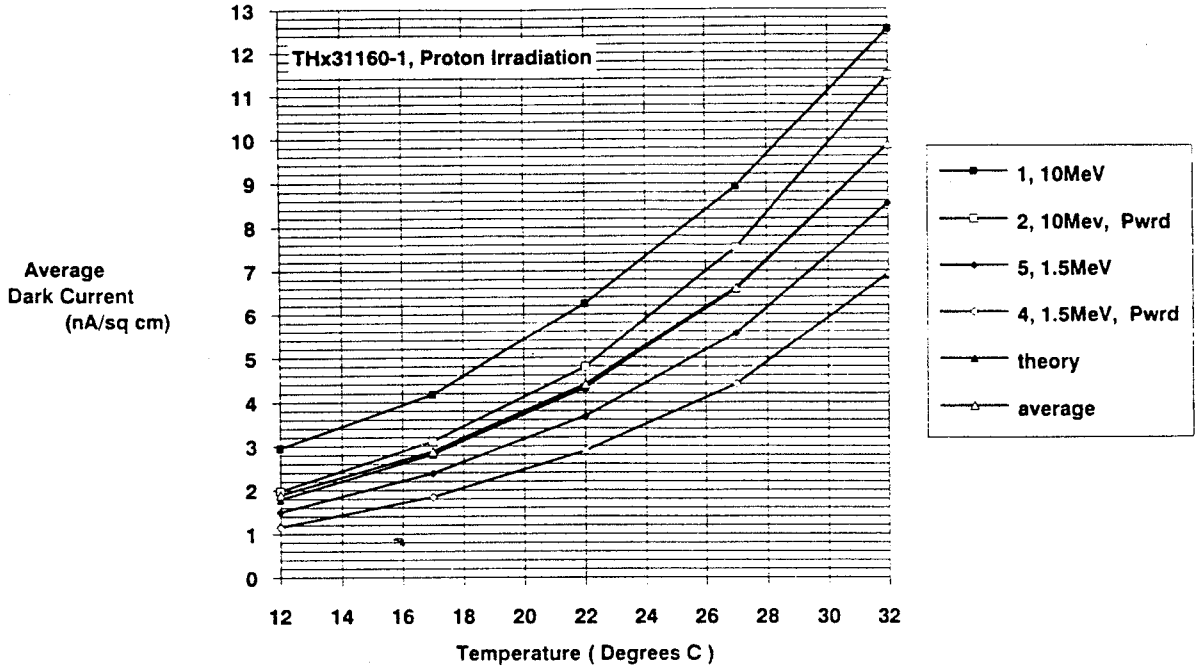

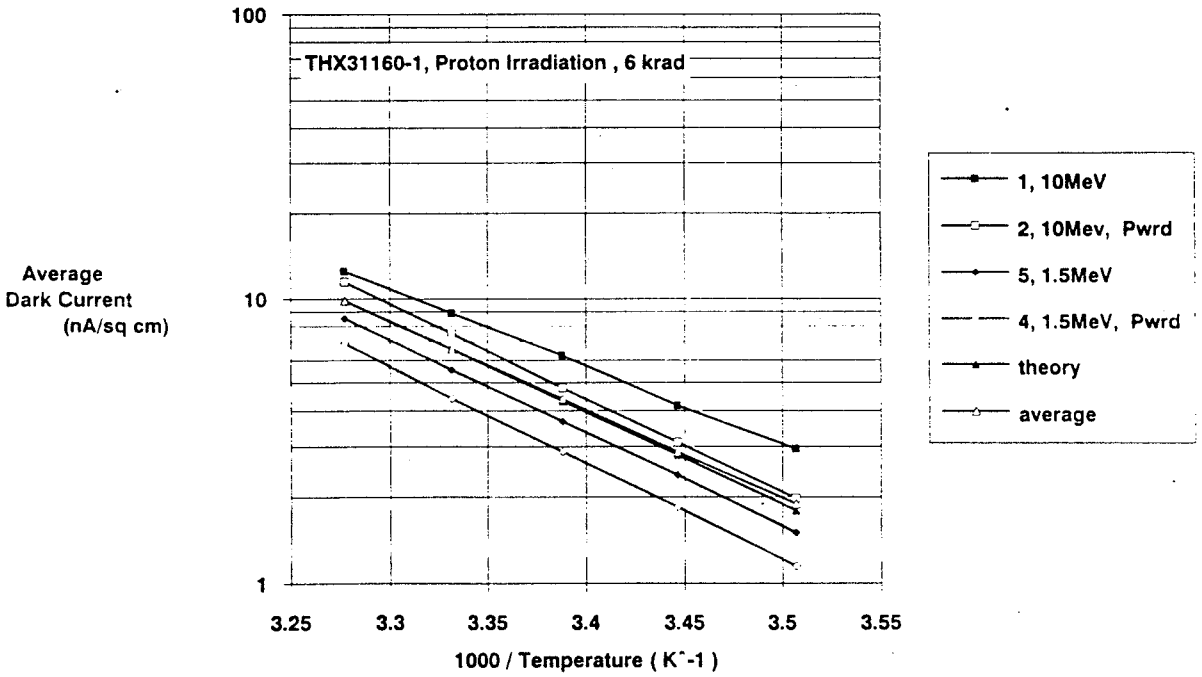

Figure 7.3-2 changes in average dark current with temperature for THX31160-1 devices

Plots of dark current non-uniformity for temperatures in the range 12 to 32 °C are given in figures 7.3-12 to 7.3-15. it is seen that the appearance of the non-uniformity does not change appreciably over this temperature range. Figure 7.3-16 shows the rms value as a function of 1000 /T. The expected linear variation is found but with a slope somewhat less than expected from equation 6.3-1 of para 6.3.1.1. In fact an Arrhenius relation can be fitted with a slope of 0.54 eV which is less than the values found for the THX31160-1 mean level (0.63 eV) and for the TH7863 (0.68 eV). This tends to support the suggestion that field enhancement, and its associated reduction in activation energy, is important (c.f. para 3.3).

Device 01

	1	2	3	4	5	6	7	8	9	10	11	12	13	14
1	-1.6	1.6	-4.8	-1.6	-4.8	4.7	4.7	11	1.6	1.6	1.6	-8	-14	-43
2	1.6	11	4.7	-4.8	1.6	4.7	7.9	4.7	1.6	-1.6	7.9	-4.8	-11	-52
3	1.6	1.6	14	1.6	4.7	7.9	1.6	-1.6	-1.6	1.6	14	4.7	-4.8	-46
4	-4.8	-1.6	11	-4.8	4.7	-1.6	1.6	-4.8	1.6	-4.8	4.7	7.9	-17	-52
5	-1.6	4.7	1.6	7.9	7.9	1.6	4.7	-1.6	1.6	1.6	-1.6	-1.6	-8	-46
6	4.7	-1.6	11	1.6	-1.6	4.7	1.6	4.7	1.6	7.9	-1.6	7.9	-8	-56
7	1.6	1.6	11	1.6	4.7	7.9	4.7	1.6	4.7	7.9	11	1.6	-4.8	-46
8	-4.8	-1.6	1.6	-1.6	-4.8	7.9	4.7	4.7	7.9	7.9	7.9	1.6	-14	-49
9	-1.6	1.6	1.6	-1.6	-1.6	14	1.6	7.9	4.7	4.7	4.7	7.9	-14	-43
10	-1.6	7.9	11	-8	7.9	7.9	1.6	-1.6	4.7	1.6	4.7	-1.6	-8	-46
11	7.9	1.6	17	1.6	4.7	-4.8	-1.6	1.6	11	-1.6	11	4.7	-11	-40
12	4.7	11	7.9	17	14	4.7	1.6	7.9	1.6	4.7	7.9	1.6	1.6	-37
13	11	11	11	4.7	14	1.6	-1.6	7.9	11	14	7.9	11	1.6	-37
14	7.9	14	24	11	4.7	11	7.9	17	7.9	14	17	17	4.7	-21
15	33	24	21	11	11	17	14	17	21	24	27	24	33	-110
16	-97	-100	-100	-100	-100	-100	-100	-100	-100	-100	-100	-100	-100	-100

% Deviations from Average Level

Device 02

	1	2	3	4	5	6	7	8	9	10	11	12	13	14
1	-0.4	2.4	2.4	2.4	2.4	7.8	2.4	-0.4	7.8	-0.4	-0.4	-3.1	-17	-47
2	-8.6	11	7.8	-0.4	2.4	11	13	7.8	7.8	2.4	7.8	2.4	-17	-47
3	-3.1	13	2.4	5.1	-0.4	-0.4	5.1	5.1	5.1	2.4	-5.9	5.1	-8.6	-39
4	-3.1	2.4	5.1	5.1	5.1	-0.4	7.8	-0.4	19	-3.1	-0.4	11	-5.9	-42
5	-3.1	7.8	-0.4	2.4	7.8	2.4	-3.1	-3.1	5.1	2.4	-5.9	2.4	-11	-42
6	-0.4	2.4	11	2.4	-0.4	11	2.4	7.8	2.4	5.1	2.4	2.4	-3.1	-42
7	5.1	5.1	5.1	13	7.8	2.4	11	2.4	7.8	5.1	2.4	2.4	-14	-44
8	2.4	-0.4	7.8	2.4	-3.1	5.1	-0.4	-3.1	7.8	2.4	-0.4	-0.4	-5.9	-42
9	-8.6	5.1	16	5.1	2.4	-5.9	2.4	7.8	2.4	-5.9	5.1	5.1	-11	-36
10	-8.6	7.8	2.4	13	-0.4	5.1	-0.4	5.1	7.8	7.8	2.4	5.1	-11	-36
11	-0.4	2.4	7.8	5.1	2.4	2.4	-0.4	5.1	-0.4	11	5.1	-0.4	-8.6	-42
12	-3.1	-0.4	7.8	2.4	7.8	7.8	-0.4	2.4	2.4	16	7.8	-3.1	-8.6	-28
13	7.8	7.8	11	5.1	2.4	5.1	5.1	7.8	7.8	5.1	2.4	11	-5.9	-33
14	7.8	16	13	11	7.8	7.8	11	11	11	7.8	7.8	11	13	-22
15	22	22	19	16	13	11	2.4	13	13	16	22	22	24	-110
16	-99	-99	-99	-99	-99	-102	-99	-99	-102	-99	-102	-99	-99	-99

% Deviations from Average Level

Device 05

	1	2	3	4	5	6	7	8	9	10	11	12	13	14
1	8.2	5.6	-2.3	0.3	0.3	0.3	3	-2.3	3	0.3	-2.3	3	-15	-37
2	-2.3	8.2	0.3	3	0.3	0.3	-2.3	0.3	3	0.3	-4.9	0.3	-4.9	-42
3	5.6	3	5.6	-2.3	3	8.2	-10	3	0.3	-4.9	8.2	-2.3	-10	-34
4	0.3	5.6	0.3	5.6	3	3	0.3	-7.6	0.3	0.3	3	0.3	-4.9	-34
5	-4.9	5.6	0.3	0.3	5.6	0.3	3	0.3	0.3	-2.3	5.6	5.6	-4.9	-34
6	0.3	5.6	-2.3	0.3	3	5.6	-2.3	3	3	0.3	0.3	11	-13	-34
7	3	5.6	0.3	8.2	11	5.6	3	5.6	0.3	-2.3	5.6	5.6	-2.3	-29
8	-15	3	8.2	5.6	-2.3	0.3	0.3	3	5.6	-4.9	0.3	5.6	-2.3	-31
9	0.3	3	11	0.3	8.2	5.6	5.6	3	3	-4.9	3	8.2	-4.9	-37
10	-2.3	0.3	0.3	5.6	11	3	-2.3	11	-2.3	-4.9	3	0.3	-13	-37
11	-2.3	3	3	5.6	-2.3	5.6	5.6	3	-2.3	3	3	3	-2.3	-39
12	5.6	8.2	-2.3	11	-7.6	-4.9	13	5.6	8.2	11	3	3	0.3	-34
13	3	13	11	5.6	8.2	5.6	5.6	8.2	0.3	11	8.2	16	-2.3	-23
14	19	11	0.3	13	11	3	5.6	13	11	16	11	11	-2.3	-13
15	19	24	13	21	16	11	11	13	8.2	13	21	29	32	-108
16	-100	-100	-100	-100	-100	-100	-100	-100	-100	-100	-100	-100	-100	-100

% Deviations from Average Level

Device 04

	1	2	3	4	5	6	7	8	9	10	11	12	13	14
1	-1.7	7.2	4.3	1.3	1.3	-1.7	4.3	-11	10	1.3	1.3	-1.7	-17	-52
2	-7.6	7.2	4.3	4.3	4.3	-1.7	4.3	-1.7	1.3	7.2	4.3	7.2	-17	-49
3	7.2	10	4.3	7.2	4.3	10	7.2	4.3	7.2	7.2	-1.7	-1.7	-4.7	-49
4	-1.7	-1.7	1.3	-1.7	-1.7	-1.7	7.2	-4.7	7.2	1.3	10	10	-4.7	-49
5	1.3	1.3	7.2	4.3	10	1.3	1.3	-1.7	7.2	1.3	4.3	1.3	-7.6	-55
6	1.3	4.3	10	4.3	-1.7	1.3	-1.7	4.3	4.3	4.3	4.3	1.3	-4.7	-49
7	1.3	7.2	-1.7	4.3	1.3	1.3	-1.7	-4.7	10	4.3	1.3	10	-1.7	-49
8	4.3	4.3	10	4.3	1.3	-4.7	-1.7	1.3	7.2	7.2	4.3	4.3	-4.7	-58
9	-1.7	4.3	4.3	7.2	13	1.3	-1.7	4.3	1.3	7.2	4.3	1.3	-4.7	-49
10	4.3	1.3	1.3	7.2	7.2	7.2	4.3	-4.7	1.3	4.3	-4.7	1.3	1.3	-49
11	7.2	4.3	10	7.2	4.3	-1.7	-1.7	1.3	1.3	1.3	1.3	4.3	-4.7	-46
12	4.3	1.3	10	10	10	16	1.3	1.3	7.2	7.2	4.3	4.3	-1.7	-49
13	16	4.3	16	10	13	4.3	7.2	7.2	7.2	7.2	16	13	1.3	-52
14	13	10	13	13	7.2	7.2	7.2	10	13	13	13	16	7.2	-28
15	31	19	25	19	13	13	7.2	4.3	22	22	25	31	31	-109
16	-97	-100	-100	-100	-100	-100	-100	-100	-100	-100	-100	-100	-103	-100

% Deviations from Average Level

Figure 7.3-3 THX31160-1 dark current maps before irradiation

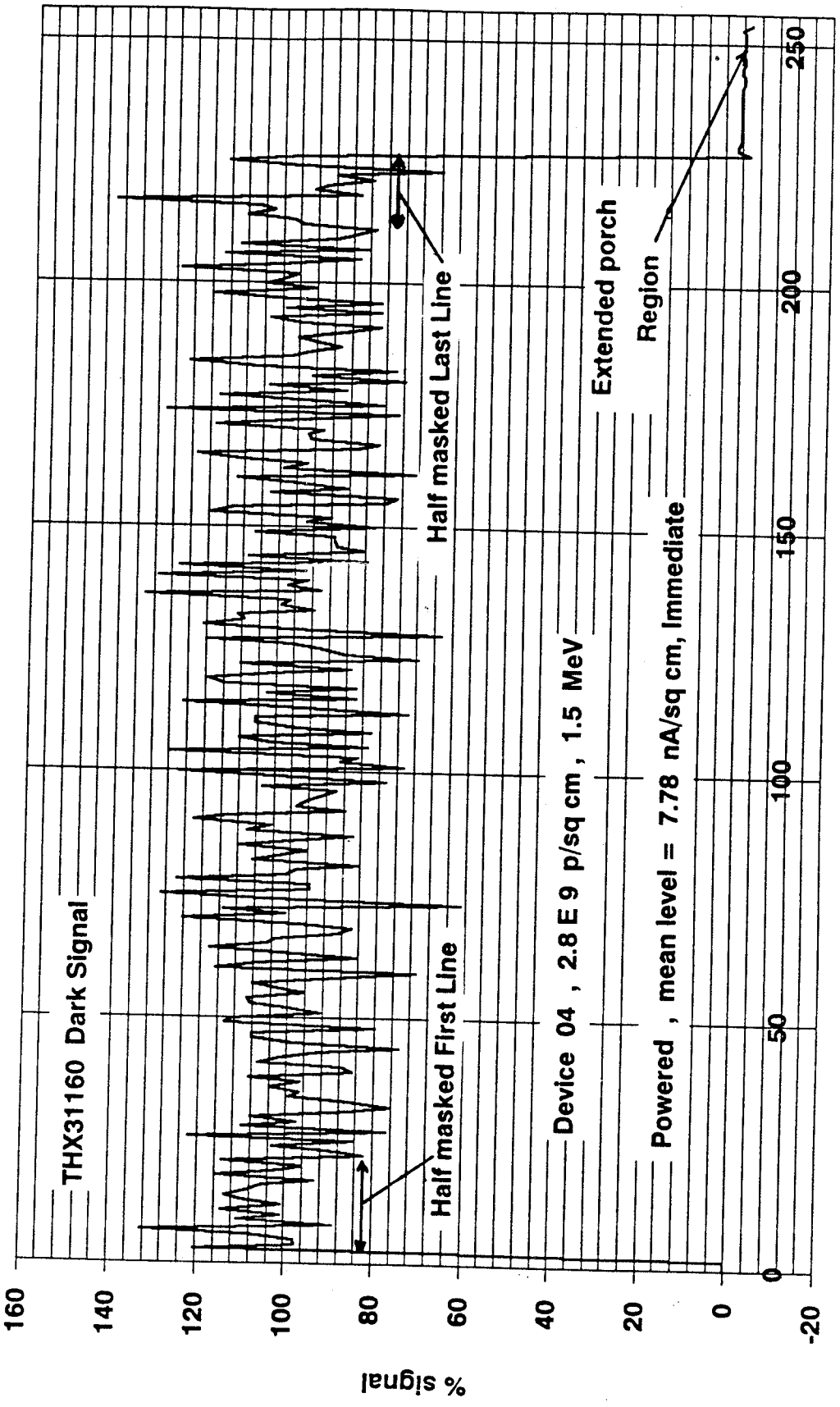

Figure 7.3-4 Plot of dark signal for a THX31160-1 at 22 °C

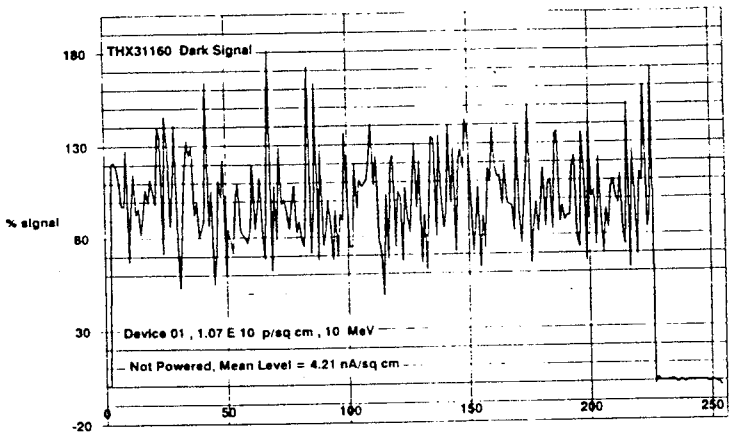

	1	2	3	4	5	6	7	8	9	10	11	12	13	14
1	-1	12	4.6	-1.9	40	34	-29	45	28	-14	10	41	-22	-4
2	-10	15	32	25	30	-7.4	-1	-19	-15	-10	64	-14	5.5	-4
3	-28	11	1.8	22	-40	-16	-22	-29	2.7	9.2	-16	-19	-20	-2
4	-14	19	-16	-5.6	13	-15	-31	18	80	-38	8.3	-22	29	-1
5	0.9	-5.6	-16	-2.8	8.3	-18	-11	-21	-25	9.2	72	-29	-4.6	6
6	-32	30	-25	-19	0	-11	-32	-5.6	-31	-7.4	-11	36	-1.9	-2
7	-26	19	-4.6	11	7.4	9.2	12	22	41	8.3	25	-21	-29	-5
8	2.7	-32	20	24	-26	4.6	1.8	-33	6.4	-9.3	-19	6.4	30	-4
9	21	-34	-8.3	-38	0.9	33	32	-19	34	2.7	-16	-6.5	40	-3
10	28	-29	20	27	17	42	33	6.4	-29	-15	6.4	-37	-9.3	-2
11	17	9.2	38	18	12	13	-2.8	18	-1.9	-2.8	-3.7	-18	39	-6
12	-25	-1	18	50	-35	-16	-1.9	-19	-1	17	-16	8.3	10	-1
13	34	36	-13	-3.7	-12	-9.3	-9.3	18	23	-21	-27	35	13	-3
14	42	0.9	4.6	-26	22	-10	-30	-5.6	-17	5.5	10	1.8	-2.8	1
15	-19	-26	51	-38	26	2.7	-31	14	9.2	60	-17	-8.3	69	-10
16	-98	-100	-100	-100	-100	-100	-99	-100	-101	-100	-100	-101	-100	-10

% Deviations from Average Level

24 IS % RMS VALUE

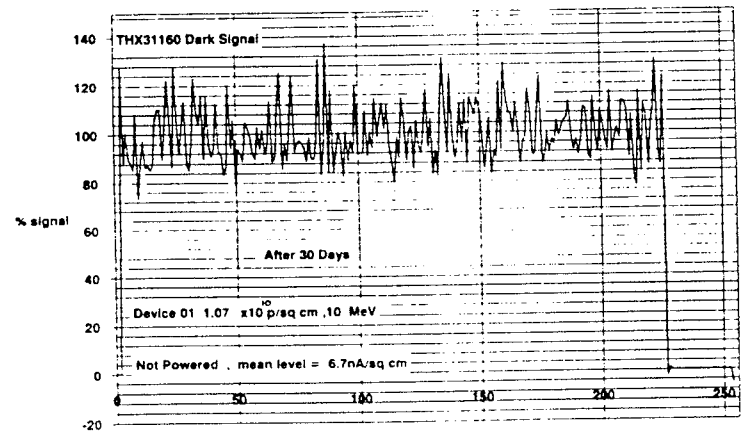

	1	2	3	4	5	6	7	8	9	10	11	12	13	1
1	10	10	-10	1.5	22	5.8	-14	27	2.6	-8.2	4.7	13	-13	-1
2	-1.7	23	8	3.7	16	-10	16	-3.9	-9.3	-6.1	12	-7.1	-8.2	-1
3	-14	20	-6.1	5.8	-21	-6.1	-8.2	-11	4.7	2.6	-1.7	-8.2	-10	2
4	-6.1	1.5	-8.2	-5	13	-11	-9.3	10	25	-15	-3.9	-11	5.8	2
5	-7.1	-3.9	-2.8	-3.9	-6.1	-11	-1.7	-10	-10	-2.8	31	-17	-3.9	3
6	-16	18	-16	-8.2	0.4	-2.8	-18	0.4	-11	-2.8	-8.2	20	-7.1	-8
7	-8.2	9.1	-9.3	0.4	-6.1	14	-1.7	5.8	12	1.5	11	-5	-13	-2
8	-1.7	-10	14	5.8	-11	0.4	2.6	-15	4.7	-5	-8.2	1.5	18	-6
9	5.8	-17	-7.1	-18	12	31	8	-8.2	24	-0.7	-10	-5	11	-3
10	13	-13	14	11	6.9	14	10	1.5	-15	-6.1	5.8	-17	-7.1	-1
11	21	-7.1	28	16	8	8	0.4	12	0.4	-13	-3.9	-1.7	18	9
12	-9.3	-8.2	11	23	-13	-10	-0.7	-8.2	-2.8	-5	4.7	-1.7	2.6	4
13	5.8	12	-1.7	-7.1	-2.8	-9.3	-1.7	10	9.1	-9.3	-11	14	-1.7	-8
14	9.1	3.7	-2.8	-7.1	17	-8.2	-1.7	1.5	-2.8	12	12	9.1	-10	6
15	-18	-22	17	-16	11	6.9	-14	2.6	10	30	-7.1	-14	23	-1
16	-99	-100	-100	-100	-100	-100	-100	-100	-100	-100	-100	-100	-100	-1

% Deviations from Average Level

12 IS % RMS VALUE

Figure 7.3-5 Dark signal non-uniformity at at 22 °C for device 01 (10 MeV)

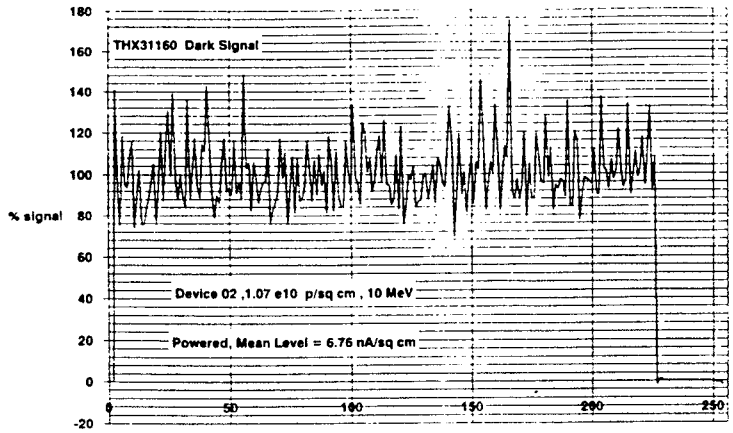

	1	2	3	4	5	6	7	8	9	10	11	12	13
1	-2.7	4.8	-24	-5.6	20	-13	14	30	-0.8	39	-1.8	-12	-0.8
2	-16	36	-12	1	17	-4.6	-11	14	10	43	14	-8.4	-22
3	-14	4.8	17	-8.4	-6.5	-10	15	-9.3	-3.7	-12	48	2.9	5.8
4	5.8	-0.8	-14	-7.4	-3.7	-3.7	12	-23	-8.7	-14	-8.4	17	-1.8
5	-24	-6.5	8.6	-19	7.7	-13	-11	-5.6	16	2.9	-13	6.7	-10
6	-5.6	2	-19	18	5.8	-18	10	-10	-19	-16	15	2	-7.4
7	-1.8	-3.7	-15	25	20	1	7.7	-8.4	-2.7	10	18	-3.7	26
8	-5.6	-15	-11	9.5	-17	23	-24	-16	-0.8	-2.7	3.9	-16	-13
9	-0.8	0.1	-12	-4.6	3.9	-14	7.7	4.8	-3.7	-6.5	14	32	13
10	-4.6	19	-10	1	-19	-2.7	7.7	-15	5.8	2	45	21	-18
11	5.8	0.1	33	14	-18	-0.8	13	7.7	7.5	-8.4	-12	-2.7	-12
12	20	-21	4.8	-11	-12	19	7.7	-3.7	-4.8	27	-1.8	12	-18
13	-7.4	-2.7	-3.7	-11	35	-15	-16	20	1.6	-23	-9.3	-1.8	-2.7
14	-4.6	11	-10	-10	37	2.9	1	-7.4	3.7	-2.7	2	21	2
15	-2.7	33	-10	-0.8	10	-1.8	3.9	17	5.6	10	31	-8.4	7.7
16	-99	-99	-100	-100	-100	-100	-100	-100	-100	-100	-100	-100	-100

% Deviations from Average Level

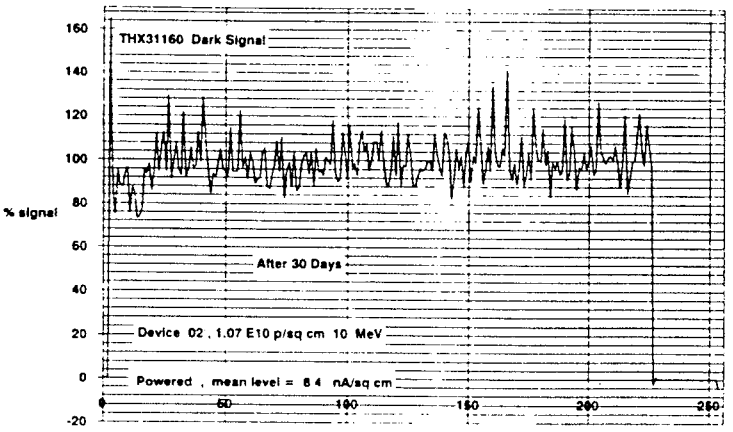

	1	2	3	4	5	6	7	8	9	10	11	12	13
1	-6.3	-1.9	-14	-5.4	12	-5.4	6.7	13	-5.4	29	-8.9	-1.1	7.6
2	-7.1	21	-8	-4.5	5.9	-3.7	-2.8	13	-1.1	28	8.5	-2.8	-16
3	-8	-1.9	5	-3.7	-5.4	-8	15	-5.4	-5.4	-5.4	22	-3.7	1.5
4	3.3	-0.2	-11	-8.9	-8	2.4	5.9	-11	-2.3	-7.1	-1.9	8.5	-5.4
5	-18	-4.5	-1.1	-12	4.1	-14	-12	-1.9	2.4	3.3	-6.3	4.1	-11
6	-5.4	-4.5	-7.1	1.5	-0.2	-1.9	18	-5.4	-8.8	-8	13	4.1	-8.9
7	-3.7	-1.1	-7.1	7.6	14	4.1	7.6	-4.5	10.7	8.5	8.5	0.7	14
8	-11	-11	-3.7	11	-7.1	17	-11	-1.9	2.8	12	2.4	-11	-11
9	-3.7	-4.5	-3.7	-0.2	-0.2	-4.5	12	3.3	-2.8	-7.1	13	11	3.3
10	-8	5.9	-3.7	2.4	-11	3.3	9.3	-9.8	2.4	-1.1	24	9.3	-11
11	6.7	-4.5	34	4.1	-1.9	-2.8	5.9	2.4	4.1	-3.7	-8.9	-1.1	-11
12	11	-11	-5.4	3.3	-8.9	24	5.9	0.7	-2.2	15	-1.9	5	-17
13	-3.7	-0.2	-6.3	-4.5	19	-8.9	-5.4	15	4.1	-13	-2.8	-4.5	3.3
14	0.7	6.7	-6.3	-4.5	27	4.1	1.5	-1.1	1.5	2.4	0.7	6.7	-1.9
15	1.5	21	-15	-8.9	-0.2	-0.2	12	21	4.1	-1.9	16	6.7	-2.8
16	-99	-100	-100	-100	-100	-100	-100	-100	-100	-100	-100	-100	-100

% Deviations from Average Level

10 IS % RMS VALUE

Figure 7.3-6 Dark signal non-uniformity at 22 °C for device 02 (10 MeV)

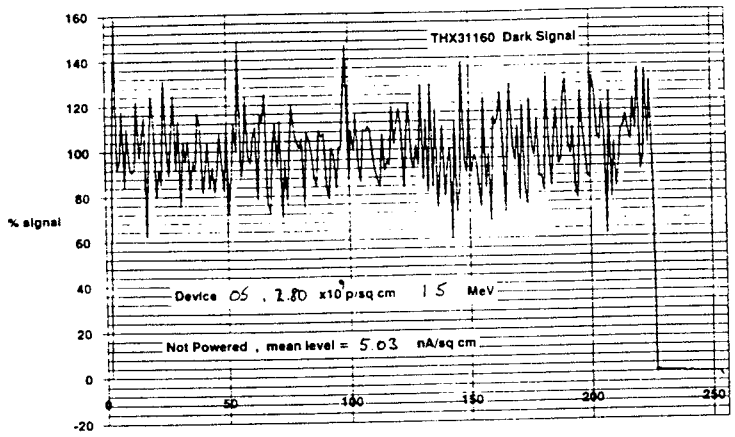

	1	2	3	4	5	6	7	8	9	10	11	12	13	14
1	2.8	23	9.2	-20	-7.7	-15	31	4.9	-11	7.1	25	-7.7	14	-2
2	4.2	-4.9	4.2	-17	-4.9	-8.4	16	12	-18	-9.9	3.5	-16	-6.3	-1
3	-7	7.1	-6.3	-18	11	-27	-7.7	12	-0.7	48	-11	-4.9	23	-2.
4	-5.6	5.7	9.9	-22	16	12	25	-23	-27	0	12	-7	13	-3
5	-4.9	-24	4.2	19	7.1	3.5	0.7	4.9	-25	7.8	4.2	-0.7	-12	-1
6	8.5	5.7	7.1	-15	-22	0.7	-2.8	-17	0.7	1.4	27	46	-13	8.
7	-0.7	16	-7	-14	8.5	7.8	9.9	8.5	-3.5	-9.1	-13	-16	6.4	-9.
8	-4.9	-7	18	2.1	12	18	5.7	-17	8.5	20	-4.2	-8.4	1.4	
9	27	-13	13	-19	28	-17	17	-27	-8.4	9.9	-21	-7	0	-4
10	11	-28	-18	38	-4.9	-11	15	-11	-2.8	-5.6	-17	-26	22	-1
11	-2.8	-32	13	9.9	14	24	-0.7	-28	9.2	27	0.7	-5.6	9.2	-2
12	18	-16	-25	21	0	-3.5	13	-13	-13	-19	31	1.4	-17	3.
13	17	-7	-4.9	22	30	1.4	-2.8	8.5	-20	-23	24	8.5	-2.1	-1
14	-13	31	25	5.7	2.8	19	5.7	-39	24	-23	2.1	-18	-4.9	7.
15	9.2	14	6.4	2.8	21	6.4	35	-9.9	-4.2	34	1.4	29	-15	-10
16	-99	-99	-99	-99	-99	-99	-99	-99	-99	-99	-99	-100	-100	-9

% Deviations from Average Level

17 IS % RMS VALUE

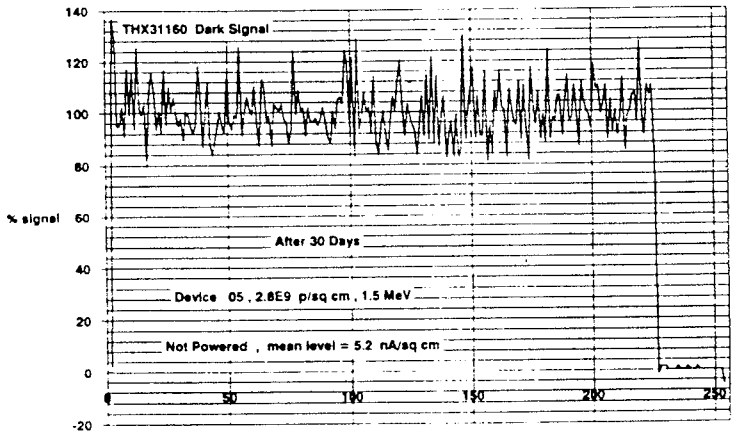

	1	2	3	4	5	6	7	8	9	10	11	12	13
1	8.8	16	7.4	-6.5	0.5	-7.9	17	-5.1	10	0.5	6.1	-0.9	-5.1
2	-11	0.5	-0.9	-5.1	-7.9	-5.1	19	7.4	-14	-0.9	12	-12	-16
3	-5.1	0.5	-5.1	-7.9	16	-3.7	-6.5	-0.9	-2.3	26	-9.3	-0.9	6.1
4	-0.9	10	-5.1	-14	13	10	-3.7	-0.9	-14	3.3	1.9	0.5	3.3
5	-3.7	-12	-6.5	24	-0.9	8.8	0.5	1.9	-9.3	1.9	-3.7	-3.7	-2.3
6	-2.3	1.9	-3.7	-9.3	-12	0.5	-6.5	4.7	6.1	3.3	24	19	-5.1
7	-18	28	-6.5	-2.3	7.4	0.5	1.9	-7.9	14	-11	-16	-6.5	0.5
8	-15	-3.7	6.1	0.5	13	20	0.5	-9.3	3.3	-0.9	-5.1	-6.5	-16
9	6.1	-9.3	14	-11	21	-12	14	-14	-0.9	6.1	-18	-9.3	-3.7
10	-0.9	-18	-14	30	-11	0.5	8.8	17	-11	6.1	-9.3	-9.3	16
11	-5.1	-16	7.4	0.5	16	1.9	0.5	-18	8.8	1.9	-3.7	-5.1	12
12	10	-5.1	-19	17	1.9	-5.1	7.4	-11	-0.9	-12	24	-11	-2.3
13	6.1	6.1	-9.3	1.9	14	-3.7	-2.3	10	-0.9	-14	12	4.7	0.5
14	-6.5	19	8.8	10	-0.9	3.3	10	-11	4.7	-7.9	0.5	-9.3	-2.3
15	-15	-2.3	0.5	6.1	7.4	-3.7	27	-0.9	-9.3	10	6.1	10	-14
16	-99	-99	-99	-100	-100	-100	-100	-99	-100	-100	-100	-99	-100

% Deviations from Average Level

10 IS % RMS VALUE

Figure 7.3-7 Dark signal non-uniformity at 22 °C for device 05 (1.5 MeV)

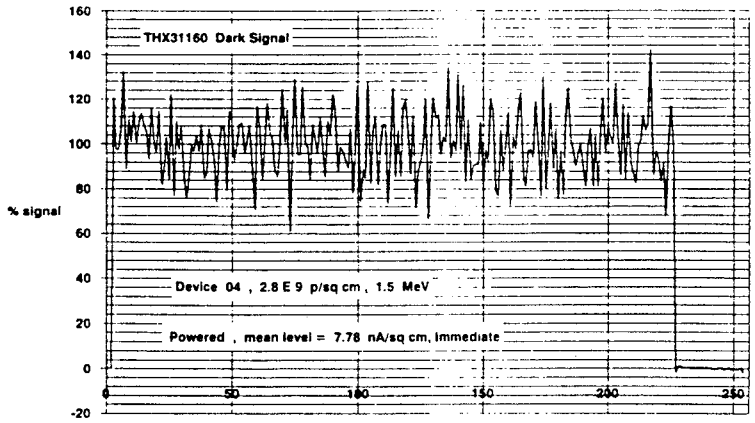

	1	2	3	4	5	6	7	8	9	10	11	12	13
1	16	0.9	-4.1	14	-18	-12	-3	-15	22	-23	10	-2.6	7.9
2	-24	-15	-0.5	-3.4	3.7	-3.4	8.6	-15	-12	6.5	1.6	-7.6	-26
3	7.9	7.9	-20	14	13	-7.6	0.2	8.6	33	-4.1	3	7.9	-11
4	16	7.2	-16	-1.2	18	5.1	3	-11	-15	-1.9	24	0.9	15
5	5.1	29	-4.8	-4.8	25	0.9	-1.2	-16	8.6	1.6	-4.1	11	-1.9
6	10	4.4	22	14	-12	-1.2	-3.4	-6.9	20	6.5	-22	3.7	25
7	-11	-15	28	-17	5.1	12	-18	-1.2	4.8	8.6	-27	-2.6	25
8	5.8	-15	16	19	4.4	-13	12	-29	32	-6.9	0.2	19	-34
9	21	11	13	-4.8	3	0.9	34	-6.2	36	-3.4	31	-2.6	26
10	11	-16	-9.7	-9	-9	9.3	-18	-2.6	33	19	14	-20	-23
11	-12	-0.5	14	-27	3	-2.6	13	-23	-14	-19	-3.4	-2.6	-6.2
12	-0.5	-23	30	-20	-5.5	18	-11	-6.5	-29	-3.4	-22	9.3	25
13	-1.9	-9.7	-4.1	0.2	-10	-19	-0.5	-6.5	19	3	-19	5.8	19
14	7.2	3.7	0.2	27	4.4	-14	17	-16	14	-8.3	-12	-17	-0.5
15	12	5.8	9.3	42	-14	-3.4	-6.2	-17	53	-32	0.2	16	0.2
16	-99	-99	-100	-100	-100	-100	-100	-100	33	-100	-100	-100	-100

% Deviations from Average Level

14 IS % RMS VALUE

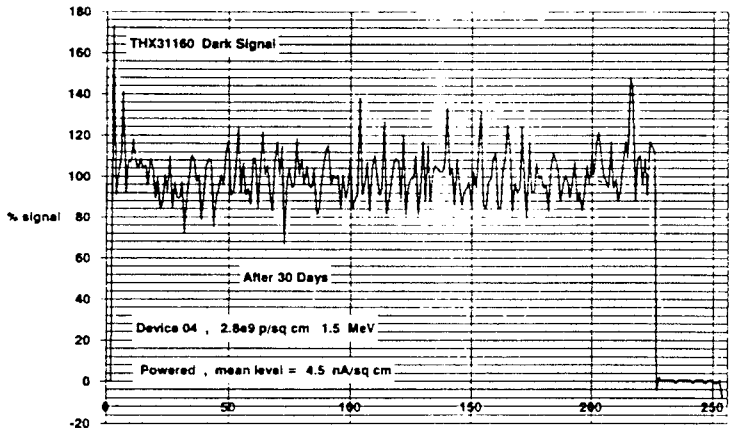

	1	2	3	4	5	6	7	8	9	10	11	12	13
1	8.7	5.4	-11	-1	-16	-14	0.6	-7.5	10	-16	-2.6	-11	-1
2	-28	-11	0.6	10	8.7	-2.6	0.6	-22	-7.5	5.4	8.7	7.1	-2
3	-5.9	0.6	-4.3	12	17	-9.1	-7.5	5.4	23	-7.5	7.1	-9.1	-5
4	8.7	8.7	-16	3.8	22	0.6	5.4	-7.5	-17	7.1	17	0.6	1
5	-2.6	3.8	-5.9	-4.3	18	0.6	8.7	-4.3	5.4	-4.3	-5.9	3.8	-1
6	-2.6	5.4	14	15	-4.3	0.6	-1	0.6	-16	0.6	-11	-5.9	8
7	-11	-9.1	38	-9.1	-2.6	7.1	-17	3.8	10	0.6	-9.1	-5.9	2
8	-11	-2.6	7.1	8.7	7.1	-11	20	-19	4.3	-1	-1	10	-1
9	17	-12	15	-12	2.2	5.4	3.8	2.2	2.2	7.1	33	0.6	3
10	8.7	-2.6	-14	-7.5	-5.9	-2.6	-14	2.2	5.9	14	31	-14	-1
11	-1	8.7	12	-16	-16	2.2	10	25	12	-17	-2.6	-7.5	-5
12	-5.9	-20	17	-7.5	-7.5	7.1	-1	0.6	-5.9	-4.3	-17	3.8	1
13	2.2	-12	-4.3	0.6	-2.6	-11	-1	7.1	-12	-7.5	-17	-7.5	5
14	10	0.6	17	22	8.7	0.6	-2.6	-5.9	17	-5.9	-1	-12	-5
15	17	8.7	47	43	-12	8.7	10	-4.3	8.7	-9.1	17	15	12
16	-98	-100	-100	-100	-100	-100	-100	-101	-100	-100	-100	-100	-100

% Deviations from Average Level

12 IS % RMS VALUE

Figure 7.3-8 Dark signal non-uniformity at 22 °C for device 04 (1.5 MeV)

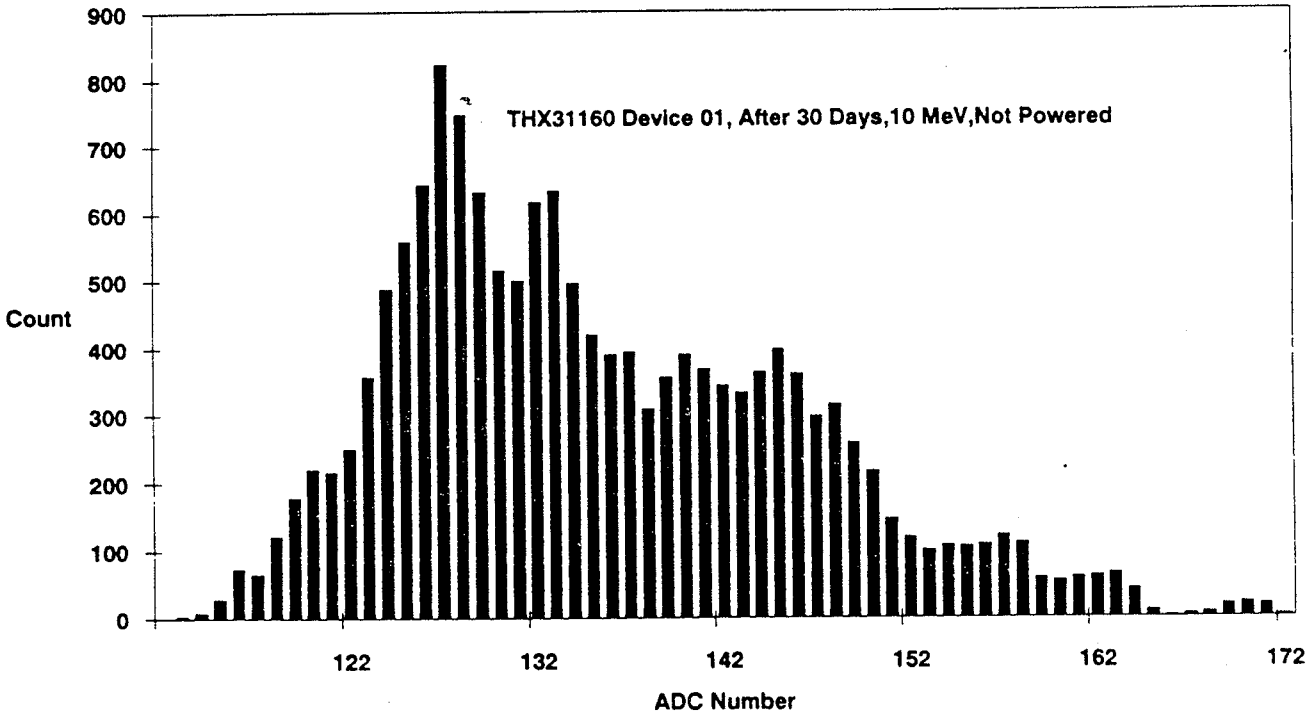

Figure 7.3-9 Dark current histogram for a typical THX31160-1 device
(1 ADC unit = 0.0714 nA/.cm^2 at 22 °C; baseline (porch level = 42.6 ADU)

THX31160-1 Dark Images Before and After 6 krad of 10 MeV Protons

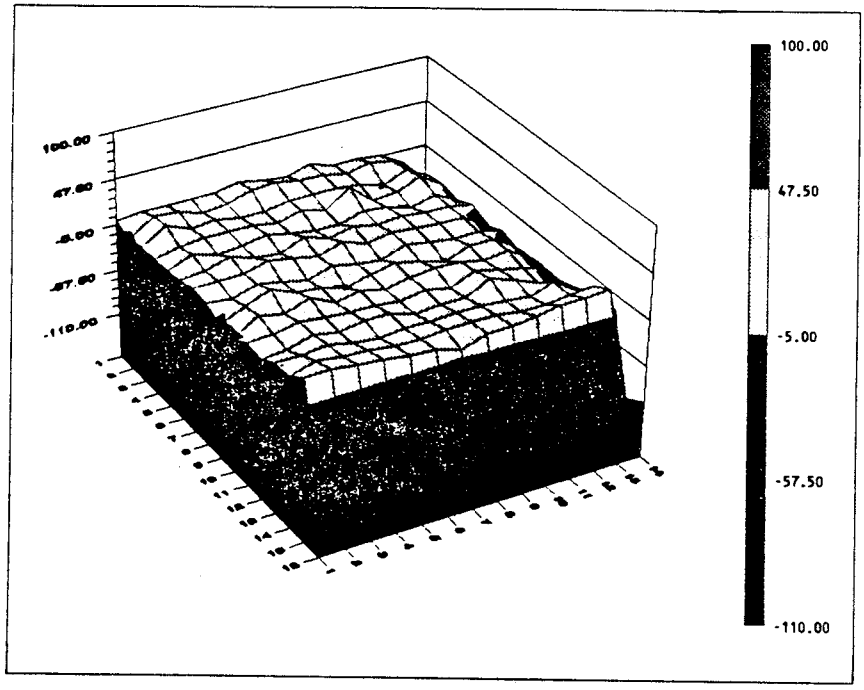

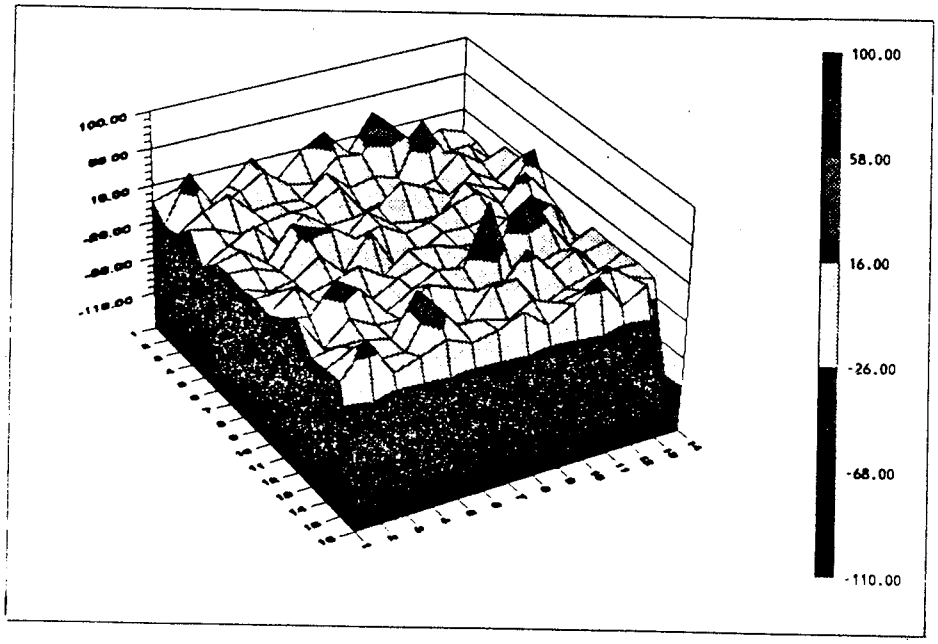

Figure 7.2-10 Dark current maps for a typical THX31160 device

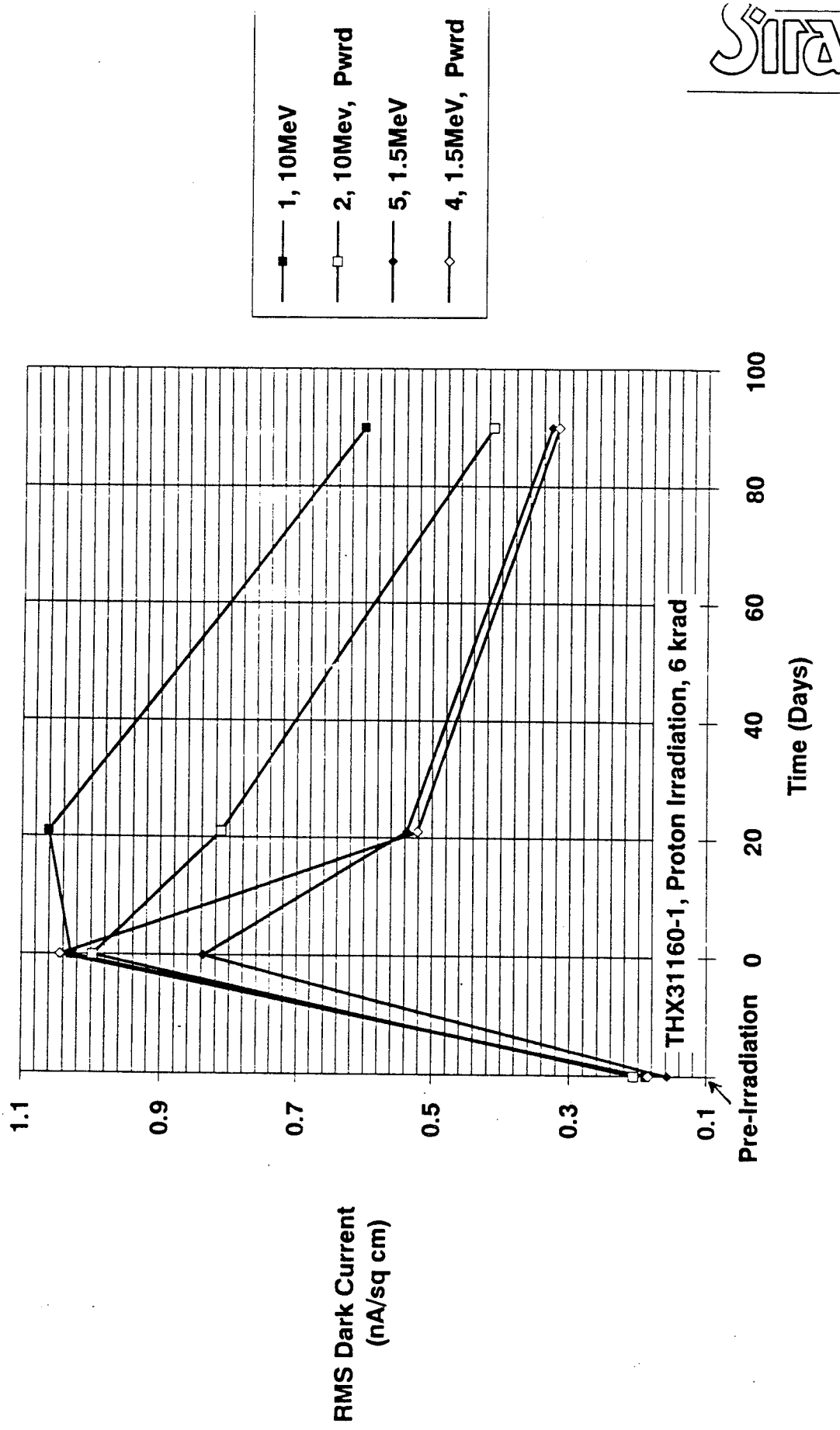

Figure 7.3-11 rms dark non-uniformity for THX31160-1 devices

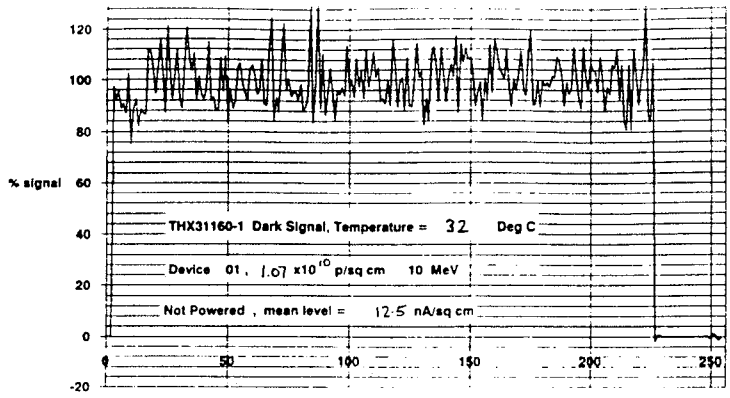

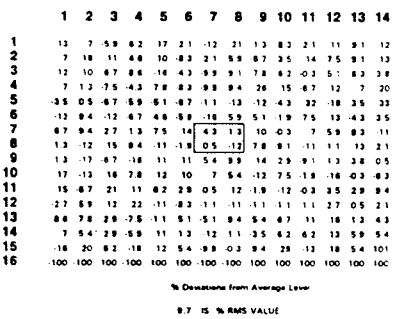

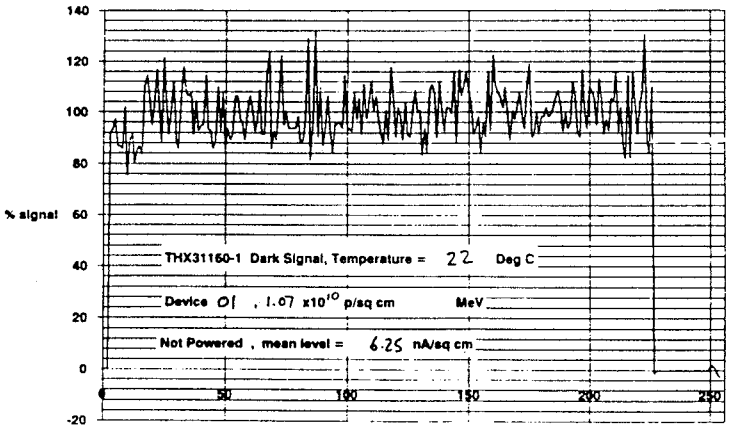

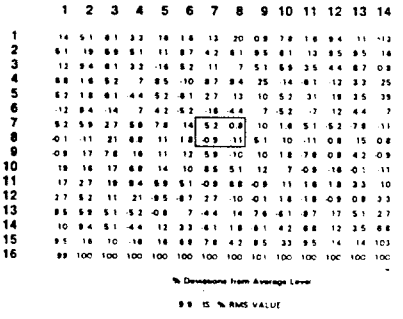

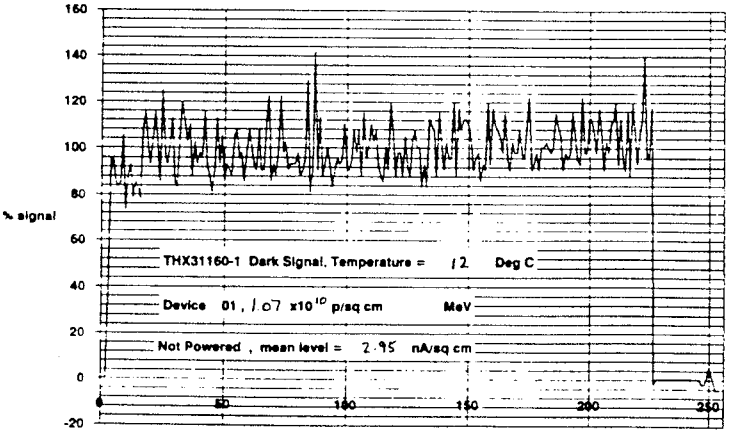

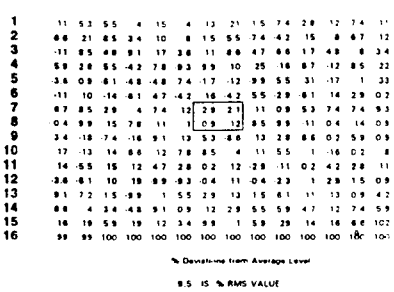

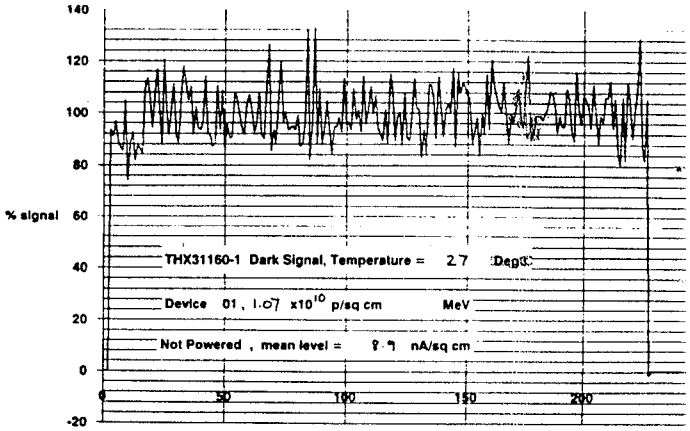

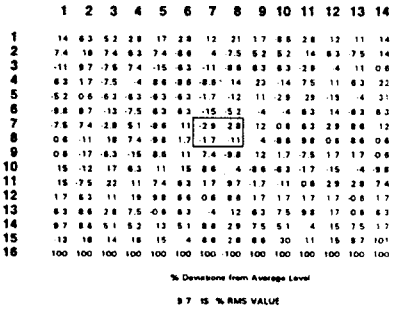

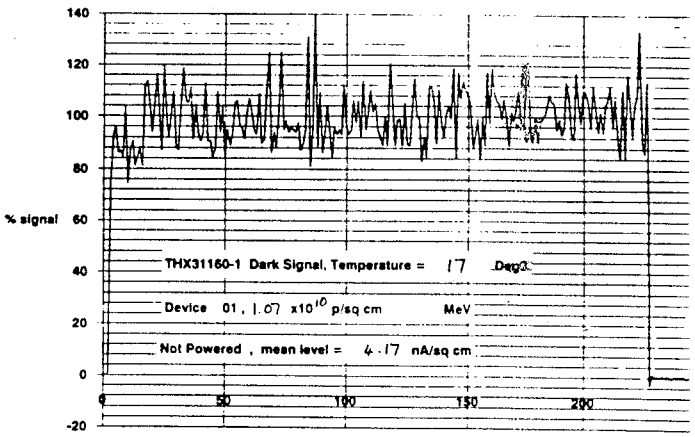

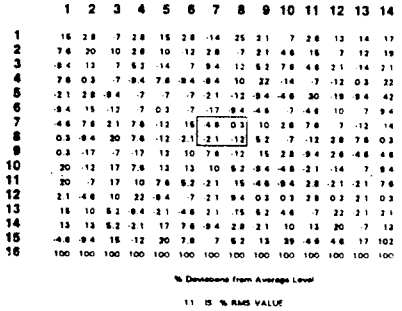

Figure 7.3-12 Dark current non-uniformity for device 01 at various temperatures

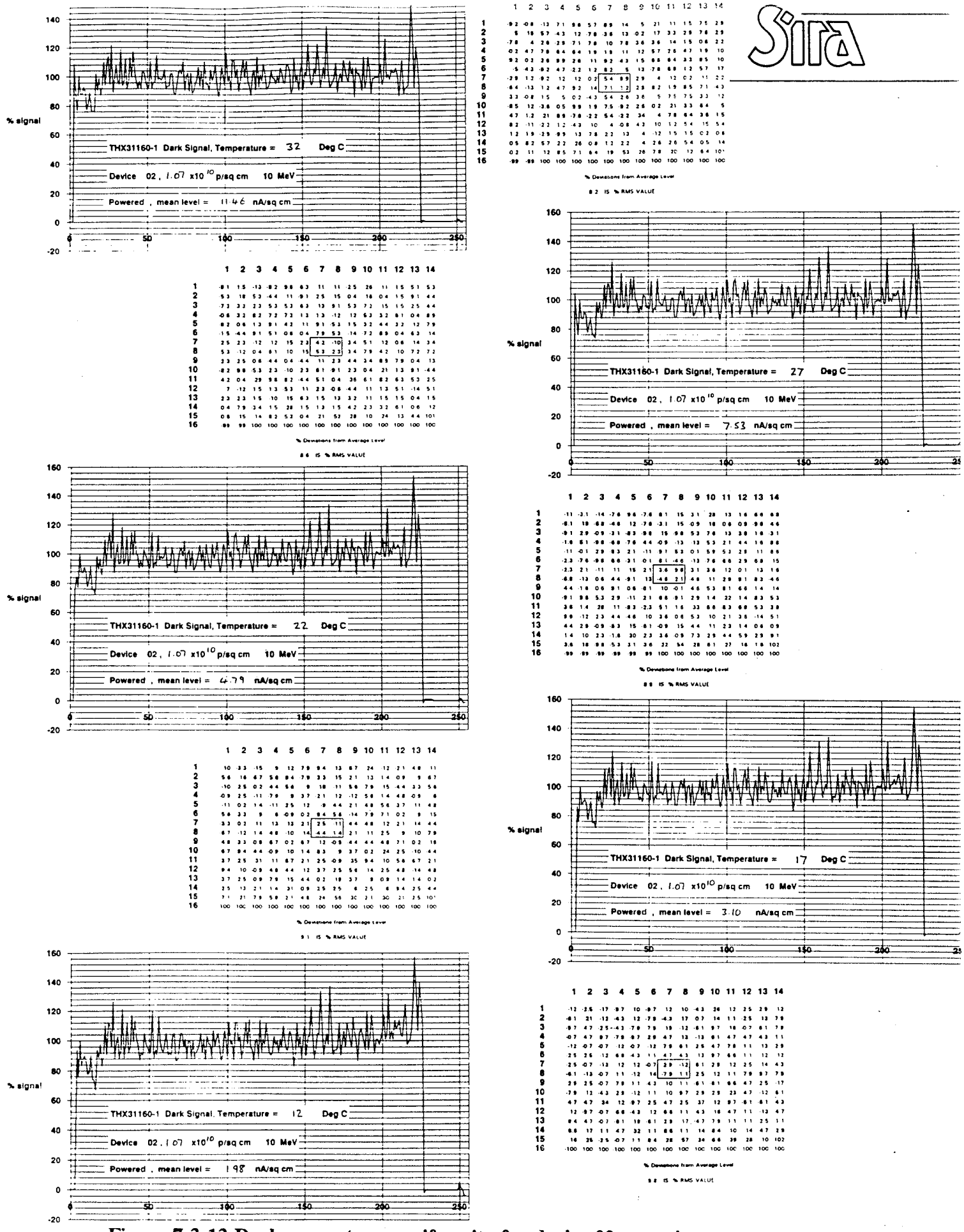

Figure 7.3-13 Dark current non-uniformity for device 02 at various temperatures

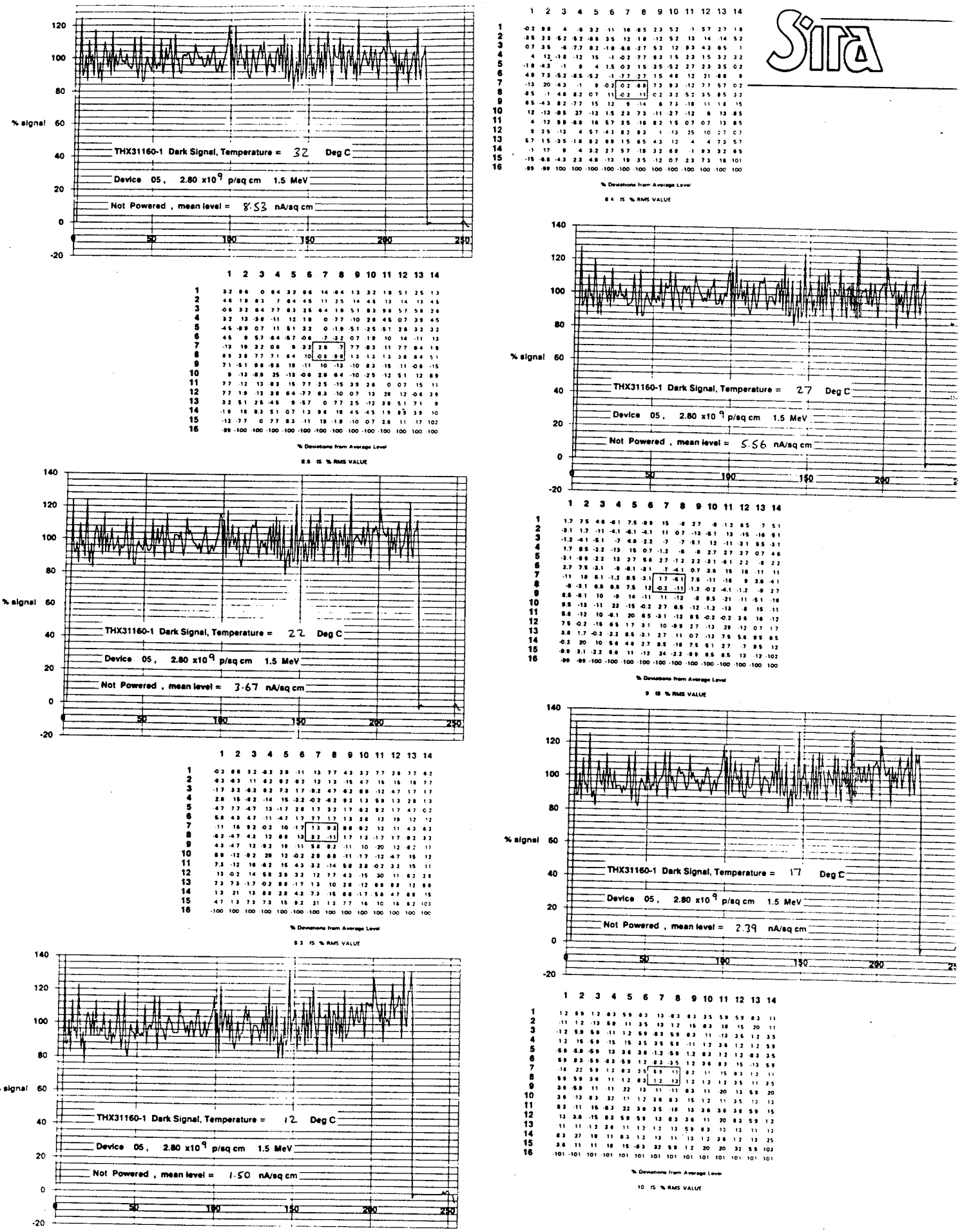

Figure 7.3-14 Dark current non-uniformity for device 05 at various temperatures

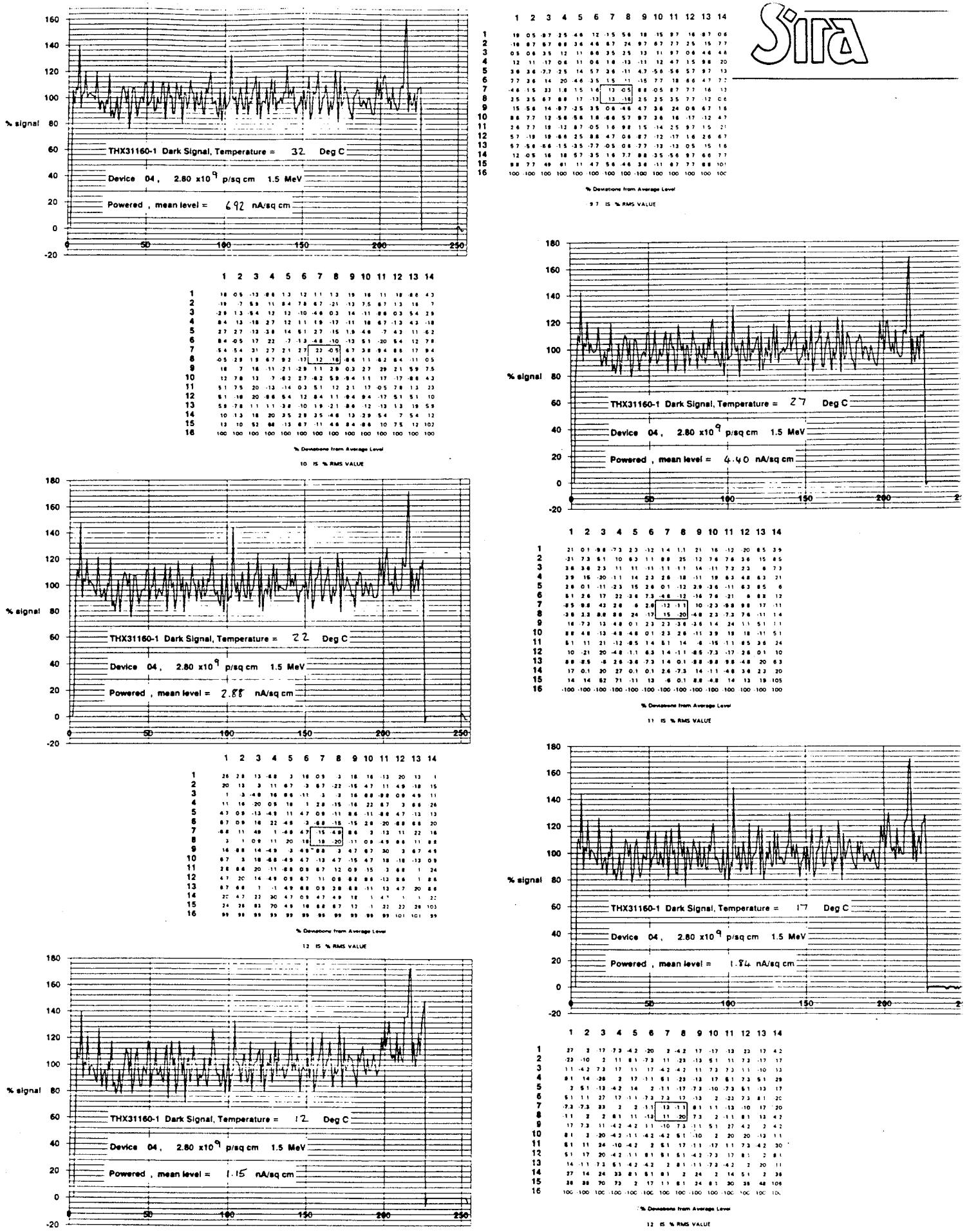

Figure 7.3-15 Dark current non-uniformity for device 04 at various temperatures

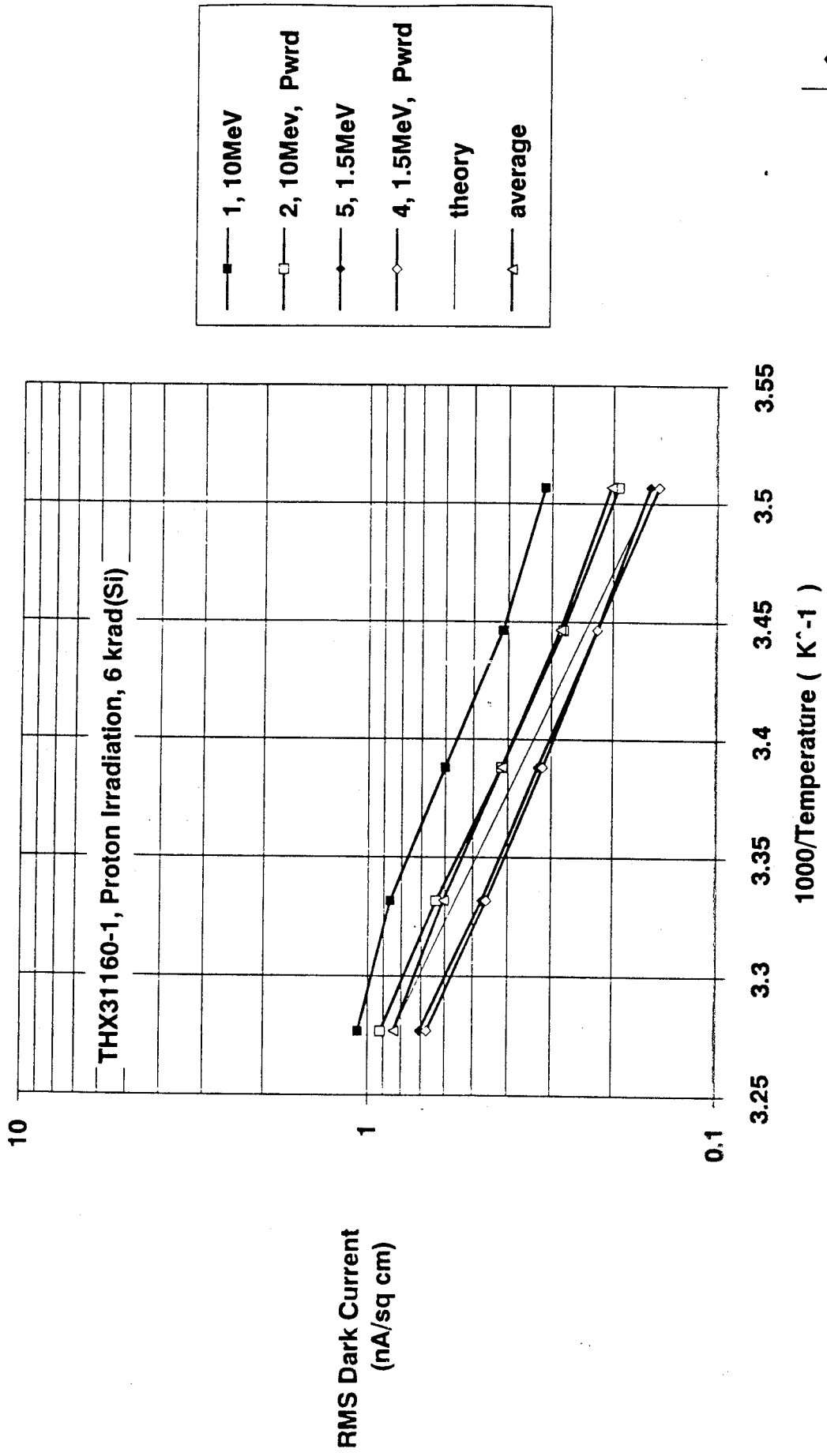

Figure 7.3-16 rms dark signal non-uniformity versus 1000/T for THX31160 devices

7.4 Bright Field Measurements

The operation without windows on the chip packages inevitably meant that there was particulate contamination of the surface of the CCDs. Accordingly, no serious attempt was made to measure dark-spot image blemishes (since in most cases these would have been due to the contamination). In any case, as discussed in the Co^{60} report [1], no change in bright field response with radiation was expected.

7.5 Readout Noise

This was measured for zero signal pixels in the over clocked porch region of the CCD waveform (c.f. para 4.4 of [1]). These values therefore represent the noise from the on-chip amplifier and the external electronics system. The noise for valid CCD pixels will be the root sum square of this noise and the shot noise on both the signal and the dark charge.

A correlated double sample (CDS) amplifier was used. This was of the clamp and sample type. Previous versions of this amplifier used by Sira have achieved noise levels of ~40 electrons rms with the THX31160 device at the present readout rate (pixel rate = 3 MHz). However the camera head was of a general purpose design which gave a readout noise of roughly 100 electrons rms unchanged by radiation. This is considerably below the required noise level for SILEX.

7.6 Threshold Voltages

7.6.1 V_{DR} Threshold Voltage

As in the previous Co^{60} investigation [1], the V_{DR} voltage supply to the reset transistor was decreased until there was a noticeable change in the appearance of bright field images. This method was found to give a consistent measure of the V_{DR} threshold voltage to an accuracy of ~0.1 V. An investigation of more quantitative methods is to be carried out in future but is outside the scope of the present report.

Results obtained 6 months after irradiation were as follows:

Device	Minimum V_{DR} voltage (V) after 6 krad (Si)
01, 10 MeV	10.7
02, 10 MeV,P	10.8
05, 1.5 MeV	10.8
04, 1.5 MeV,P	10.6

Unfortunately, due to time constraints at the radiation facility, no measurements were made before irradiation. However the above values are consistent with only small changes in the V_{DR} threshold voltage (of order 0.1 V). As for the TH7863 device only small changes are expected because of the decreased yield of electron - hole pairs in the oxide occasioned by low energy proton rather than high energy of Co^{60} radiation (c.f. para 3.2). The results of reference [1] remain the baseline database for changes in V_{DR} voltage.

7.6.2 Clock Threshold Voltages

As with the V_{DR} voltage discussed above, the clock high supply voltage (for all 3 clocks) was reduced and the clock low value increased to see if there was any change in threshold voltage. It was found that in all cases (ie. after each dose step) $V\phi_{high}$ could be reduced from 5.0 V to ~3.6 V before there was any noticeable effect. Likewise $V\phi_{low}$ could be

increased from 0 V to -3.0 V. The conclusion is that the radiation had no significant effect on the performance of the on-chip clock drivers.

7.6.3 V_{OS} DC Output Voltage

In the Co^{60} study [1] it was found that throughout all irradiations the smoothed value of the DC output voltage from the CCDs remained in the range 8.7 ± 0.3 V for all the devices measured, indicating that this parameter is not sensitive to radiation damage and varies little from device to device. Accordingly V_{OS} DC was not measured during these tests.

7.7 Power Consumption

Measurements of the I_{DD} drain current to the output amplifier were made using a DMM, with the CCDs operating in the dark at room temperature and with the standard clocking sequence (frame time = 100 μs). The results were as follows:

device	IDD (mA), Dose = 6 Krad (Si)			
	pre-irradiation	immediate	after 21 days	after 6 months
01, 10 MeV	19.00	19.56	19.05	19.29
02, 10 MeV,P	19.00	19.68	19.65	19.63
05, 1.5 MeV	18.47	18.82	18.85	18.81
04, 1.5 MeV	18.62	18.66	18.96	18.62

Thus only negligible changes in power consumption were found, as might be expected from previous comments on the electron-hole yield for low energy protons.

7.8 Charge Transfer Efficiency

The discussion of para 3.3.3.2 indicated that, for a fluence of 5 x 10^9 10 MeV p/cm^2, we might expect a charge transfer inefficiency given by

$$CTI \sim \frac{4.4}{S} \quad \frac{(\text{electrons})}{(\text{electrons})} \quad \text{per pixel at -50 °C}$$

where S is the signal size. Therefore for Cd^{109} x-ray illumination (S ~6000 electrons) we would expect a CTI of ~7.3 x 10^{-4} per pixel. In para 6.8 it was found that no damage was observed for TH7863 devices and the same was found for the THX31160-1. However, unlike the TH7863 case, here we only have a small number (~20) of transfers and so would expect from the JPL data an overall global CTI of only ~0.02 at most.

As discussed in section 6.8, this is on the limit of the present measurement accuracy (both for x-ray and spot illumination methods). All that can be said is that no change in CTI could be measured with the present techniques and no degradation is expected for SILEX.

7.9 Pocket Pumping and EPER Measurements

These are techniques using specialised bi-directional clocking schemes for measuring trapping states and charge transfer efficiency in more detail. These were used for the TH8763 device (para 6.9 and 6.9 of ref[1]) but cannot be used with the THX31160-1 since only 2-phase clocks are used and charge can only be clocked in one direction.

8. RESULTS FOR EEV CCD-02 DEVICES

These measurements were made as a by-product of Sira in-house programmes and use was made of breadboard drive electronics which was only temporarily available and which did not control the operating temperature of the CCDs. The only measurements were of charge to voltage conversion factor (plus deferred charge) and of dark images. These results are included in this report for comparison purposes only. The devices were irradiated in exactly the same way (ie. the same energies, fluences and masking technique) as the TH7863 devices, but only with 10MeV protons (since only two rather than four devices were irradiated).

8.1 Charge to Voltage Conversion Factor and Deferred Charge

As with the Thomson-CSF devices (para 6.1) a Cd^{109} x-ray source was used to provide a calibration of the output amplifier in electrons/ADC unit. These measurements gave a calibration of 159 $\pm$2 electrons/ADU which is equivalent to a charge to voltage conversion factor of 0.82μV/electron. Note, though, that this last value is somewhat uncertain because of the lack of an accurate measurement of the gain of the breadboard electronics amplifier. However this value is consistent with expectations (it cannot be greater than 0.9 or less than 0.5μV/electron). Only the overall calibration of 159 electrons/ADU is used here, and values of dark current in electrons/pixel were converted to nA/cm^2 using the formula

$$\text{dark current } (\text{nA/cm}^2) = \text{dark current (electrons/pixel)} \times \frac{1.6\times10^{-10}}{(22\times10^{-4})^2} \times \frac{1}{\text{integration time (s)}}$$

Since the pixel size is 22x22μm^2. The integration time was 0.149 or 0.250s depending on the clocking scheme used.

At the same time as performing an output calibration the charge deferred from 'single pixel' x-ray events to surrounding pixels could be measured. As for the TH7863 (para 6.3) no deferred charge was observable (to an accuracy ~2%) implying no change in CTE. As discussed in para 6.8 this implies that the degradation for room temperature conditions and fast clock rates is less than as measured by previous workers for low temperature (~-50°C) and slow scan conditions (though in the present case the frame rate was slower than for the TH7863 devices: 7Hz rather than 24Hz).

8.2 Dark Field Measurements

Although the CCD temperature was not actively controlled during these measurements, the CCD was mounted on a heatsink block in a temperature controlled room and the CCD packages were expected to be at 19 $\pm$1°C throughout. All measurements were made on averages of 16 frames and the same analysis procedures as for the TH7863 were used. As for the TH7863 CCDs, the devices were operated in frame transfer mode. As mentioned in para 6.3, there are two components to the dark current which arise from generation at the surface (and influenced by ionisation damage) and generation in the depletion regions (and influenced by displacement damage). Unlike the TH7863 which has diode protection structures which do not allow operation of the device with clock-low voltages below substrate voltage, the diode protection circuits on EEV devices allow the substrate voltage to be increased and the devices to be operated in a partially inverted mode. This was achieved with clock low voltages at 0V (clock high's at 10V) with the substrate voltage increased from its usual value of 7.5V (non inverted) to -9V. In this way the surface of the device under two of the clock electrodes (those at 0V) is inverted from n to p-type and surface states which generate dark charge are filled by holes (from the channel stops) [37].

Thus surface generated image area dark charge is suppressed by a factor ~3 (the ratio of the surface areas which can generate dark charge).

A similar reduction (factor 3) might be expected for the component generated in the storage region. However during readout the storage region clocks are operating (to transfer charge out of the device) and it can happen that the clock switching time is less than the trapping time of the interface states. In this case these interface traps are kept permanently full and surface generation is completely suppressed, as recently discussed by Burke and Gajar [39]. Measurements were made 12 days after irradiation, with non-inverting conditions and for one device (number 02) partially inverted and after 75 days storage for both devices partially inverted. Figure 8.2-1 shows plots of the maximum signal in any column versus column number for images with the dark charge slope (ie. storage component) subtracted - ie. for the image component. The four dose regions can be clearly seen as can the size of the largest dark spikes.

8.2.1 Ionisation Damage

As with the TH7863 devices, measurements were made of the average dark current and of the image and storage components estimated as shown in figure 6.3-1.

Figure 8.2-2 shows the average, image and storage dark currents for the four dose regions (0, 3, 6 and 9krad) on each device at 12 days and 75 days. From these plots we can make several conclusions. It should be noted however that, as discussed in para 3.2, the effects of 10MeV protons may be a factor 2-3 less than for the space environment (and for Co^{60} gamma rays)

i) dark current increases linearly with 10MeV dose (or fluence).

ii) the increases in storage region dark current, even when operating non-inverted, are much less than for the TH7863.

iii) the image region component (non-inverted) is similarly small and does not show anomalous annealing/dose rate effects as noted for the TH7863.

iv) partial inversion suppresses the image region component by the expected factor 3 and the storage region component for the zero dose region is reduced to near zero (from 1.1 down to 0.1 nA/cm^2). Presumably because the clocking operation is giving a pseudo fully inverted operation, as discussed above.

v) after irradiation however the storage component for the partially inverted devices increases; the fractional increase being large. This is an important result, and may be due to radiation-induced traps having different time constants from the pre-existing ones. The indication is that radiation effects on the operation of inverted mode devices should be considered in more detail in future programmes.

vi) Despite the increase in storage component the average dark current for partial inversion is only ~$1nA/cm^2$ at room temperature after 9krad(Si) of 10MeV protons and is comparable with the pre-irradiation value for EEV and TH7863 CCDs when operated non-inverted. Even the non-inverted value is only ~$3nA/cm^2$ after 9krad(Si).

vii) The partially inverted device measured after 12 days shows somewhat erratic and non-uniform behaviour (the zero dose storage component is negative). This is probably because the substrate voltage, V_{SS}, was rather high (9.4V)

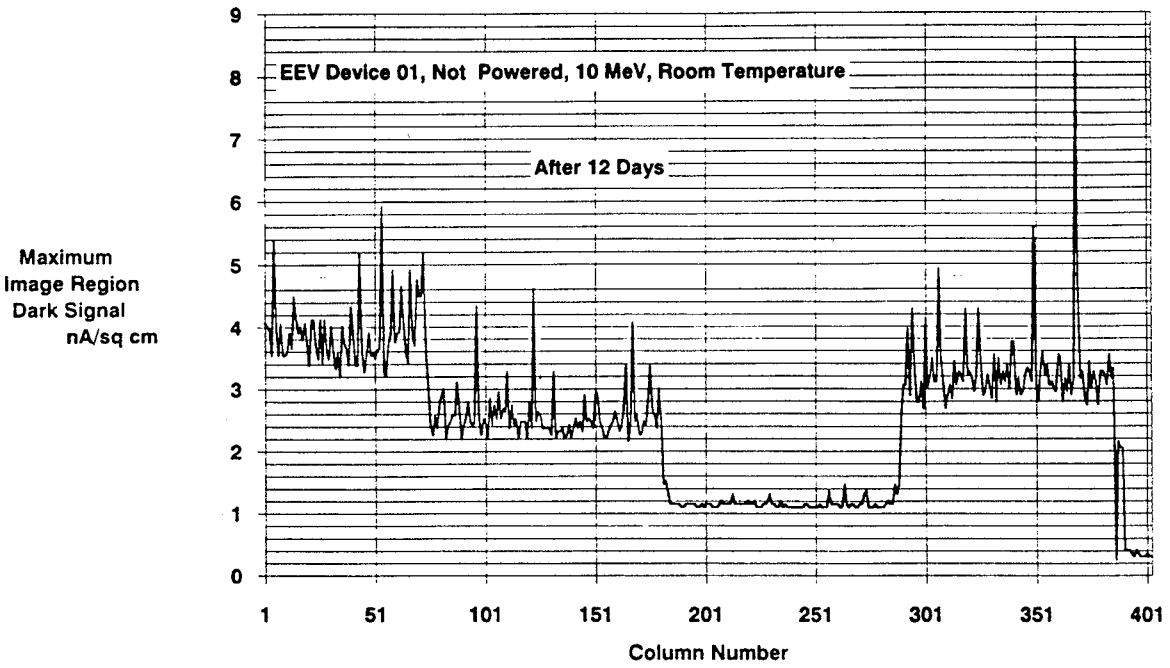

Figure 8.2-1 Maximum signal in each column for EEV CCD-02 devices (image region component)

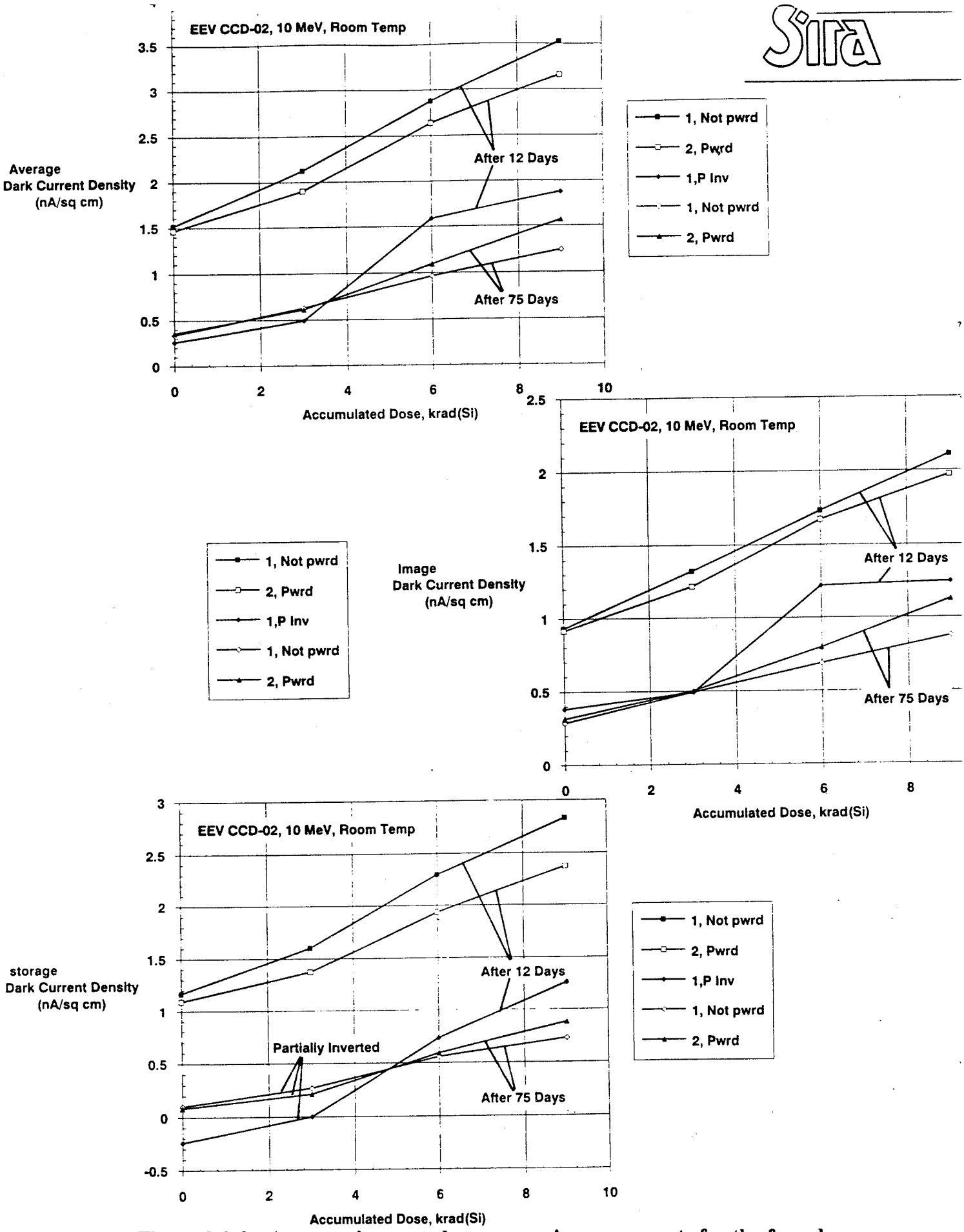

Figure 8.2-2 Average, image and storage region components for the four dose regions on each EEV CCD

and this caused some large scale non-uniformity. V_{SS} was later reduced to 9.0V. It should be noted that results after 12 and 75 days are comparable and there is no evidence for reverse annealing.

viii) In contrast to the results for Thomson-CSF devices, the device powered during irradiation does not show the most damage - if anything the unbiased CCD shows the higher dark current.

8.2.3 Displacement Damage

Measurements of dark signal nonuniformity were made for images with the storage component subtracted. Figures 8.2-3 and 8.2-4 show histograms for the two devices and figure 8.2-5 shows the variance of the nonuniformity for the four dose regions (0, 3, 6 and 9krad). We make the following comments:

i) as for the TH7863 CCDs the bulk damage is independent of bias state during irradiation.

ii) operating in partial inversion has no effect on bulk damage (compare 12 day data).

iii) as for the TH7863 CCDs there is significant annealing of the damage with storage at room temperature (compare 12 and 75 day data). Hence it is important that long term annealing should be taken into account when assessing the effect of displacement damage.

iv) the variance of the nonuniformity is proportional to proton fluence (as for the TH7863 devices in figure 6.3-32 and expected from theory [32]).

v) the scale of the nonuniformity is less for EEV devices; ie. on average, the dark charge spikes are of smaller size (a more detailed comparison will be made in section 9).

The largest dark current spikes can be seen in the extreme value statistics plots of figures 8.2-6 and 8.2-7. These were derived using the method explained in para 6.3.2.4. As for the TH7863 there are several spikes of size ~2nA/cm^2 which lie outside the main distribution and it is postulated that these are caused by elastic collisions which happen to occur in high field regions of the CCD (eg. near the channel stops) and therefore give rise to field-enhanced emission. It has already been stated that operating in partial inversion does not, in general, change the displacement-damage distributions and so the 12 day (non-inverted) and 75 day (partially inverted) plots can be directly compared. In doing this it can be seen that, as stated above, the smaller dark charge spikes show significant annealing after storage at room temperature. However this is not always so for the larger spikes, some of which remain largely unchanged.

Looking at figure 8.2-7 which compares non-inverted and partially inverted plots for the same device (at the same annealing time) it can again be seen that partial inversion does not, in general, change the distribution but the two largest bins were significantly increased when operating at higher substrate voltage.

In fact looking at actual pixel values it can be seen that a large new spike is present in the partially inverted image which was not present before (c.f. figure 8.2-8). These changes may be due to variations in the field distribution within the device.

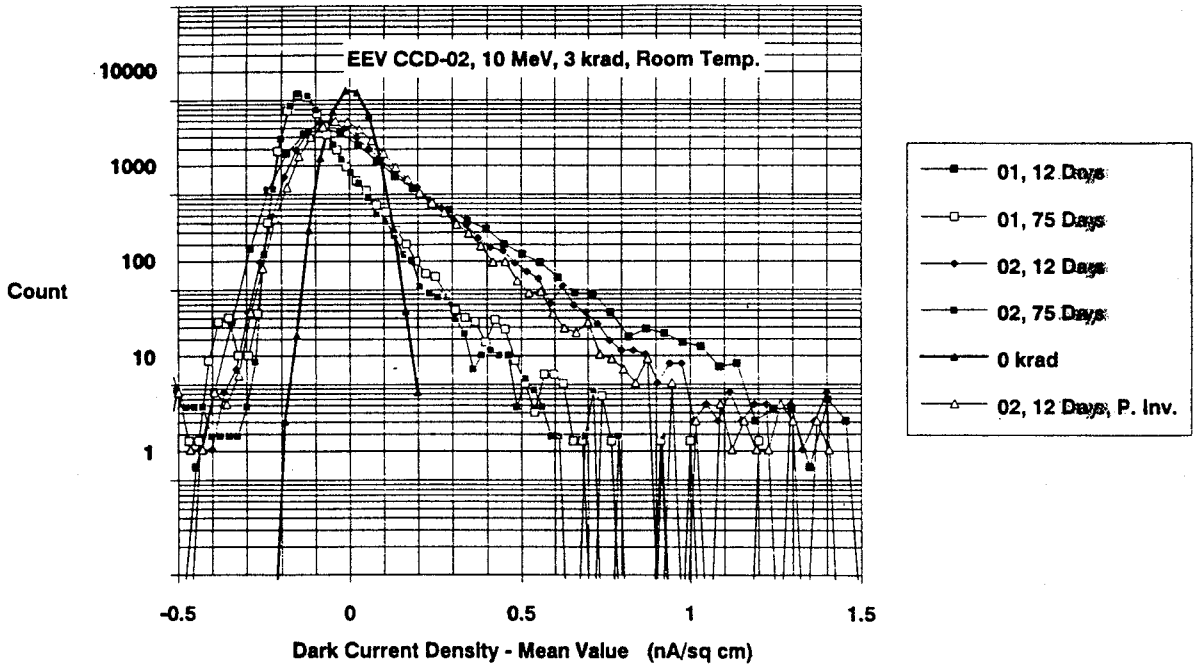

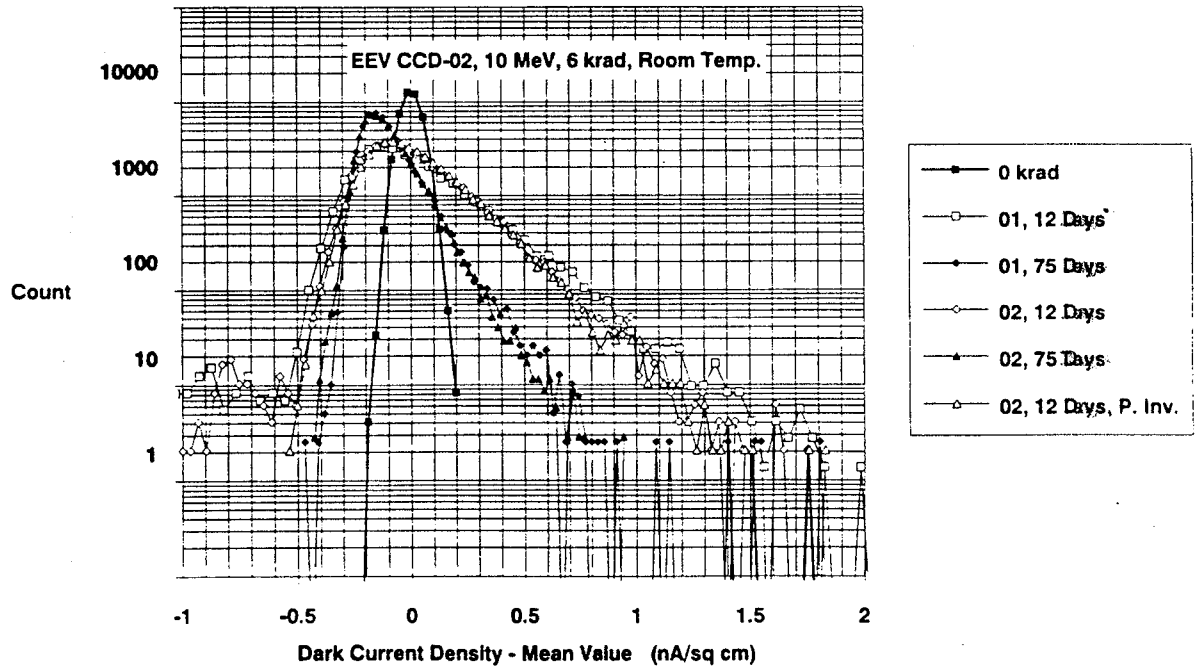

Figure 8.2-3 Dark current histograms for EEV CCD-02 devices at room temperature

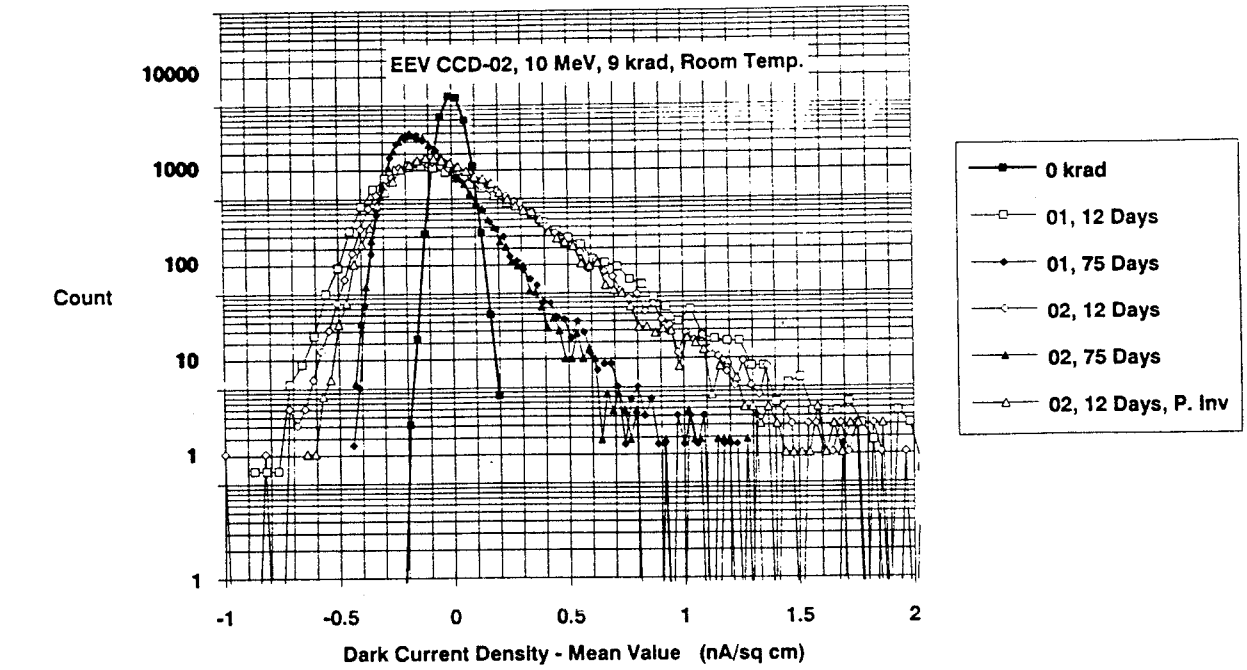

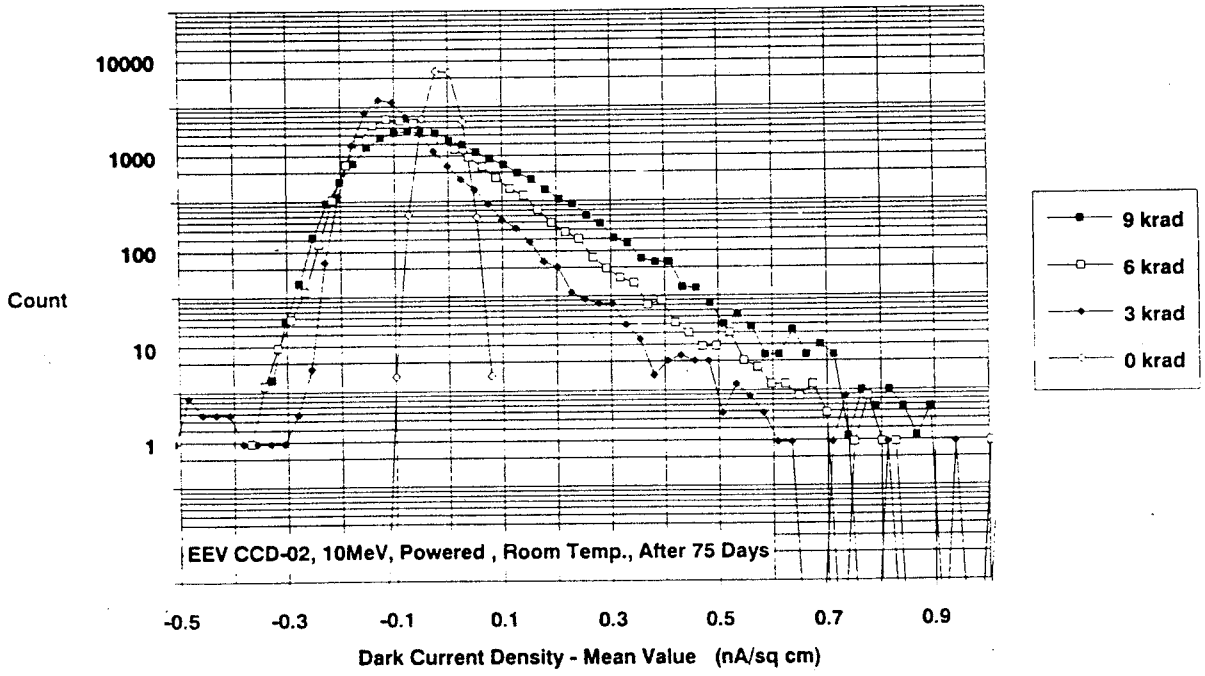

Figure 8.2-4 Dark current histograms for EEV CCD-02 devices at room temperature

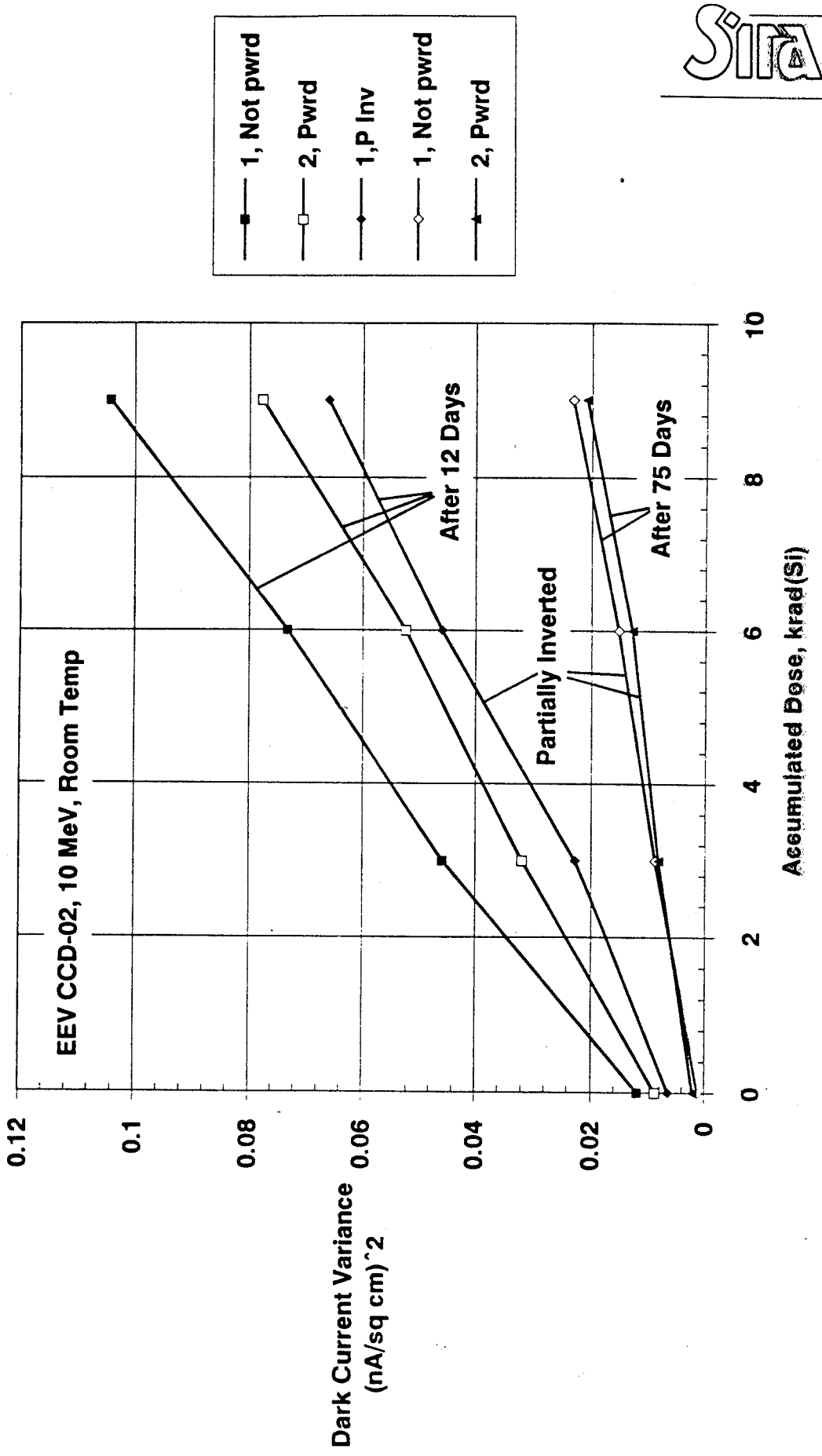

Figure 8.2-5 Variance of the dark signal nonuniformity versus dose for EEV CCD-02 devices at room temperature

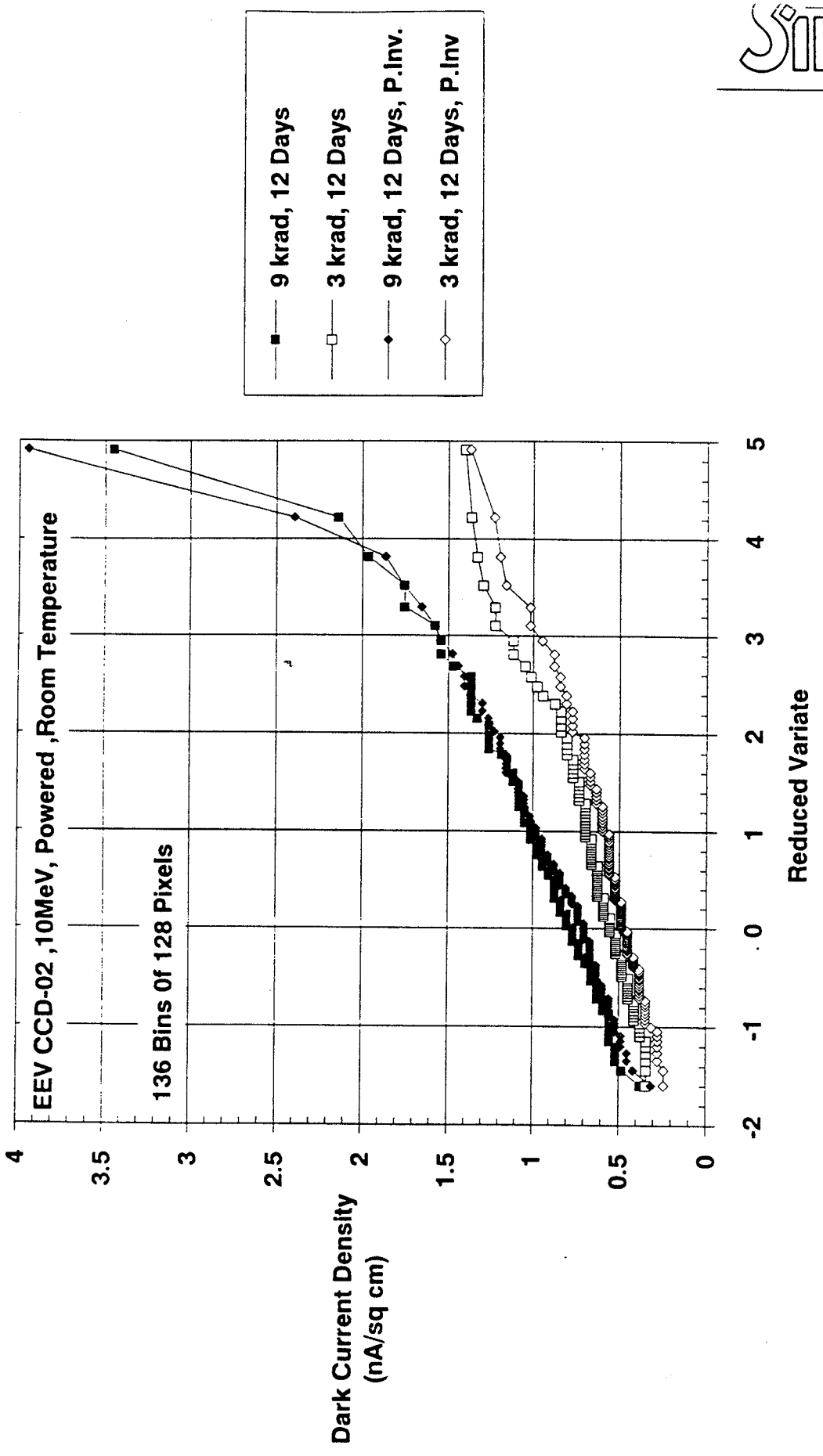

Figure 8.2-6 Extreme value statistics plots for EEV CCD-02 devices at room temperature

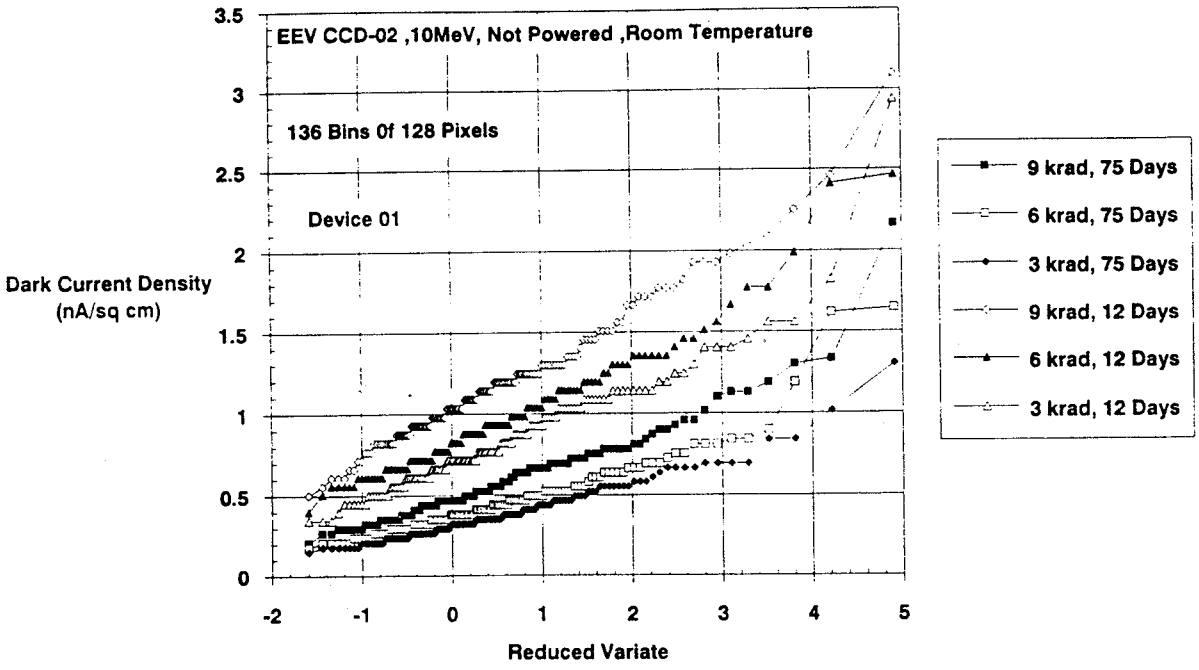

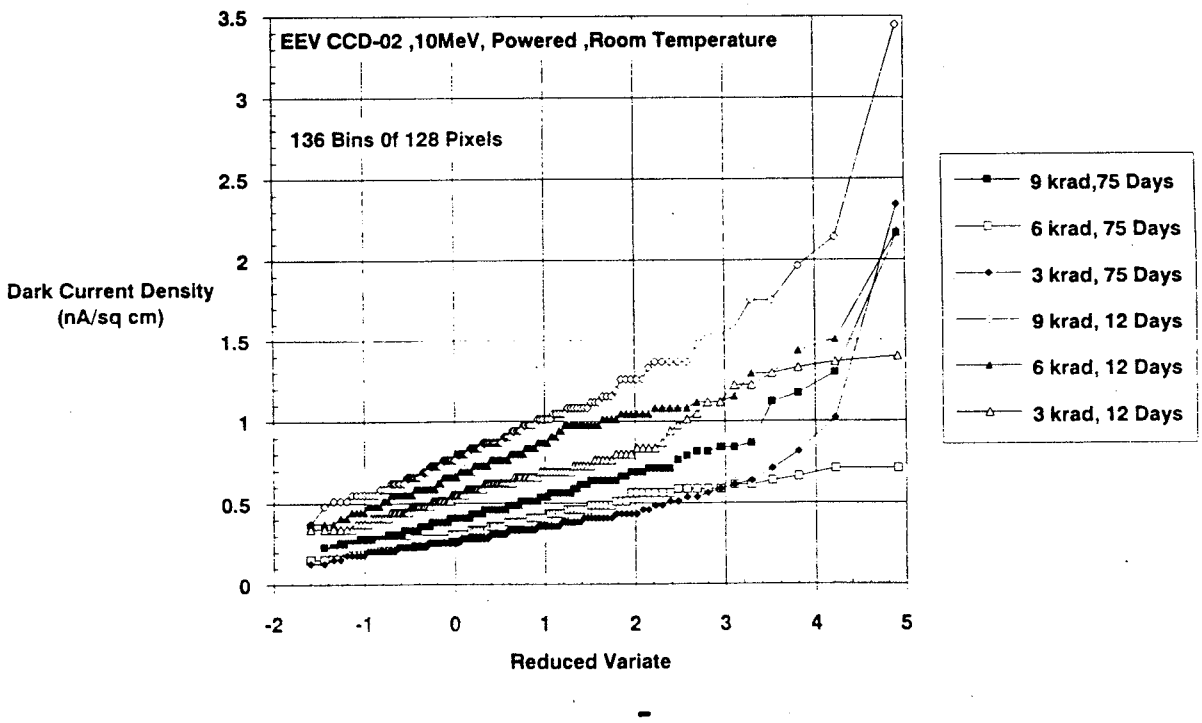

Figure 8.2-7 Extreme value statistics plot for EEV CCD-02 device 02 showing the effect of operating in partial inversion

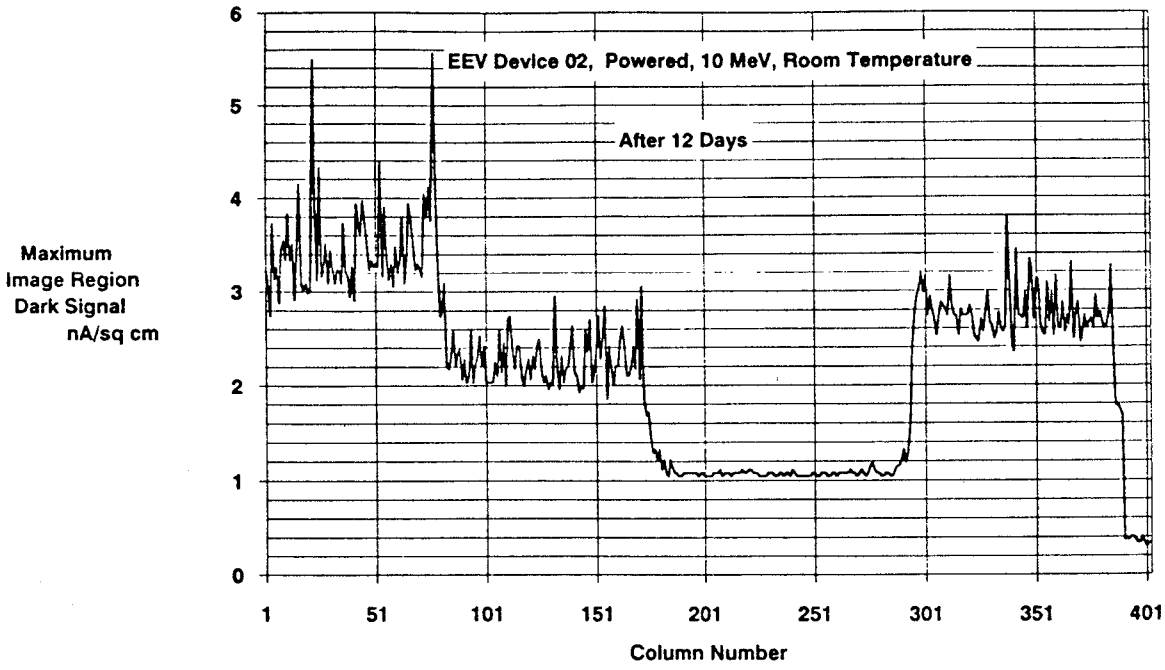

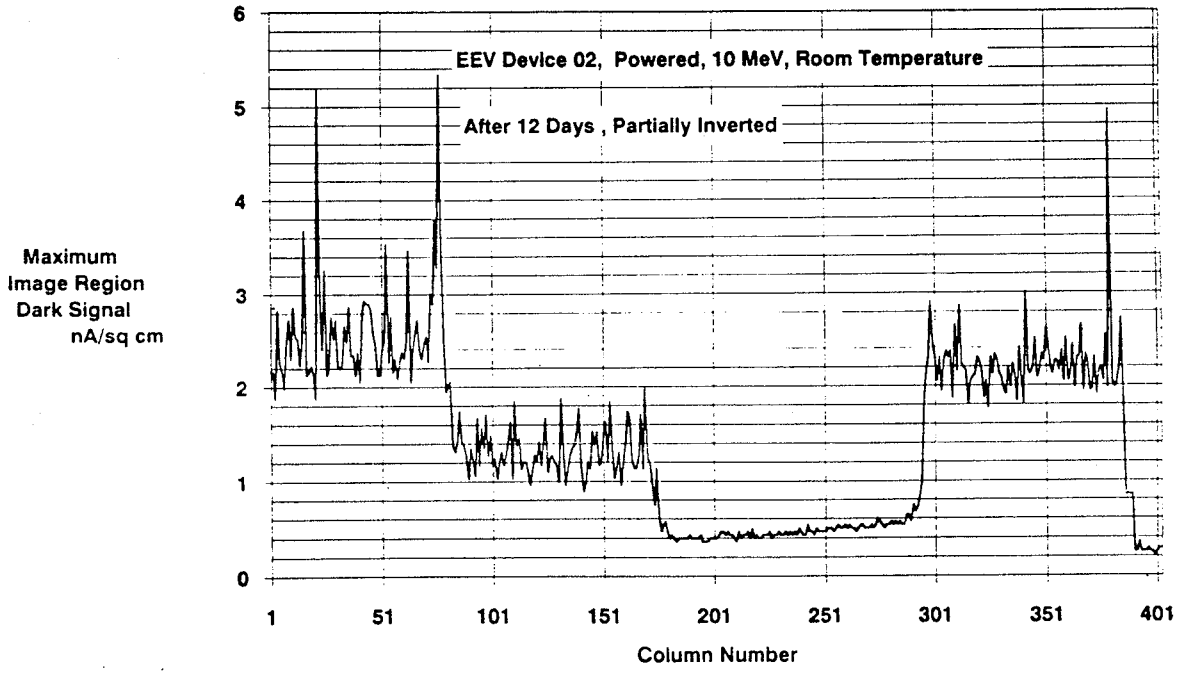

Figure 8.2-8 Plots of the maximum signal in each column for non-inverted and partially inverted operation showing the appearance of a new dark charge spike

9. INTERPRETATION OF DATA AND DEVICE MODELLING

We return now to the questions posed in the overview in section 2 of this report. An examination of the data given in the previous three sections provides answers to most of these:

Ionisation damage

i) We have seen that the ionisation damage for 1.5 and 10MeV protons for the present batches of devices is less than predicted from the previous Cobalt60 tests [1] and that the damage is worse for 10MeV, than for 1.5MeV irradiation. However this is consistent with our expectations since low energy protons have a high rate of energy loss (dE/dx) in SiO_2 and the average densities in the particle tracks will be high - particularly at 1.5MeV. Hence the chances of electron-hole recombination before holes can become trapped and cause damage is also high. Thus we expect less damage for low energy protons compared with Co^{60} gamma rays or the high energy protons present in the trapped radiation belts and solar flares (and less damage at 1.5 compared with 10MeV). The reduction in damage will depend on the nature of the damage mechanisms and on the electric field present (which affects the electron-hole recombination rate) and so it is difficult to make exact predictions from proton data - particularly as the dose rates used are large and there are further errors introduced because of space charge effects and differences in annealing behaviour. These uncertainties mean that, in general, ionisation damage effects are best studied using Co^{60} rather than proton irradiation. Nevertheless it can be said that the present data is consistent with the previous results and gives some degree of confirmation. As found previously for Thomson-CSF devices the damage is worse for devices which are biased during irradiation; but, in contrast, for EEV devices no significant bias dependence was found for dark current damage.

ii) When annealing behaviour is taken into account, the tolerance of the present Thomson-CSF devices appears broadly similar to those previously studied; however the uncertainties in damage production for proton irradiation and the differences in annealing behaviour mean that a detailed comparison cannot be made.

For the EEV devices studied the ionisation-induced dark current appeared to be less and showed no reverse annealing. In addition these devices were capable of being operated in a partially inverted mode where a fraction of the surface dark charge was suppressed.

iii) For the TH7863 devices the storage region dark charge increases quickly, as found before. However the reverse annealing of the image area component (which arises from the part of the CCD not masked by aluminium) was very slow at room temperature - so that virtually no change was observed after 3 months storage. Reverse annealing did occur after a high temperature anneal, and anomalous large scale nonuniformity affects disappeared at the same time. These results could be explained by a relatively small change in the activation energy for image component reverse annealing (~0.7eV rather than ~0.5eV).

iv) Spot illumination measurements of linearity and full well capacity for the Thomson-CSF devices show that for the TH7863 the pre-irradiation value of saturation level is reduced from ~10^6 electrons (uniform) to ~6.4×10^5 electrons (spot) and that a further decrease is observed after irradiation. Allowing for the reduced damage for low energy protons a value of 2 to 3×10^5 electrons might be predicted after 6krad(Si) of space radiation. For the THX31160-1 however the spot results were little different from the uniform illumination results and were unchanged by the radiation.

Bulk displacement damage

v) Degradation of charge transfer efficiency does not appear to be a problem for SILEX conditions.

vi) For both TH7863 and EEV devices the proton-induced displacement damage produces a tail in the nonuniformity histograms which extends to spikes ~1nA/cm^2 at 22°C. This is for several months storage at room temperature. The initial damage is higher. Measurements on the TH7863 indicate that the shape of the spike distribution scales with temperature in the usual way for silicon dark current generation in the depletion region. For both devices the damage is independent of bias state during irradiation and partial inversion of EEV devices does not suppress the bulk component (as expected).

vii) Both the TH7863 and EEV devices gave a small number of large dark charge spikes which lay outside the main distribution. These ranged in size up to ~3nA/cm^2 at room temperature and tended to show rather erratic behaviour with temperature and long term storage. These spikes are tentatively associated with field-enhanced emission. It can certainly be said, though, that field enhancement effects are much less severe than encountered with some virtual phase CCDs ([17], [30]) where avalanche breakdown effects seem to occur. The THX31160-1 devices showed fairly high nonuniformity but with the small number of pixels it is difficult to tell whether this is due to field enhancement or statistical fluctuations.

viii) So far we have only discussed the damage found at 1.5 and 10MeV. These energies are appreciably lower than those expected for the use environment where protons of energy up to several hundred MeV will be encountered. It is therefore necessary to discuss the nature of the dark charge histograms expected for higher energy protons. This discussion forms the remainder of this section. Consideration of implications for mission performance is postponed until section 10.

9.1 Modelling of Displacement Damage Induced CCD Dark Current Nonuniformity

As discussed in para 3.3, we expect the average increase in dark current (and CTI) to be proportional to the non-ionising energy loss (NIEL) of the particles. This allows a way of predicting the effects for any particle spectrum once the constant of proportionality is found (from measurements at a few selected energies) and the NIEL is found from the known variation with particle type and energy (c.f. figure 3-7). However in our situation the average dark current cannot be measured because it cannot be separated from the (generally larger) component due to ionisation damage - only in devices operating in a fully inverted mode, where only the bulk dark current is important, can the average displacement-induced dark current be found. In any case it is the non-uniformity which is of most importance to us and this is <u>not</u> predicted by average NIEL calculations.

Instead it is necessary to model the displacement damage in detail by considering the cross sections for the proton interactions and modelling the damage produced in each case. This has been done by workers at NRL and their associates [31] and their approach is discussed here.

As mentioned in para 3.3.1, both elastic and inelastic collisions need to be considered. Table 9-1 below gives cross sections, damage energies (ie. the energy loss which goes into production of lattice displacements) and variances of the damage energy for proton energies of 12, 22 and 63MeV. It is seen that elastic collisions have much the largest cross sections but the damage energy is much less. Since the dark current is proportional to damage energy (c.f. para 3.3.3) it is the inelastic collisions (though rare) which are

responsible for the tail on the dark current distribution (neglecting, for a moment, field enhancement). Note that the table is taken from reference [31] which gives damage energies slightly different from those quoted in [29] and [35] because of changes in the calculation of recoil ionisation energy loss and the inclusion of nuclear elastic interactions.

Table 9-1 Parameters for Proton Interactions in Silicon (from [31])

Elastic reactions

Proton energy (MeV)	Cross-section (barns)	Mean damage energy (MeV)	Variance damage energy $(MeV)^2$
12	1548	1.76×10^{-4}	4.77×10^{-6}
22	857	2.13×10^{-4}	7.71×10^{-6}
63	318	2.87×10^{-4}	1.62×10^{-5}
Inelastic reactions			
12	0.670	0.0765	2.05×10^{-3}
22	0.723	0.111	2.71×10^{-3}
63	0.523	0.152	3.11×10^{-3}

Note that the variance of the damage energy arises from Poisson statistics and is proportional to fluence.

The mean damage energy and its variance can only be derived from a knowledge of the target recoil spectra and calculations for other proton energies are outside the scope of the present study. Fortunately data is given at 12MeV, which is close to the 10MeV energy used here. Hence it should be possible to compare the theory with the present data at that energy.

The cross sections for inelastic reactions can, however, be predicted for any energy greater than 10MeV using the empirical formulae given by Letaw et al [41]:

$$\sigma(E) = \sigma(he)[1-0.62e^{-E/200} \sin(10.9E^{-0.28})] \quad (9\text{-}1)$$

where the high energy asymptote, $\sigma(he)$, is given by

$$\sigma(he) = 45A^{0.7} [1+0.016 \sin(5.3-2.63 \ln A)] \text{ mb} \quad (9\text{-}2)$$

here A is the atomic mass and E the proton energy (in MeV). Figure 9-1 shows values from equations (9-1) and (9-2) for silicon and values are tabulated in table 9-2 below. Letaw et al do not give values below 10MeV because of the presence of resonances in that

region (and because the experimental data are not so accurate). However Janni [42] gives values for aluminium (A=27) which will be close to those for silicon (A=28) down to 1.0MeV and these are given in table 9-3. It is seen that at energies around 1.5MeV the inelastic cross-section is small (~0.1 barns). Note that the values for the inelastic total cross-sections at 12, 22 and 63MeV as taken from table 9-2 are the same as given in table 9-1: thus revealing the source of the NRL data.

Knowing the cross-sections, damage energies and damage energy variances the shape of the CCD damage histograms can be modelled.

Elastic reactions

Since the cross-section for elastic scattering is high, it is often the case that there will be a large number of interactions per pixel. For example taking the 12MeV value of 1548 barns as applicable to our 10MeV data we would expect the number of interactions to be given by

$$n_{elastic} = \sigma \rho V. \frac{N_A}{A} \times \phi$$

where ρ is the density (=2.32 g/cm^3), A is the atomic weight (=28), N_A is Avagadro's number (=6.02x10^{23}), ϕ is the fluence and V is the interaction volume of each pixel, ie. the volume of the depletion region. Allowing for the presence of the CCD channel stops we take V as 18x18x4μm^3 = 1300μm^3, though an exact value is not known (coincidentally this is the same volume as used for the CCDs tested by the NRL group). For a dose of 3krad of 10MeV protons the fluence was 5.37x10^9 p/cm^2 and hence we get

$$n_{elastic} = 537 \text{ interactions per pixel}$$

Because this number is large, the spectrum of the damage energy given to the CCD (which is proportional to the dark current histogram) will be gaussian in shape with a mean given by n times the mean single event damage energy variance ie.

$$\text{Mean}_{elastic} = 537 \times 1.76 \times 10^{-4} = 0.0945 \text{ MeV}$$

$$\text{Variance}_{elastic} = 537 \times 4.77 \times 10^{-6} = 0.00256 \text{ (MeV)}^2$$

Inelastic collisions

Again using 12MeV data as valid at 10MeV (and assuming ϕ=5.37x10^9 p/cm^2, V=1300μm^2) we get

$$n_{elastic} = 0.23 \text{ interactions per pixel}$$

(or n=0.21 using the actual value at 10MeV from table 9-2).

Table 9-2 Total Inelastic Cross-sections for Protons on Silicon, Calculated from [41]

Proton energy (MeV)	σ (barns), 1 barn=10^{-28} m^2
10	0.613
12	0.670
15	0.714
20	0.727
22	0.723
25	0.711
30	0.683
35	0.654
40	0.625
45	0.599
50	0.575
55	0.553
60	0.534
63	0.523
70	0.502
80	0.477
90	0.457
100	0.442
120	0.421
140	0.409
160	0.403
200	0.400

Table 9-3 Total Inelastic cross-sections for protons on Aluminium, from reference [42]

Proton energy (MeV)	σ (barns)
1.0	0.0157
2.0	0.108
3.0	0.192
5.0	0.322
6.0	0.389
9.0	0.550
10.0	0.641

Since this number is small, according to [31], we should consider a discrete Poisson distribution of inelastic collisions; ie. the probability of having N inelastic recoils in a given pixel is given by

$$\text{Probability}_N = \frac{n^N \; e^{-n}}{N!} \qquad (9\text{-}3)$$

where in this case $n = n_{eleastic} = 0.23$. Thus we have the following probabilities.:-

Table 9-4 Poisson Probabilities (for 5.37×10^9 p/cm^2)

Number of inelastic events	Probability (12MeV)	(22MeV)	(63MeV)
0	0.795	0.779	0.835
1	0.183	0.195	0.150
2	0.021	0.024	0.0135
3	0.0016	0.0020	0.00081
4	0.000093	0.00013	0.000037
$n_{elastic}$	0.23	0.25	0.18

The NRL group [31] used a two parameter gamma distribution as an approximation to the probability density function (pdf) for single events. This function is commonly used in statistical and reliability theory. It is given by

$$\text{pdf}(x) = \frac{\lambda}{\Gamma(a)} (\lambda x)^{a-1} \; e^{-\lambda x} \qquad (9\text{-}4)$$

where $\Gamma(a)$ is the gamma function

the mean $(\mu) = a/\lambda$

and $\sigma = a^{1/2} / \lambda$

ie. $\lambda = \mu/\sigma^2$ and $a = (\mu/\sigma)^2$

In our case we have $\mu = 0.0765$ MeV and $\sigma^2 = 2.05 \times 10^{-3}$ (MeV)^2

giving $\lambda = 37.32$ MeV^{-1} and $a = 2.855$ for our single event distribution.

Note that the factor $\lambda/\Gamma(a)$ is simply for nomalisation ($\Gamma(a)$ is simply found from tables; $\Gamma(2.855) = 1.76$). It is the parameter $a = (\mu/\sigma)^2$ ie. the relative variance which determines the shape of the single event probability density function. The gaussian

distribution (for 537 elastic events) and the gamma function (for 1 inelastic event) are shown in figure 9-1 as a function of damage energy. As we move to different proton energies the gaussian shape of the elastic distribution will not change (though μ and σ will) provided that the number of collisions per pixel is still large (still valid for 5.37×10^9 63MeV protons/cm^2). However the shape of the inelastic distribution will change with proton energy. Hence, as the proton energy increases from 12 to 63MeV the balance between elastic and inelastic contributions changes (resulting in a more pronounced tail to the dark current histograms).

Since the elastic and inelastic collisions occur independently the total damage probability is the convolution of the separate probability density functions. Thus for zero elastic collisions we simply have the gaussian distribution, for one inelastic we have the convolution of a gaussian and the gamma distribution of equation (9-3), for 2 inelastics we have the gamma function convoluted with itself, in turn convoluted with the gaussian function - and so on. Thus a complete spectrum can be built up. For the 12MeV data and a fluence of 5.37×10^9 p/cm^2 this gives the plots of figure 9-2 where the separate components due to 0, 1 and 2 inelastics are shown as well as gaussian approximations for 3 and 4 inelastics. These latter functions were plotted under the assumption that the 3- and 4-fold convolutions will be near gaussian with mean and variance 3 and 4 times the single event values. It can be seen, in fact, that these approximations are probably not valid but by this time the probability function has in any case fallen to very small values. Note that in figure 9-2 the separate distributions are weighted according to the values in table 9-4.

Having now determined the shape of the damage probability function we have one free parameter to obtain a fit to the dark current histograms. This is the constant of proportionality between lattice damage and dark current. This will be a device specific parameter which is determined by the number of displacements which result in stable defects and on the effectiveness of these stable defects in generating dark charge (ie. on their energy level). Figures 9-3 and 9-4 show attempted fits for the 3krad 10MeV proton data (5.37×10^9 p/cm^2) for the TH7863 and EEV devices. These were obtained with the following damage-to-dark current factors:

Device	Damage-to-dark current factor at 10MeV (12MeV nuclear parameters)
TH7863 after 3 months	2.4nA/cm^2 per MeV damage
EEV after 75 days	1.0 nA/cm^2 per MeV damage
EEV after 12 days	2.2 nA/cm^2 per MeV damage

It is seen that the fits are reasonably good for the EEV device and for the TH7863 device after 75 days, but the immediate TH7863 data gives a poor fit. The smaller amount of damage for the EEV device at 75 days reflects the annealing which has occurred.

These damage factors are comparable with those found for CIDs by the NRL group [31] who found a value of 2.2 nA/cm^2 per MeV. Note that the value for the EEV device after long term storage is a factor 2 less than for the TH7863.

Using these damage factors, although approximate, allows a method for predicting the dark charge histograms for an environment with higher energy protons. The increase in the mean dark current density caused by bulk damage is given by

$$\text{dark current density}_{\text{bulk damage}} = \text{damage factor} \times (n_e E_e + n_i E_i)$$

where the e's and i's refer to elastic and inelastic collisions. At 10MeV (12MeV data) we have n_e=537, E_e=1.76x10^{-4} MeV and n_i=0.23, E_i=0.0765 MeV.

Hence for a TH7863 (damage factor = 2.4nA/cm^2 per MeV damage) we expect

$$\text{dark current density}_{\text{bulk damage}} = 0.27\text{nA/cm}^2 \text{ at } 22°\text{C}.$$

This supports the assumption that, for the TH7863, the change in mean level is dominated by ionisation effects.

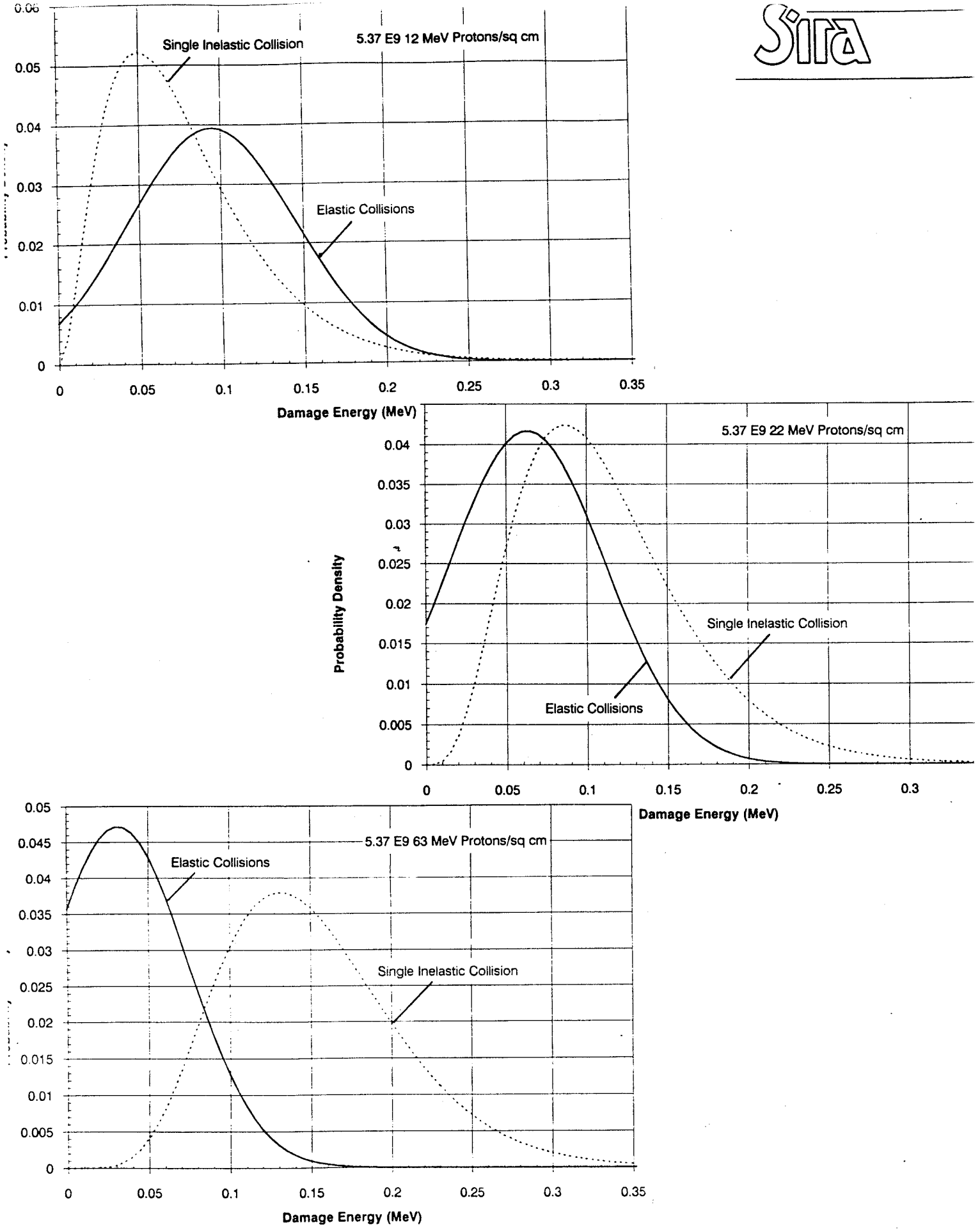

Figure 9-1 Probability density functions for elastic and single inelastic collisions for 5.37×10^2 12, 22 and 63MeV protons/cm^2 (V=1300μm^3)

A/9058/00

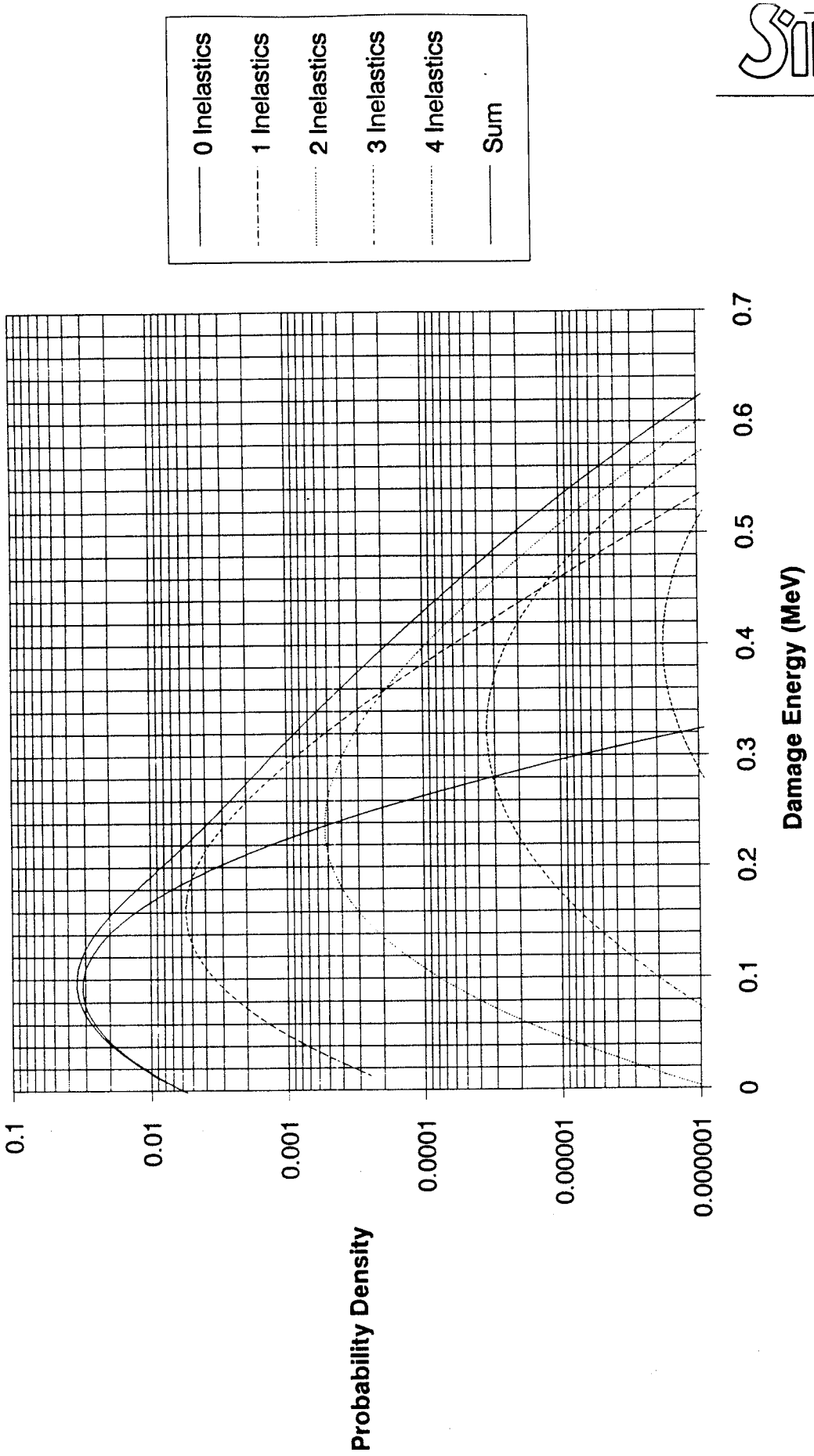

Figure 9-2 Approximation to the complete damage distribution for 5.37×10^9 12MeV p/cm^2 (V=1300μm^3)

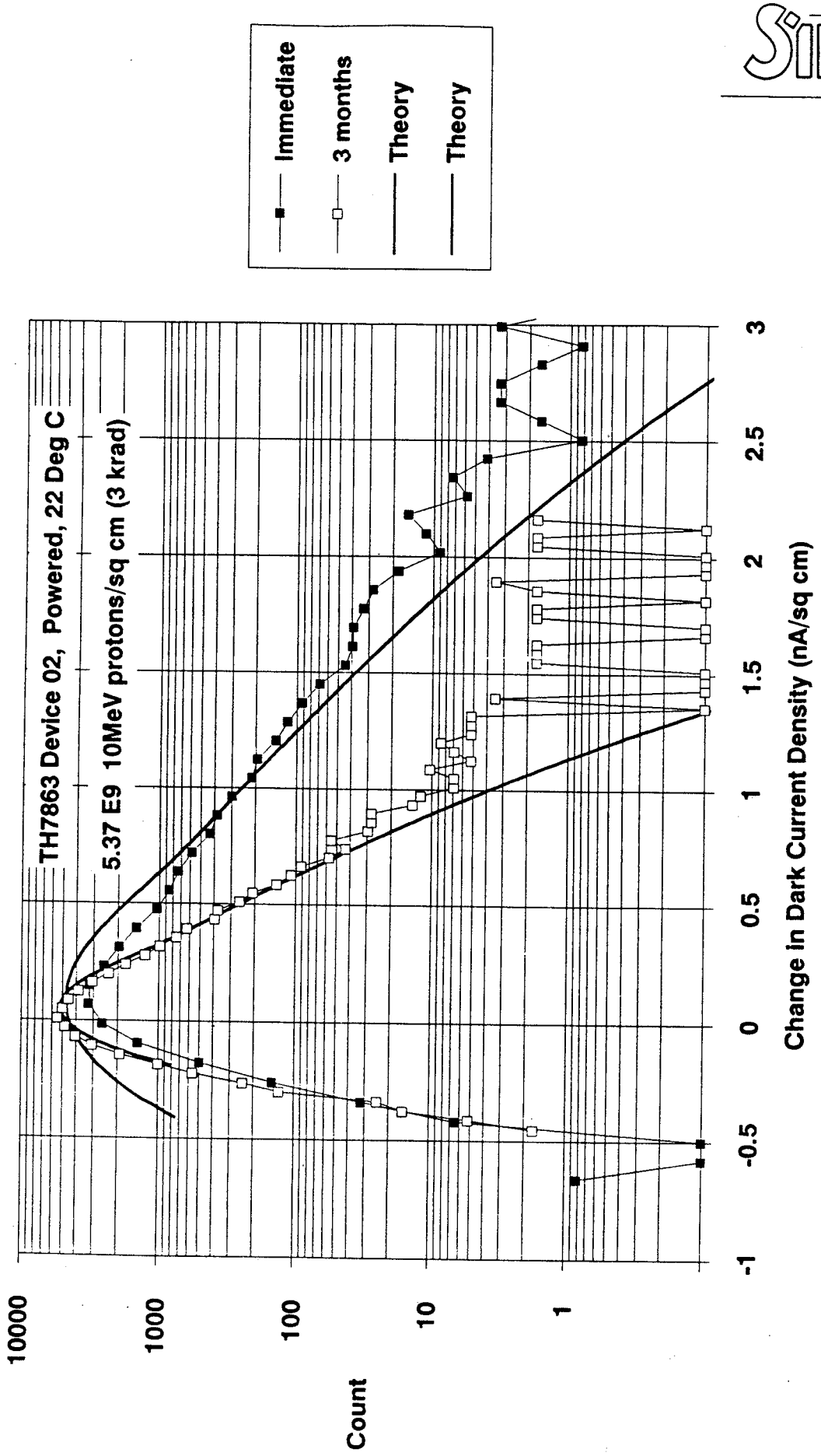

Figure 9-3 Dark current histograms for a TH7863 device given 5.37×10^9 10MeV p/cm^2 and theoretical fits

A/9058/00

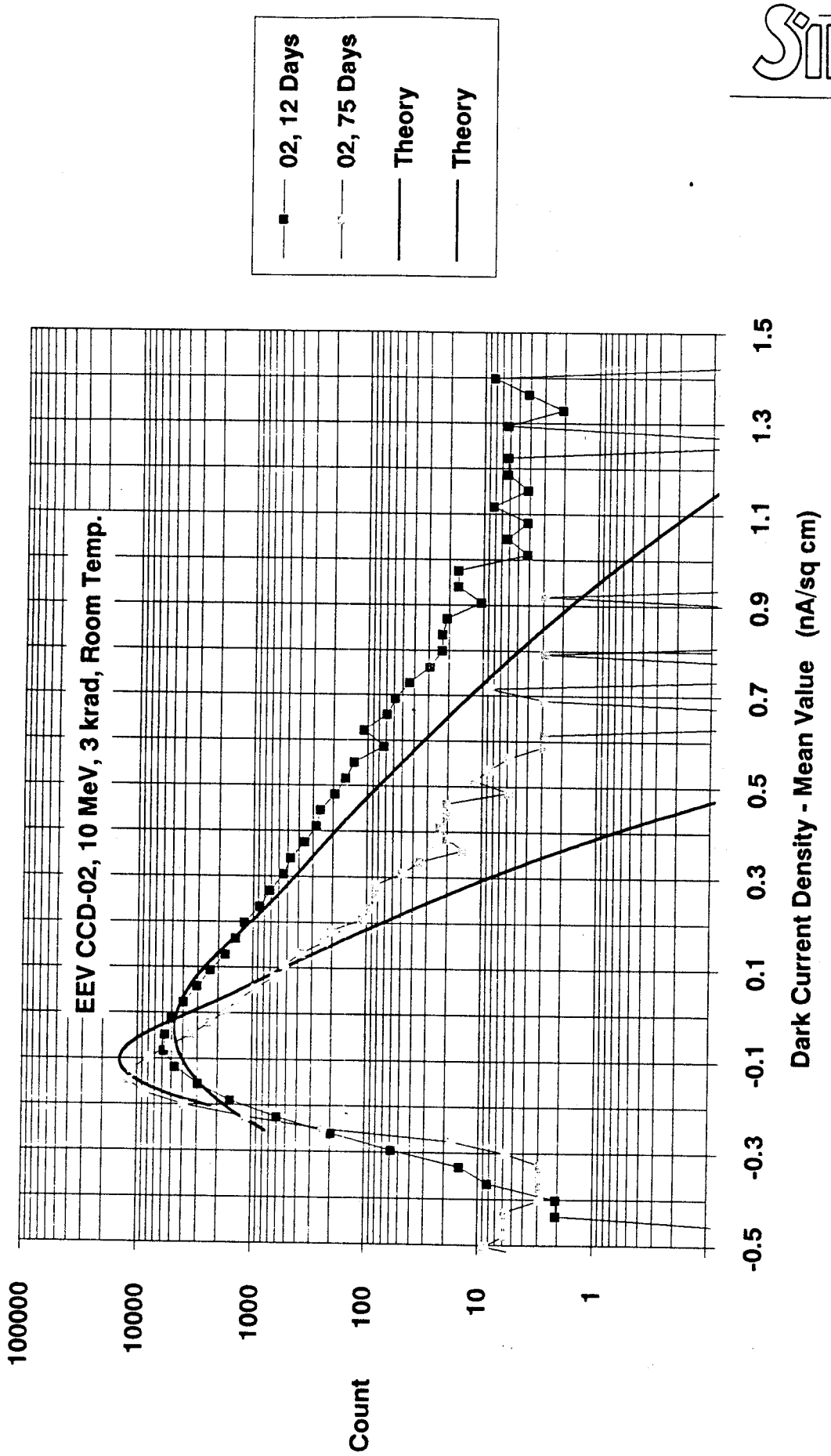

Figure 9-4 Dark current histograms for an EEV CCD-02 device gives 5.37×10^9 10MeV p/cm^2 and theoretical fits

10. DISCUSSION

10.1 Implications for the SILEX Programme

The effect of proton radiation damage should be assessed in relation to the particular modes of operation of the CCDs in the SILEX application and the performance required. A detailed study is not within the scope of the present work but a brief summary of the likely implications is given here.

The tracking sensors (which would use the THX31160) run at a high readout speed (~10 kHz) and so the mean dark charge level (and its shot noise) should not be a problem. The dark charge non-uniformity is more significant, since this produces offsets in the measured beam position. The tracking system works on a nulling principal with the light spot illuminating the central 2x2 block of pixels for most of the time. Whether the amount of DSNU found here (which is comparable with the worst case results from the Co^{60} study [1]) will degrade performance can only be ascertained by detailed system modelling but if so then there is always the option of in-flight calibration (ie. dark charge mapping). The same considerations apply to response nonuniformity. Large signals may also suffer changes to the charge transfer efficiency (and hence changes to the profile of spot images) but these effects appear to be negligible for the SILEX conditions (this applies to the TH7863 also).

The Acquisition Sensor (which would use the TH7863) needs only to detect the beacon signals. In the present concept the signals involved are large : ~10% to 2 or 3x saturation. It was seen in [1] that after doses ~6 krad the devices would be nearly saturated with ionisation-induced dark current if operated at 35°C and continuously powered. However there is the possibility of only powering on when needed. This may save a factor ~2 on dark charge but there may still be significant problems. Certainly a variable detection threshold which takes into account the vertical dark charge slope (caused by frame transfer operation) and perhaps the horizontal large scale nonuniformity is recommended. There is also the possibility that prolonged storage under power may reduce the reverse annealing effects found here (which were obtained with unpowered storage) however this requires more investigation. Other options are to use a thermoelectric cooler to reduce the CCD temperature or to increase the shielding provided by the instrument and hence reduce the accumulated dose (by this mean a dose of ~2 krad can probably be achieved for LEO and 5 krad for GEO). It would appear that the nonuniformity found here for proton-induced displacement damage will not be significant compared with the large changes in surface generated dark current. Field enhancement of some spikes does seem to occur but the multiplication factor (related to the field strength in the CCD) is much less than for virtual phase devices.

It may be that full confidence in systems operation can only be achieved by using breadboard systems employing previously irradiated CCDs.

Changes in V_{DR} threshold voltages are consistent with the findings of [1] where it was stated that the changes were ~0.1V/krad for both device types when continuously powered. This limits powered operation to doses ~15 krad(s) or less depending on the margin of safety required. Again, running the CCDs unpowered for part of the time will reduce the effects. Similarly, there are modest changes (~10% for 15 krad) in I_{DD} currents for both CCDs which will affect the power consumption and this should be allowed for in systems budgets. Monitoring of I_{DD} currents gives a useful measure of accumulated dose and could be employed in flight. Accurate dosimetry might prove useful in deciding such things as power on/off duty cycles and switching between redundant and non-redundant units.

If use were to be made of devices manufactured with the EEV process rather than Thomson devices (for either the acquisition or tracking sensors) then it would be expected, from the present data, that the dark current increases would be considerably less. There would also be the possibility of operating with the CCD surface under inversion (which suppresses surface generated dark charge).

10.2 Implications for Other Programmes

It is difficult to speculate about the implications for other missions which will use CCDs because of the wide variety of use conditions which range from slow-scan, cooled, applications such as x-ray, IR, or visible astronomy to high speed, room temperature, operation in for example tracking and acquisition (or scene visualisation) systems. However we make the following general comments regarding proton testing for bulk displacement damage effects:

i) It appears that for the Thomson-CSF and EEV devices displacement damage is independent of bias state during irradiation. Operating unbiased can save costs if the transport of test equipment to the radiation facility can be avoided (eg. by arranging fast transport of devices back to the laboratory for quick-look testing before annealing effects occur).

ii) Long term storage at room temperature seems to reduce the damage and this should be allowed for; however the effect of re-irradiation of a previously annealed device has not been studied to see if damage proceeds at a faster rate. Acceleration of the annealing process using high temperatures (ie. temperatures higher than the mission operation temperature) may however be unwise since the activation energy for annealing is unknown.

iii) Using data at a small number of discrete proton energies to predict the effects for the overall space environment is possible in principle, but to predict dark charge effects requires a knowledge of the damage energy and its variance for a range of proton energies. However the computer simulations involve use of multiple convolutions and are somewhat time consuming. Also there are uncertainties as to whether the same types of lattice defects are created at all energies and as to the nature of annealing effects. These subjects are in need of further exploration.

iv) It appears that CTE degradation for SILEX conditions can be ignored. Applications such as space-based astronomy which use CCDs under different conditions are known to be prone to proton-damaged induced CTE problems. It is not known to what extent applications such as high accuracy star tracking (which are also sensitive to CTE - see para 6.8) will be affected. This is another subject in need of further study.

v) In view of the errors involved in predicting ionisation damage from proton tests it is recommended that Co^{60} gamma ray irradiation is used instead (as, in fact, is common practice). Proton tests can be used as confirmation, if necessary.

vi) All the measurements discussed so far have been for protons at normal incidence to the CCD. In space the flux is omnidirectional. This can be expected to give some differences in damage.

vii) For dark charge non-uniformity it would seem that high energy protons are the most important in causing damage. This may be true for CTE also, once directional effects (vi, above) and the extended nature of the proton spectrum in a space environment (on a linear scale) are taken into account. (c.f [29a]).

viii) Batch dependence of radiation effects (ie. variations with CCD lot) cannot be ruled out at this stage (and have been noticed with EEV devices [43]) and tests should, if possible, be carried out on a systematic basis with chips all from the same diffusion lot.

10.3 Suggestions for Future Work

General areas in need of further study have been briefly considered in para 10.2. Here we make suggestions directly relevant to SILEX and closely related programmes.

i) It would be useful to compare the 1.5 and 10MeV damage with effects at a higher proton energy, eg. 63 or 22MeV (these energies are chosen since we have the nuclear parameters from the NRL work [31]). Spare CCDs are available for this.

ii) It would be useful to measure the effect of re-irradiating some devices to see if the rate of increase of dark charge is the same after the previous irradiation and annealing steps as it was initially.

iii) The batch dependence of ionisation damage has not been fully covered. It is recommended that radiation effects for candidate flight batches are fully explored as part of lot acceptance testing (LAT).

iv) With the very slow reverse annealing of the image area dark current noticed with the particular lot of CCDs tested in this report, there may be some merit in using CCDs without an aluminium store shield.

11. REFERENCES

1. Hopkinson G R, "Co^{60} radiation testing of THX31160 and TH7863 CCDs for the SILEX programme", ESTEC contract report 7787/88/NL/DG (March 1991).

2. Oldham T R, "Recombination along the tracks of heavy charged particles in SiO_2 films", J. Appl. phys., 57 (8), 2695-2702 (1985).

3. McLean F B, Boesch Jr. H E and Oldham T R, "Electron-hole generation, transport and trapping in SiO_2", in ionising radiation effects in MOS devices and circuits, eds Ma T P and Dressendorfer PV (Wiley interscience, New York, 1989).

4. Winokur P S, "Radiation-induced interface traps" ibid.

5. Deal B E, "The current understanding of charges in the thermally oxidised silicon structures", J. Electrochem Soc, 121, 198C (1974).

6. Aitken J M, "1μm MOSFET VLSI Technology : Part III - radiation effects", IEEE J. Solid State Circuits, SC-14 (2), 294 (1979).

7. Ziegler J F, Biersack J P and Littmark U, The stopping and range of ions in solids, (Pergamon Press, 1985), PC version developed by Biersack J P and Ziegler J F, IBM-Research, York Town, New York 10598, USA.

8. Benedetto J M and Boesch Jr. H E, "The relationship between Co^{60} and 10keV damage in MOS devices", IEEE Trans. on Nuclear Science, NS-33(6), 1318 (1986).

8a. Tallon R W, Kemp W T, Ackermann M R, Owen M H and Hoffland A H, "Radiation damage in MOS transistors as a function of the angle between an applied electric field and various incident radiations (protons, electrons and Co^{60} gamma rays)", IEEE Trans on Nuclear Science, NS-34(6), 1208-1213 (1987).

9. Burke E A, "Energy dependence of proton-induced displacement damage in silicon", IEEE Trans. on Nuclear Science, NS-33(6), 1276-1281 (1986).

10. Dale C J, Marshall P W, Burke E A, Summers G P and Wolicki E A, "High energy electron-induced displacement damage in silicon", IEEE Trans. on Nuclear Science, NS-35(6), p1208-1214 (1988).

11. Summers G P, Burke E A, Dale C J , Wolicki E A, Marshall P W and Gehlhausen M A, "Correlation of particle-induced displacement damage in silicon", IEEE Trans. on Nuclear Science, NS-34(6), 1134-1139 (1987).

12. Burke E A, Dale C J, Campbell A B, Summers G P, Stapor W J, Xapsos M A and Palmer T, "Energy dependence of proton-induced displacement damage in Gallium Arsenide", IEEE Trans. on Nuclear Science, NS-34(6), 1220-1226 (1987).

13. Troxell J R, "Ion-implantation associated defect production in silicon", Solid State Electronics, 26(6), 539-548 (1983).

14. Fengmei W and Xiangqin Z, "Structure of electron-induced defects in silicon", in Properties of Silicon, emis datareviews no.4 (IEE, INSPEC, 1988).

15. Svensson J H, Svensson BG and Monemar B, "Infrared absorption studies of the divacancy in silicon : new properties of the singly negative charge state", phys. Rev B, 38(6), 4192-4197 (1988).

16. Kimerling L C, "New developments in defect studies in semiconductors", IEEE Trans. on Nuclear Science, NS-23(6), 1497-1505 (1976).

17. Janesick J, Soli G, Elliott T and Collins S, "The effects of proton damage on charge-coupled devices", Proc. SPIE, 1447 (1991).

18. Kimerling L C, Asom M T, Benton J L, Drevinsky P J and Caefer C E, "Interstitial defect reactions in silicon", Materials Science Forum Vols 38-41, 141-150 (1989).

19. Asom M T, Benton J L, Sauer R and Kimerling L C, "Interstitial defect reactions in silicon", Appl. Phys. Lett. 51(4), 256-258 (1987).

20. Song L W, Benson B W and Watkins G D, "Identification of a bistable defect in silicon : the carbon-interstatial carbon substitutional pair", Appl. Phys. Lett. 51(15), 1155-1157 (1987).

21. Song L W, Benson B W and Watkins G D, "New vacancy-related defects in n-type silicon", Phys. Rev B, 33(2), 1452-1455 (1986).

22. Benton J L, Asom M T, Sauer R and Kimerling L C, "Identification of interstitial carbon related defects in silicon" in Defects in Electronic Materials, Stavola M, Pearton S J and Davies G (eds), Mater. Res. Soc. Proc., 104, 85-91 (Pittsburgh, 1988).

23. Hallen A, Sundqvist B U R, Paska Z, Svensson B G, Rosling M and Tiren J, "Deep level transient spectroscopy analysis of fast ion tracks in silicon", J. Appl. Phys., 67(3), 1266-1271 (1990).

24. Bourgoin J and Lanoo M, Point defects in Semiconductors II, Ch9. (Springer Verlag, Berlin, 1983).

25. Sze S M, Physics of semiconductor devices (2nd edn.), p90 (Wiley Interscience, New York, 1981).

26. Mohsen A M and Tompsett M F, "The effects of bulk traps on the performance of bulk channel charge-coupled devices", IEEE Trans. on Electron Devices, ED-21 (11), 701-712 (1974).

27. Kimata M, Denda M, Yutani N, Tsubouchi N N and Uematsu S, "Low-temperature characteristics of buried channel charge-coupled devices", Japanese J. Appl. Phys. 22(6), 975-980 (1983).

28. Collett M G, "The influence of bulk traps on the charge-transfer inefficiency of bulk charge-coupled devices", IEEE Trans. on Electron Devices, ED-23(2), 224-227 (1976).

29. Dale C J, Marshall P W, Burke E A, Summers G P, and Bender G E, "The generation lifetime damage factor and its variance in silicon", IEEE Trans. on Nuclear Devices, NS-36(6), 1872-1881 (1989).

29a. Dale C J, Marshall P W and Burke E A, "Particle-induced displacement damage in silicon imagers", in charge coupled devices and solid state optical sensors II, Proc SPIE 1447 (1991).

30. Srour J R and Hartmann R A, "Enhanced displacement damage effectiveness in irradiated silicon devices", IEEE Trans. on Nuclear Science, NS-36(6), 1825-1830 (1989).

31. Marshall P W, Dale C J and Burke E A, "Proton-induced displacement damage distributions and extremes in silicon microvolumes", IEEE Trans. on Nuclear Science, NS-37(6), 1776-1783 (1990).

32. Dale C J, Marshall P W and Burke E A, "Particle-induced dark current fluctuations in focal plane arrays", IEEE Trans. on Nuclear Science, NS-37(6), 1784-1791 (1990).

33. Pavelka T and Ferenczi G, "Interpretation of the electric field dependent thermal emission data of deep traps", Materials Science Forun, 38-41, 803-808 (1989).

34. Hopkinson G R and Ch. Chlebek, "Proton damage effects in an EEV CCD imager", IEEE Trans. on Nuclear Science, NS-36(6), 1865-1871 (1989).

35. Marshall P W, Dale C J, Burke E A, Summers G P and Bender G E, "Displacement damage extremes in silicon depletion regions", IEEE Trans. on Nuclear Science, NS-36(6), 1831-1839 (1989).

36. Abbey A, Holland A and McCarthy K, "Further proton damage effects in EEV charge-coupled devices", presented at the ESA Electronics Components Conference, ESTEC, Noordwijk, The Netherlands, 12-16 November. ESA SP-313, 307-318 (1991).

37. Saks N S, "A technique for suppressing dark current generated by interface states in buried channel CCD imagers", IEEE Electron Device Letters, EDL-1(7), 131-133 (1980).

38. Dunston D J, "Indirect energy gap of Si, temperature dependence", Emis datareviews no.4 (IEE, INSPEC, 1988).

39. Burke B E, and Gajar S A, "Dynamic suppression of interface-state dark current in buried channel CCDs", IEEE Trans. on Electron Devices, ED-38(2), 285-290 (1991).

40. Grove A S and Fitzgerald D J, "Surface effects on p-n junctions : characteristics of surface space-charge regions under non equilibrium conditions", Solid State Electronics, 9, 783-806 (1966).

41. Letaw J R, Silberberg R and Tsao C H, "Proton-nucleus total inelastic cross-sections : an empirical formula for E> 10MeV", Astrophys J. Suppl., 51, 271-276 (1983).

42. Janni J F, "Proton range-energy tables", Atomic and Nuclear Data Tables, 27 (2/3), 147-529 (1982).

43. Hopkinson G R, "Space radiation effects on CCDs", presented at the ESA Electronics Components Conference, ESTEC, Noordwijk, The Netherlands, 12-16 November 1990. ESA SP-313, 301-306 (1991).